Journal of Heat Transfer

Published Monthly by ASME

VOLUME 127 • NUMBER 5 • MAY 2005

Transactions of the ASME, Journal of Heat Transfer (ISSN 0022-1481) is published monthly by The American Society of Mechanical Engineers, Three Park Avenue, New York, NY 10016. Periodicals postage paid at New York, NY and additional mailing offices. POSTMASTER: Send address changes to Transactions of the ASME, Journal of Heat Transfer, c/o THE AMERICAN SOCIETY OF MECHANICAL ENGINEERS, 22 Law Drive, Box 2300, Fairfield, NJ 07007-2300.
CHANGES OF ADDRESS must be received at Society headquarters seven weeks before they are to be effective. Please send old label and new address.
STATEMENT from By-Laws. The Society shall not be responsible for statements or opinions advanced in papers or ... printed in its publications (B7.1, Para. 3), **COPYRIGHT**

The ASME Journal of Heat Transfer is abstracted and indexed in the following:

Applied Science and Technology Index, Chemical Abstracts, Chemical Engineering and Biotechnology Abstracts (Electronic equivalent of Process and Chemical Engineering), Civil Engineering Abstracts, Compendex (The electronic equivalent of Engineering Index), Corrosion Abstracts, Current Contents, E & P Health, Safety, and Environment, Ei EncompassLit, Engineered Materials Abstracts, Engineering Index, Enviroline (The electronic equivalent of Environment Abstracts), Environment Abstracts, Environmental Engineering Abstracts, Environmental Science and Pollution Management, Fluidex, Fuel and Energy Abstracts, Index to Scientific Reviews, INSPEC, International Building Services Abstracts, Mechanical & Transportation Engineering Abstracts, Mechanical Engineering Abstracts, METADEX (The electronic equivalent of Metals Abstracts and Alloys Index), Petroleum Abstracts, Process and Chemical Engineering, Referativnyi Zhurnal, Science Citation Index, SciSearch (The electronic equivalent of Science Citation Index), Theoretical Chemical Engineering

Journal of Heat Transfer

Preface

Special Issue on Gas Turbine Heat Transfer: Part 2

It is with great pleasure that we present this issue of the ASME J. of Heat Transfer to the heat transfer community dedicated to *Gas Turbine Heat Transfer*. Part 1 appears in the April 2005 issue. Gas turbines are used in military and commercial aircraft, and for land-based power generation, and contribute significantly to the nation's economy. In modern gas turbine engines, the turbine inlet temperatures exceed the operating limits of the turbine blades, and one of the major technical challenges is the ability to effectively cool the turbine components with minimum coolant usage. Improvements in turbine efficiencies can be achieved with higher turbine inlet temperatures, and therefore, there is a significant ongoing effort in the gas turbine community (industry, academia, and federal laboratories) to explore new materials and material coatings that can withstand higher temperatures, and to explore more effective cooling strategies.

The special issues are an effort to communicate to the larger heat transfer community the opportunities and challenges in gas turbine heat transfer. The issues consist of 2 Technology Reviews (one on film cooling and the other on impingement cooling), 14 full-length Research Papers, and 2 Technical Briefs. The topics covered run the gamut of cooling strategies, both internal and external, and the authors represent researchers from both academia and industry. It is our hope that these issues will serve as a resource for researchers in the gas turbine field and that it will motivate new researchers looking for challenging problems.

This preface ends with a note of thanks to all of the contributing authors in this special issue on *Gas Turbine Heat Transfer*. It is no coincidence that so many papers in one topic area become available for publication simultaneously. This requires considerable effort and discipline on the part of the authors and reviewers, as well as the ASME Journal of Heat Transfer publishing staff. Accordingly, we acknowledge the enthusiastic support and help we received from many reviewers who worked hard to meet the stringent deadlines of the review process for these issues. We also acknowledge the continuous encouragement and support we received from Professor Vijay Dhir in bringing out these special issues, and the wonderful help provided by Jenell Rae, Editorial Assistant for the ASME Journal of Heat Transfer, who patiently guided us and the authors from start to finish. All must be commended and we hope that you, the reader, will benefit from, and appreciate, these efforts.

Sumanta Acharya
Louisiana State University

Phil Ligrani
University of Utah

Heat Transfer, Pressure Loss and Flow Field Measurements Downstream of Staggered Two-Row Circular and Elliptical Pin Fin Arrays

Oguz Uzol

Cengiz Camci

Turbomachinery Heat Transfer Laboratory,
Pennsylvania State University,
University Park, PA 16802

This paper presents the results of heat transfer, total pressure loss, and wake flow field measurements downstream of two-row staggered elliptical and circular pin fin arrays. Two different types of elliptical fins are tested, i.e., a Standard Elliptical Fin (SEF) and a fin that is based on NACA four digit symmetrical airfoil shapes (N fin). The results are compared to those of a corresponding circular pin fin array. The minor axis lengths for both types of elliptical fins are kept equal to the diameter of the circular fins. Experiments are performed using Liquid Crystal Thermography and total pressure probe wake surveys in a Reynolds number range of 18 000 and 86 000 as well as Particle Image Velocimetry (PIV) measurements at $Re_D = 18\,000$*. The pin fins had a height-to-diameter ratio of 1.5. The streamwise and the transverse spacings were equal to one circular fin diameter, i.e.,* $S/D = X/D = 2$*. For the circular fin array, average Nusselt numbers on the endwall within the wake are about 27% higher than those of SEF and N fin arrays. Different local heat transfer enhancement patterns are observed for elliptical and circular fins. In terms of total pressure loss, there is a substantial reduction in case of SEF and N fins. The loss levels for the circular fin are 46.5% and 59.5% higher on average than those of the SEF and N fins, respectively. An examination of the Reynolds analogy performance parameter show that the performance indices of the SEF and the N fins are 1.49 and 2.0 times higher on average than that of circular fins, respectively. The thermal performance indices show a collapse of the data, and the differences are much less evident. Nevertheless, N fins still show slightly higher thermal performance values. The wake flow field measurements show that the circular fin array creates a relatively large low momentum wake zone compared to the SEF and N fin arrays. The wake trajectories of the first row of fins in circular, SEF and N fin arrays are also different from each other. The turbulent kinetic energy levels within the wake of the circular fin array are higher than those for the SEF and the N fin arrays. The transverse variations in turbulence levels correlate well with the corresponding local heat transfer enhancement variations.* [DOI: 10.1115/1.1860563]

Keywords: Elliptical Pin Fins, Turbine Blade Cooling, Liquid Crystal Thermography, Particle Image Velocimetry

Introduction

Efficient internal cooling of turbine blades can be achieved by enhancing the heat transfer in internal coolant passages while keeping the related pressure losses as low as possible. In-line and staggered arrays of short cylindrical pin fins with circular cross sections are one of the most common types of internal cooling devices used for this purpose. These pin fin arrays enhance the heat transfer by increasing the turbulence and unsteadiness of the coolant flow within their wakes. However, it is by no means clear that the circular cylinder is the most efficient geometry in terms of both heat transfer enhancement and pressure loss minimization.

Most of the previous pin fin research are mainly investigations on the heat transfer and pressure loss characteristics of different array configurations with circular pin fins (e.g., Brown et al. [1], Van Fossen [2], Metzger and Haley [3], Simoneau and Van Fossen [4], Metzger et al. [5], Lau et al. [6], Chyu et al. [7], Al Dabagh and Andrews [8], Hwang and Lui [9], Ligrani and Mahmood [10], and Won et al. [11]). A review of heat transfer and pressure loss data for staggered arrays of circular pin fins in turbine cooling applications is performed by Armstrong and Winstanley [12]. More recently, Ligrani et al. [13] compared various heat transfer augmentation techniques used in internal coolant passages, including pin fins. There has also been some effort in investigating different pin fin shapes and concepts as alternatives to circular fins. For example, oblong pin fins (Metzger et al. [14]), partial length circular pin fins (Steuber and Metzger [15], Arora and Abdel-Messeh [16]), tapered pin fins (Wang and Ji [17]), diamond-shaped pin fins (Grannis and Sparrow [18], Chyu et al. [19]), square pin fins (Minakami et al. [20], Chyu et al. [19]), stepped diameter circular pin fins (Goldstein et al. [21]), elliptical pin fins Li et al. [22] and drop-shaped pin fins (Chen et al. [23]) are investigated. However, detailed information on the endwall heat transfer enhancement characteristics, wake flow fields, generated turbulence levels or transverse distributions of aerodynamic penalty levels is hard to find for those proposed pin fin concepts.

This paper presents the results of an experimental investigation on the endwall heat transfer enhancement, total pressure loss, and wake flow field characteristics of circular and elliptical pin fin arrays. Two different types of elliptical pin fin arrays are investigated: a Standard Elliptical Fin (SEF) and an N fin, which is derived from NACA four-digit symmetrical airfoil series. Experi-

Manuscript received January 28, 2004; revision received September 2, 2004. Review conducted by: P. M. Ligrani.

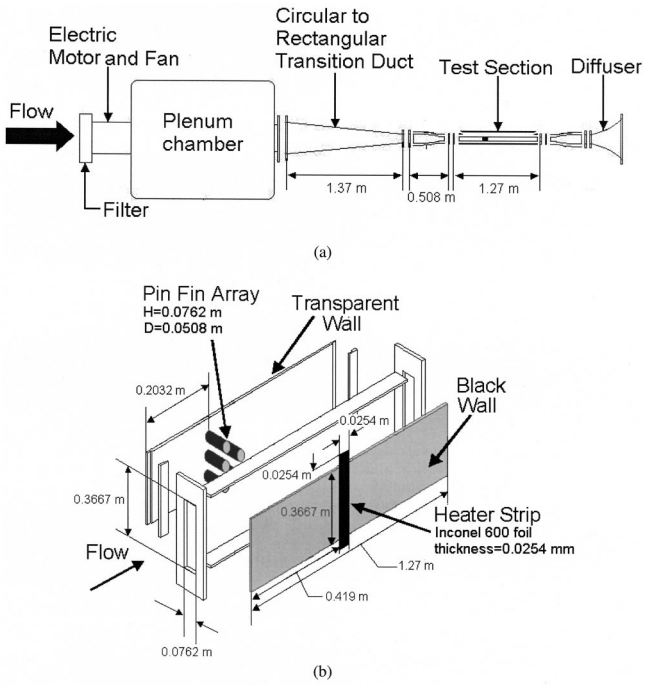

Fig. 1 (*a*) Low Speed Heat Transfer Research Facility at Pennsylvania State University and (*b*) the layout and the dimensions of the acrylic test section shown in (*a*)

ments include measurements of convective heat transfer coefficients on the endwall within the wakes using Liquid Crystal Thermography, total pressure loss surveys by Kiel probe traverses and two-dimensional Particle Image Velocimetry (PIV) measurements within the wakes at the midplane of the test section. Measurements are performed in a Reynolds number range of 18 000 and 86 000 (based on the maximum velocity and the circular fin diameter) and for 2-row staggered array configurations with $S/D = X/D = 2.0$ and $H/D = 1.5$. The minor axis lengths for both types of elliptical fins are kept equal to the diameter of the circular fins in order to obtain the same effective frontal area. The heat transfer enhancement, total pressure loss, and wake flow field characteristics are compared to those of a circular fin array.

Experimental Setup and Procedures

A Facility. The experiments are performed at the "Low Speed Heat Transfer Research Facility" at the Turbomachinery Heat Transfer Laboratory of the Pennsylvania State University. This is an open-loop wind tunnel that consists of an axial air blower, a diffuser with multiple screens, a plenum chamber, a high area ratio circular nozzle, a circular to rectangular transition duct, a converging nozzle, the test section, a diverging nozzle, and a diffuser. The schematic of the facility is shown in Fig. 1(*a*).

An axial flow fan is used to draw the ambient air into the facility. A $0.66\times0.66\times0.39$ m^3 filter box encloses the inlet of the axial fan. A 7.5 kW electric motor drives the 0.46 m tip diameter fan, which has a potential to provide a pressure differential of 0.15 m of water over a range of flow rates. The speed of the electric motor is controlled by using an adjustable frequency ac drive. After the fan, the flow passes through a series of screens and enters a 1.73 m^3 plenum chamber. Downstream of the plenum the air accelerates through a circular nozzle of area ratio 8.65, and then transitions to a 0.3667×0.15 m^2 rectangular cross section by a 1.37 m long duct. The cross section is further reduced to 0.3667×0.076 m^2 by a converging rectangular cross-section nozzle that is 0.508 m long. After the converging nozzle there is the test section that is a 1.27 m long straight rectangular duct made out of 0.0127 m thick clear acrylic and has a 0.3667×0.076 m^2 cross section (Fig. 1(*b*)).

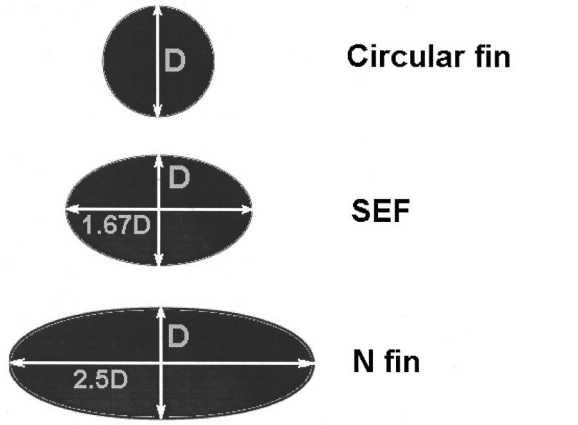

Fig. 2 The shapes and relative dimensions of the circular fin, Standard Elliptical Fin (SEF), and the N fin ($D = 0.0508$ m)

B Pin Fin Shapes. One circular and two different elliptical pin fin shapes are investigated in the current study. The shapes and the relative dimensions of the elliptical fins are presented in Fig. 2. The elliptical fins are defined as follows:

i. The Standard Elliptical Fin (SEF): This pin fin has a standard elliptical cross section with the minor axis length being equal to the circular fin diameter, resulting in the same effective frontal area as the circular fin. This is necessary in order to be able to make meaningful comparisons of total pressure loss levels. The major axis length is 1.67 times the minor axis length. The surface area is 1.35 times the surface area of the circular fin.

ii. The N Fin: This fin shape is derived from the NACA four-digit symmetrical airfoil series. The thickness distribution for the four-digit series of airfoils is given in Abbott and Von Doenhoff [24] as

$$y = \frac{t_C}{0.2}(0.29690\sqrt{x} - 0.12600x - 0.3516x^2 + 0.2843x^3 - 0.1015x^4), \quad (1)$$

where t_C is the maximum thickness as a fraction of the chord length. This distribution gives the maximum thickness at a 30% chord location. In order to obtain the N fin shape, the NACA0024 airfoil is taken as a basis, which has 24% maximum thickness, and only the airfoil geometry up to the maximum thickness location is used to construct the forward half of the fin. The backward half is constructed by taking the mirror image of the forward half. Similar to SEF, the minor axis length is equal to the diameter of the circular fin. The major axis length is 2.5 times the minor axis length, and the surface area of the N fin is 1.85 times larger than the surface area of the circular fin.

C Setup. The pin fin arrays are placed approximately $4D$ downstream from the entrance of the test section (D is the diameter of a circular fin, $D = 0.0508$ m). Figure 3(*a*) shows the layout of the staggered pin fin array configuration. Although the flow properties are not fully developed, but developing in this region and the pin fins were placed in the entry length of the test section, the upstream inlet velocity and thermal boundary conditions were carefully measured, monitored, and kept the same for all pin fin shapes and Reynolds numbers used in this study, in order to ensure the validity of the relative heat transfer and pressure loss comparisons presented in this paper. These measurements were performed at the test section inlet, $4D$ upstream of the pin fins,

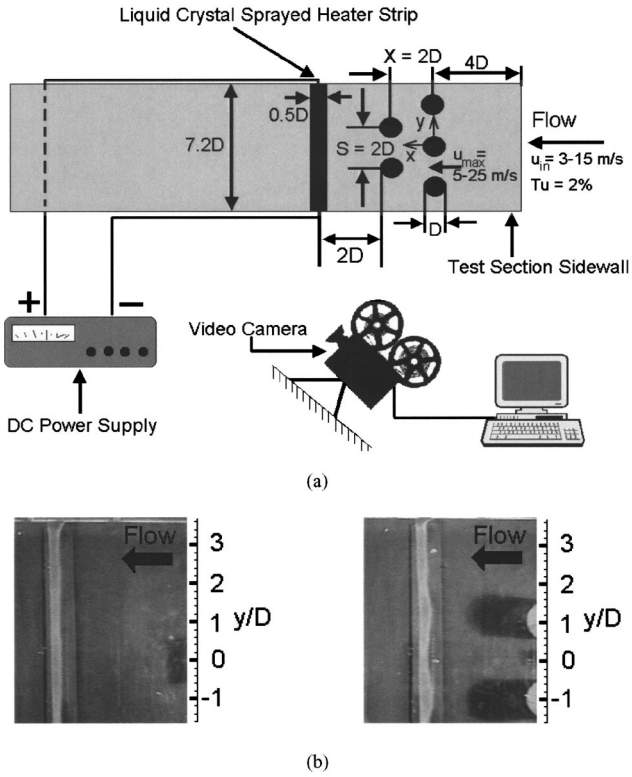

Fig. 3 (*a*) Layout of the two-row staggered pin fin configuration within the test section, and the end wall heat transfer measurement setup using Liquid Crystal Thermography and (*b*) sample images of the liquid crystal sprayed heater strip for empty tunnel (left) and with circular fin array (right) cases

and on the centerline, using a pitot-static probe and a thermistor-based temperature sensor. The inlet velocity changed between 3–15 m/s. The speed of the electric motor was precisely adjusted to obtain the same inlet velocity for different pin fin arrays, at the desired Reynolds numbers.

The duct continues up to 10D downstream of the arrays. The height to diameter ratio (H/D) of the pin fins is 1.5, which is a typical value for turbine blade cooling applications (Armstrong and Winstanley [12]). The pin fin arrays are placed inside the test section in a staggered array configuration consisting of two rows of fins, with three fins in the first row and two fins in the second row (Fig. 3(*a*)). The transverse and streamwise distance between each fin is taken equal to the diameter of the circular fin such that $S/D=X/D=2$. Using only two rows of pin fins is not enough to establish a fully developed pattern inside the test section. However, it was sufficient for determining the relative endwall heat transfer enhancement, total pressure loss, and wake flow field characteristics.

D Heat Transfer Measurement Procedure. Measurements of convective heat transfer coefficients on the endwall downstream of the pin fin arrays are performed using Liquid Crystal Thermography. For this purpose a rectangular Inconel 600 foil heater strip, which is 0.0254 m (0.5D) wide, 0.419 m (8.2D) long, and 0.0254 mm thick, is placed 2D downstream of the arrays and attached on the tunnel sidewall. The length of the heater strip that is inside the test section and exposed to the flow is 7.2D. The heater strip material, Inconel 600, is a low resistivity steel foil, which has a low temperature coefficient of resistivity ($0.112\times10^{-3}\,°\mathrm{C}^{-1}$). This restrains a change in resistance of the foil within the experimental temperature range (less than 0.5%). Although the width of the heater strip is small compared to the pin fin diameter and tunnel dimensions, it was sufficient for obtaining line distributions of the convective heat transfer coefficient along the centerline of the heater strip. The heater strip height allowed 0.0254 m excess on either end of the strip for bus bar connections to the dc power supply. The strip surface is painted black in order to obtain the best color contrast for the liquid crystals. A thin coat of liquid crystals with an event temperature of approximately 45 deg and a bandwidth of 1 deg is sprayed onto the black painted heater strip. Figure 3(*a*) shows the experimental setup for endwall heat transfer measurements.

During an experiment, a dc voltage is applied across the heater strip, which was measured using a four-wire arrangement. The applied dc voltage results in an increase in the surface temperatures on the heater strip, which in turn results in the appearance of color bands on the surface due to the thermochromic properties of the liquid crystal material. The dc voltage is started from zero and slowly increased until the color bands started to appear. At this point, steady-state conditions are allowed to be reached, and then a 352×240 pixels^2 color image of the black tunnel sidewall, with the heater strip in the field of view, is captured in bitmap format through a video camera and a computer. After the image is recorded, the power to the heater strip is then increased causing a shift in the position of the color bands. This process is repeated until the color bands have covered the entire heater strip surface. The illumination during this procedure is supplied by two 150 W incandescent light bulbs in reflectors positioned on either side of the test section. Direct radiative heating of the liquid crystal coated surface is minimized by only illuminating the lights when data were being taken. Figure 3(*b*) shows sample images of the liquid crystal sprayed heater strip both for the empty tunnel and circular fin cases.

The recorded images are analyzed to obtain the hue, saturation, intensity (HSI) information on the heater strip. The hue attribute is used to determine the surface temperature at a given pixel location on the image using the calibration curve (Uzol [25]). The calibrations were performed in situ and with the same lighting used in the experiments. For each pixel row on the column of pixels corresponding to the heater strip in the original image (about 25 pixels), hue values around the centerline of the heater strip are determined using standard conversion formulas from Red Green Blue (RGB) to HSI (Russ [26]). Although the strip covered a region of about 25 pixels, the useful color information was generally obtained from about 10 pixels. The streamwise variation in heat transfer along these 10 pixels was less than 2%. The intensity values are used for filtering. Intensities lower than 50 usually cause the hue values to become unstable and the pixel cannot be used to obtain the accurate temperature (Camci et al. [27]). Also if the intensity value of a pixel exceeds 200, the hue value becomes less accurate due to the saturation of the sensor in the video camera. Therefore, a filtering process is performed such that any pixels with intensities less than 50 and higher than 200 are rejected. Also, if the hue value for a pixel is outside the calibration range, that pixel is not considered. Using this filtering procedure, the valid pixels and corresponding hue values around the centerline are determined and the endwall temperatures are calculated using the calibration curve. The temperature values around the centerline are then used to determine the average temperature on the centerline of the heater strip for each power setting. The minimum number of valid pixels used in this averaging process is also controlled such that if this number is below a certain value, that pixel row is skipped.

The convective heat transfer coefficient, h, at the centerline of the heater strip at each pixel row is then calculated from Newton's Law of Cooling,

$$h=\frac{q''_T-q''_C-q''_R}{T_W-T_\infty}, \tag{2}$$

where q''_T is the total generated heat flux, q''_C is the conduction heat loss, q''_R is the radiation heat loss, and T_W is the measured wall temperature. The free-stream temperature, T_∞, is assumed to be

equal to the measured total temperature at the test section inlet, due to the very low Mach numbers of the current experiments.

The total generated heat flux, q''_T, on the rectangular heater strip is calculated from Joulean heating using

$$q''_T = \frac{V_S^2}{R_S A_S} \tag{3}$$

where V_S is the voltage across the heater strip, R_S is the resistance of the heater strip, and A_S is the area of the heater strip. It must be kept in mind that Eq. (3) is valid only for rectangular heater geometries with any aspect ratio. A more detailed technique to calculate the total generated heat for arbitrarily shaped boundaries is explained in detail in Wiedner and Camci [28].

The conduction heat loss term is obtained using

$$q''_C = k_W \frac{T_W - T_A}{t_W}. \tag{4}$$

Here T_A is the temperature on the ambient side of the wall, t_W is the wall thickness, and k_W is the thermal conductivity of acrylic wall. T_A is measured using a K-type cement-on thermocouple attached on the wall surface on the ambient side. The effects of lateral conduction is not accounted for in this study based both on our previous measurements in a different test setup and on the fact that even at regions with high gradients in h, the maximum temperature differences on the heater strip was less than 0.5°C, which would result in a low lateral contribution to conduction heat loss. Wiedner and Camci [28] investigated the effects of lateral conduction in their liquid crystal measurements in a 90 deg. turning duct, and found that the lateral conduction increased the total conduction heat flux by only 0.25% of the total generated heat flux. In the current study, the average conduction heat fluxes were about 18% of the average total heat flux during a typical experiment.

A blackbody enclosure model and the assumption of thermal equilibrium between the free-stream air and the unheated duct walls were used to estimate the radiative heat loss. Hence,

$$q''_R = \sigma(\epsilon_W T_W^4 - \epsilon_\infty T_\infty^4) \tag{5}$$

where σ is the Stefan–Boltzmann constant, ϵ_W and ϵ_∞ are the heater strip and tunnel wall surface emissivities, respectively. The radiation heat losses were about 7% of the total generated heat flux. The values of ϵ_W and ϵ_∞ are both taken as 0.94.

Measured convective heat transfer coefficient values are then used to calculate the Nusselt numbers using

$$\mathrm{Nu}_D = \frac{hD}{k_{\mathrm{air}}}, \tag{6}$$

where D is the diameter of the circular fin. The thermal conductivity of air, k_{air}, is determined using the inlet temperature.

Due to the nature of the measurement technique, there exists a developing thermal boundary layer along the width of the heater strip. The character of this thermal boundary layer will be similar for each pixel row on the heater strip such that the convective heat transfer coefficients will start from a maximum and will decrease as the thermal boundary layer develops. However the levels of heat transfer enhancement will be different along the length of the heater strip depending on the relative location with respect to the wake of the pin fin array. The main objective of the current experiments is to capture these differences in the levels of heat transfer enhancement for pin fin arrays with different fin shapes with different wake characteristics.

Measurements are performed for six different Reynolds numbers varying between 18 000–86 000, based on the maximum velocity and the fin diameter (or SEF/N fin minor axis length). The maximum velocity occurred between the pin fins, where the area is a minimum. It was measured using a pitot-static probe in between the pin fins at the midplane, and it changes between 5–25 m/s in this Reynolds number range. The inlet turbulence intensity is about 2%.

E Total Pressure Loss Measurement Procedure. Total pressure losses inside the wakes of the pin fin arrays are measured by traversing a Kiel probe with a 3.175 mm shield diameter across the test section $2D$ downstream of the pin fin arrays and at the midplane. Measured total pressure data are used to calculate relative total pressure loss with respect to the inlet conditions. The per row total pressure drop (or friction coefficient) is defined as

$$f = \frac{P_{t_I} - P_{t_W}}{0.5\rho u_{\max}^2 N_R}, \tag{7}$$

where P_{t_I} is the inlet total pressure, P_{t_W} is the total pressure in the wake, $u_{\max}$ is the maximum velocity in the test section, and N_R is the number of pin fin rows in the array.

In previous pin fin research, the variation in the transverse direction is not usually reported, i.e., static pressures are measured at a single point on the wall before and after the pin fin arrays and the static pressure loss across the pin fin array was used to calculate the friction coefficient (e.g., Metzger and Haley [3], Lau et al. [6], Metzger et al. [14], Steuber and Metzger [15], Chyu et al. [19], Goldstein et al. [21], Li et al. [22], Chen et al. [23], Chyu [29]). In this study, however, complete transverse distributions of the total pressure loss levels in the wakes of the pin fin arrays are measured, in order to be able to compare the effects of the different wake structures of pin fins with different shapes. Keep in mind that all the pin fins used in the current experiments have the same effective frontal area. The experiments are conducted in the same Reynolds number range as in the endwall heat transfer measurements, i.e., 18 000–86 000. Although the cause and effect relationships on the generation of pressure losses in this $3D$ flow field cannot be resolved in detail since the data is only at the midplane, it is still sufficient to make accurate relative comparisons of pressure losses generated by different pin fin shapes.

F Wake Flow Field Measurement Procedure. In order to better understand the wake flow field structure and loss mechanisms of the circular, SEF and N fin arrays, two-dimensional Particle Image Velocimetry (PIV) measurements are performed for a Reynolds number of 18 000 and on the midplane of the test section. The wake flow field is divided into five separate PIV measurement domains in the midplane, covering the halfwidth of the tunnel and up to $2D$ downstream of the second row. The flow field is seeded with fog particles using a commercial fog generator and is illuminated using a 50 mJ/pulse Nd:YAG laser sheet with an emitted radiation wavelength of 532 nm. Pairs of particle images are captured using a $1k \times 1k$ pixels^2 Kodak Megaplus ES 1.0 digital camera, which is fully synchronized with the pulsating laser sheet. After the camera and the laser sheet are aligned normal to each other, 90 instantaneous image pairs are collected for each PIV domain. The image maps are then divided into 32×32 pixels^2 interrogation areas and 25% overlap is used, which generated 1722 vectors in each vector map. All 90 image pairs are cross-correlated, peak-validated, moving averaged/filtered, and then ensemble averaged in order to obtain the true-mean flow field inside the wakes of the pin fin arrays. The ensemble-averaged values for the x and y components of the velocity vector for each and every interrogation area in the vector map are calculated using

$$\overline{u}(x,y) = \frac{1}{M}\sum_{i=1}^{M} u_i(x,y), \quad \overline{v}(x,y) = \frac{1}{M}\sum_{i=1}^{M} v_i(x,y), \tag{8}$$

where M is the total number of samples used in the ensemble averaging process. The turbulent kinetic energy is calculated using

$$k(x,y) = \frac{1}{2}\frac{1}{M}\sum_{i=1}^{M} [(u_i(x,y) - \overline{u}(x,y))^2 + (v_i(x,y) - \overline{v}(x,y))^2]. \tag{9}$$

Although the three-dimensional effects may be significant for these short ($H/D = 1.5$) pin fins, current $2D$ measurements pro-

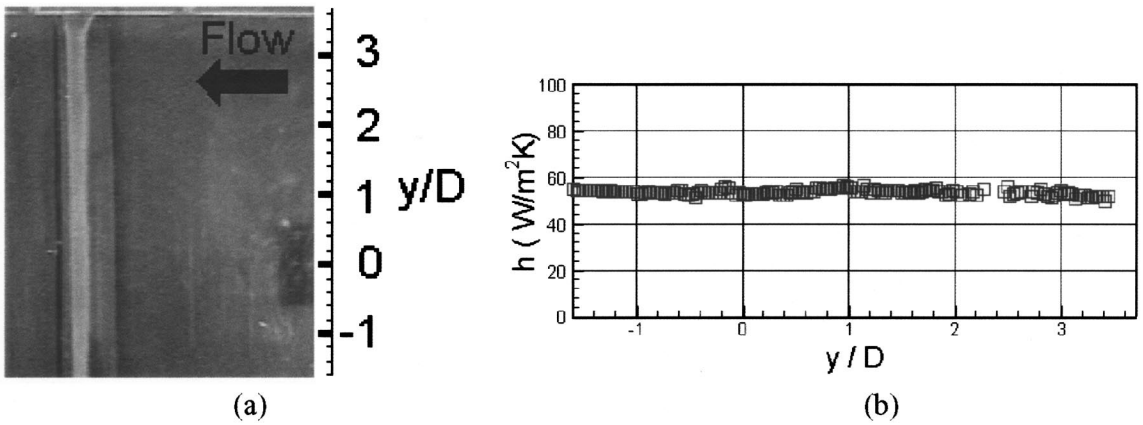

Fig. 4 (*a*) **A sample liquid crystal image for the empty tunnel case obtained at** Re_{D_h}**=75,000 (**D_h**=0.126 m) and (*b*) the corresponding measured *h* distribution on the heater strip**

vide invaluable information about the turbulence and velocity field structures of the wakes of the elliptical and circular pin fin arrays.

G Uncertainty Estimates. The uncertainty in the measurement of the temperature value from the hue value is estimated as ±0.3°C and the uncertainty in the measured convective heat transfer coefficients is estimated as ±4% using the root-sum-square method described in Moffat [30]. The uncertainty in friction coefficient measurements is estimated as 7% using the same method. The estimated level of uncertainty in the ensemble averaged PIV results, obtained using 90 instantaneous samples, is about 10% for the velocity components. This is calculated using the theoretical standard error estimation procedures described in Uzol [25] and Ullum et al. [31]. The turbulent kinetic energy results could be used only for relative qualitative comparisons, because using 90 instantaneous samples is not enough to obtain converged statistics of turbulence variables.

Results and Discussion

A Endwall Heat Transfer

A.1 Baseline Empty Tunnel Measurements. Baseline empty tunnel measurements are performed to check the consistency of the current measurements with standard Nu–Re correlations as well as to generate reference data to be used for normalizing the pin fin results. In addition, the spanwise variations on the heater strip are also quantified. Figure 4(*a*) shows a sample liquid crystal image for the empty tunnel case at a Reynolds number of Re_{Dh} =75 000, based on the test section inlet velocity and the hydraulic diameter. The corresponding measured *h* distribution is presented in Fig. 4(*b*). The average spanwise variation in *h* is about 1.6%.

The empty tunnel measurement results are compared with the unenhanced duct flow heat transfer as well as with the flat plate with unheated starting length correlations, as given in Incropera and DeWitt [32] (Fig. 5). These correlations are given as

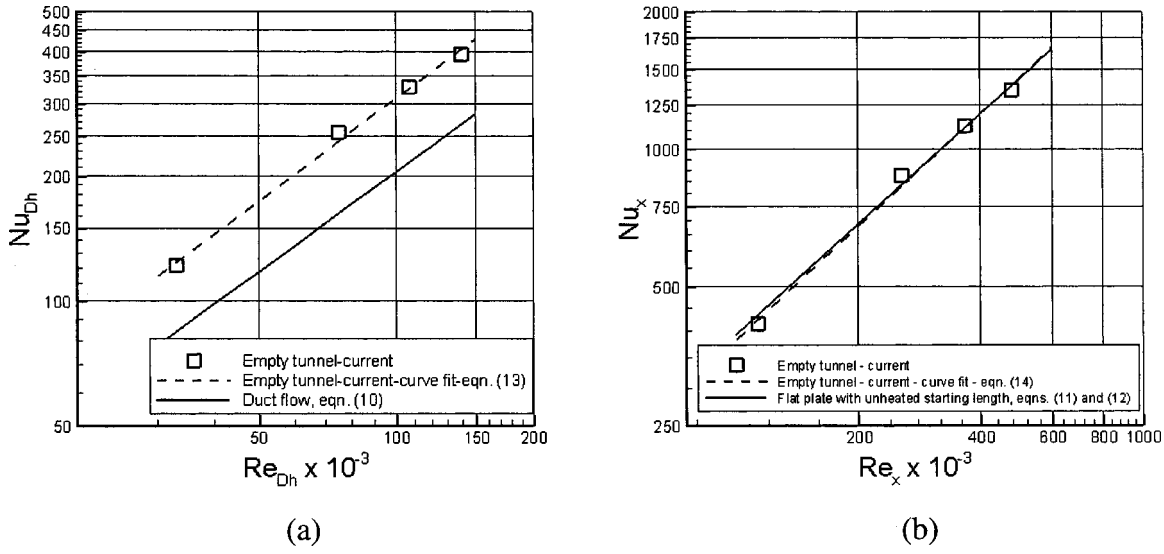

Fig. 5 A comparison of current baseline empty tunnel measurements with (*a*) fully developed turbulent duct flow (Eq. (10)) and (*b*) flat plate with unheated starting length [Eqs. (11) and (12)] correlations as given in Incropera and DeWitt [34]

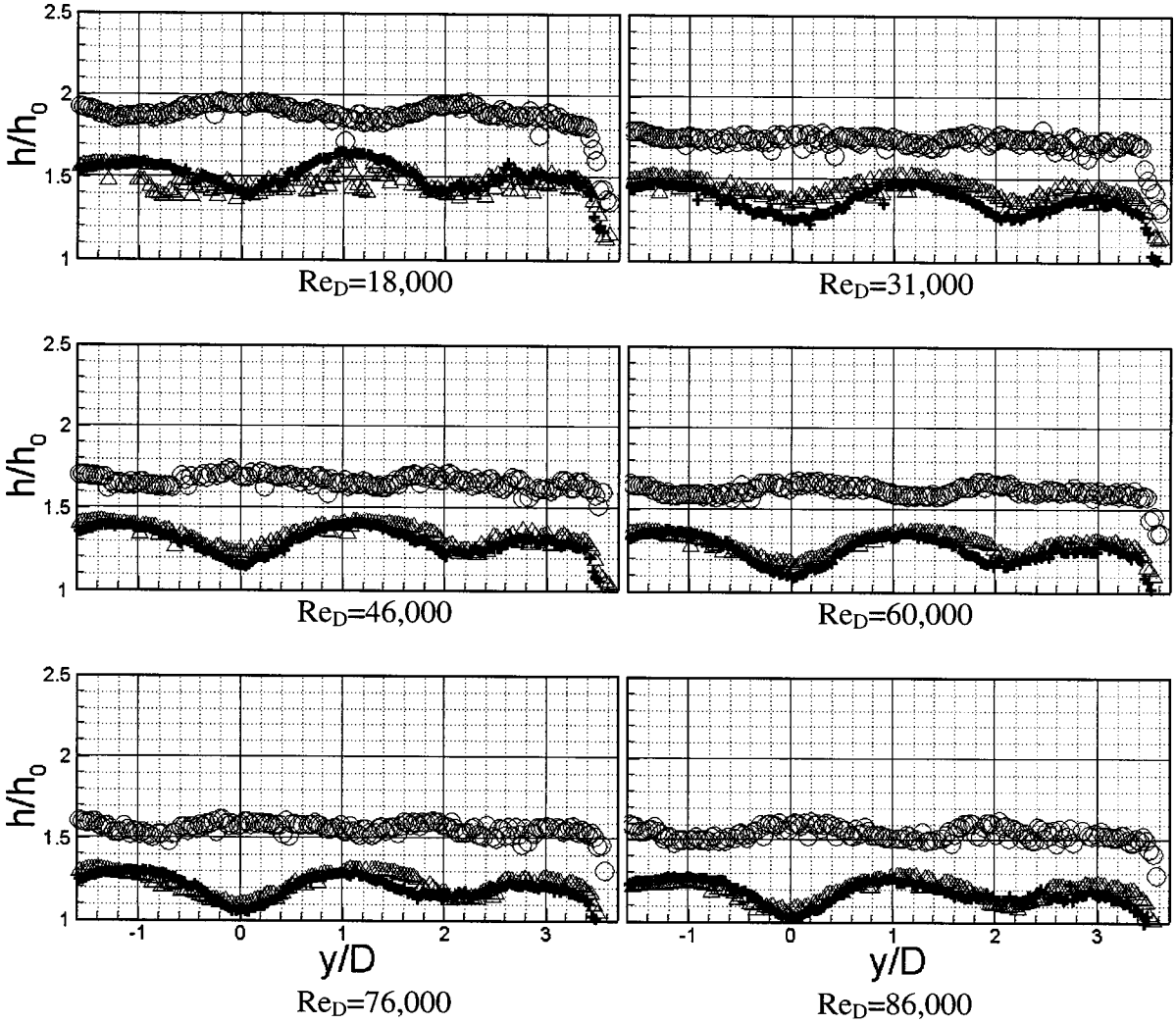

Fig. 6 Relative convective heat transfer coefficient distribution on the endwall for circular (○), SEF (△) and N (+) fin arrays, 2*D* downstream (h_0: baseline empty tunnel value). Re_D is calculated using the maximum velocity and the circular fin diameter, $D=0.0508$ m (or SEF/N fin minor axis length that is equal to *D*).

$$\mathrm{Nu}_{Dh}=0.023\,\mathrm{Re}_{Dh}^{0.8}\,\mathrm{Pr}^{1/3}$$

(fully developed turbulent duct flow, Fig. 5(*a*)) (10)

$$\mathrm{Nu}_x=\frac{\mathrm{Nu}_x|_{\xi=0}}{[1-(\xi/x)^{9/10}]^{1/9}}$$

(flat plate with unheated starting length, Fig. 5(*b*)) (11)

$$\mathrm{Nu}_x|_{\xi=0}=0.0296\,\mathrm{Re}_x^{0.8}\,\mathrm{Pr}^{1/3}. \quad (12)$$

Equation (10) is the Colburn equation for turbulent flow in circular tubes, and modified using the hydraulic diameter for the current noncircular cross section. In Eqs. (11) and (12), ξ is the distance from the leading edge where the thermal boundary layer development begins. Here, ξ is taken as the distance between the test section entrance and the heater strip starting position, which is 8.25*D*, and *x* is the middle of the heater strip, which is 8.5*D* (*D* is the circular fin diameter, 0.0508 m). The Prandtl number is 0.71 and the hydraulic diameter is $D_h=0.126$ m. As expected, current empty tunnel measurements are about 1.5 times larger than the results given by Eq. (10), due to the entry region characteristics of the flow (Fig. 5(*a*). On the other hand, the data agrees very well with the correlation for a flat plate with an unheated starting length (Fig. 5(*b*)). The equations for the curve fit lines for the current empty tunnel measurements are

$$\mathrm{Nu}_{Dh}=0.0239\,\mathrm{Re}_{Dh}^{0.8227}\ \text{(Fig. 5(}a\text{))}, \quad (13)$$

$$\mathrm{Nu}_x=0.0297\,\mathrm{Re}_x^{0.8227}\ \text{(Fig. 5(}b\text{))}. \quad (14)$$

The difference in average baseline empty tunnel convective heat transfer coefficient values, i.e., h_0, estimated from Eqs. (13) and (14) is less than 0.09%. Therefore, Eq. (13) is chosen to estimate the value of h_0, at various pin fin measurement conditions. This is achieved first by calculating Re_{Dh}, using the test section inlet velocity measured at that pin fin measurement condition and the hydraulic diameter. Then, Nu_{Dh} is estimated from Eq. (13), and h_0 is calculated using Nu_{Dh}, the hydraulic diameter and k_{air}. Calculated h_0 values are used for the nondimensionalization of the measured pin fin *h* distributions on the endwall, which will be presented in the next section.

A.2 Pin Fin Measurements. The distributions of relative convective heat transfer coefficients for six different Reynolds numbers are presented in Fig. 6. These relative results are the values over the baseline empty tunnel measurements explained in the previous section.

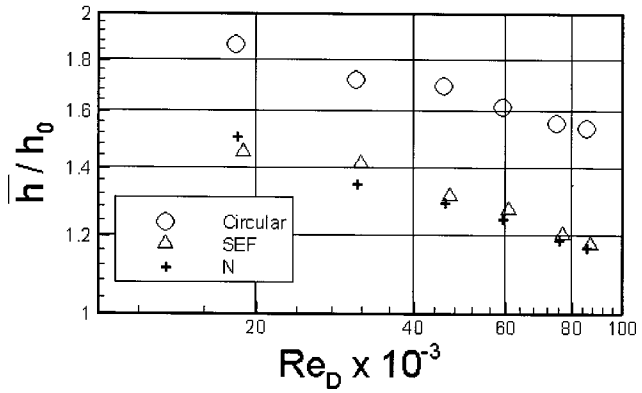

Fig. 7 Average relative convective heat transfer coefficient variation with Reynolds number

In case of the circular fin array, the heat transfer enhancement levels are higher than the levels for the SEF and N fin arrays, for all Reynolds numbers. The levels for the SEF and N fin arrays are close to each other. There are differences between the local enhancement patterns of the circular and elliptical pin fin arrays. Local enhancements inside the wakes of the SEF and N fin arrays are clearly visible in the form of two peaks in the line distributions. Although the local peaks are not as distinct in case of circular fins, they can still be depicted. For example, at $\mathrm{Re}_D = 18\,000$, there exists a local maximum around the centerline, $y/D = 0.0$, whereas this location shows a local minimum for SEFs and N fins. Furthermore, the levels show a local minimum around $y/D = \pm 1.2$, however, this location is the local maximum for SEFs and N fins. Keep in mind that the centers of the two pin fins in the second row are located at $y/D = \pm 1.0$. This indicates that, for the circular pin fins, the local minimum in the heat transfer coefficients occurs *within* the wakes of the second row fins around the wake centerline. However, for the elliptical fins, this region shows local maximum. These differences in local enhancement patterns are mainly due to the differences between the wake flow fields of the circular and elliptical fins. More details related to the wake flow structures will be given in the coming sections from the results of the PIV measurements. Similar differences are also observed at the other Reynolds numbers. Note that the sudden drop in the h/h_0 levels after $y/D = 3.4$, for all arrays and at all Reynolds numbers, is due to the presence of the corner boundary layer in that region.

Figure 7 shows the variation of the average relative heat transfer enhancement (h/h_0) with Reynolds number. For all fin shapes, the relative enhancement levels decrease with increasing Reynolds number. This is mainly due to the fact that the Reynolds number dependency of the empty tunnel case is much stronger than the one for the pin fins. For the empty tunnel, the Reynolds number exponent is 0.8227 whereas it is 0.7, 0.678 and 0.661 for the circular, SEF and N fins, respectively, (see Table I). Therefore as the Reynolds number increases, the Nusselt number levels of the pin fins do not increase as fast as the empty tunnel values, hence resulting in a decreasing trend. The relative enhancement levels for the SEF and N fins decrease more sharply than the levels for the circular fins.

Figure 8(*a*) shows the line-averaged Nusselt number variation with Reynolds Number for the circular pin fins and the comparison of the current data with the previously reported correlations of Metzger et al. [5] and Zukauskas [33] for staggered circular pin fin arrays. The Metzger et al. [5] correlation is given as

$$\mathrm{Nu}_D = 0.135\,\mathrm{Re}_D^{0.69}(X/D)^{-0.34}. \tag{15}$$

This correlation is evaluated and verified with published data by Armstrong and Winstanley [12] and is applicable for $H/D \leqslant 3$, $1.5 \leqslant X/D \leqslant 5$, $2.0 \leqslant S/D \leqslant 4.0$, and $10\,000 \leqslant \mathrm{Re}_D \leqslant 100\,000$, which covers the range of the current experiments ($H/D = 1.5$, $X/D = S/D = 2.0$, $18\,000 \leqslant \mathrm{Re}_D \leqslant 86\,000$). For comparison purposes, the correlation further needs to be modified to account for the number of pin rows tested (two rows tested in the current experiments). This modification can be performed, as suggested by Armstrong and Winstanley [12], using the row-by-row variation curve presented in Metzger et al. [5]. The Metzger correlation plotted in Fig. 8(*a*) uses Eq. (15) and is modified for a two-row array configuration. It is evident that the current data is in close agreement with the Metzger correlation. The Zukauskas [33] correlation for arrays of long circular cylinders is also plotted in Fig. 8(*a*) as a reference and comparison. It is given as,

$$\mathrm{Nu}_D = 0.35(S/X)^{0.2}\,\mathrm{Re}_D^{0.6}\,\mathrm{Pr}^{0.36}. \tag{16}$$

In Fig. 8, the baseline empty tunnel data is plotted using a modified version of Eq. (13), which includes the pin fin diameter instead of the hydraulic diameter and the maximum velocity instead of the inlet velocity. The correlation coefficients for the current measurements as well as the mentioned previous experiments are summarized in Table I.

Figure 8(*b*) shows the line-average Nusselt number variation with Reynolds number for the current circular, SEF and N fin arrays, as well as for various other pin fin shapes investigated by previous researchers. Before discussing the results presented in Fig. 8(*b*), some issues on making a consistent comparison with the previously published data will be addressed as follows:

1. In the current study, the Nusselt numbers and the Reynolds numbers are calculated using the diameter of the circular fins or the minor axis lengths of the SEF/N fins. These two are kept equal in order to obtain the same effective frontal area that is needed to make consistent comparisons of the pressure loss and wake flow field characteristics. However, different definitions of pin fin diameters are used by previous researchers for different pin fin shapes in the calculation of the Reynolds numbers and Nusselt numbers. For example, in their investigation of elliptical and drop-shaped pin fins, Li et al. [22] and Chen et al. [23] used an ''equal circumference diameter'' definition that gives diameters larger than the actual minor axis lengths of the pin fins. Chyu et al. [19] used one side length as the diameter definition both for the cubic and diamond pin fins, but the actual effective frontal area for diamond fins corresponds to the diagonal of the fins, not the side length. Therefore, in order to be able to make consistent comparisons with the current study, necessary modifications are

Table 1 Correlation coefficients for the current and previously published data for various pin fin shapes ($\mathrm{Nu}_D = a\,\mathrm{Re}_D^b$)

Pin fin shape	a	b
Circular current	0.0776	0.7
SEF current	0.077	0.678
N current	0.0916	0.661
Circular-Metzger et al. [5], Eq. (15) (for $x/D = 2$ and corrected for two rows using $\mathrm{Nu}_2/\mathrm{Nu}_{10} = 0.9$, as suggested in Armstrong and Winstanley [12])	0.096	0.69
Circular-Zukauskas [30]—Eq. (16)—long fins (for $s/x = 1$ and $\mathrm{Pr} = 0.707$)	0.31	0.6
Cubic-Chyu et al. [19]	0.12	0.704
Diamond-Chyu et al. [19] (modified using diagonal as D)	0.08	0.732
Oblong—Metzger et al. [14]	0.0479	0.752
Elliptical—Li et al. [22] (modified using actual minor axis length as D)	0.392	0.53
Drop-shaped—Chen et al. [23] (modified using actual minor axis length as D)	0.155	0.645
Empty tunnel—current (based on the tunnel hydraulic diameter, $D_h = 0.1262$ m)	0.0239	0.8227

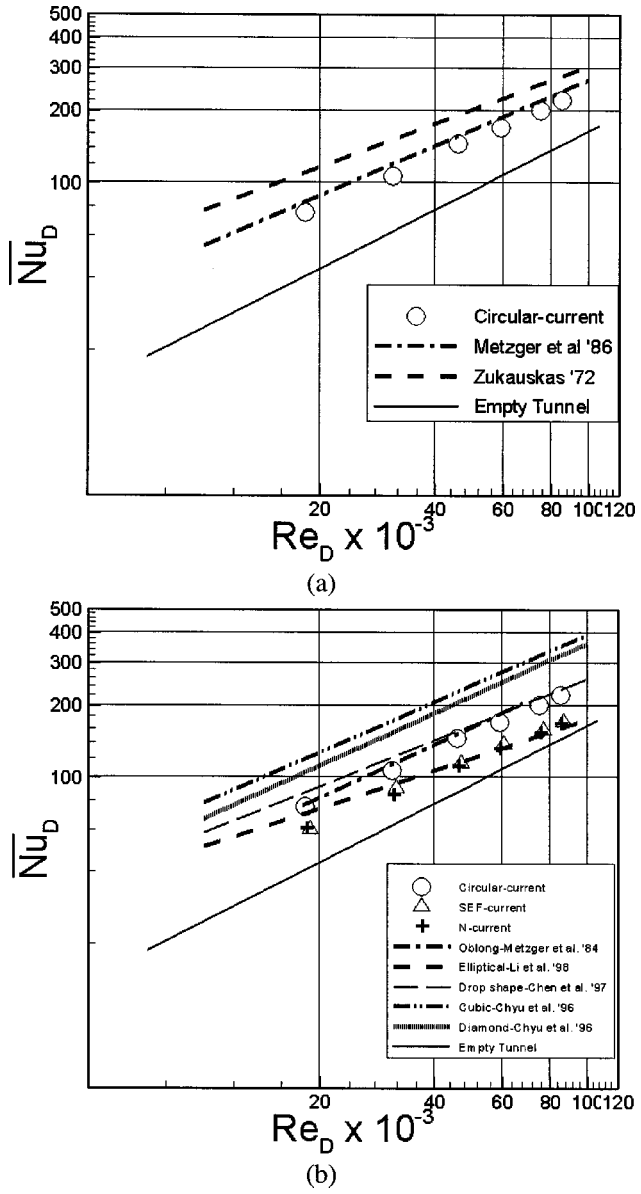

Fig. 8 Average Nusselt number versus Reynolds number comparisons of (*a*) current measurements with previously reported correlations for staggered circular pin fin arrays, and (*b*) circular, SEF, and N fin arrays with previously reported measurements for various pin fin shapes. Empty tunnel results are the current measured data with no pin fins.

made to their correlations such that the diameters corresponding to their actual effective frontal areas are used in the Nusselt number and Reynolds number calculations.

2. Not all of the previously reported heat transfer data are obtained on the endwall. Some of them are on the pins (e.g., Chyu et al. [19]) and some are combined pin-endwall results (e.g., Li et al. [22] and Chen et al. [23]). However, it is reported in Metzger and Haley [3] that the endwall heat transfer coefficients are generally almost at the same level as the combined pin-endwall averages.

Therefore, keeping in mind the points mentioned above, several observations can readily be made:

a. Current measurements indicate that the Nusselt number levels for the circular fin are higher than those for the SEF and N fin arrays. At the lowest Reynolds number, the average Nusselt number for the circular fin array is 26% and 23% higher than the average Nusselt numbers for the SEF and N fins, respectively. Similarly at the highest Reynolds number, the circular fin array is 28.8% and 29.5% higher than the respective values of the SEF and the N fin arrays.

b. The elliptical pin fin results of Li et al. [22] and the current results for SEF and N fins are close to each other in the Reynolds number range of 30 000 and 90 000, but they deviate from each other at Reynolds number below 30 000 (the experiments of Li et al. [22] are actually performed up to Reynolds numbers of 10 000. The curve fit equation given in their paper is used for comparison at these higher Reynolds numbers). Note that the elliptical pin fins of Li et al. [22] show a much weaker Reynolds number dependency than the SEF and N fins, as can be seen from the exponents of the Reynolds numbers listed in Table I.

c. It is also evident that the cubic and the diamond fins of Chyu et al. [19] have the highest Nusselt numbers in the presented Reynolds number range whereas the elliptical fins (SEF, N, and Li et al. [22]) have the lowest values.

d. The variation of the oblong fins (at zero incidence angle, Metzger et al. [14]) and the drop-shaped fins (Chen et al. [23]) are close to that of the current circular fins.

To summarize, the SEFs and the N fins seem to be the least effective devices in terms of heat transfer enhancement among all other pin fin shapes. The circular pin fins perform about 27% better in average than the SEF and N fins in this Reynolds number range. Furthermore, the elliptical pin fins, i.e., SEFs, N fins, and elliptical fins of Li et al. [22], all seem to have weaker Reynolds number dependency compared to the circular pin fins. This is most probably because of the different boundary layer, surface pressure, separation, and the wake characteristics of those pin fin shapes.

B Total Pressure Loss. Figure 9 shows the measured friction coefficient distributions inside the wakes of the circular, SEF, and N fin arrays. It is evident that there is substantial reduction in the total pressure loss in the case of SEF and N fin arrays. The levels for the SEF and the N fin are close to each other, but the N fin creates slightly less pressure loss inside the wake. In case of the circular fin array, the wake region created by the two fins in the second-row of the array are clearly visible in the form of two peaks in the friction coefficient distribution. Wakes of the first row fins are not distinctly visible in case of circular pin fins whereas they are clearly identifiable for the SEFs for all Reynolds numbers in the form of two outer peaks in the distributions (the two middle peaks are created due to the wakes of the two fins in the second row for SEFs). In case of N fins, the first row wakes are identifiable up to Reynolds number 60 000. However, for higher Reynolds numbers, the individual wake signatures become much less obvious, even for the two second-row fins. The differences between the pressure loss distribution patterns of circular SEF and N fin arrays indicate that the wake structures and mixing mechanisms are different. As will be explained in detail in the next section from the results of the PIV measurements, in case of SEFs and N fins, the wakes of the first row fins do not mix or interact with each other or with the fins in the second row, but, instead, the localized losses created inside the individual wakes are carried downstream separately. In case of circular fins, however, the wakes of the first row fins interact with the second row pin fins, resulting in an early separation from the second row fins as well as bending of the first row fin wakes. These interactions generate a relatively large wake zone behind the second row, which in turn results in high levels of total pressure loss in this region.

Figure 10(*a*) shows the line-average friction coefficient variation with Reynolds number for the current circular fin array, and the results are compared with previously published data. The solid line in this figure is a correlation proposed by Metzger et al. [34] for $10^4 < \mathrm{Re}_D < 10^5$, and is given by

$$f^* = 1.76\,\mathrm{Re}_D^{-0.318}, \tag{17}$$

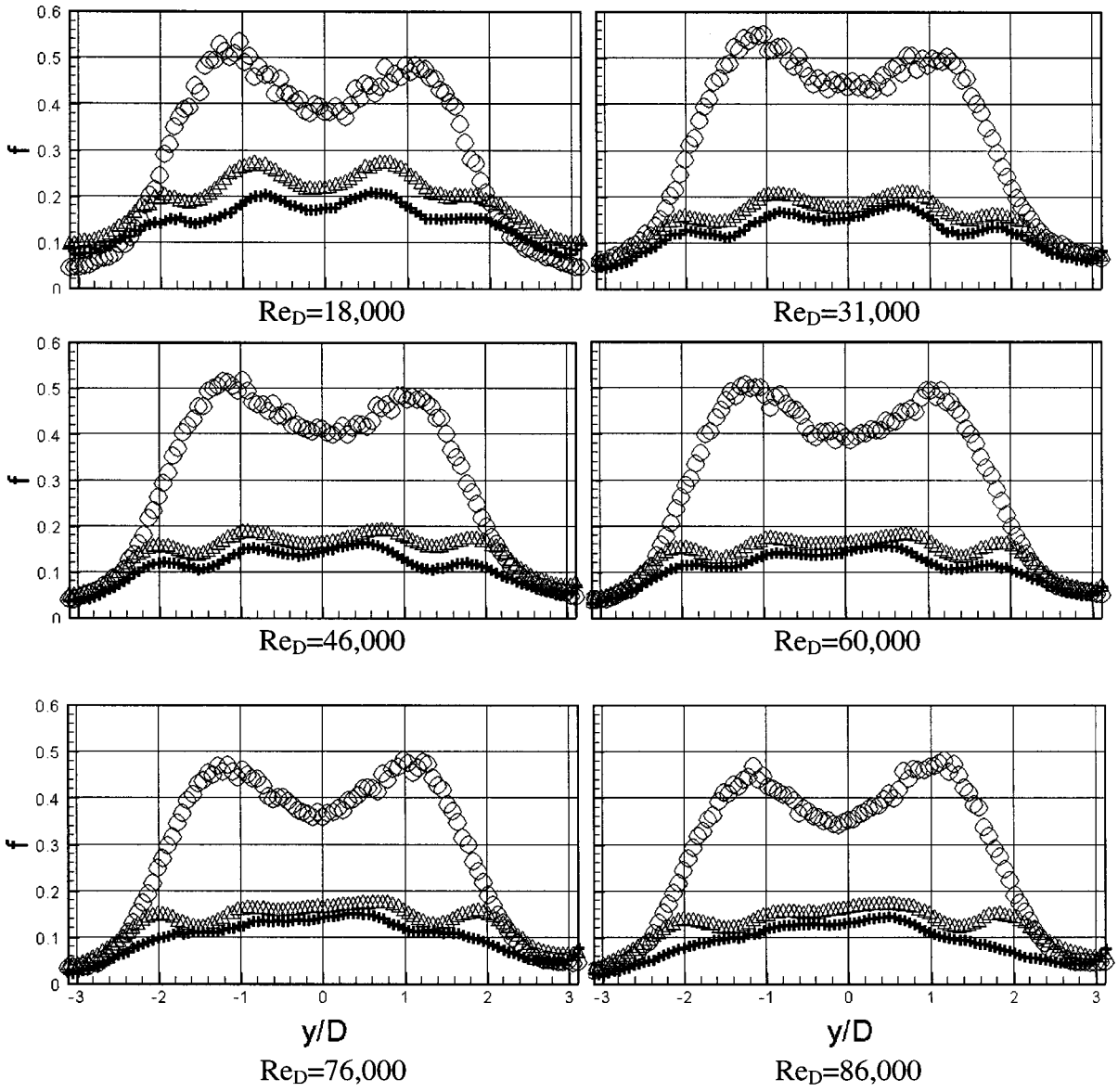

Fig. 9 Friction coefficient distributions inside the wakes of circular (○), SEF (△), and N (+) fin arrays, 2*D* downstream

$$f^* = \frac{\Delta P}{2\rho u_{\max}^2 N_R} = 0.25f. \tag{18}$$

The definition of f^* is slightly different than f used in this paper, as seen in Eq. (18). Therefore, it is modified accordingly to be able make a consistent comparison in Fig. 10(*a*). The error bars show a ±15% range also proposed by Metzger et al. [34]. Current circular fin data is within this range below $\mathrm{Re}_D = 20\,000$, and starts to deviate from this correlation with increasing Reynolds number. However, it is still in good agreement with the data provided by Lau et al. [6]. Keep in mind that, in the previous studies, the static pressures are measured at a single point on the wall before and after the pin fin array and the static pressure loss across the array was used to calculate the friction coefficient., whereas current study uses the average results of the complete transverse total pressure distributions at the midplane. In this Reynolds number range, the separation on both first and second row circular fins is most probably a laminar separation, which occurs at about 80°. This is also partly confirmed by the Particle Image Velocimetry data presented in the next section. Relatively flat distribution of the friction coefficient is possibly due to this fact.

Figure 10(*b*) shows the comparison of the current circular fin, SEF, and N fin pressure loss measurements with the pressure loss levels of various other pin fin shapes reported by previous researchers. Clearly, the diamond- and cubic-shape pin fins investigated by Chyu et al. [19] have the highest levels of pressure loss. The circular fin generates lower pressure losses (about 25%) than those fins but the levels are still substantially higher than those of the elliptical fins. The average loss levels for the circular fin are 37% and 51% higher than the levels of the SEF and N fins, respectively, for the lowest Reynolds number. For the highest Reynolds number, the circular fin has 56% and 68% more loss with respect to the SEF and N fins, respectively. In case of circular pin fins, the friction coefficient shows much less Reynolds number dependency compared to the SEFs and the N fins. The loss levels decrease relatively fast with the Reynolds number, whereas they almost do not change for the circular fins. This can also be seen by comparing the exponent of Re_D, in the curve fit equations for each pin fin shape, as given below:

$$\overline{f} = 0.3849\,\mathrm{Re}_D^{-0.065\,88} \quad \text{(circular fin)}, \tag{19}$$

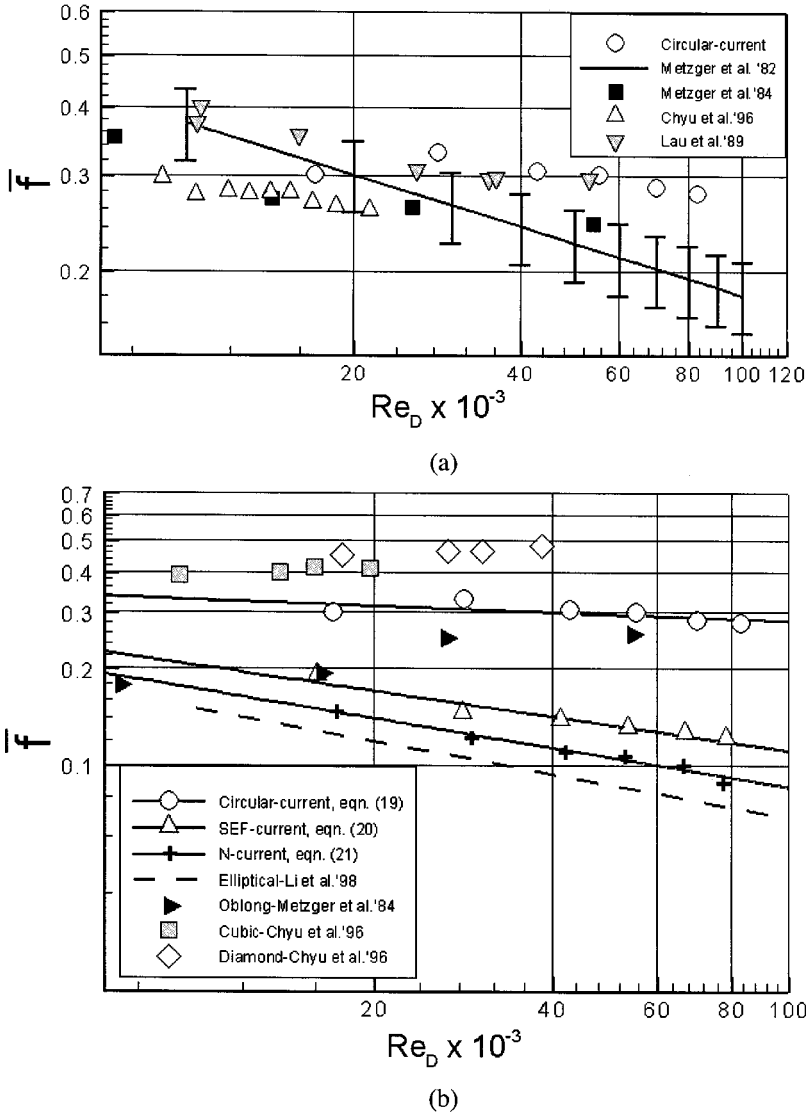

Fig. 10 Average friction coefficient versus Reynolds number for circular, SEF, and N fin arrays. (*a*) A comparison with previously published circular fin data. Error bars show ±15% range given for the correlation given by Metzger et al. [35], Eq. (17). (*b*) A comparison with previously published pressure loss data for various other pin fin shapes.

$$\overline{f} = 0.3811\,\mathrm{Re}_D^{-0.2664} \quad \text{(SEF)}, \tag{20}$$

$$\overline{f} = 0.3520\,\mathrm{Re}_D^{-0.3053} \quad \text{(N fin)}. \tag{21}$$

The friction coefficient for the N fin has the lowest levels among the currently tested pin fin shapes. It creates about 25% less pressure loss than the SEFs. It is interesting to note that the oblong fins tested by Metzger et al. [14] behave close to elliptical fins in the lower Reynolds number range ($\mathrm{Re}_D < 20\,000$), whereas their loss levels get close circular fins when the Reynolds numbers increase. The elliptical pin fins of Li et al. [22] show lower losses than the current SEFs, most probably because of their smaller minor axis lengths.

C Thermal Performance Comparisons. The relation between the heat transfer enhancement, total pressure loss, and flow Reynolds number is presented in Fig. 11. In this figure, $\overline{\mathrm{Nu}}_0$ is determined using the estimated h_0 values and the circular fin diameter (D). The friction coefficient, f_0, is calculated from the Blasius power-law correlation for a fully developed flow in a turbulent duct (Kays and Crawford [35]),

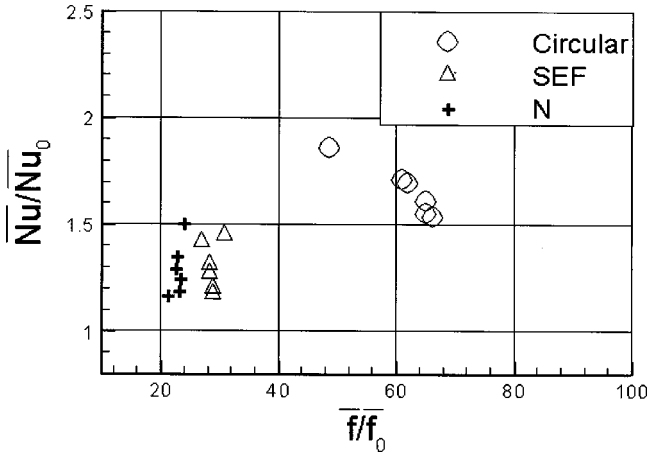

Fig. 11 Relative Nusselt number variation with relative total pressure loss. $\overline{\mathrm{Nu}}_0$ is the baseline empty tunnel Nusselt number obtained using the estimated h_0 values from Eq. (13) and modified using the pin fin diameter instead of hydraulic diameter; f_0 is calculated using the Blasius power-law correlation (Kays and Crawford [32]), Eq. (22).

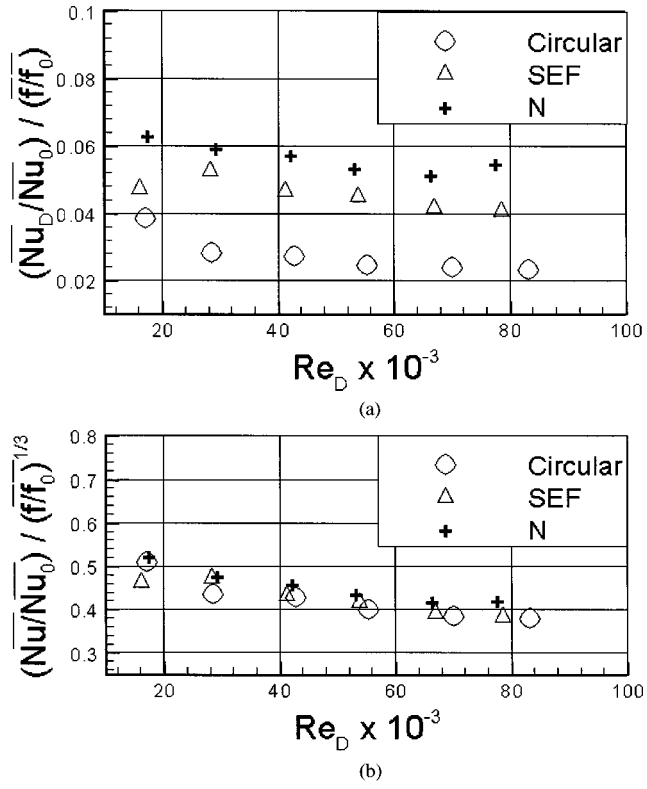

Fig. 12 (*a*) Reynolds analogy performance index and (*b*) Thermal performance (TP) parameter variation with Reynolds number for circular, SEF, and N fin arrays

$$\overline{f_0} = 0.078\,\mathrm{Re}_D^{-0.25}. \tag{22}$$

Figure 11 shows that the SEFs and N fins have almost constant f/f_0 values within the current Reynolds number range with Nusselt numbers changing between 1.1–1.5 times the baseline empty tunnel values. For SEFs, f/f_0 stays about 28 and for the N fins it is about 24. On the other hand, the circular fin f/f_0 values are spread between 48–64 with Nusselt numbers changing from 1.5 to 1.9 times the empty tunnel values, within the Reynolds number range. Although the heat transfer enhancement capability of the circular fins is clearly larger than the current elliptical fins, the average pressure losses that they generate are 2 and 2.3 times larger than those of SEF and N fins, respectively. The relative heat transfer enhancement is much more sensitive to f/f_0 variations in case of SEF and N fin arrays. The main reason is that as the Reynolds number increases, the average friction coefficient levels decrease for the SEFs and N fins. Since f_0 also decreases, f/f_0 remains almost constant while the heat transfer enhancement levels are decreasing. However, for the circular pin fins, since the average friction coefficient almost stays constant in the current Reynolds number range, and f/f_0 also increases slowly with increasing Reynolds number. This results in the relatively slow decrease in the heat transfer levels for circular fins as f/f_0 increases.

The Reynolds analogy performance parameter $\overline{\mathrm{Nu}}_D/\overline{\mathrm{Nu}}_0/(\overline{f}/\overline{f}_0)$ and the thermal performance parameter $\overline{\mathrm{Nu}}_D/\overline{\mathrm{Nu}}_0/(\overline{f}/\overline{f}_0)^{1/3}$, as suggested by Gee and Webb [36], are presented in Figs. 12(*a*) and 12(*b*), respectively. These parameters provide a convenient way to evaluate the overall performances of pin fin arrays with different pin shapes. The results show that, in terms of Reynolds analogy, the performance indices of the SEF and the N fins are 1.23 and 1.64 times that of the circular fins, respectively, at the lowest Reynolds number. Similarly, at the highest Reynolds number, the performance indices of the SEFs and the N fins are 1.75 and 2.36 times higher, respectively. The thermal performance indices, presented in Fig. 12(*b*), show that all data collapses together, and the differences are much less evident. Nevertheless, N fins still show slightly higher thermal performance values.

D Wake Flow Field. Figure 13 shows the ensemble-averaged velocity magnitude, vorticity, as well as turbulent kinetic energy distributions within the wakes of the circular, SEF, and N fin arrays at $\mathrm{Re}_D = 18\,000$. The circular fin array creates a relatively large low momentum wake zone compared to the SEF and N fin arrays. The separation on the circular fins at the second row occurs very early. In fact, a close examination of the data reveals that the separation occurs at around a 80 deg point from the leading edge, indicating a laminar separation on the fins in the second row. The separation on the SEFs and N fins occur very close to their trailing edge because of the relatively smooth acceleration and deceleration of the flow due to their geometrical shape. As a result, SEFs and N fins have a much smaller wake region compared to circular fins. This is basically the main reason that the SEF and N fin arrays have very low total pressure loss levels compared to the circular fin arrays.

The wake of the bottom fin in the first row is also clearly visible in Fig. 13. This wake is evident as a region with low velocity magnitude and opposite signs of vorticity around $x/D = 1.8$ and $y/D = -2.4$. This wake region is most obvious in the case of circular pin fins. As is evident from Fig. 13, the trajectory of this wake shows substantial differences between the three pin fin arrays. In the case of circular fins it is significantly bent toward the sidewall, for SEF array it is relatively straight and for N fin array it is slightly bent toward the midchannel. The bending toward the sidewall in the case of circular fins is primarily due to the early laminar separation that exists on the fins in the second row. This early separation pushes the upstream wake toward the sidewall, and, as a result, after the second row of fins, a very wide area of the flow is occupied by low momentum wakes. This interaction of the first row fin wakes with the second row fins and wakes is the main reason behind the increased total pressure loss and turbulence levels within the wake flow field. In the case of SEFs and N fins, the wakes of the first row fins convect downstream with minimal interaction with the second row fins and wakes. They get advected separately while getting diffused. This is basically the main reason that the first row wakes are visible in the friction coefficient distribution plots presented in Fig. 9. Also, in case of N fins, note that the peaks in the friction coefficient distributions corresponding to the second row of pins (Fig. 9, $\mathrm{Re}_D = 18\,000$, at $y/D = \pm 0.7$) are much closer to each other compared to the SEF and circular fin distributions. This is consistent with the slight bending of the second row N fin wakes toward the midchannel, as observed from the current PIV measurements.

The turbulent kinetic energy levels within the wake of the circular fin array are higher than those for the SEF and the N fin arrays. For all pin fin arrays, the turbulence is mainly generated within the wakes of the first and second row fins and then convected downstream. In case of circular fins however, an additional turbulence production mechanism exists that is due to the jet-like flow in between the two fins in the second row. Because of this accelerated flow zone, very high velocity gradients are present at the edges of this jetlike region that generate additional turbulence around the centerline. This is probably the reason for the enhanced local heat transfer levels around the centerline in case of circular pin fins, as discussed before. In case of SEFs and N fins, the local heat transfer enhancement levels were a minimum around the centerline and this correlates well with the relatively low turbulent kinetic energy levels in this region. The turbulence levels within the wakes of the SEF and N fin arrays are higher than those at the centerline. This is also consistent with the heat transfer coefficient distributions in which two peaks in the wake region of the SEFs and N fins were observed.

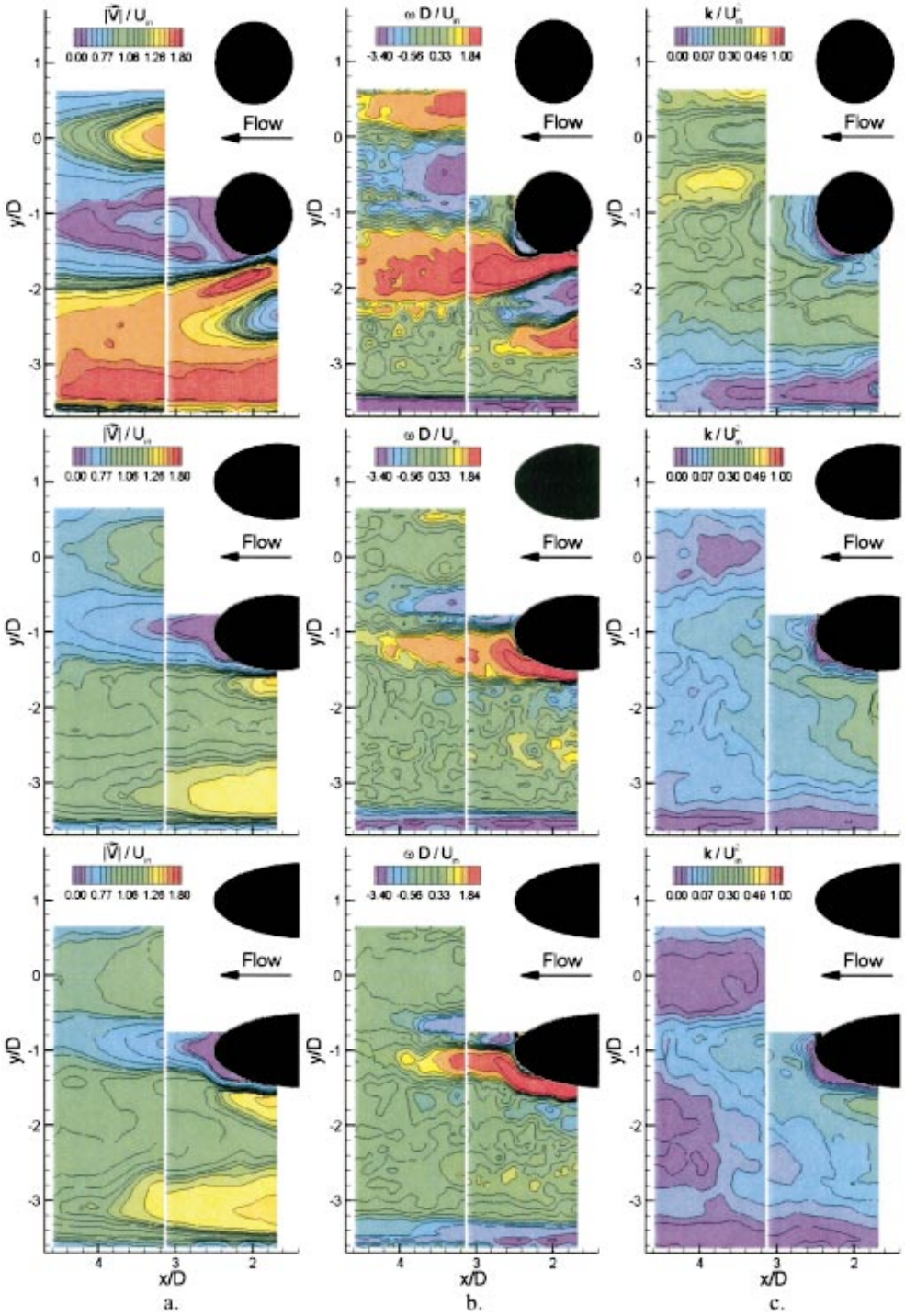

Fig. 13 Ensemble-averaged (*a*) velocity magnitude, (*b*) vorticity, and (*c*) turbulent kinetic energy distributions within the wakes of circular, SEF, and N fin arrays (from top to bottom) for Re_D =18 000 and at the midplane. $y/D=0$ is on the centerline of the channel and $x/D=0$ is on the centers of the circular cylinders in the first row.

Conclusions

Heat transfer, total pressure loss, and wake flow field measurements are performed downstream of two-row staggered elliptical and circular pin fin arrays. Two different types of elliptical fins are tested, i.e., a Standard Elliptical Fin (SEF) and a fin that is based on NACA four-digit symmetrical airfoil shapes (N fin). The results are compared to those of a corresponding circular pin fin array. The pin fins had a height-to-diameter ratio of 1.5. The streamwise and the transverse spacings were equal to one circular fin diameter, i.e., $S/D=X/D=2$. The measurements are obtained in a Reynolds number range of $Re_D=18\,000$ to $Re_D=86\,000$.

The Nusselt number levels for the circular fin array are about 27% higher on average than the levels for the SEF and N fin arrays. The levels for the SEF and N fin arrays are close to each other. Differences between the local enhancement patterns of the circular and elliptical pin fin arrays are observed. The SEFs and N

fins have a weaker Reynolds number dependency compared to the circular pin fins, possibly due to boundary layer and separation characteristics. It is determined that, in terms of heat transfer enhancement performance, the SEFs and the N fins not only have a lower performance compared to the circular fins, but also they seem to be the least effective devices among some of the other pin fin shapes that have been investigated by previous researchers.

In terms of pressure loss, there is a substantial reduction in case of SEF and N fin arrays. The levels for the SEF and the N fin are close to each other, but N fin creates slightly less pressure loss inside the wake. The loss levels for the circular fin are 46.5% and 59.5% higher on average than those of the SEF and N fins, respectively. In the case of circular pin fins, the relatively flat distribution of the average friction coefficient indicates that it is almost Reynolds number independent in this range. However, for the SEFs and the N fins there is a strong Reynolds number dependency.

The Reynolds analogy and the thermal performance parameters are examined to evaluate the overall performances of pin fin arrays with different pin shapes. The results show that, in terms of Reynolds analogy, the performance indices of the SEF and the N fins are 1.49 and 2.0 times higher on average than that of circular fins, respectively. The thermal performance indices show a collapse of the data, and the differences are much less evident. Nevertheless, N fins still show slightly higher thermal performance values.

The wake flow field measurements show that the circular fin array creates a relatively large low momentum wake zone compared to the SEF and N fin arrays. A laminar separation occurs on the fins in the second row. The wake trajectories of the first row fins for circular, SEF, and N fin arrays are substantially different from each other. In the case of circular fins it is bent toward the sidewall, for the SEF array it is relatively straight, and for the N fin array it is slightly bent toward the midchannel. The turbulent kinetic energy levels within the wake of the circular fin array are higher than those for the SEF and the N fin arrays. For all pin fin arrays, the turbulence is mainly generated within the wakes of the first and second row fins and then convected downstream. In the case of circular fins, however, an additional turbulence production mechanism exists that is due to the jetlike flow in between the two fins in the second row.

Nomenclature

A_S = surface area of the heater strip (m^2)
D = circular fin diameter or SEF/N fin minor axis length (m)
f = friction coefficient (total pressure loss coefficient), $f = (P_{t_l} - P_{t_w})/0.5\rho u_{\max}^2 N_R$
h = convective heat transfer coefficient ($W/m^2\,K$)
h_0 = average baseline empty tunnel convective heat transfer coefficient
H = pin fin height (m)
k = turbulent kinetic energy (m^2/s^2)
k_{air} = thermal conductivity of air (W/mK)
N_R = number of pin fin rows
N fin = pin fin derived from NACA four-digit symmetrical airfoil series
Nu_D = Nusselt number, hD/k_{air}
M = total number of instantaneous PIV vector maps
P_{t_l} = total pressure at the test section inlet (Pa)
P_{t_w} = total pressure within the wake (Pa)
Pr = Prandtl number
q'' = heat flux on the heater strip (W/m^2)
R_S = electrical resistance of the heater strip (Ohms)
Re_D = Reynolds number, $u_{\max}D/\nu$
S = pin fin array transverse spacing (m)
SEF = standard elliptical fin
t_W = wall thickness (m)
t_C = airfoil maximum thickness (m)
T = temperature (°C or K)
u = velocity in x direction (m/s)
$u_{\max}$ = maximum u in the pin fin array (m/s)
v = velocity in y direction (m/s)
V_S = voltage across the heater strip (V)
X = pin fin array streamwise spacing (m)

Greek

ϵ = surface emissivity
σ = Stefan–Boltzmann constant, $5.67\times10^{-8}\,W/m^2\,K^4$
ξ = distance of thermal boundary layer starting point from the leading edge (m)

References

[1] Brown, A., Mandjikas, B., and Mudyiwa, J. M., 1980, "Blade Trailing Edge Heat Transfer," ASME 80-GT-45.
[2] Van Fossen, G. J., 1982, "Heat Transfer Coefficients for Staggered Arrays of Short Pin Fins," ASME J. Eng. Power, **104**, pp. 268–284.
[3] Metzger, D. E., and Haley, S. W., 1982, "Heat Transfer Experiments and Flow Visualization for Arrays of Short Pin Fins," ASME 82-GT-138.
[4] Simoneau, R. J., and Van Fossen, Jr., G. J., 1984, "Effect of Location in an Array on Heat Transfer to a Short Cylinder in Crossflow," ASME J. Heat Transfer, **106**, pp. 42–48.
[5] Metzger, D. E., Shepard, W. B., and Haley, S. W., 1986, "Row Resolved Heat Transfer Variations in Pin Fin Arrays Including Effects of Non-Uniform Arrays and Flow Convergence," *Proceedings of the International Gas Turbine Conference and Exhibit, Dusseldorf*, West Germany, 86-GT-132.
[6] Lau, S. C., Han, J. C., and Batten, T., 1989, "Heat Transfer, Pressure Drop and Mass-Flow Rate in Pin Fin Channels With Long and Short Trailing Edge Ejection Holes," ASME J. Turbomach., **111**, pp. 116–123.
[7] Chyu, M. K., Natarajan, V., and Metzger, D. E., 1992, "Heat/Mass Transfer From Pin Fin Arrays With Perpendicular Flow Entry," *ASME HTD Fundamental and Applied Heat Transfer Research for Gas Turbine Engines*, Vol. 226, pp. 31–39.
[8] Al Dabagh, A. M., and Andrews, G. E., 1992, "Pin Fin Heat Transfer: Contribution of the Wall and the Pin to the Overall Heat Transfer," *presented at the International Gas Turbine and Aeroengine Congress and Exposition Cologne*, Germany, 92-GT-242.
[9] Hwang, J. J., and Lui, C. C., 2000, "Detailed Heat Transfer Distribution on the Endwall of a Pin Fin Trapezoidal Duct," *Proceedings of the 8th International Symposium on Transport Phenomena and Dynamics of Rotating Machinery*, ISROMAC-8, Vol. 2, pp. 738–745.
[10] Ligrani, P. M., and Mahmood, G. I., 2003, "Variable Property Nusselt Numbers in a Channel With Pin-Fins," AIAA J. Thermophys. Heat Transfer, **17**, pp. 103–111.
[11] Won, S. Y., Mahmood, G. I., and Ligrani, P. M., 2004, "Spatially-Resolved Heat Transfer and Flow Structure in a Rectangular Channel With Pin Fins," Int. J. Heat Mass Transfer, **47**, pp. 1731–1743.
[12] Armstrong, J., and Winstanley, D., 1988, "A Review of Staggered Array Pin Fin Heat Transfer for Turbine Cooling Applications," ASME J. Turbomach., **110**, pp. 94–103.
[13] Ligrani, P. M., Oliveira, M. M., and Blaskovich, T., 2003, "Comparison of Heat Transfer Augmentation Techniques," AIAA J., **41**, pp. 337–362.
[14] Metzger, D. E., Fan, C. S., and Haley, S. W., 1984, "Effects of Pin Shape and Array Orientation on Heat Transfer and Pressure Loss in Pin Fin Arrays," ASME J. Eng. Gas Turbines Power, **106**, pp. 252–257.
[15] Steuber, G. D., and Metzger, D. E., 1986, "Heat Transfer and Pressure Loss Performance for Families of Partial Length Pin Fin Arrays in High Aspect Ratio Rectangular Ducts," *Proceedings of the 8th International Heat Transfer Conference*, Vol. 6, pp. 2915–2920.
[16] Arora, S. C., and Abdel-Messeh, W., 1990, "Characteristics of Partial Length Circular Pin Fins As Heat Transfer Augmentors for Airfoil Internal Cooling Passages," ASME J. Turbomach., **112**, pp. 559–565.
[17] Wang, B. G., and Ji, H. H., 1987, "An Experimental Investigation of Heat Transfer and Friction Loss in Taper Pin Fin Configurations of Air Cooled Turbine Blades," *Proceedings of the ASME–JSME Thermal Engineering Joint Conference*, Vol. 4, pp. 127–133.
[18] Grannis, V. B., and Sparrow, E. M., 1991, "Numerical Simulation of Fluid Flow Through an Array of Diamond Shaped Pin Fins," Numer. Heat Transfer, Part A, **19**, pp. 381–403.
[19] Chyu, M. K., Hsing, Y. C., and Natarajan, V., 1996, "Convective Heat Transfer of Cubic Pin Fin Arrays in a Narrow Channel," *Proceedings of the International Gas Turbine and Aeroengine Congress and Exposition*, Birmingham, UK, 96-GT-201.
[20] Minakami, K., Mochizuki, S., Murata, A., Yagi, Y., and Iwasaki, H., 1992, "Visualization of Flow Mixing Mechanisms in Pin Fin Arrays," *Proceedings of the International Symposium on Flow Visualization*, pp. 504–508.
[21] Goldstein, R. J., Jabbari, M. Y., and Chen, S. B., 1994, "Convective Mass Transfer and Pressure Loss Characteristics of Staggered Short Pin Fin Arrays," Int. J. Heat Mass Transfer, **37**, pp. 149–160.
[22] Li, Q., Chen, Z., Flechtner, U., and Warnecke, H. J., 1998, "Heat Transfer and Pressure Drop Characteristics in Rectangular Channels With Elliptic Pin Fins," Int. J. Heat Fluid Flow, **19**, pp. 245–250.

[23] Chen, Z., Li, Q., Meier, D., and Warnecke, H. J., 1997, ''Convective Heat Transfer and Pressure Loss in Rectangular Ducts With Drop-Shaped Pin Fins,'' Heat Mass Transfer, **33**, pp. 219–224.
[24] Abbott, I. H., and Von Doenhoff, A. E., 1959, *Theory of Wing Sections*, Dover, New York.
[25] Uzol, O., 2000, ''Novel Concepts and Geometries As Alternatives to Conventional Circular Pin Fins for Gas Turbine Blade Cooling Applications,'' Ph.D. thesis, Pennsylvania State University, University Park, PA.
[26] Russ, J. C., 1995, *The Image Processing Handbook*, CRC Press, Boca Raton, Fl.
[27] Camci, C., Kim, K., and Hippensteele, S. A., 1992, ''A New Hue-Capturing Technique for the Quantitative Interpretation of Liquid Crystal Images Used in Convective Heat Transfer Studies,'' ASME J. Turbomach., **114**, pp. 765–775.
[28] Wiedner, B. G., and Camci, C., 1996, ''Determination of Convective Heat Flux on Steady-State Heat Transfer Surfaces With Arbitrarily Specified Boundaries,'' ASME J. Heat Transfer, **118**, pp. 1–8.
[29] Chyu, M. K., 1990, ''Heat Transfer and Pressure Drop for Short Pin-Fin Arrays With Pin Endwall Fillet,'' ASME J. Heat Transfer, **112**, pp. 926–932.
[30] Moffat, R. J., 1988, ''Describing the Uncertainties in Experimental Results,'' Exp. Therm. Fluid Sci., **1**, pp. 3–17.
[31] Ullum, U., Scmidt, J. J., Larsen, P. S., and McCluskey, D. R., 1998, ''Statistical Analysis and Accuracy of PIV Data,'' J. Visualization, **1**, pp. 205–216.
[32] Incropera, F. P., and DeWitt, D. P., *Introduction to Heat Transfer*, 2nd ed., Wiley, New York.
[33] Zukauskas, A., 1972, ''Heat Transfer From Tubes in Crossflow,'' Schweiz. Ing. Archit., **8**, pp. 93–160.
[34] Metzger, D. E., Fan, Z. X., and Shepard, W. B., 1982, ''Pressure Loss and Heat Transfer Through Multiple Rows of Short Pin Fins,'' *Heat Transfer 1982*, Vol. 3, edited by U. Grigull et al., eds., Hemisphere, Washington, pp. 137–142.
[35] Kays, W. M., and Crawford, M. E., 1980, *Convective Heat and Mass Transfer*, McGraw-Hill, New York.
[36] Gee, D. L., and Webb, R. L., 1980, ''Forced Convection Heat Transfer in Helically Rib-Roughened Tubes,'' Int. J. Heat Mass Transfer, **23**, pp. 1127–1136.

A Critical Assessment of Reynolds Analogy for Turbine Flows

J. Bons
Associate Professor
Brigham Young University,
Provo, UT 84602-4201

The application of Reynolds analogy ($2St/c_f \cong 1$) for turbine flows is critically evaluated using experimental data collected in a low-speed wind tunnel. Independent measurements of St and c_f over a wide variety of test conditions permit assessments of the variation of the Reynolds analogy factor (i.e., $2St/c_f$) with Reynolds number, freestream pressure gradient, surface roughness, and freestream turbulence. While the factor is fairly independent of Reynolds number, it increases with positive (adverse) pressure gradient and decreases with negative (favorable) pressure gradient. This variation can be traced directly to the governing equations for momentum and energy which dictate a more direct influence of pressure gradient on wall shear than on energy (heat) transfer. Surface roughness introduces a large pressure drag component to the net skin friction measurement without a corresponding mechanism for a comparable increase in heat transfer. Accordingly, the Reynolds analogy factor decreases dramatically with surface roughness (by as much as 50% as roughness elements become more prominent). Freestream turbulence has the opposite effect of increasing heat transfer more than skin friction, thus the Reynolds analogy factor increases with turbulence level (by up to 35% at a level of 11% freestream turbulence). Physical mechanisms responsible for the observed variations are offered in each case. Finally, synergies resulting from the combinations of pressure gradient and freestream turbulence with surface roughness are evaluated. With this added insight, the Reynolds analogy remains a useful tool for qualitative assessments of complex turbine flows where both heat load management and aerodynamic efficiency are critical design parameters. [DOI: 10.1115/1.1861919]

Introduction/Background

The two-dimensional boundary layer equations for steady, incompressible flow over a flat plate with no streamwise pressure gradient and negligible viscous dissipation can be written as

$$\frac{\partial u}{\partial x}+\frac{\partial v}{\partial y}=0 \tag{1}$$

$$u\frac{\partial u}{\partial x}+v\frac{\partial u}{\partial y}\cong\nu\frac{\partial^2 u}{\partial y^2} \tag{2}$$

$$u\frac{\partial T}{\partial x}+v\frac{\partial T}{\partial y}\cong\alpha\frac{\partial^2 T}{\partial y^2} \tag{3}$$

The similarities between Eq. (2) for streamwise momentum and Eq. (3) for fluid temperature naturally lead to the expectation of similarity in the distributions of u and T in the boundary layer under these conditions. Thus, it was over a century ago that Osborne Reynolds [1] postulated the existence of an analogy between wall shear and heat flux based on studies with fully developed pipe flow and self-similar external boundary layers. In its most basic form, this ''Reynolds Analogy'' can be stated as follows:

$$\frac{|q_w|}{\tau_w}=\frac{|\kappa(\partial T/\partial y)_w|}{\mu(\partial u/\partial y)_w}=\frac{\kappa}{\mu}\left|\frac{dT}{du}\right|_w \tag{4}$$

where $|dT/du|_w$ is the ratio between the thermal and hydrodynamic boundary layer slopes near the wall. When rewritten in terms of dimensionless convective heat transfer coefficient (Stanton number) and skin friction (c_f) coefficient, this relation takes the familiar form

$$\frac{2\mathrm{St}}{c_f}=\frac{1}{\mathrm{Pr}}\frac{(T-T_w)/(T_\infty-T_w)}{u/U_\infty} \tag{5}$$

From Eq. (5) one can readily deduce that for similar thermal and hydrodynamic boundary layer profiles (i.e., when $\delta\cong\delta_t$, which occurs when $\nu\cong\alpha$ or $\mathrm{Pr}\cong 1$) and constant U_∞, T_∞, T_w:

$$\frac{2\mathrm{St}}{c_f}\approx\frac{1}{\mathrm{Pr}} \tag{6}$$

Though this exact relation is rarely used to provide precise quantitative measures of St from c_f (or vice-versa) in turbine flows, the intuition behind it is used or implied routinely [2,3]. And despite ample warnings about its limitations, Reynolds analogy is often relied on in the design of laboratory experiments for turbine research. Though considerable data and analyses exist suggesting limits to the applicability of this analogy, in many cases its use is convenient and seems physically sound. The objective of this paper is to evaluate the appropriateness of the Reynolds analogy for flow features that are relevant to high pressure (HP) and low pressure (LP) turbines (external flows only). The specific parameters that are considered include: boundary layer state (laminar or turbulent), Reynolds number, freestream pressure gradient, surface roughness, and freestream turbulence. Some combinations of these parameters are also evaluated. By presenting experimental data for all of these parameters from a single comprehensive research study with the same facility, definitive statements about the appropriate use of this analogy for complex turbine flows can be made.

Description of Experimental Facility

Wind Tunnel Facility. The research facility used for the experiments is described in detail in Ref. [4] and only a brief summary will be given here. The open loop wind tunnel located at Wright-Patterson AFB uses a centrifugal blower to provide a nominal mass flow of 1.2 kg/s to the test section (Fig. 1). Two different mass flow settings were studied for this report, yielding approximately $\mathrm{Re}_x\cong 500{,}000$ and 900,000 at the test section. A

Contributed by the Heat Transfer Division of ASME for publication in the JOURNAL OF HEAT TRANSFER. Manuscript received March 5, 2004; revised manuscript received September 28, 2004. Review conducted by: S. Acharya.

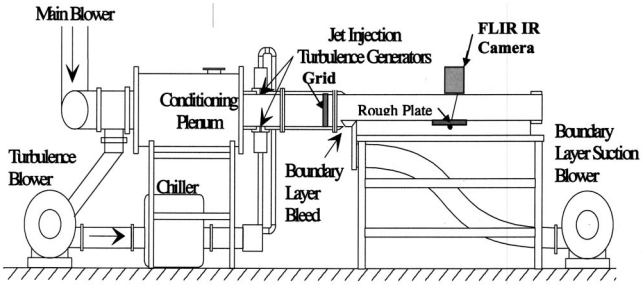

Fig. 1 Schematic of flat plate wind tunnel at AFRL

heat exchanger was used to vary the flow temperature from 18 to 54°C for heat transfer measurements. The flow from the blower enters a conditioning plenum of 0.6 m diameter before reaching the final rectangular wind tunnel section. The freestream turbulence level at the measurement location is 1%. This background level of turbulence can be augmented up to 5% through the use of a passive turbulence-generating grid or 11% with a jets-in-crossflow turbulence generator. At 1.22 m from the plenum exit a knife-edge boundary layer bleed with suction removes the bottom 1.27 cm of the growing boundary layer, making the aspect ratio (span/height) of the final wind tunnel section approximately 1.7 (with no pressure gradient). The top wall of this final section was adjusted in order to set three (roughly linear) pressure gradients in the tunnel: favorable, zero (nominally), and adverse. The three $U_e(x)$ profiles (Fig. 2) have nearly identical boundary layer edge velocities (and thus constant $\mathrm{Re}_x \cong 900{,}000$) at the measurement location (centered at $x=1.18$ m). Acceleration parameters (K) at the measurement location for the three pressure gradients are: 4.73×10^{-7}, 3.52×10^{-8}, and -2.25×10^{-7} for favorable, zero, and adverse, respectively. More details about the individual pressure gradient test conditions can be found in Ref. [5].

For the experiments with surface roughness, this study employed the same roughness characterizations used in previous studies by the author [4–6]. Surface measurements were made on nearly 100 land-based turbine components assembled from four manufacturers: General Electric, Solar Turbines, Siemens-Westinghouse, and Honeywell Corporation. The components were selected by each manufacturer to be representative of surface conditions generally found in the gas turbine inventory. Chord dimensions on the assembled blades and vanes ranged from 2 to 20 cm and included samples with thermal barrier coatings (TBC). In order to respect proprietary concerns of the manufacturers, strict source anonymity has been maintained for all data in this publication.

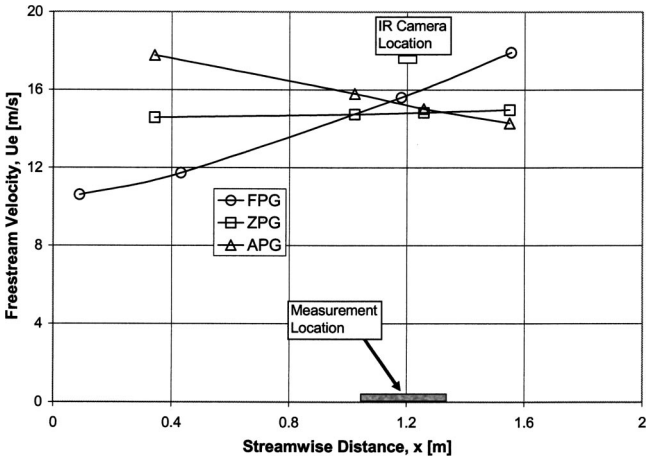

Fig. 2 Freestream velocity distribution for three pressure gradients in AFRL wind tunnel

Extensive two-dimensional (2D) and three-dimensional (3D) surface measurements were made on the assembled hardware using a Taylor-Hobson Form Talysurf series 2 contact stylus measurement system. The complete results are reported in Refs. [4,6]. Of the surfaces available, six different configurations were selected for this study. These include one pitted surface, two coated/spalled surfaces, one fuel deposit surface, and two erosion/deposit surfaces. The surfaces were scaled to match the roughness height to boundary layer momentum thickness ratios typical of other turbine studies ($0.5<k/\theta<3$, where $\theta=2.2$ mm for the zero pressure gradient flow) [7,8]. Roughness classifications spanned the range from transitionally rough ($5<k^+<70$) to fully rough ($k^+>70$). The scaled models were fabricated into 280 mm (streamwise) $\times$360 mm (cross-stream)$\times$7 mm (thick) test panels using a Stratasys Inc. GeniSys Xi 3D plastic printer.

The roughness panels are preceded by 1.04 m of smooth Plexiglas wall (of comparable thermal properties to the plastic panels). Accordingly, the flow experiences a transition from a smooth to rough wall condition at the leading edge of the roughness panels. This experimental setup departs from traditional roughness experiments in which the entire development length of the boundary layer is roughened. Previous work by other researchers [9,10] suggests that St recovers its rough wall value within 3–4 boundary layer thicknesses. To mitigate the effect of this transition region, the heat transfer data were taken on the downstream half of the roughness section (beyond the expected adjustment length). The c_f measurement, however, was made using a bulk method (as described later) and represents an average value over the entire roughness panel set. To reduce the influence of the initial overshoot, the first 20 mm of roughness was scaled to transition linearly from the smooth upstream wall to the full roughness height. Nonetheless, the effect could not be altogether eliminated and its influence on the measured value of c_f was not assessed. That said, the turbine roughness measurements reported by Bons et al. [6] and Taylor [11] show rapid spatial variations in surface character. So, this experimental configuration may actually be more representative of the real turbine blade surface than constant roughness from the leading edge of the tunnel.

***c_f* Measurement.** The present work uses a hanging element balance to obtain the skin friction measurement. This apparatus is described in detail in Ref. [4]. Essentially, the balance consists of a free-floating test section suspended from an apparatus atop the tunnel using thin Nichrome wires. The wires are positioned outside the wind tunnel and are affixed to the four corners of a metal support plate upon which the plastic test panels are mounted. The test panels are positioned flush with the bottom of the wind tunnel. When air is flowing in the tunnel, the plate moves downstream under the applied shear force. This motion was a maximum of approximately 2.5 mm for the highest drag case tested. For such small plate translations, the restoring force of the suspended apparatus is approximately linear with streamwise plate deflection. Using a string-pulley calibrator with factional gram weights, this restoring force was calibrated over the full range of deflections observed in practice. The plate deflection was measured using a Capacitec model No. 4100-S capacitance meter mounted to the side of the test plate, outside the tunnel walls. The wire-pulley calibration is remarkably linear and repeatable with least squares correlation coefficients of 0.9999 and repeatable slopes within $\pm1.5\%$.

The test plate is suspended with a 0.5 mm gap at the leading edge and a trailing edge gap which is set to 0.5 mm greater than the maximum expected excursion. These gaps allow unrestrained motion of the plate under the applied shear force. The gaps also permit differential pressure forces to affect the net displacement of the test plate. To mitigate these pressure forces, the leading edge gap was covered with a 0.05-mm-thick stainless steel sheet with 7

mm overlap with the roughness panels. The initial 10 mm of each panel was smooth to accommodate this overlap without interference. Despite this precaution, differential pressures still contributed to the net plate motion. To calculate this component of the force, three pressure taps were installed at midplate thickness on the adjoining stationary plexiglass pieces, both upstream and downstream of the suspended aluminum support plate with the roughness panels. The three pressure taps were ganged together to produce mean pressures for both the leading and trailing edge of the free-floating test section. A Druck LPM-5481 low pressure transducer was used to monitor this differential pressure and deduct it from the total displacement (force) measured by the Capacitec meter. With these precautionary measures, baseline c_f values (smooth plate with zero pressure gradient and low freestream turbulence) were found to be within 5% of a correlation from Mills [Eq. (10)] [12]. Repeatability was within $\pm 2\%$ and bias uncertainty was estimated at ± 0.0002 for the base line measurement of $c_{f0}=0.0035$ at $\mathrm{Re}_x \cong 900{,}000$.

With the top wall adjusted for a negative (favorable) pressure gradient, the pressure in the wind tunnel exceeds the ambient pressure surrounding the facility. In this case there was a nonnegligible flow out of the downstream gap during the c_f measurement. This created a slightly lower pressure at the downstream sides of the test plate compared to the pressures measured at the three center pressure tap locations. A small bias offset was required to correct for this nonuniformity in the pressure force calculation. Measurement accuracy suffered accordingly and c_f uncertainty worsened to $\pm 12\%$ for some of the rough test panels. The positive (adverse) pressure gradient tests experienced similar complications due to flow leakage (now into the tunnel from the higher ambient pressure) and measurement uncertainty is similar for these test cases. Fortunately, the heat transfer measurement is made without the hanging balance, so there are no gaps in the tunnel and repeatability was within $\pm 5\%$.

St Measurement. For the heat transfer measurements, a FLIR Thermacam SC 3000 infrared (IR) camera system is mounted over a hole in the Plexiglas ceiling of the tunnel. The camera setup and data reduction procedure are documented in Ref. [4]. The optical port is sealed to the camera lens using a cylindrical housing. This prevents air from exiting or entering through this port during tests with variable pressure gradient. For this study, the focal distance of the camera was kept constant regardless of the height of the adjustable tunnel ceiling. The camera field of view is roughly 70×90 mm, centered at $x=1.2$ m. The surface temperatures recorded by the camera were area-averaged to obtain the surface temperature history required by the St calculation algorithm. The Stanton number was determined from this surface temperature history using the method of Schultz and Jones [13]. This transient technique uses Duhamel's superposition method to calculate the surface heat flux given the surface temperature history. It assumes the panels are a semi-infinite solid at constant temperature at the start of the transient. To accomplish this, the plastic panels were mounted on a 12-mm-thick acrylic sheet rather than an aluminum plate for this measurement. This acrylic has approximately the same thermophysical properties as the plastic panels to avoid thermal wave reflections at the contact surface. A thermocouple sandwiched between the panels and the plexiglass sheet indicated a slight rise in temperature after approximately 30 s for the typical test case. Thermocouples mounted to the underside of the plexiglass support sheet showed no significant change within the total test time of approximately 90 s. This confirmed the use of the semi-infinite conduction assumption in the data processing.

Prior to testing, the entire test section was maintained at room temperature for several hours. Using the flow heat exchanger, hot air flow was then initiated instantaneously while monitoring the freestream velocity and temperature above the measurement site as well as the average surface temperature (with the IR camera). The spatially averaged heat transfer coefficient (h) at each time step was then calculated using the expression in Ref. [4]. With this procedure, base line St values (smooth plate with zero pressure gradient and low freestream turbulence) were found to be within 3% of a correlation from Mills [Eq. (11)] [12]. Repeatability was within $\pm 5\%$ and bias uncertainty was estimated at ± 0.00015 for the base line measurement of $\mathrm{St}_0=0.00215$ at $(\mathrm{Re}_x \cong 900{,}000)$. Due to this transient method of St measurement, the thermal and velocity boundary layers in the tunnel begin simultaneously at $x=0$ (without an unheated starting length). Also, the thermal boundary condition at the wall is neither constant wall temperature nor constant wall heat flux, since the heat transfer measurement is transient.

Reynolds Analogy Factor Uncertainty. Combining the quoted uncertainties for c_f and St yields an uncertainty in the Reynolds analogy factor $(2\mathrm{St}/c_f)$ of $\pm 9\%$ for the base line smooth, zero pressure gradient case with low freestream turbulence (RA_0). Due to the larger bias errors associated with the nonzero pressure gradient tests, the uncertainty in Reynolds analogy factor can reach as high as 13% for the favorable and adverse pressure gradient cases. Since the majority of this is due to bias error associated with the c_f measurement, the relative uncertainty is eliminated by normalizing the data by the base line value, RA_0. This is the data format used in the majority of what follows.

Results and Discussion

The change in the Reynolds analogy factor as the boundary layer transitions from laminar to turbulent with increasing Reynolds number is presented first. This is followed by assessments with pressure gradient, surface roughness, and freestream turbulence. Following this, data are presented for the combined effects of pressure gradient with roughness and freestream turbulence with roughness.

Effect of Boundary Layer State and Reynolds Number. Though boundary layers in turbines are often considered to be turbulent due to high levels of freestream turbulence and the high Reynolds number flow, strong accelerations near the leading edge of a HP airfoil can delay transition for up to 30% of the suction surface length [14]. In the LPT, this laminar flow regime can extend even further down the suction surface when chord Reynolds numbers drop below 100,000 [15]. Pressure surface boundary layers are more susceptible to early transition due to the Goertler flow instability. Thus the variation of Reynolds analogy factor with boundary layer state is relevant to turbine flows.

Blasius' [16] solution of the flat plate boundary layer equations for laminar flow [Eqs. (1) and (2)] yields an analytical expression for c_f; while Polhausen's [17] subsequent analysis including the energy equation [Eq. (3), with the constant T_w boundary condition] yields a corresponding expression for St (valid for a wide range of Pr):

$$c_f = \frac{0.664}{\mathrm{Re}_x^{1/2}} \tag{7}$$

$$St = \frac{0.332}{\mathrm{Re}_x^{1/2}\,\mathrm{Pr}^{2/3}} \tag{8}$$

When combined to form the Reynolds analogy for flat plate laminar flow, there follows what is variously referred to as the ''modified'' Reynolds analogy, Chilton–Colburn, or just Colburn relation [18,19]:

$$\frac{2\mathrm{St}}{c_f} = \frac{1}{\mathrm{Pr}^{2/3}} \tag{9}$$

The dependence of this relation on pressure gradient can be evaluated using the Falkner–Skan analytical solutions, coupled with the energy equation for constant wall temperature (as shown by White [20]). These solutions are valid for similar boundary layers with a power-law $U_e(x)$ distribution (e.g., $U_e=k_1x^m$). Fig-

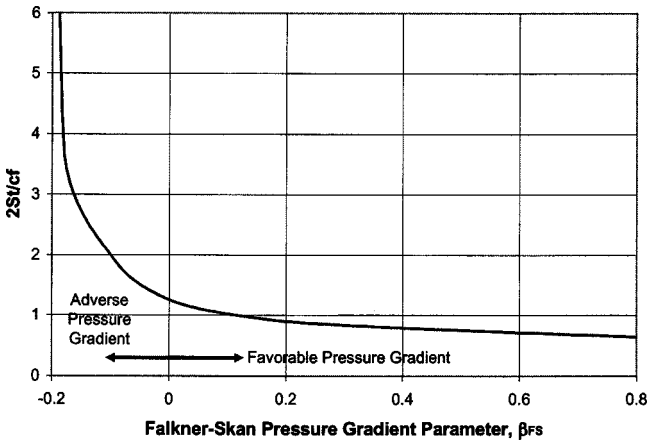

Fig. 3 Variation in Reynolds analogy factor with pressure gradient for laminar boundary layer (Pr=0.71)

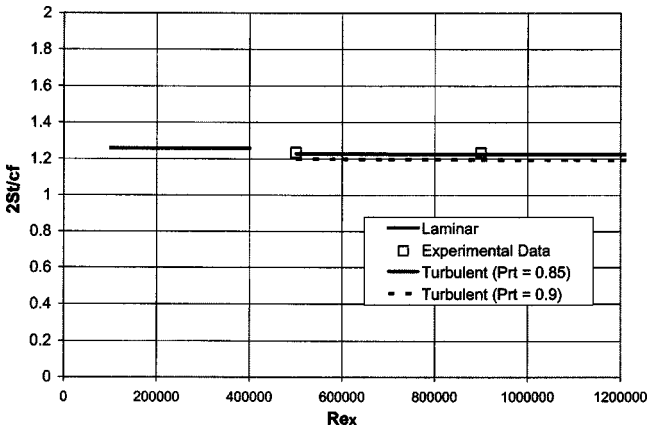

Fig. 4 Variation in Reynolds analogy factor with Reynolds number for laminar and turbulent boundary layers (Pr=0.71)

ure 3 shows the variation of the Reynolds analogy factor with the Falkner–Skan pressure gradient parameter, β_{FS}, for Pr=0.71 (Note: the exponent $m=\beta_{FS}/(2-\beta_{FS})$, thus $-0.1988<\beta_{FS}<0$ is for adverse pressure gradients and $0<\beta_{FS}<1$ is for favorable pressure gradients). The considerable variation of $2St/c_f$ shown in Fig. 3 results from the fact that St is much less sensitive to changes in pressure gradient than c_f. For example, as β_{FS} approaches -0.1988, which is the smallest β_{FS} value for which a stable (attached) boundary layer solution is possible, the wall shear falls to zero $[(du/dy)_w=0]$. At the same time, St is still at a healthy 70% of its zero pressure gradient ($\beta_{FS}=0$) value. Because of this disparity, $2St/c_f$ is unbounded as β_{FS} approaches -0.1988. This is because stagnant near wall fluid still conducts heat, even when the momentum exchange in the boundary layer is completely halted. In like fashion, a separation bubble on a turbine blade will experience net heat transfer though the mean wall shear is negligible. A similar trend is evident for accelerated flow (e.g., $\beta_{FS}=0.3$), where the c_f increase from its $\beta_{FS}=0$ value is nearly 80% compared to only a 20% increase for St. Thus $2St/c_f$ drops from 1.25 at $\beta_{FS}=0$ to 0.83 at $\beta_{FS}=0.3$ in Fig. 3. The explanation for this strong c_f dependency on pressure gradient is straightforward. Laminar flow is characterized by ordered ''laminae'' (Latin for ''thin sheets'') of fluid in the boundary layer. Thus, laminar heat transfer occurs primarily via conduction regardless of the pressure gradient (though there is a small nonzero wall-normal velocity component which does convect some energy). Laminar skin friction, on the other hand, is directly proportional to the velocity gradient at the wall, which is determined from a balance of the rate of change of fluid momentum flux with the streamwise pressure gradient.

Though the precise Reynolds number at which transition to a turbulent boundary layer takes place is dependent on many factors, when it occurs transition typically results in a factor of 2–4 increase (depending on Re) in both c_f and St due to the heightened mixing of momentum and energy. The increase in c_f is slightly greater than that for St, so that the zero-pressure gradient value of the Reynolds analogy factor is generally taken to be slightly less than the laminar flat plate value of 1.25 (for air with Pr≅0.71). The exact value depends on the assumed value for the turbulent Prandtl number, Pr_t, which represents the ratio of eddy viscosity and eddy thermal diffusivity, ν_t/α_t. Figure 4 shows the Reynolds analogy factor obtained by combining turbulent correlations for c_f and St [12]:

$$c_f=\frac{0.026}{Re_x^{1/7}} \tag{10}$$

$$St=\frac{0.5c_f}{Pr_t+\sqrt{0.5c_f}[5Pr+5\ln(5Pr+1)-14Pr_t]} \tag{11}$$

Lines are shown for two values of Pr_t: 0.85 (as recommended by Kader and Yaglom [21] for flat plate turbulent boundary layers) and 0.9 (the value used in Ref. [5]). The Reynolds analogy factor decreases with increasing Pr_t since one is essentially the reciprocal of the other for turbulent boundary layers with no pressure gradient.

Figure 4 also shows the base line experimental data, which appear to correspond to the lower Pr_t value of 0.85. Before and after transition, the Reynolds analogy factor is relatively independent of Reynolds number since, for the case of a smooth wall with no pressure gradient and low freestream turbulence, the hydrodynamic and thermal profiles are similar (for Pr≅1) and both St and c_f decrease with increasing Reynolds number.

Effect of Streamwise Pressure Gradient. Unlike laminar boundary layers, it is expected that turbulent boundary layers will experience similar variations of c_f and St with pressure gradient. Turbulent mixing is the primary mechanism for energy and momentum transfer and convection replaces conduction as the dominant heat transfer process. This intuition is summarized by Incropera and DeWitt [22] with the statement that, '' . . . [compared to laminar flow] turbulent flow is less sensitive to the effect of pressure gradient and [Eq. (9)] remains approximately valid.'' To explore this effect analytically, So [23] extended the equilibrium turbulent boundary layer analysis of Mellor and Gibson [24] to the thermal boundary layer. He thus obtained an expected trend for the Reynolds analogy factor with pressure gradient. In So's analysis, the pressure gradient is characterized using Clauser's equilibrium parameter

$$\beta_{CL}=\frac{\delta^*}{\tau_w}\frac{dp_e}{dx}=-\frac{2}{c_f}\frac{\delta^*}{U_e}\frac{dU_e}{dx}=-\frac{2}{c_f}Re_{\delta^*}K \tag{12}$$

where K is the acceleration parameter

$$K=\nu\frac{dU_e}{dx}\frac{1}{U_e^2}$$

The predictions of So for two values of Pr_t are plotted in Fig. 5 (normalized by RA_0). In this figure and all succeeding plots, the Reynolds analogy factor is normalized by its value for a smooth wall, zero-pressure gradient turbulent boundary layer with no freestream turbulence (i.e., $\beta_{CL}=0$). The experimental data shown in Fig. 5 (and all the plots to follow) are for $Re_x=900{,}000$ and use a turbulent boundary layer base line value of $RA_0=1.20$ for the normalization. [Note: The c_f data with nonzero

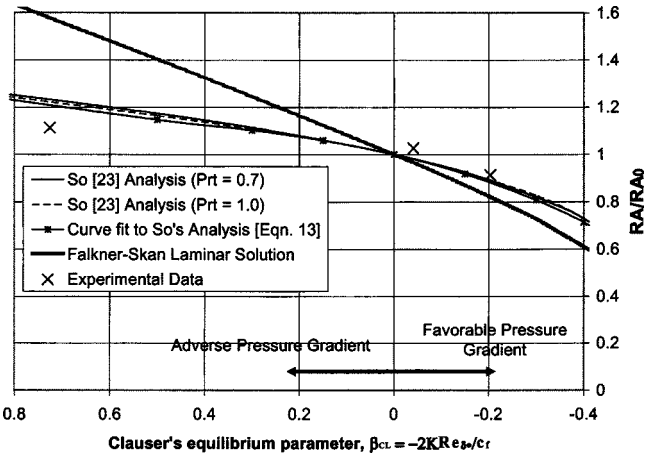

Fig. 5 Variation in normalized Reynolds analogy factor with pressure gradient for turbulent and laminar boundary layers (Pr=0.71). Data for $Re_x \cong 900{,}000$.

pressure gradient were actually taken at a slightly lower Re_x than the corresponding St data (800,000 vs 900,000), but given the weak Reynolds number dependency of c_f, this was not considered to be significant.] The So analysis is only strictly valid for equilibrium turbulent boundary layers with constant wall temperature. As discussed in Ref. [5], the thermal boundary condition for this transient heat transfer experiment varies from roughly constant T_w for adverse pressure gradient to a power law $T_w(x)$ for favorable pressure gradient. This coupled with the fact that the experimental boundary layers are not classical ''equilibrium'' turbulent boundary layers may explain the deviation from So's prediction, though the predictions do fall within the uncertainty bounds of the experimental data. It is important to note here that Clauser's equilibrium parameter is defined so that $\beta_{CL}<0$ is for a negative (favorable) pressure gradient while $\beta_{CL}>0$ is for a positive (adverse) pressure gradient. This is, unfortunately, opposite to the sign convention used for the Falkner–Skan pressure gradient parameter, β_{FS} (Fig. 3). Accordingly, Fig. 5 plots β_{CL} from +0.8 to −0.4 (adverse to favorable, similar to Fig. 3). The Falkner–Skan laminar boundary layer curve is also plotted versus β_{CL} for comparison (normalized by $RA_0=1.25$ for laminar flow). A polynomial approximate curve fit to the two So analytical curves is indicated in Fig. 5 for use later in this report. [Note: as indicated previously, the value of RA_0 varies inversely with Pr_t.]

$$\frac{RA}{RA_0} = 1 + 0.4626\beta_{CL} - 0.5032\beta_{CL}^2 + 0.3243\beta_{CL}^3 \qquad (13)$$

Both data and prediction show a greater effect of pressure gradient on c_f than on St (though certainly not as pronounced as in the laminar case). For example, when β_{CL} decreases from 0 to −0.2 (favorable pressure gradient), the experimental c_f measurement increases from 0.0035 to 0.004,54 (30%) while St increases from 0.00215 to 0.00248 (only 16%). Similarly, for the adverse pressure gradient data point, the reduction in c_f is 14% compared to 7% for St. This finding has been noted by others, dating back to the late 1960's nozzle flow experiments of Back et al. [25,26]. In two different cases, the $2St/c_f$ factor dropped from 1.25 at zero pressure gradient to approximately 0.7 in the accelerated zone of the nozzle (i.e., $RA/RA_0 \cong 0.56$). Back et al.'s acceleration parameters (K) were 2–4 times higher than for the present study, explaining the more significant drop in RA/RA_0 with acceleration. Boundary layer temperature and velocity measurements indicated that the thermal resistance of the turbulent boundary layer (the enthalpy thickness, Δ) was much less responsive to acceleration than the momentum thickness (θ). Indeed, temperature profiles taken in their converging nozzle varied only slightly with axial distance while the velocity profiles exhibited a large shift of momentum down to the wall. Thus, though the effect of pressure gradient on the Reynolds analogy factor for turbulent boundary layers is not as dramatic as for laminar boundary layers (Fig. 5), contrary to the statement quoted earlier from Ref. [22], it is still significant.

Figure 5 depicts the variation of RA/RA_0 with β_{CL}, a parameter which is not readily available to turbine designers. To provide a sample range of β_{CL} values for turbine flows, two recent studies were consulted. Dorney et al.'s [27] two-stage LPT unsteady calculations of an experimental configuration reported by Halstead et al. [14] shows a β_{CL} variation from −0.35 to 0.14 on the LP nozzle suction surface. A second study by Sharma et al. [28] for two HP nozzle configurations (aft-loaded and squared-off) reports suction surface β_{CL} ranges from −1.1 to 0.65 for the aft-loaded vane and from −0.04 to 1.0 for the squared-off vane. While these β_{CL} values are only estimates pieced together from the assorted experimental and computational data provided in these two studies, they do suggest that turbulent boundary layers on modern turbine airfoils could see Reynolds analogy fluctuations by a factor of 2 from the most aggressive favorable pressure gradient to the most severe adverse pressure gradient. If the flow acceleration is too pronounced, it is possible for near-wall turbulent fluctuations to be attenuated and boundary layer relaminarization can occur (such as following a suction surface separation bubble [29]). Such a phenomenon would result in a dramatic reduction in St as convection gives way to the more benign conduction heat transfer. The corresponding drop in skin friction would be more modest, thus the Reynolds analogy factor would drop appreciably in such a relaminarization zone.

One final note is in order regarding these findings with a turbulent boundary layer and pressure gradient. Some researchers have reported precisely the opposite trend in St with pressure gradient. For example, Moretti and Kays [30] report a decrease in St as freestream acceleration is increased for their low-speed wind tunnel data [as opposed to the increase in St with favorable pressure gradient (FPG) reported here]. This discrepancy can be explained by reviewing differences between the two experimental configurations. Moretti and Kays' St comparison is made at the same streamwise (x) position and for the same tunnel inlet ($x=0$) velocity in each case. Thus, their favorable pressure gradient case has a U_e at the measurement location nearly four times that of their zero pressure gradient case. Since St and c_f are normalized by U_e, this is accounted for in their plots, except for the fact that the Re_x values still differ by the same factor of 4. Also, their unheated starting length produces a thermal boundary layer thickness that is much smaller than the velocity boundary layer, hence the damping of near-wall turbulent velocity fluctuations that occurs under an accelerating freestream has a more pronounced effect on heat transfer than if $\delta \cong \delta_t$. This is because the bulk of the thermal boundary layer is located in the region of highest turbulent mixing. Thus it is important to bear in mind the experimental conditions when considering the application of experimental findings. The present facility compares data at a constant Re_x condition but with different tunnel inlet velocities. Also, there is no unheated starting length, since a turbine blade has none. Thus the thermal and hydrodynamic boundary layer thicknesses are comparable ($\delta \cong \delta_t$) and the boundary layer dimensions at the measurement location vary considerably with pressure gradient (42, 27, and 12 mm for adverse, zero, and favorable pressure gradient, respectively). An alternative (and perhaps more academically correct) test procedure would be to compare the three pressure gradient flows with matched Re_θ (for c_f) and Re_Δ (for St) at the measurement location. This would provide an unambiguous comparison of pressure gradient effects since θ and Δ are integrated measures of momentum and energy (respectively) which account for all upstream effects. To do this would require a much more elaborate test facility and it was not attempted here. That said, the momentum thickness values for the three pressure gradients were:

4.7, 2.2, and 1 mm for adverse, zero, and favorable pressure gradient respectively (yielding Re_θ values from 3500 to 750). The enthalpy thickness was not measured due to the transient nature of the heat transfer measurement.

Surface Roughness Correlations. Historically, turbine roughness has been characterized by relating it to the uniform sandgrain size (k_s) that would produce an "equivalent" increase in c_f. Schlichting [31] introduced this concept of "equivalent sandgrain roughness" by comparing skin friction data for a number of different roughness elements (with various shapes, sizes, and spacings) to sandgrain-roughened pipe flow data from Nikuradse [32]. Schlichting tabulated k_s/k ratios for these various elements, which have subsequently seen wide application for over half a century. (Note: Schlichting's k_s analysis has since been updated by the careful evaluation of Coleman et al. [33].) With these k_s/k tables, engineers can empirically estimate the increase in c_f and St [which is commonly based on c_f and k_s, see Eq. (11)] from a readily measured quantity, k, the average roughness element height.

Numerous researchers have attempted to replace the cumbersome use of such tables with broader roughness correlations. As a more recent example, Sigal and Danberg [34] correlated the k_s/k data from Schlichting (and others) to a roughness element shape-density parameter, Λ_s. This parameter was developed for uniform arrays of two- and three-dimensional roughness elements mounted to a flat surface of area S. It is essentially the product of two area ratios:

$$\Lambda_s = \frac{S}{S_f}\left(\frac{A_f}{A_s}\right)^{-1.6} \tag{14}$$

"S" is the surface area without roughness elements while "S_f" is the forward (windward) facing projected area of all roughness elements. Thus, S/S_f is inversely proportional to the density of roughness elements on the surface. "A_f" is the windward projected surface area of a single roughness element while "A_s" is the windward wetted surface area of the element. Thus, A_f/A_s represents the individual roughness element shape. For example, a hemisphere mounted to a flat surface has an $A_f/A_s=0.5$ while a flat, vertical tab oriented perpendicular to the flow direction has an $A_f/A_s=1$. Using Λ_s, Sigal and Danberg correlated a variety of existing k_s/k data for three-dimensional roughness elements using a single expression

$$\log\left(\frac{k_s}{k}\right) = -1.31\log(\Lambda_s) + 2.15 \text{ (valid for } \Lambda_s > 15) \tag{15}$$

A large value of Λ_s represents a surface with sparse, gradually sloped roughness elements while a small value of Λ_s signifies densely packed, abrupt elements. Below $\Lambda_s \approx 15$ the elements are too dense to exert their full negative effect on c_f and a different correlation with positive slope is more appropriate.

Before turbine components have seen service, their surfaces are well characterized using tabulated correlations derived from uniform roughness elements. For non-TBC-coated turbine surfaces, Forster [35] used $k_s/\mathrm{Ra} \approx 2$ based on $k/\mathrm{Ra} \approx 5$ and $k_s/k \approx 0.4$ for machine-ground surfaces. Likewise, Bammert and Sandstede [36] presented an identical k_s/Ra expression for typical milled surfaces. Koch and Smith [37] estimated a value of $k_s/\mathrm{Ra} \approx 6$ for emery paper of various grit sizes; a surface representation that might be used to approximate a TBC-coated turbine surface after polishing and before service.

Unfortunately, as a result of service use, turbine surfaces quickly become much more varied than these simple, uniform representations. Thus, surface measurements taken from serviced turbine components display characterizations that differ significantly from a flat surface with an ordered array of uniform roughness elements [6,11]. For example, Fig. 6 shows representative 2D traces from the six roughness panels used in this study (Note: vertical scale is magnified for clarity). Each trace is composed of

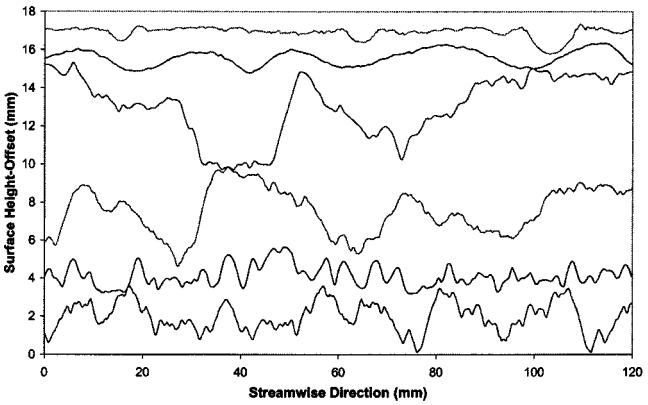

Fig. 6 Sample 2D traces from each of the six scaled roughness surfaces. Surfaces are ordered top to bottom as listed in Table 1. Vertical scale is magnified and traces are offset vertically for clarity. For reference, the tunnel boundary layer thickness for zero pressure gradient is $\delta \cong 27$ mm.

a wide variety of roughness sizes, shapes, and distributions. Since turbine roughness is highly nonuniform and random, some adaptation is required to use the $k_s/k = f(\Lambda_s)$ correlation of Sigal and Danberg [Eq. (15)]. Instead of identifying individual roughness elements, a three-dimensional surface topography (map) must be analyzed point-by-point to determine the windward projected and wetted areas of each "cell" of the overall roughness map. (A cell is defined as the surface area bounded by four contiguous surface height point measurements in a rectilinear grid or map.) Thus, referring to Eq. (14), S becomes the planform area of the surface map (with surface curvature removed) while S_f is equivalent to the summation of the windward projected area of each cell. A_f is the average windward projected area of all cells, while A_s is the average windward wetted area of all cells. Equation (14) thus becomes Eq. (16)

$$\Lambda_s = \frac{\Sigma A_{\text{cell}}}{\Sigma A_{f,\text{cell}}}\left(\frac{\frac{1}{N}\sum A_{f,\text{cell}}}{\frac{1}{N}\sum A_{s,\text{cell}}}\right)^{-1.6} \tag{16}$$

This Λ_s quantity was calculated for the six scaled roughness models in Fig. 6 and the results were presented in Ref. [4]. Then, using experimental c_f measurements reported in that study, the equivalent sandgrain roughness, k_s, for each model was determined using Schlichting's correlation [38] for fully rough surfaces

$$c_f = [2.87 + 1.58\log(x/k_s)]^{-2.5} \tag{17}$$

Finally, the roughness height, k, for each roughness model was estimated based on the average of the maximum peak-to-valley height difference (Rz) in each 20 mm square of the 360 mm×280 mm roughness models. These three measurements (Λ_s, k_s, and k) allowed a formal comparison to the correlation of Sigal and Danberg [Eq. (15)]. The result for these six turbine roughness models yielded a slightly different equation than that presented in Ref. [34]:

$$\log\left(\frac{k_s}{k}\right) = -0.43\log(\Lambda_s) + 0.82 \tag{18}$$

This relation was proposed as a correlation for characterizing the "real" turbine roughness models used in this study, as compared to the "simulated" roughness arrays on which Eq. (15) was based.

Unfortunately, turbine operators and maintenance personnel do not typically have access to three-dimensional surface-mapping equipment, or if they do, the instruments are too unwieldy to make measurements while the turbine is assembled. Instead, two-

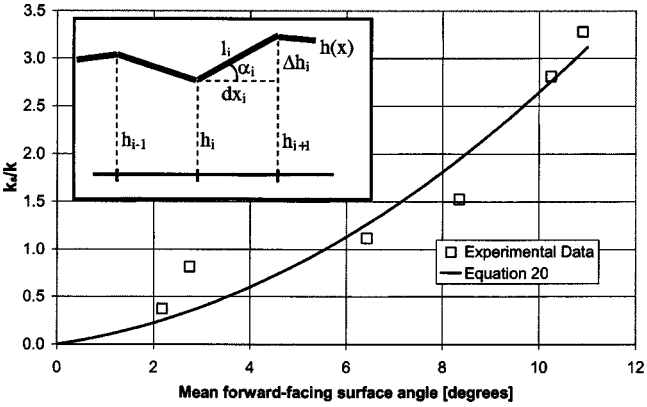

Fig. 7 k_s/k versus $\overline{\alpha_f}$ from 2D surface assessments of the six scaled roughness surfaces. Inset schematic shows 2D surface height representation for Eq. (19).

dimensional surface roughness measurements are routinely made with a contact stylus device during inspections and refurbishment. Thus, it would be more useful to have two-dimensional representations of Λ_s and k for the k_s/k correlation. Accordingly, a single streamwise surface trace can be evaluated to provide 2D approximations for A_{cell}, $A_{f,\text{cell}}$, and $A_{s,\text{cell}}$. As an illustration, the surface height distribution, $h(x)$, schematic shown in the upper left corner of the plot in Fig. 7 shows that for a generic 2D surface trace, the $A_{\text{cell}}/A_{f,\text{cell}}$ ratio can be approximated by a ratio of the streamwise distance dx_i, to the step height difference Δh_i. Likewise the $A_{f,\text{cell}}/A_{s,\text{cell}}$ ratio is approximated by $\Delta h_i/l_i$. In this manner, Eq. (16) can be re-evaluated for a 2D streamwise surface trace by summing over all surface elements with $\Delta h_i > 0$ (windward facing elements only)

$$\Lambda_s = \frac{\Sigma\, dx_i}{\Sigma \Delta h_i}\left(\frac{\Sigma \Delta h_i}{\Sigma\, l_i}\right)^{-1.6} \tag{19}$$

To obtain an accurate roughness characterization, this 2D measurement must be made multiple times in the region of interest for the turbine component being inspected. This quantity was calculated for the six roughness models used in this study and the results differed from their 3D counterpart [i.e., Eq. (16)] by only 6% on average. Revisiting the 2D schematic in Fig. 7, it is apparent that both length ratios in Eq. (19) can be represented as a function of the forward-facing surface angle, α_i ($dx_i/\Delta h_i = 1/\tan\alpha_i$ and $\Delta h_i/l_i = \sin\alpha_i$). Representing both trigonometric functions by their small angle approximation, the $\Lambda_{s,i}$ contribution from each "i" surface step is then proportional to $\alpha^{-2.6}$. Thus, the three-dimensional shape-density parameter of Sigal and Danberg [34] and the average forward-facing surface angle ($\overline{\alpha_f}$) obtained from a series of 2D roughness measurements are related geometrically. Thus, it is expected that k_s/k should correlate as well with $\overline{\alpha_f}$ as it does with Λ_s. Interestingly, the rms deviation of surface angles, α_{rms}, was proposed by Acharya et al. [39] as an essential parameter for characterizing random (real) roughness.

As was done with Λ_s in Ref. [4], this roughness shape parameter, $\overline{\alpha_f}$, was correlated to the k_s/k measurements for the six roughness models. This required careful consideration of the value of k, the average roughness height. For Eq. (18), k was estimated based on the average of the maximum peak-to-valley height difference (Rz) in each 20 mm square of the 3D surface map. Since the use of α_f is intended to eliminate the need for 3D surface roughness measurements, a 2D measure for k is also necessary. Bogard et al. [7] estimated the average roughness height (k) based on the five largest peak-to-valley distances in 8 mm long 2D turbine surface traces. This is equivalent to 1 peak per 2.5 mm, a distance equal to 30 times the estimated boundary layer momentum thickness for their turbine blade application. For this study, the 2D estimate for k was based on the seven largest peak-to-valley distances in the 280 mm streamwise distance, or 1 peak per 40 mm. This is equivalent to roughly 20 momentum thicknesses for the zero pressure gradient case. Table 1 contains this 2D estimate for the average roughness height, k, as well as $\overline{\alpha_f}$ and other relevant roughness statistics from Ref. [4].

Figure 7 shows the k_s/k versus $\overline{\alpha_f}$ data based on 2D roughness assessments only. A polynomial curve fit to the data is offered below (correlation coefficient, $R^2 = 0.93$):

$$\frac{k_s}{k} = 0.0191\overline{\alpha_f^2} + 0.0736\overline{\alpha_f} \equiv f_\alpha \tag{20}$$

This relation is denoted by the symbol f_α in the remainder of this report. It is a dimensionless roughness shape function. The author prefers this roughness correlation to the one from Ref. [4] based on Λ_s [Eq. (18)] since $\overline{\alpha_f}$ is easier to calculate in practice. Also, the correlation from $\overline{\alpha_f}$ to k_s/k has the physically realistic result that in the limit of a smooth surface ($\overline{\alpha_f} = 0$), $k_s = 0$. As such, the Reynolds analogy data in this report is presented as a function of kf_α (which, from Eq. (20), is equivalent to k_s) normalized by the local boundary layer momentum thickness without roughness, θ (2.2 mm for the zero pressure gradient baseline case). Though the broader application of Eq. (20) to roughness characterizations other than those evaluated in this study has not been assessed, normalizing the roughness height by θ provides a relative roughness measure that has been used by others to compare results at different Reynolds numbers, pressure gradients, etc... [7,9].

Effect of Surface Roughness. Numerous studies have documented the degradation of smooth turbine airfoil surfaces with service use [6,7,11,40]. Though surface roughness has many different causes (e.g., erosion, deposition, spallation, etc.), the net result is increased convective heat transfer and increased skin friction. The latter increase is by far the more significant of the two. The individual c_f and St measurements for the scaled roughness surfaces in this study have been reported previously [4]. St increases (at constant Re_x) were 10–45% while c_f increases were as much as four times this amount. Figure 8 shows the variation of RA/RA_0 with kf_α/θ for the six panels in Table 1. The largest reduction in RA/RA_0 (roughly 50%) represents a 43% increase in St accompanied by a 200% increase in c_f. The physical explanation for this is that increases in c_f due to roughness are primarily due to pressure (or form) drag on the individual roughness elements. There is no heat transfer analog to this form drag component of c_f augmentation. In fact, nearly half of the observed increases in St can be explained by the increase in wetted surface area compared to the smooth baseline surface (S_w/S). The re-

Table 1 Surface statistics for scaled roughness models

Type	Ra [mm]	k from 2D [mm]	Rt [mm]	α_{rms} [deg]	S_w/S	$\overline{\alpha_f}$ [deg]	$k^+ \equiv \text{Re}_k$	kf_α [mm]
Pitted	0.12	0.627	2.08	7.23	1.016	2.8	20	0.22
TBC debond	0.30	1.082	2.01	5.48	1.009	2.2	15	0.27
TBC spalled	0.84	2.561	6.43	16.4	1.08	6.4	135	3.23
Fuel deposits	1.17	4.041	7.3	20.6	1.224	8.4	322	7.86
Erosion/deposits	0.46	2.240	4.05	24.1	1.197	10.3	330	6.18
Erosion/deposits	0.52	2.678	4.23	25.3	1.198	10.9	481	8.23

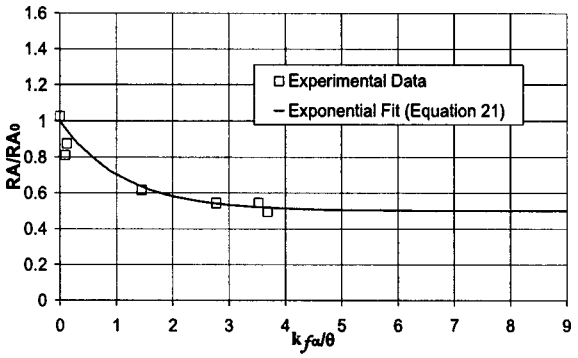

Fig. 8 Variation in normalized Reynolds analogy factor with kf_α/θ for roughness models. $Re_x \cong 900{,}000$.

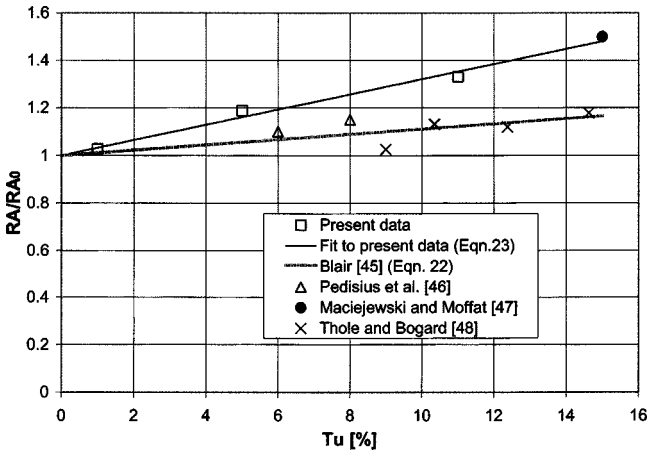

Fig. 9 Variation in normalized Reynolds analogy factor with freestream turbulence (Tu). Data for $Re_x \cong 900{,}000$.

mainder of the St rise can be attributed to enhanced mixing due to the unsteady shedding of turbulent eddies from individual roughness elements.

Also indicated in Fig. 8 is an exponential curve fit to the experimental data that is used later in this report

$$\frac{\mathrm{RA}}{\mathrm{RA}_0} = 0.5[1 + e^{-0.9kf_\alpha/\theta}] \tag{21}$$

Belnap et al. [3] also reported Reynolds analogy factor variation with roughness for fully developed turbulent channel flow with roughened walls. In their study, $\mathrm{RA/RA_0}$ dropped by 10–15% for surface roughness $k^+(\mathrm{Re}_k)$ levels in the range from 10 to 30. This is comparable to the decrease shown in Fig. 8 for the first two roughness panels, which have similar levels of k^+ (20 and 15, respectively, see Table 1). Incidentally, the smooth wall $\mathrm{RA_0}$ value for the Belnap et al. study is approximately 0.95. Due to the favorable pressure gradient inherent in a fully developed channel flow, the Reynolds analogy is lower than the turbulent, zero pressure gradient value of $\mathrm{RA_0} = 1.2$ (as expected from the foregoing discussion).

Effect of Freestream Turbulence. Gas turbine combustor exit turbulence has been documented at levels from 10% to 20%, depending on the specific configuration [41,42]. Film cooling in the HP can increase this level locally depending on injection angle and blowing ratio. The level of freestream turbulence is reduced significantly by the time the flow reaches the LPT, where levels may be closer to 2–7% [43]. In addition, convected blade wakes create periodic high turbulence fluid events which sweep across the downstream row of airfoils [44]. Finally, separation bubbles in LPTs show heightened turbulence levels when the flow reattaches to close the bubble [29]. Clearly, freestream turbulence is a staple of turbine flowfields.

The variation of $\mathrm{RA/RA_0}$ with freestream turbulence is shown in Fig. 9. Also shown is a correlation from Blair [45] based on grid-generated turbulence data up to 7%:

$$\frac{\mathrm{RA}}{\mathrm{RA}_0} = 1 + 0.011\mathrm{Tu} \tag{22}$$

In Eq. (22), freestream turbulence level (Tu) is in percent. A linear fit to the present data is also shown in the figure

$$\frac{\mathrm{RA}}{\mathrm{RA}_0} = 1 + 0.032\mathrm{Tu} \tag{23}$$

Data from several other experimental facilities are included as well [46–48]. The two lines appear to bound the data, though the Tu coefficient in Eq. (23) is nearly three times the value in Eq. (22). Despite this scatter in the various results, the bias of freestream turbulence to St over c_f is evident. For example, the present data point at 11% turbulence represents a 50% rise in St but only a 16% increase in c_f.

Since there is no form drag component, freestream turbulence does not overwhelmingly favor c_f (as was the case for surface roughness). Elevated freestream turbulence results in fuller thermal and velocity boundary layer profiles, which means increased opportunities for mixing down in the viscous sublayer. As the freestream turbulence level increases, the spatial extent of cross-boundary layer mixing increases as well. Eventually, large freestream motions (''outer'' turbulence) overwhelm the smaller-scale turbulent motions (''inner'' turbulence) that are responsible for shear stress production. Thole and Bogard [48] hypothesized that these larger structures are not as active at producing shear stress since they are characterized by large streamwise fluctuations but reduced vertical turbulence (due to attenuation at the wall). They are still thermally active, however, and thus produce a disproportionate increase in St compared to c_f.

Several researchers have reduced the data scatter in Fig. 9 by using a combination of turbulence level with turbulence lengthscale. For this facility, for example, the integral lengthscale more than doubles (from 3.5 to 8 cm) with the change from grid (5%) to jet (11%) generated turbulence. While there is ample evidence that both St and c_f are reduced somewhat as the turbulence lengthscale is increased at constant intensity level [45,49], the data scatter is only partially resolved with this added complexity as evidenced in the data presentation of Thole and Bogard [48]. The integral lengthscale to boundary layer thickness ratios for the two turbulence levels in this study are 1.3 and 3, which fall in the range of ratios studied by others [48] for simulating turbine flows.

Pressure Gradient and Surface Roughness. There are a number of different methods that could be used to assess the combined effects of roughness and pressure gradient on c_f, St, and their ratio ($2\mathrm{St}/c_f$). Of critical importance to the designer is whether results with pressure gradient alone can be simply added to results with roughness alone to approximate the effect when both are present. If true, this would imply a lack of synergy between the two mechanisms. This is attractive because it allows correlations to be simply superposed in a design code without additional parametric testing. One way to determine the degree to which two mechanisms are synergistic is to compare results obtained with both mechanisms present to that achieved by adding their individual effects. For example, if the smooth plate c_f increase due to favorable pressure gradient was 20% and the c_f increase of a rough plate (with no pressure gradient) was 30%, the additive method would predict a combined effect of 50%. This

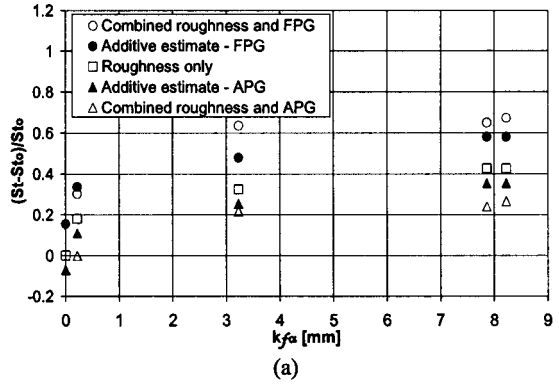

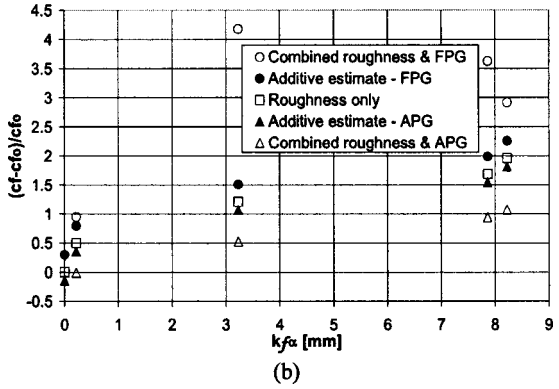

Fig. 10 Comparison of combined roughness and pressure gradient effects with roughness only and with additive estimate. (*a*) change in St (*b*) change in c_f. Changes in c_f and St Data for $Re_x \cong 900{,}000$.

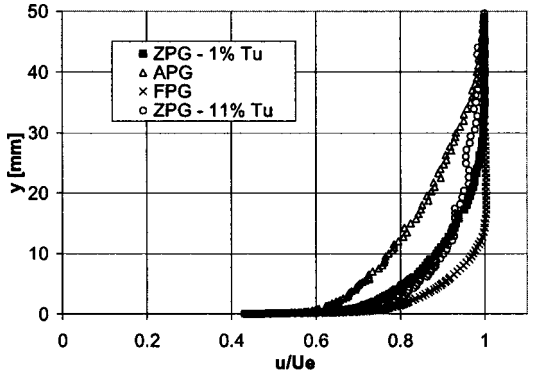

Fig. 11 Boundary layer profiles for adverse pressure gradient (APG), zero pressure gradient (APG), zero pressure gradient (ZPG with low Tu), favorable pressure gradient (FPG), and high (11%) freestream turbulence (ZPG). Data for $Re_x \cong 900{,}000$.

could then be compared to data acquired with both effects present simultaneously to determine the degree of synergy.

This analysis technique was applied to both St and c_f for the combined effects of pressure gradient and roughness. The results are summarized in Figs. 10(a) and 10(b) for $(St - St_0)/St_0$ and $(c_f - c_{f0})/c_{f0}$ versus kf_α for adverse and favorable pressure gradient. (Note: St_0 and c_{f0} are the zero pressure gradient, smooth wall values reported earlier. Also, data were only available for four of the six rough surfaces for this part of the study.) The $(St - St_0)/St_0$ data show that on average the additive estimate underpredicts the combined effects by 8% for favorable pressure gradient, but overpredicts the combined results by 10% for adverse pressure gradient. This demonstrates that there is indeed some physical coupling between the two effects that is responsible for the synergistic behavior when they are combined. A proposed mechanism for this synergy with favorable pressure gradient is the interaction of roughness generated eddies with the accelerating freestream. Using hot-wire measurements in the turbulent boundary layer, Bons and McClain [5] noted a 50% increase in streamwise turbulent kinetic energy generated over the rough panels with favorable pressure gradient compared to the case with no pressure gradient (a corresponding decrease was noted with adverse pressure gradient). This observed variation with pressure gradient may be due to the stretching of turbulent eddies generated from roughness elements in the boundary layer. Figure 11 shows mean boundary layer profiles for all three pressure gradients measured with a single element hotwire at the center of the smooth test panel ($x = 1.18$ m). The thinner accelerating boundary layer ($\delta \cong 12$ mm versus 27 mm for no pressure gradient) has a steeper mean velocity gradient which will increase the transfer of mean kinetic energy to turbulent kinetic energy via the vortex stretching mechanism. By the same argument, the larger adverse pressure gradient boundary layer ($\delta \cong 42$ mm) will impede this turbulence generation mechanism.

There is a much stronger synergy between pressure gradient and roughness for c_f (Fig. 10(b), note larger y-axis scale), due to the roughness element form drag. The favorable pressure gradient increases the near-wall momentum (Fig. 11), thus producing an even larger increase in c_f than would be predicted for pressure gradient and roughness separately. This synergy creates an enormous disconnect between the additive estimates and the actual data for $(c_f - c_{f0})/c_{f0}$. Thus, a design code that employed a simple near wall damping function to model roughness would underestimate its effect on c_f when a significant pressure gradient is present. The strong dependency of rough wall skin friction on near wall momentum is further manifest by plotting the roughness induced skin friction augmentation versus kf_α normalized by θ (Fig. 12(a)). In this figure, θ is the value measured with the smooth wall (4.7 mm, 2.2 mm, and 1 mm for adverse, zero, and favorable pressure gradients respectively). Also, the change in c_f due to roughness is referenced to its smooth-wall value with pressure gradient (c_{fPG}) in order to eliminate the influence of wall shear on the results and focus exclusively on the form drag component. Because of the large variation in θ, the data in Fig. 10(b) nearly collapse to a single curve (Eq. (24)) when normalized by θ in this way.

$$\frac{c_f - c_{fPG}}{c_{fPG}} = 2.2[1 - e^{-0.6kf_\alpha/\theta}] \tag{24}$$

This excellent data correlation suggests that all of the observed synergy between pressure gradient and roughness in Fig. 10(b) can be accounted for by scaling the roughness by the local smooth- wall value of momentum thickness. The data that does not follow the asymptotic trend line is for the largest roughness models ($Rt > 6$ mm, see Table 1) with a favorable pressure gradient. In this case, the roughness exceeds 50% of the boundary layer height ($\delta \cong 12$ mm), thus presenting a substantial blockage to the natural boundary layer evolution. It is likely that this disruption creates local three-dimensional flow accelerations around the large roughness elements, resulting in even higher form drag on the downstream roughness peaks. As such, the curve fit (Eq. (24)) is only suitable for $Rt/\delta < 0.5$.

Though the relevant boundary layer parameter for heat transfer is the enthalpy thickness, Δ, rather than θ, the $(St - St_{PG})/St_{PG}$ data also collapse to an asymptotic trend line with kf_α/θ (Fig. 12(b)).

$$\frac{St - St_{PG}}{St_{PG}} = 0.45[1 - e^{-1.1kf_\alpha/\theta}] \tag{25}$$

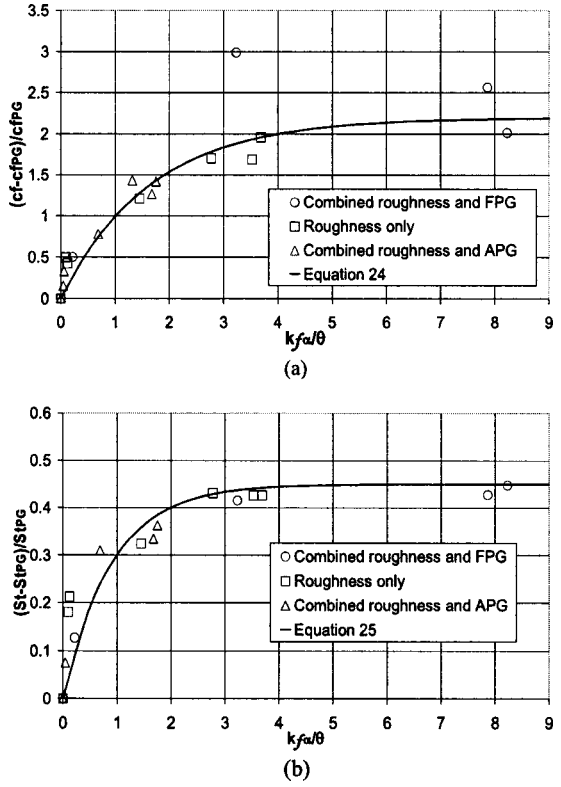

Fig. 12 Comparison of combined roughness and pressure gradient effects on (*a*) c_f and (*b*) St plotted versus kf_α/θ. Changes to c_f and St normalized by smooth-wall values with pressure gradient. Data for $Re_x \cong 900{,}000$.

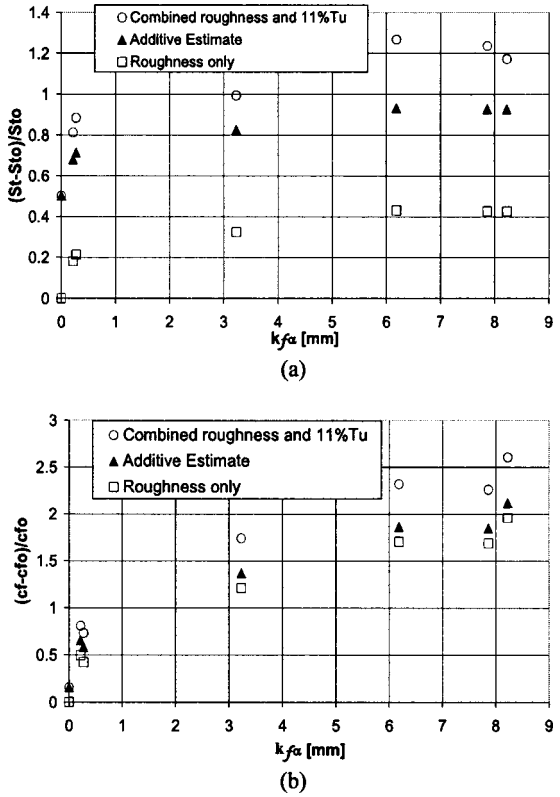

Fig. 14 Comparison of combined roughness and freestream turbulence (Tu) effects with roughness only and with additive estimate. (*a*) change in St (*b*) change in c_f. Changes in c_f and St normalized by smooth-wall, low Tu values. Data for $Re_x \cong 900{,}000$.

This unanticipated result is likely due to specific features of the experimental facility. Since there is no unheated starting length in the wind tunnel, it is expected that $\delta \cong \delta_t$ and thus Δ will scale with θ.

The imbalance between the St and c_f synergies with pressure gradient and roughness is evident in the final plot of RA/RA_0 versus kf_α/θ (Fig. 13). For the roughness models shown, changes in pressure gradient produce up to a factor of 2.8 drop in the Reynolds analogy factor. This is considerably larger than the pressure gradient effect for the baseline smooth surface (Fig. 5). Combining the curve fits for RA/RA_0 (β_{CL}) [Eq. (13)] and RA/RA_0 (kf_α/θ) (Eq. (21)), it is possible to generate an empirically-based prediction for the variation of RA/RA_0 with pressure gradient and roughness (Eq. (26)).

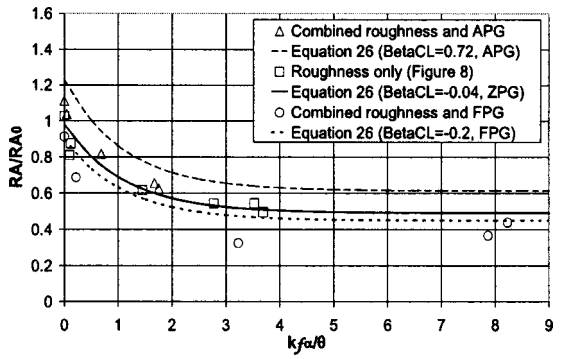

Fig. 13 Variation in normalized Reynolds analogy factor with roughness and pressure gradient compared to roughness only. Data for adverse (APG) and favorable (FPG) pressure gradients. $Re_x \cong 900{,}000$.

$$\frac{RA}{RA_0} = \frac{RA}{RA_0}(\beta_{CL})\frac{RA}{RA_0}(kf_\alpha/\theta) \tag{26}$$

These predictions are also shown in Fig. 13 for the adverse, zero, and favorable pressure gradient flows (β_{CL} = 0.73, -0.04, and -0.2, respectively). Despite the synergies between roughness and pressure gradient, normalizing kf_α by θ allows this simple compound correlation to capture most of the trends in the experimental data. The poorer agreement with the adverse pressure gradient data is not unexpected since the pressure gradient curve fit (Eq. (13)) to So's [23] analytical results does not match the experimental data well for this case (see Fig. 5).

Freestream Turbulence and Surface Roughness. This same analysis technique was applied to the data with elevated freestream turbulence and roughness. The results are summarized in Figs. 14(a) and 14(b) for $(St-St_0)/St_0$ and $(c_f - c_{f0})/c_{f0}$ versus kf_α for Tu = 11% only. The additive estimates for St and c_f are on average 20% and 29% (respectively) lower than the actual data with roughness and turbulence. This demonstrates that there is again a physical coupling between the two effects that is responsible for the added enhancement when they are combined.

In the case of skin friction, the mechanism for this positive synergy is the fuller boundary layer created with freestream turbulence. The boundary layer profile corresponding to 11% freestream turbulence is also shown in Fig. 11 and clearly shows a greater near wall momentum in the region of the roughness elements ($y<10$ mm). As with the favorable pressure gradient boundary layer, this increases the form drag component of c_f. Thus, the combined effect of freestream turbulence and surface roughness on c_f is greater than the sum of their effects measured separately. To evaluate the dependency of this synergy on near wall momen-

tum the data in Fig. 14(b) were replotted versus kf_α/θ (Fig. 15(a)).

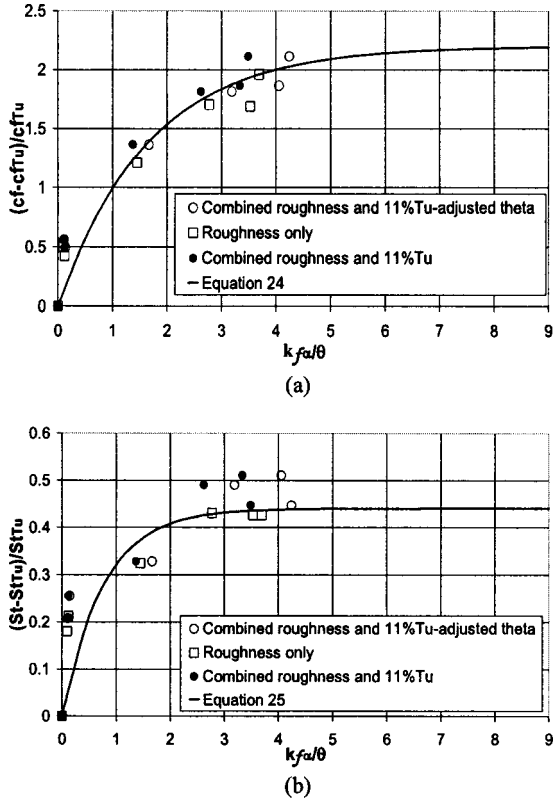

Fig. 15 Comparison of combined roughness and freestream turbulence effects on (*a*) c_f and (*b*) St plotted versus kf_α/θ. Changes to c_f and St normalized by smooth-wall values with turbulence. Data for $Re_x \cong 900{,}000$.

As in Fig. 12(a), the smooth wall momentum thickness value is used for both low and high freestream turbulence (2.2 mm and 2.4 mm for 1% and 11% Tu, respectively). Also, the change in c_f due to roughness is referenced to its smooth-wall value with turbulence (c_{fTu}) in order to eliminate the influence of wall shear on the results and focus exclusively on the form drag component. The correlation used in Fig. 12(a) (Eq. (24)) is also shown in Fig. 15(a). Though the agreement is reasonable, it actually can be improved by adjusting the momentum thickness for the high Tu case to account for the change in boundary layer shape. From Fig. 11 it is clear that the 11% Tu boundary layer has more momentum in the region of the roughness elements ($y<10$ mm). Yet, the momentum thickness is actually larger (2.4 mm) for this case than at low Tu (2.2 mm). This is because the high level of freestream turbulence causes a fundamental change in the boundary layer shape. Heightened mixing augments the momentum in the near wall (log) layer while reducing the momentum in the wake region and increasing δ from 27 mm to 38 mm. The net effect of freestream turbulence for this case is thus a reduction in total boundary layer momentum (i.e., increase in momentum thickness). Nevertheless, at the level of the roughness elements, the increase in momentum with freestream turbulence causes an increase in form drag. The normalization of kf_α by θ does not account for this change in boundary layer shape. If the momentum thickness integral is truncated at the edge of the roughness region ($y<$Rt), the high turbulence result has 13% less momentum thickness than the low turbulence result. Accordingly, Fig. 15(a) also shows the 11% Tu data using a θ value that is 13% smaller than the low Tu value, based on this truncated, near-wall momentum thickness comparison. The agreement with the correlation is improved. This finding is noteworthy since it suggests that all c_f

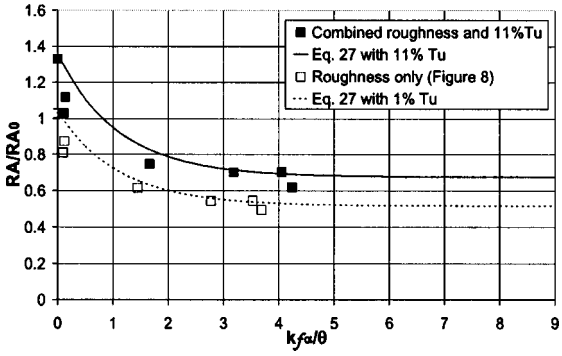

Fig. 16 Variation in normalized Reynolds analogy factor with roughness and freestream turbulence (Tu) compared to roughness only. $Rex \cong 900{,}000$.

-related synergies with roughness can be captured with a single correlation if the roughness is scaled by the appropriate boundary layer momentum thickness.

Plotting the heat transfer (St) data in a similar manner produces a comparable result (Fig. 15(b)). The agreement with the correlation developed for the pressure gradient data (Eq. (25)) is again improved by adjusting the momentum thickness to better reflect the boundary layer momentum in the vicinity of the roughness elements. Some of the data for the largest roughness surfaces in Fig. 15(b) lie above the correlation (Eq. (25)), suggesting the possibility of additional synergies not captured by the momentum thickness normalization. As discussed previously, higher levels of freestream turbulence also increase the rate at which large "outer" turbulence structures come in contact with the near-wall fluid. These structures, which are more effective at transferring energy than momentum, may displace smaller (less effective) eddies generated from the roughness elements themselves. This would create an additional positive synergy for heat transfer.

When these effects are combined to form the Reynolds analogy factor, the result reflects the competing influence of the two mechanisms (Fig. 16). For small roughness, the St increase with 11% freestream turbulence more than compensates for the increased form drag on roughness elements, resulting in a net increase in RA/RA_0 . For the larger roughness models, the form drag increase dominates, and $RA/RA_0 < 1$.

Using the empirical curve fits for RA/RA_0 (Tu) (Eq. (23)) and RA/RA_0 (kf_α/θ) (Eq. (21)), it is possible to assess their predictive accuracy for the case where both turbulence and roughness are present (Eq. (27)).

$$\frac{RA}{RA_0} = \frac{RA}{RA_0}(\mathrm{Tu})\,\frac{RA}{RA_0}(kf_\alpha/\theta) \tag{27}$$

Because the effects of freestream turbulence and surface roughness on c_f and St exhibit significant synergy, this compound estimate of RA/RA_0 successfully captures the trends in the data. Normalization of kf_α by the appropriately adjusted boundary layer momentum thickness again makes this good agreement possible.

Pressure Gradient and Freestream Turbulence. Though no experiments were performed under this combination of conditions, it is possible to speculate on the combined effects of pressure gradient and freestream turbulence based on their individual effects and perceived synergies. Since a favorable pressure gradient on a smooth wall increases c_f more than St (Fig. 5), adding elevated Tu (with its bias toward St increase over c_f) would be in direct competition and thus reduce the drop in the Reynolds analogy factor. From reviewing the two relevant figures (Figs. 5 and 9) it is clear that certain combinations of FPG and Tu could exactly offset each other, producing no net change in RA. Conversely for an adverse pressure gradient, the disproportionate drop in c_f due to adverse pressure gradient (APG) would combine with

the disproportionate rise in St due to freestream turbulence to produce a more significant increase in the Reynolds analogy factor. An obvious mechanism for synergy is the interaction between the mean velocity gradient (i.e., mean strain rate) and turbulent eddies convected into the boundary layer from the freestream. A favorable pressure gradient (with a steeper mean velocity profile) would then produce a positive synergy with elevated turbulence while an adverse pressure gradient would produce a negative synergy with turbulence.

Summary and Conclusions

Heat transfer and skin friction measurements have been made over a wide variety of test conditions in a low-speed wind tunnel. Based on this data, assessments are made of the variation of the Reynolds analogy factor ($2\mathrm{St}/c_f$) with Reynolds number, freestream pressure gradient, surface roughness, and freestream turbulence. Based on the findings, the following conclusions are made.

(1) Reynolds analogy factor is fairly independent of Reynolds number for both laminar and turbulent flow.

(2) The Reynolds analogy factor increases with positive (adverse) pressure gradient and decreases with negative (favorable) pressure gradient. This variation is much more significant for laminar boundary layers than for turbulent boundary layers.

(3) Surface roughness introduces a large pressure drag component to the net skin friction measurement with only a modest corresponding increase in heat transfer. Accordingly, the Reynolds analogy factor decreases dramatically with surface roughness (by as much as 50% as roughness elements become more prominent).

(4) Freestream turbulence has the opposite effect of increasing heat transfer more than skin friction, thus the Reynolds analogy factor increases with turbulence level (by 35% at a level of 11% freestream turbulence).

(6) When freestream turbulence and surface roughness are both present, their different influences on the Reynolds analogy factor are opposing. For small surface roughness this can result in no net adjustment to the $2\mathrm{St}/c_f$ ratio.

(5) When pressure gradient and surface roughness are both present, the effects on the Reynolds analogy factor are complementary, resulting in dramatic variations with pressure gradient.

(6) When freestream turbulence and surface roughness are both present, their different influences on the Reynolds analogy factor are opposing. For small surface roughness this can result in no net adjustment to the $2\mathrm{St}/c_f$ ratio.

(7) The correlation of rough-wall c_f and St with the product of the average roughness height and the mean forward facing surface angle function, kf_α, normalized by the boundary layer momentum thickness, θ, is reasonably accurate over the range of parameters presented. New correlations for this effect are proposed (Eqs. (20), (21), (24), and (25)). Only in the case of an accelerating freestream does this correlation break down appreciably. This suggests a limit to the application of kf_α/θ as a suitable roughness parameter when the peak roughness height (Rt) exceeds 50% of the boundary layer thickness.

There are, of course, other significant factors present in turbine flowfields that are not treated in this study. Most HP turbines are transonic, and as such, compressibility and shock-boundary layer interaction are important considerations. Hopkins and Inouye [50] conclude that for near adiabatic wall conditions, the Reynolds analogy factor for a turbulent boundary layer remains near a value of 1.2 for low supersonic Mach numbers. When wall cooling is considerable (as in an internally cooled HP blade) they suggest a lower value for RA of nearly unity. The more important consideration, of course, is the effect of moving shock structures from an upstream vane or blade row. Shocks greatly amplify the levels of turbulent fluctuations and turbulent shear stress in the boundary layer [51]. At the same time, the abrupt adverse pressure gradient associated with the shock impingement can lead to boundary layer separation and/or transition. The combination of amplified turbulence and incipient separation will yield large increases in RA due to factors already addressed in this report.

High pressure turbines are also extensively film cooled, with multiple rows of cooling holes generally concentrated near the leading edge of the airfoils. The injection of coolant flow into the boundary layer introduces heightened levels of mixing and elevated turbulence. At the same time, Bons et al. [6] found cooling holes to be more prone to erosion and TBC spallation than any other location on the turbine blade surface. When located near the leading edge, film cooling can also trigger boundary layer transition. These various effects paint a complex picture for the Reynolds analogy near regions of extensive film cooling.

Acknowledgment

The author is indebted to numerous personnel at the four industrial partners for providing turbine hardware. Primary among these are: Dr. Boris Glezer formerly of Solar Turbines, Dr. Ron Bunker and Paul Suttmann at General Electric, Mohan Hebbar at Siemens-Westinghouse, and Dr. William Troha and Shawn Pollock of Honeywell Corporation. The author would also like to acknowledge those who assisted in the collection of this data: Captain Jess Drab and 2Lt Christine Ellering at the Air Force Institute of Technology and Cadets Nathan Loucks and Dick Janssen of the United States Air Force Academy. In addition, collaborations with Dr. Keith Hodge at Mississippi State University, Dr. Steve McClain at the University of Alabama-Birmingham, and Dr. Richard Rivir and Dr. Rolf Sondergaard of the Air Force Research Lab are greatly appreciated. The assistance offered by Dr. Brent Webb in reviewing the manuscript is also acknowledged. The testing was conducted at the Air Force Research Lab Aero-thermal research laboratory with technical support from William Nilson, Jay Anderson, and Andy Pitts. The assistance of Nikki Widmor at the University of Dayton Research Institute in determining the plastic properties is gratefully acknowledged. This work was sponsored by the US Department of Energy—National Energy Technology Laboratory through a cooperative agreement with the South Carolina Institute for Energy Studies at Clemson University.

Nomenclature

- APG = adverse pressure gradient
- A = planform (flat) surface area
- A_f = windward frontal surface area of roughness elements on sample
- A_s = windward wetted surface area of roughness elements on sample
- c_f = skin friction coefficient, $\tau_w/(0.5\rho U_e^2)$
- c_p = specific heat at constant pressure
- f_α = mean angle function [Eq. (20)]
- FPG = favorable pressure gradient
- H = boundary layer shape factor
- h = convective heat transfer coefficient
- $h(x)$ = surface height as a function of x
- h_i = local surface height from 2D trace
- K = acceleration parameter $(\nu U_e^{-2} dU_e/dx)$
- k = average roughness height
- k_s = equivalent sandgrain roughness
- k_l = constant in $U_e(x)$ relation
- k^+ = $k_s u_\tau/\nu \equiv \mathrm{Re}_k$
- l_i = local surface wetted distance from 2D trace
- m = exponent in $U_e(x)$ relation
- N = number of cells in 3D surface map
- p = pressure
- Pr = Prandtl number $(\nu/\alpha)(=0.71)$
- Pr_t = turbulent Prandtl number (ν_t/α_t)
- RA = Reynolds analogy factor $(2\mathrm{St}/c_f)$
- Ra = centerline average roughness

Re_x = Reynolds number ($U_e x/\nu$)
Re_θ = momentum thickness Reynolds number ($U_e\theta/\nu$)
Rt = maximum peak to valley roughness
Rz = average peak to valley roughness based on 3D surface map
S = surface area of sample without roughness
S_f = total frontal surface area of sample
S_w = total wetted surface area of sample
St = Stanton number, $h/(\rho c_p U_e)$
T = temperature
Tu = freestream turbulence, $u'/U_\infty(\%)$
U_∞ = freestream velocity
u = streamwise velocity
u' = fluctuating velocity (rms)
u_τ = friction or shear velocity $\sqrt{\tau_w/\rho}$
v = wall normal velocity
x = streamwise distance from leading edge
y = wall normal distance
ZPG = zero pressure gradient
α = thermal diffusivity ($\kappa/\rho c_p$)
$\overline{\alpha_f}$ = average forward-facing surface angle
α_i = local surface angle from 2D surface trace
α_{rms} = rms deviation of surface roughness slope angles
α_t = eddy thermal diffusivity
Δ = boundary layer enthalpy thickness
β_{CL} = Clauser's equilibrium parameter [Eq. (12)]
β_{FS} = Falkner–Skan pressure gradient parameter
δ = hydrodynamic boundary layer thickness
δ_t = thermal boundary layer thickness
δ^* = boundary layer displacement thickness
κ = thermal conductivity
Λ_s = roughness shape/density parameter [Eq. (14)]
ν = kinematic viscosity
ν_t = eddy viscosity
θ = boundary layer momentum thickness
ρ = density
τ_w = wall shear

Subscripts

cell = subset of 3D surface map
e = boundary layer edge
i = index in 2D surface trace
PG = smooth plate reference with pressure gradient (APG, ZPG, or FPG)
Tu = smooth plate reference with turbulence (1% or 11%)
w = wall
0 = smooth plate reference at low freestream turbulence and zero pressure gradient
∞ = freestream value

References

[1] Reynolds, O., 1874, "On the Extent and Action of the Heating Surface for Steam Boilers," Manchester Lit. Phil. Soc., **14**, pp. 7–12.
[2] Abuaf, N., Bunker, R. S., and Lee, C. P., 1998, "Effects of Surface Roughness on Heat Transfer and Aerodynamic Performance of Turbine Airfoils," ASME J. Turbomach., **120**(3), pp. 522–529.
[3] Belnap, B. J., vanRij, J. A., and Ligrani, P. M., 2002, "A Reynolds Analogy for Real Component Surface Roughness," Int. J. Heat Mass Transfer, **45**, pp. 3089–3099.
[4] Bons, J. P., 2002, "St and c_f Augmentation for Real Turbine Roughness With Elevated Freestream Turbulence," ASME J. Turbomach., **124**(4), pp. 632–644.
[5] Bons, J. P., and McClain, S., 2003, "The Effect of Real Turbine Roughness and Pressure Gradient on Heat Transfer," presented at the June 2003 IGTI in Atlanta, GA, No. GT2003-38738.
[6] Bons, J. P., Taylor, R., McClain, S., and Rivir, R. B., 2001, "The Many Faces of Turbine Surface Roughness," ASME J. Turbomach., **123**, pp. 739–748.
[7] Bogard, D. G., Schmidt, D. L., and Tabbita, M., 1998, "Characterization and Laboratory Simulation of Turbine Airfoil Surface Roughness and Associated Heat Transfer," ASME J. Turbomach., **120**(2), pp. 337–342.
[8] Barlow, D. N., and Kim, Y. W., 1995, "Effect of Surface Roughness on Local Heat Transfer and Film Cooling Effectiveness," presented at the June, 1995 ASME International Gas Turbine Exposition in Houston, Texas, ASME Paper No. 95-GT-14.
[9] Antonia, R. A., and Luxton, R. E., 1971, "The Response of a Turbulent Boundary Layer to a Step Change in Surface Roughness. Part 1: Smooth to Rough," J. Fluid Mech., **48**, pp. 721–726.
[10] Taylor, R. P., and Chakroun, W. M., 1992, "Heat Transfer in the Turbulent Boundary Layer With a Short Strip of Surface Roughness," presented at the 30th AIAA Aerospace Sciences Meeting and Exhibit, Reno, Nevada, 6–9 January, 1992, AIAA Pap. No. 92-0249.
[11] Taylor, R. P., 1990, "Surface Roughness Measurements on Gas Turbine Blades," ASME J. Turbomach., **112**(1), pp. 175–180.
[12] Mills, A. F., 1992, *Heat Transfer*, 1st ed., Irwin, Illinois.
[13] Schultz, D. L., and Jones, T. V., 1973, "Heat-Transfer Measurements in Short-Duration Hypersonic Facilities," *Advisory Group for Aerospace Research and Development*, No. 165, NATO.
[14] Halstead, D. E., Wisler, D. C., Okiishi, T. H., Walker, G. J., Hodson, H. P., and Shin, H.-W., 1997, "Boundary Layer Development in Axial Compressors and Turbines: Part 1 or 4—Composite Picture," ASME J. Turbomach., **119**, pp. 114–127.
[15] Matsunuma, T., Abe, H., Tsutsui, Y., and Murata, K., 1998, "Characteristics of an Annular Turbine Cascade at Low Reynolds Numbers," presented at IGTI 1998 in Stockholm, Sweden, June 1998, Paper No. 98-GT-518.
[16] Blasius, H., 1908, "Grenzschichten in Flussikeiten mit Kleiner Reibung," Z. Angew. Math. Phys., **56**, pp. 1–37 (English translation in NACA Technical Memo. 1256).
[17] Pohlhausen, E., 1921, "Der Warmeaustausch Swischen Festern Korpen und Flussigdeiten mit Kleiner Reibun und Kleiner Warmeleitung," Z. Angew. Math. Mech., **1**, pp. 115–121.
[18] Colburn, A. P., 1933, "A Method of Correlating Forced Convetion Heat Transfer Data and a Comparison With Fluid Friction Data," AIChE J., **29**, pp. 174–210.
[19] Chilton, T. H., and Colburn, A. P., 1934, Ind. Eng. Chem., **26**, pp. 1183.
[20] White, F. M., 1991, *Viscous Fluid Flow*, 2nd ed., McGraw-Hill, New York.
[21] Kader, B. A., and Yaglom, A. M., 1972, "Heat and Mass Transfer Laws for Fully Turbulent Wall Flows," Int. J. Heat Mass Transfer, **15**, pp. 2329–2351.
[22] Incropera, F. P., and DeWitt, D. P., 1985, *Fundamentals of Heat and Mass Transfer*, 2nd ed., Wiley, New York.
[23] So, R. M. C., 1994, "Pressure Gradient Effects on Reynolds Analogy for Constant Property Equilibrium Turbulent Boundary Layers," Int. J. Heat Mass Transfer, **37**, pp. 27–41.
[24] Mellor, G. L., and Gibson, D. M., 1966, "Equilibrium Turbulent Boundary Layers," J. Fluid Mech., **24**, pp. 225–253.
[25] Back, L. H., and Cuffel, R. F., 1971, "Turbulent Boundary Layer and Heat Transfer Measurements Along a Convergent-Divergent Nozzle," ASME J. Heat Transfer, **93**, pp. 397–407.
[26] Back, L. H., and Seban, R. A., 1965, "On Constant Property Turbulent Boundary Layers With Variable Temperature or Heat Flow at the Wall," ASME J. Heat Transfer, **87**(1), pp. 151–156.
[27] Dorney, D. J., Ashpis, D. E., Halstead, D. E., and Wisler, D. C., 1999, "Study of Boundary Layer Development in a Two-Stage Low-Pressure Turbine," presented at the 37th AIAA Aerospace Sciences Meeting and Exhibit, 11–14 Jan., 1999, Reno, NV, Paper No. AIAA 99-0742.
[28] Sharma, O. P., Wells, R. A., Schlinker, R. H., and Bailey, D. A., 1982, "Boundary Layer Development on Turbine Airfoil Suction Surfaces," ASME J. Eng. Power, **104**, pp. 698–706.
[29] Mayle, R. E., 1991, "The Role of Laminar-Turbulent Transition in Gas Turbine Engines," ASME J. Turbomach., **113**, pp. 509–537.
[30] Moretti, P. M., and Kays, W. M., 1965, "Heat Transfer to a Turbulent Boundary Layer With Varying Free-Stream Velocity and Varying Surface Temperature—An Experimental Study," Int. J. Heat Mass Transfer, **8**, pp. 1187–1201.
[31] Schlichting, H., 1936, "Experimental Investigation of the Problem of Surface Roughness," NACA TM-832.
[32] Nikuradse, J., 1933, "Laws for Flows in Rough Pipes," VDI-Forchungsheft 361, Series B, Vol. 4. (English Translation NACA TM 1292, 1950).
[33] Coleman, H. W., Hodge, B. K., and Taylor, R. P., 1984, "A Re-Evaluation of Schlichting's Surface Roughness Experiment," ASME J. Fluids Eng., **106**, pp. 60–65.
[34] Sigal, A., and Danberg, J., 1990, "New Correlation of Roughness Density Effect on the Turbulent Boundary Layer," AIAA J., **28**(3), pp. 554–556.
[35] Forster, V. T., 1967, "Performance Loss of Modern Steam-Turbine Plant Due to Surface Roughness," Proc. Inst. Mech. Engrs., 1966-676, **181**(1), pp. 391–405.
[36] Bammert, K., and Sanstede, H., 1976, "Influences of Manufacturing Tolerances and Surface Roughness of Blades on the Performance of Turbines," ASME J. Eng. Power, **98**, pp. 29–36.
[37] Koch, C. C., and Smith, Jr., L. H., 1976, "Loss Sources and Magnitudes in Axial-Flow Compressors," ASME J. Eng. Power, **98**, pp. 411–424.
[38] Schlichting, H., 1979, *Boundary Layer Theory*, 7th ed., McGraw-Hill, New York.
[39] Acharya, M., Bornstein, J., and Escudier, M., 1986, "Turbulent Boundary Layers on Rough Surfaces," Exp. Fluids, **4**, pp. 33–47.
[40] Tarada, F., and Suzuki, M., 1993, "External Heat Transfer Enhancement to Turbine Blading Due to Surface Roughness," presented at ASME IGTI in Cincinnati OH, May 1993, ASME Paper 93-GT-74.
[41] Goebel, S. G., Abuaf, N., Lovett, J. A., and Lee, C.-P., 1993, "Measurements of Combustor Velocity and Turbulence Profiles," ASME Paper No. 93-GT-228.
[42] Barringer, M. D., Richard, O. T., Walter, J. P., Stitzel, S. M., and Thole, K. A.,

2001, ''Flow Field Simulations of a Gas Turbine Combustor,'' ASME Paper No. 2001-GT-0170.
[43] Matsunuma, T., Abe, H., and Tsutsui, Y., 1999, ''Influence of Turbulence Intensity on Annular Turbine Stator Aerodynamics at Low Reynolds Numbers,'' presented at IGTI 1999 in Indianapolis, Indiana, June 1999, Paper No. 99-GT-151.
[44] Stieger, R. D., and Hodson, H. P., 2003, ''The Transition Mechanism of Highly-Loaded LP Turbine Blades,'' presented at the 2003 IGTI in Atlanta, GA, ASME Paper No. GT2003-38304.
[45] Blair, M. F., 1983, ''Influence of Free-Stream Turbulence on Turbulent Boundary Layer Heat Transfer and Mean Profile Development, Part II—Analysis of Results,'' ASME J. Heat Transfer, **105**, pp. 41–47.
[46] Pedisius, A. A., Kazimekas, V. A., and Slanciauskas, A. A., 1979, ''Heat Transfer From a Plate to a High-Turbulence Air Flow,'' Soviet Research, **11**(5), pp. 125–134.
[47] Maciejewski, P. K., and Moffat, R. J., 1992, ''Heat Transfer With Very High Free-Stream Turbulence: Part 1—Experimental Data,'' ASME J. Heat Transfer, **114**, pp. 827–833.
[48] Thole, K. A., and Bogard, D. G., 1995, ''Enhanced Heat Transfer and Shear Stress Due to High Free-Stream Turbulence,'' ASME J. Turbomach., **117**, pp. 418–424.
[49] Simonich, J. C., and Bradshaw, P., 1978, ''Effect of Free-Stream Turbulence on Heat Transfer Through a Turbulent Boundary Layer,'' ASME J. Heat Transfer, **100**, pp. 671–677.
[50] Hopkins, E., and Inouye, M., 1971, ''An Evaluation of Theories for Predicting Turbulent Skin Friction and Heat Transfer on Flat Plates at Supersonic and Hypersonic Mach Numbers,'' AIAA J., **9**(6), pp. 993–1003.
[51] Smits, A., and Muck, K., 1987, ''Experimental Study of Three Shock-Wave/Turbulent Boundary Layer Interactions,'' J. Fluid Mech., **182**, pp. 291–314.

Large Eddy Simulations of Flow and Heat Transfer in Rotating Ribbed Duct Flows

Mayank Tyagi
Research Associate

Sumanta Acharya*
Professor Mechanical Engineering Department
Louisiana State University
Baton Rouge, LA 70803

Large eddy simulations are performed in a periodic domain of a rotating square duct with normal rib turbulators. Both the Coriolis force as well as the centrifugal buoyancy forces are included in this study. A direct approach is presented for the unsteady calculation of the nondimensional temperature field in the periodic domain. The calculations are performed at a Reynolds number (Re) of 12,500, a rotation number (Ro) of 0.12, and an inlet coolant-to-wall density ratio ($\Delta\rho/\rho$) of 0.13. The predicted time and space-averaged Nusselt numbers are shown to compare satisfactorily with the published experimental data. Time sequences of the vorticity components and the temperature fields are presented to understand the flow physics and the unsteady heat transfer behavior. Large scale coherent structures are seen to play an important role in the mixing and heat transfer. The temperature field appears to contain a low frequency mode that extends beyond a single inter-rib geometric module, and indicates the necessity of using at least two inter-rib modules for streamwise periodicity to be satisfied. Proper orthogonal decomposition (POD) of the flowfield indicates a low dimensionality of this system with almost 99% of turbulent energy in the first 80 POD modes. [DOI: 10.1115/1.1861924]

Introduction

Modern gas turbines operate at high turbine inlet temperatures (2000°F–3000°F) for improved efficiency and specific thrust. Since the operating temperature exceeds the melting point of the blade material, the blades have to be cooled internally or externally. Turbine blades are internally cooled by circulating air through turbulated serpentine channels (Fig. 1). The enhancement in heat transfer due to rib turbulators relative to the increased pressure drop in the channel is a crucial design parameter [1]. The problem is complicated further due to the interplay of Coriolis forces and buoyancy forces. In rotating ducts, the Coriolis forces give rise to secondary flows in the crossflow-plane which destabilize the flow and enhance heat transfer along one wall, and stabilize the flow reducing heat transfer along the opposite wall. Centrifugal-buoyancy forces also influence the flow and heat transfer, particularly at high rotation numbers and density ratios.

Several experimental investigations have been reported to study the effect of centrifugal buoyancy, rotation number, and Reynolds number in internal cooling passages. In a series of papers, Wagner and Johnson (e.g., Wagner et al. [2]) have reported measurements of heat transfer coefficients using thermocouples in smooth and ribbed square-cross-section channels for various Reynolds number, rotation numbers, and density ratios. Morris and Rahmat-Abadi [3] conducted a similar experimental investigation on rotating ribbed circular ducts and proposed Nusselt number correlations that depend on the ratio of buoyancy parameter and Rossby number. Yamawaki et al. [4] presented local heat transfer measurements using thermochromic liquid crystals on a flat plate subjected to rotation, and analyzed the turbulent stress equations to determine their influence on the mean momentum transport. Acharya and coworkers have reported a series of measurements of mass (heat) transfer using naphthalene sublimation technique in rotating coolant passages with vortex generators, different aspect ratios, and orientations (e.g., Acharya and Zhou [5]; Hibbs et al. [6]; Zhou et al. [7]). Han and coworkers have reported measurements in rotating coolant passages with different aspect ratios, different rib-configurations and passage orientations, and different thermal boundary conditions. These studies have been summarized in a recent paper by Han and Dutta [8].

The literature dealing with computational studies on ribbed coolant passages is quite extensive. The majority of the numerical studies have been based on the solution of the Reynolds-averaged-Navier-Stokes (RANS) equations, and therefore their accuracy has been limited by the turbulence models employed. Bredberg [9] has provided a representative literature survey of several numerical studies reported on turbine blade internal cooling passages. Iacovides and Launder [10] have also reviewed the numerical studies related to turbine blade internal cooling and concluded that low-Reynolds number modeling of the sublayer region is essential for such flows. However, turbulence modeling using two-equation models cannot capture essential flow physics due to the assumption of isotropy in the modeled normal turbulent stresses. Naimi and Gessner [11] calculated the fully developed turbulent flow in rectangular ducts with ribs on opposite walls using three different turbulence models and noted some spurious secondary flow features in the predictions as compared to the experimental data. Iacovides [12] presented a comparison of several low-Reynolds number eddy viscosity models with low-Reynolds number second moment closure models for internal coolant passage flow and heat transfer. Bonhoff et al. [13] have compared their predictions with several turbulence models with stereoscopic Particle Image Velocimetry (PIV) measurements for 45°-ribbed coolant channels, and concluded that two-equation models have inherent deficiencies for ribbed-duct flows. In a number of studies, the second moment closure model has been shown to have the highest accuracy for stationary and rotating ribbed-coolant passages (Iacovides and Raisee [14], Saidi and Sunden [15], Hermanson et al. [16], Jang et al. [17]).

More advanced numerical strategies such as direct numerical simulation (DNS) or large eddy simulation (LES) provide promise for more accurate computations since the energy carrying turbulent flow structures are resolved in these calculations. However, only a limited number of studies with DNS and LES have been reported for internal cooling flows. Murata and Mochizuki [18,19] performed a series of LES studies to understand the unsteady dynamics of various flow structures on the heat transfer in internal coolant ducts. Pallares et al. [20] analyzed LES turbulence bud-

*Corresponding author; electronic mail: acharya@lsu.edu
Contributed by the Heat Transfer Division of ASME for publication in the JOURNAL OF HEAT TRANSFER. Manuscript received April 3, 2004; revision received, December 8, 2004. Review conducted by: P. M. Ligrani.

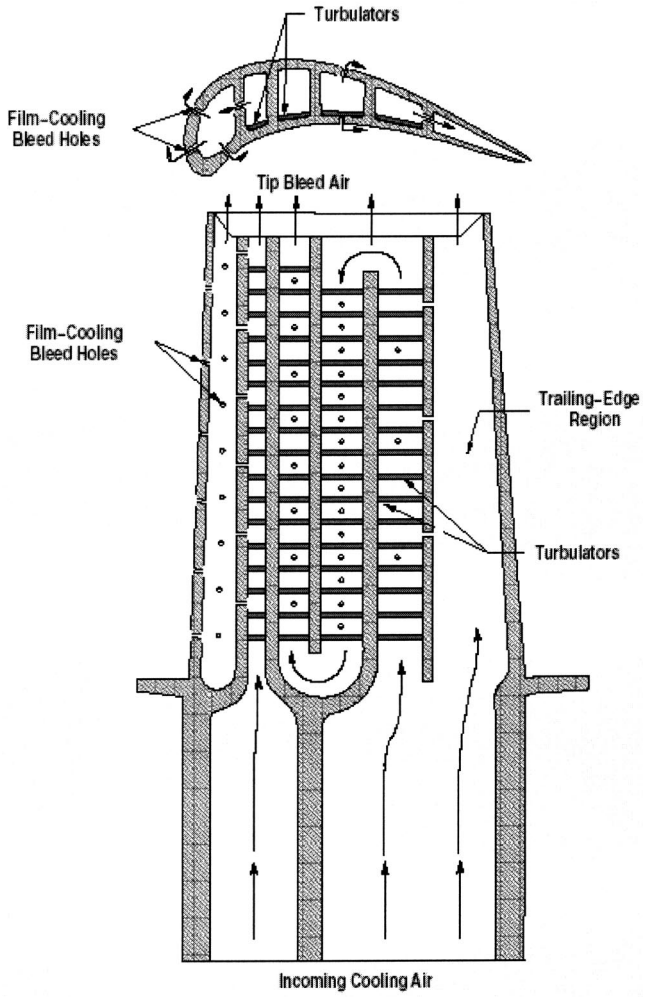

Fig. 1 Typical turbine blade internal cooling configuration (Wagner et al. [2], Roclawski et al. [21])

gets for the flow field in rotating square ducts. Roclawski et al. [21] presented calculations based on discrete dynamical system (DDS) concepts for internal cooling flows. Miyake et al. [22] carried out DNS of a channel with one ribbed wall and presented the evolution of coherent structures in the vicinity of rough wall. In a more recent study, Saha and Acharya [23] have reported unsteady-RANS (URANS) and LES computations for a rotating ribbed square duct, and have demonstrated the importance of using unsteady calculation techniques for ribbed duct flows. The resolution of energy in the periodic component (either spatial or temporal) of ribbed duct flows is important for the success of these unsteady simulations.

In the present paper, large eddy simulations (LES) are performed to study the flow physics and heat transfer in a rotating ribbed duct with isothermal walls. The physical configuration chosen corresponds to the experimental study of Wagner et al. [2], and represents a square-cross-section passage with normal ribs on leading and trailing surfaces arranged in a staggered configuration. A major objective of the present work is to provide an understanding of the unsteady flow physics and heat transfer in a rotating ribbed channel with isothermal walls. RANS studies cannot predict unsteady turbulent flow behavior, while the reported LES studies [18,19] have focused attention on parametric effects, and time-averaged results, with uniform heat flux wall boundary conditions.

A second objective of the paper is to present a noniterative strategy for the calculation of periodically developed temperature fields with uniform wall temperatures. Earlier strategies [24,25] have utilized an iterative procedure, which when applied at each time step, can result in significant computational effort. Because of this, the majority of the LES studies reported for periodically developed ribbed-duct flows with rotation have utilized constant heat flux boundary conditions. Isothermal boundary conditions are more representative of the turbine blade wall temperatures, and therefore LES/DNS calculations in ribbed-coolant passages with constant wall temperatures are needed. The noniterative strategy presented here can provide a cost-effective approach for unsteady flow calculations in periodically developed regions with isothermal boundary conditions.

Governing Equations

In LES, the spatially filtered conservation equations are solved. The filtered non-dimensional governing equations for conservation of mass, momentum, and energy for an incompressible Newtonian fluid are as follows:

$$\frac{\partial U_j}{\partial x_j}=0$$

$$\frac{\partial U_i}{\partial t}+\frac{\partial U_iU_j}{\partial x_j}=-\frac{\partial p}{\partial x_i}-\frac{dP}{dz}\delta_{i3}+\frac{1}{\mathrm{Re}}\frac{\partial^2 U_i}{\partial x_j^2}+\frac{\partial \tau_{ij}}{\partial x_j}-2Ro\,\varepsilon_{ijk}\Omega_jU_k+Bo\left(1-\frac{\Theta}{\Theta_b^0}\right)\times(\varepsilon_{ijk}\varepsilon_{klm}\Omega_j\Omega_l r_m) \tag{1}$$

$$\frac{\partial \Theta}{\partial t}+\lambda\Theta+U_j\frac{\partial \Theta}{\partial x_j}=\frac{1}{\mathrm{Re}\cdot\mathrm{Pr}}\frac{\partial^2\Theta}{\partial x_j^2}+\frac{\partial q_j}{\partial x_j}$$

where U_i is the filtered velocity field, $\Theta=(T-T_{\mathrm{ref}})/(T_w-T_{r2})$ is the nondimensional temperature with T_w representing the wall temperature, and T_{ref}, T_{r2} are reference temperatures (described later). The mean pressure gradient in the flow direction is dP/dz, and p is the periodic component of the pressure field. The distance vector r_i that appears in the centrifugal-buoyancy term can be written as $r_i=R_m\delta_{i3}+x_i$, where R_m is the mean radius of the periodic module from the rotation axis. The energy equation contains the parameter λ which, with the scaling used, can be expressed as

$$\lambda=\frac{1}{T_w-T_{r2}}\frac{\partial}{\partial t}(T_w-T_{r2})$$

The important nondimensional parameters for such flows are the Reynolds number ($\mathrm{Re}=U_mD_h/\nu$), the rotation number ($\mathrm{Ro}=\Omega D_h/U_m$), and the centrifugal buoyancy number [$Bo=[\beta(T-T_{in})\Omega^2R_mD_h^3]/\nu\alpha(\alpha/\nu)(\nu/U_mD_h)^2=Ra_\Omega/\mathrm{Pr}\,\mathrm{Re}^2$]. In this study, representative values for Re, Ro, and Bo, for which data is available in the literature [2], are used.

The subgrid scale (SGS) stress tensor and SGS scalar flux vector are given by τ_{ij} and q_j, respectively. In this study, the dynamic mixed model is used to model the SGS stress tensor and scalar flux vector (Moin et al. [26], Vreman et al. [27]). Box filters are used in the Germano identity for the calculation of dynamic coefficient and for the calculation of Leonard stresses. The dynamic coefficient is test filtered to avoid numerical instabilities.

Calculation of the Temperature Field

The calculation of the nondimensional temperature field in a periodic module needs special attention. Patankar et al. [24] described a method to solve the uniform heat flux (UHF) and uniform wall temperature (UWT) problems in ducts with periodic cross sections for steady situations. For UWT conditions, an eigenvalue parameter λ is obtained, and must be obtained iteratively. Wang and Vanka [25] also presented an iterative procedure to calculate λ. However, as will be described here, this parameter

can be calculated directly for explicit schemes, and represents a contribution of the present work. In the literature, the majority of the simulations were performed with nondimensional variables, using the friction velocity and the uniform heat flux (for UHF case) as the scaling variables. This scaling renders the sink terms in the momentum and energy equations constant, and makes the solution process relatively straightforward. In experiments, however, usually the mass flow rate and the wall temperatures are known; therefore the reference velocity should be the average velocity, and for UWT conditions, λ is no more a constant. For unsteady heat transfer calculations in periodic geometries, the following simplifying assumption is usually invoked:

$$T(x_i + L\delta_{i3}, t) = (1-\lambda)T_{\text{ref}} + \lambda T(x_i, t) \tag{2}$$

where T_{ref} is a reference temperature or flux (in appropriate units) for the problem. Simple algebra can demonstrate that the Eq. (2) is consistent with the energy equation. The scaling factor λ can be a function of time. The nondimensional temperature variable can now be defined as follows:

$$\Theta = \frac{T - T_{\text{ref}}}{T_{\text{wall}} - T_{r2}} \tag{3}$$

Here T_{wall} can be function of time and T_{r2} is another constant reference temperature (which is set not equal to T_{wall} to avoid singularity).

For constant wall temperature, we can see that T_{ref} is equal to wall temperature and it leads to a simple homogeneous boundary condition for Θ (i.e., zero on the wall). Also the denominator is merely a constant. Since $T_b(z+L,t) = (1-\lambda)T_{\text{ref}} + \lambda T_b(z,t)$, the nondimensional bulk temperature $\Theta_b = (T_b - T_{\text{ref}})/(T_{\text{wall}} - T_{r2})$, can be expressed as

$$\frac{\Theta_b(z+L)}{\Theta_b(z)} = \lambda \tag{4}$$

At geometrically periodic planes, the following relation is obtained:

$$\frac{\Theta(x_i + L\delta_{i3}, t)}{\Theta(x_i, t)} = \lambda \tag{5}$$

For constant heat flux, we can see that if T_{ref} is equal to $q_w D/k$, it leads to a simple homogeneous boundary condition for $\partial\Theta/\partial\eta$ (i.e., zero on the wall). The calculation of λ is done in a similar fashion as described above. Thus, this nondimensional temperature assumes existence of a reference temperature and a reference driving potential in the form of heat flux or applied temperature drop. Therefore, a simple energy balance and assumption of periodicity can yield the relations for these reference values. Boundary conditions for nondimensional temperature in the periodic direction is written as [using Eqs. (4) and (5)]

$$\frac{\Theta^0}{\Theta_b^0} = \frac{\Theta^L}{\Theta_b^L} \tag{6}$$

where the superscript indicates the z location and subscript b denotes the bulk nondimensional temperature. Differentiating the periodic boundary condition in the wall-normal direction we get

$$\frac{1}{\Theta_b^0}\left(\frac{\partial\Theta^0}{\partial X}\right) = \frac{1}{\Theta_b^L}\left(\frac{\partial\Theta^L}{\partial X}\right) \tag{7}$$

This is equivalent to enforcing periodicity on the Nusselt number in a periodic geometry.

Uniform Heat Flux (UHF) Case. For uniform heat flux at the boundaries,

$$\left(\frac{\partial\Theta^0}{\partial\eta}\right) = \left(\frac{\partial\Theta^L}{\partial\eta}\right) = q_w \tag{8}$$

$$\text{and} \quad \Theta_b^0 = \Theta_b^L$$

Clearly, setting Tr_2 to T_b will render the denominator as a constant. Moreover, the independence of non-dimensional bulk temperature from periodic direction implies that T_{ref} is equal to T_b. Therefore, the scaling at the inlet plane and periodicity of Nusselt number can uniquely determine the non-dimensionalization, and the sink term in the energy equation. Also, this sink term is independent of time because heat addition to the domain is constant at all time instants.

Uniform Wall Temperature (UWT) Case. From the energy balance, one can write

$$\rho C_p U_{\text{avg}}(T_b^L - T_b^0)A_c = \int\int_S q_w dS$$

$$\int\int_S q_w dS \approx \sum_{\text{in}} q_w dS + \sum (q_w^0 + q_w^L)\frac{dS}{2} \tag{9}$$

$$\rho C_p U_{\text{avg}}(T_w - T_2)(\Theta_b^L - \Theta_b^0)A_c \approx k(T_w - T_2)H\left\{\sum_{\text{in}}\left(\frac{\partial\Theta}{\partial\eta}\right)_w dS + \sum\left[\left(\frac{\partial\Theta}{\partial\eta}\right)_w^0 + \left(\frac{\partial\Theta}{\partial\eta}\right)_w^L\right]\frac{dS}{2}\right\}$$

Here η is the wall normal direction and dS is the differential area element on the wall.

For the square channel, we use Nusselt number periodicity to define the flux at the inlet in terms of the flux at the exit as

$$\left(\frac{\partial\Theta}{\partial\eta}\right)_w^0 = \frac{\Theta_b^0}{\Theta_b^L}\left(\frac{\partial\Theta}{\partial\eta}\right)_w^L \tag{10}$$

$$\lambda \equiv \frac{\Theta_b^0}{\Theta_b^L}$$

Using these relations in the energy balance, we get

$$(\Theta_b^L - \lambda\Theta_b^L)A_c \approx \left(\frac{1}{\text{Re}\cdot\text{Pr}}\right)\left[\sum_{\text{in}}\left(\frac{\partial\Theta}{\partial\eta}\right)_w dS + \sum\left(\lambda\left(\frac{\partial\Theta}{\partial\eta}\right)_w^L + \left(\frac{\partial\Theta}{\partial\eta}\right)_w^L\right)\frac{dS}{2}\right]$$

$$\therefore \lambda \approx \frac{\left\{\Theta_b^L - \left(\frac{1}{\text{Re}\cdot\text{Pr}}\right)\left[\sum_{\text{in}}\left(\frac{\partial\Theta}{\partial\eta}\right)_w dS + \sum\left(\frac{\partial\Theta}{\partial\eta}\right)_w^L\frac{dS}{2}\right]\right\}}{\left\{\Theta_b^L + \left(\frac{1}{\text{Re}\cdot\text{Pr}}\right)\left[\sum\left(\frac{\partial\Theta}{\partial\eta}\right)_w^L\frac{dS}{2}\right]\right\}} \tag{11}$$

To enforce the validity of scaling relation up to the wall, we choose T_{ref} equal to T_w. Therefore, the nondimensional temperature is zero at the wall and the scaling ensures the periodicity of the Nusselt number in the periodic geometries. On all the walls, the integration is carried up to the duct and turbulator walls, i.e., no ''log-law'' type wall function is used. In doing that, we are completely relying on the accuracy of the numerical scheme and the physical modeling of SGS motions.

Computational Method

The momentum equations [Eq. (1)] are solved using a projection method. The temporal differencing is done using an explicit second order accurate Adams-Bashforth scheme. The spatial descretization is done using a fourth-order central finite-difference scheme for all the terms except the convective term $(\partial U_\alpha U_\alpha/\partial x_\alpha)$ that is upwind-differenced with a third-order accurate scheme. The pressure-Poisson equation is solved using a direct solver based on a matrix diagonalization approach. The La-

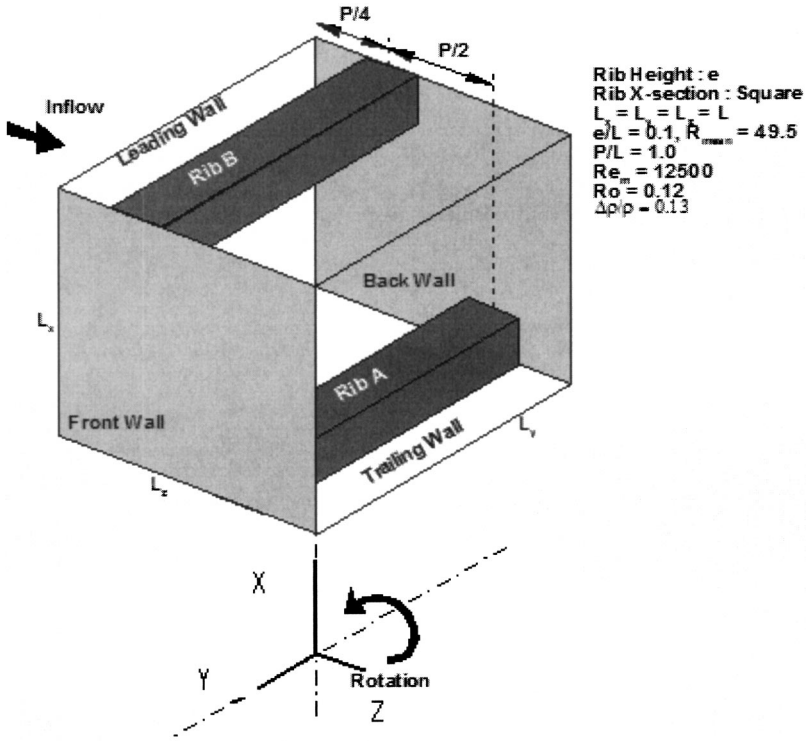

Fig. 2 Schematic of the computational domain

placian operator in the pressure equation is approximated using a fourth-order central difference for the gradient operator and a second order accurate central difference for the divergence operator. Thus, the overall spatial accuracy for momentum equations is third order. All the terms in the energy equation are differenced using fourth-order central differences. Additional details of the numerical procedure are given in Tyagi and Acharya [28] and Tyagi [29].

Results and Discussion

The computations are performed at a Reynolds number (Re) of 12,500 based on the average velocity in the duct and the hydraulic diameter of the square duct. For the computational domain ($D\times D\times 2D$) incorporating two periodic inter-rib modules (majority of the results presented), a grid size of $82\times 82\times 161$ is used. For computations with one periodic module ($D\times D\times D$), the number of grid points in the streamwise direction are reduced by a factor of 2. The rotation number (Ro) is chosen to be 0.12 and the inlet coolant-to-wall density ratio ($\Delta\rho/\rho$) is set at 0.13. The rib height-to-hydraulic diameter ratio (e/D) is 0.1 and the rib pitch-to-height ratio (P/e) is 10. The ribs are square in the cross section and are placed transverse to the flow in the duct (Fig. 2). These parameters correspond to the experimental configuration of Wagner et al. [2]. Time step for calculations is chosen small enough to resolve the vortex shedding from ribs as well as the migration of coolant over the walls.

Validation. Comparison with experimental data of Wagner et al. [2] is shown in Table 1. Also shown are the reported experimental uncertainties, and the percentage difference between the measurements and predictions. For the leading and trailing walls, the agreement between experiments and predictions are generally within the range of experimental uncertainty. For the two side walls (which should have the same time-averaged Nusselt number), the time-averaged Nusselt number predictions on each wall exhibit nearly 12% difference with each other, and for comparison purposes both the predictions and the data have been averaged over both walls. The differences in the averaged side wall predictions are due to the presence of a low-frequency unsteadiness that are not averaged out during the averaging time period used. In the computations 12 flow-through time periods were used for obtaining the time-averaged statistics, and although this is generally considered to be sufficiently long for the calculation of statistics, the presence of low frequency dynamics can require extremely long time periods that may be impractical from the perspectives of available computational resources. The larger deviation with respect to measurement along side wall 1 is partly due to statistical averaging errors. The spatial distribution of time-averaged Nusselt number on ribbed leading and trailing walls is presented in Fig. 3.

In order to resolve the issue concerning the spatial extent of the low frequency unsteadiness, the computational domain was extended to include two inter-rib geometric modules. The larger computational domain revealed the presence of oscillations that were greater than one inter-rib module in spatial extent. However, the time-averaged Nusselt numbers are not significantly different for the one-rib and two-rib computational modules for the averaging time period used in the present computations. The results presented below are therefore from the two-computational module simulations.

The three-dimensional spectrum of the instantaneous flow field is shown in Fig. 4(*a*). The grid resolution is sufficient to capture the energy producing events as well as the portion of the inertial subrange. A peak in energy spectrum is also observed around the wave number corresponding to a length scale $l/D=0.1$. This is attributed to the energy production by vortex shedding behind the

Table 1 Comparison of the averaged Nusselt number with Wagner et al. [2].

Average Nusselt number	Computed	Measurements (±uncertainty)	% difference
Leading wall	53	55(±20%)	4
Trailing wall	102	124(±15%)	18
Side wall (averaged)	80.5	64(±15%)	26

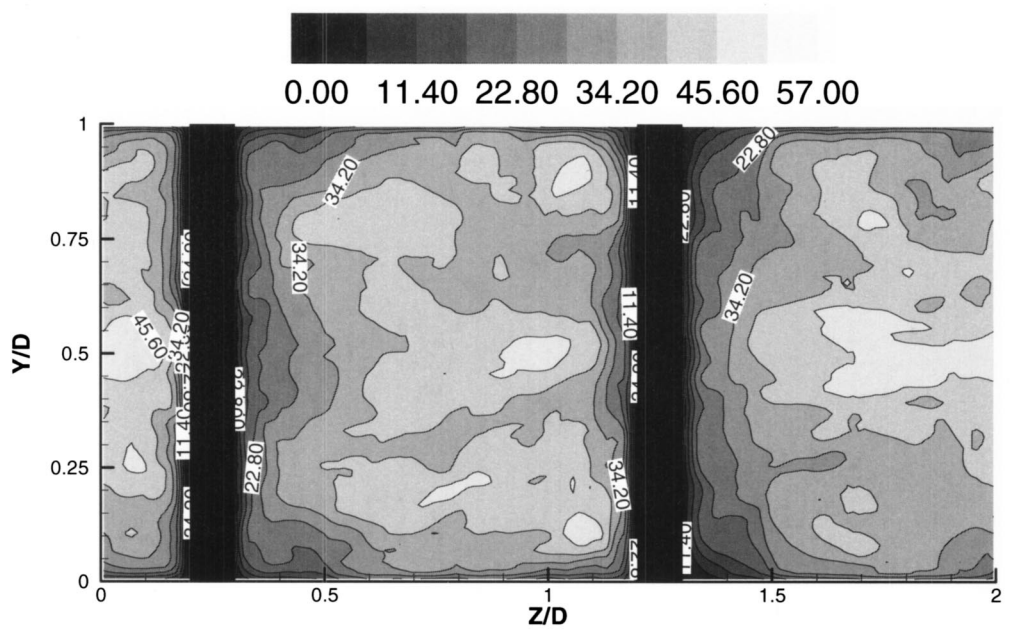

a) Leading Wall

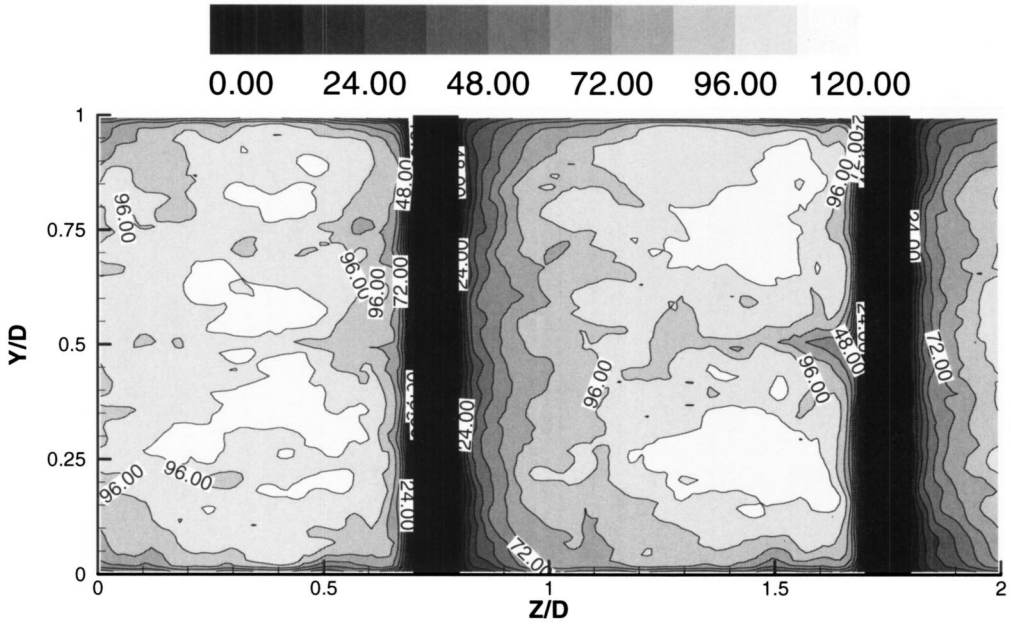

b) Trailing Wall

Fig. 3 Nusselt number distribution on the ribbed (*a*) leading wall and (*b*) trailing wall

ribs ($e/D=0.1$). Figure 4(*b*) shows the variations of the instantaneous flow rate. Note that, to maintain an average flow rate, a mean constant (in space) pressure gradient is applied. Superimposed on this mean pressure gradient are temporal and spatial variations corresponding to the periodic variations, large scale fluctuations and turbulence. These variations cause the instantaneous flow rate to vary in time, with the variation dominated by the vortex shedding frequency [Fig. 4(*b*)]. However, the average flow rate is always maintained to be 1.0 (in nondimensional units) as desired.

Flow Physics and Heat Transfer. The time-averaged velocity vectors on the spanwise midplane are shown in Fig. 5. The details near the ribs show the differences in the size of the fore-

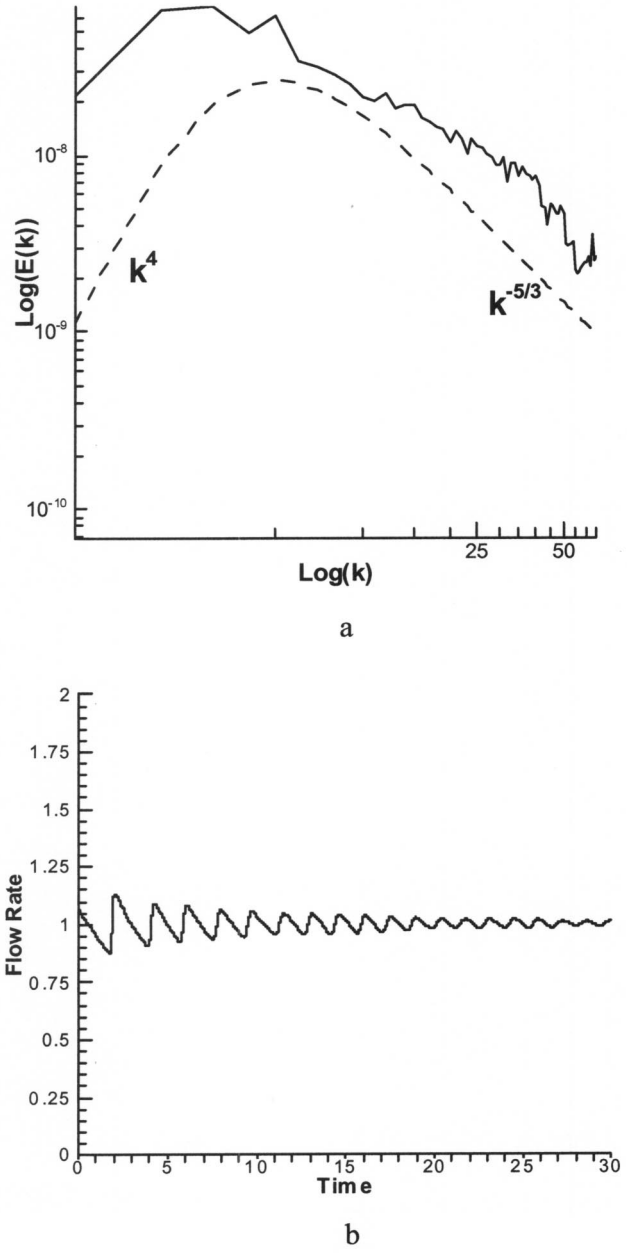

Fig. 4 (*a*) Three-dimensional energy spectrum of the flow field. (*b*) Flow rate versus time.

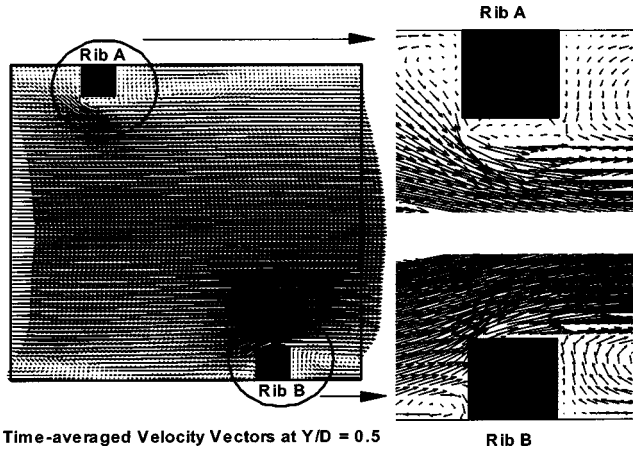

Fig. 5 Time-averaged velocity vectors and details of flow field near the ribs at the $Y/D=0.5$

and aft-recirculation region along the leading and trailing surfaces. The corner recirculation region in front of rib B (on trailing wall) is smaller than that in front of rib A (leading wall). Because of the secondary flows directed from the leading surface to the trailing surface, the upstream corner recirculation on the leading surface has a steep slope relative to the cross flow, resulting in flow separation at the upstream rib corner. The steep slope of the flow negotiating the rib corner causes the flow to remain detached on the top face of rib A (on the leading edge). Since the secondary flows are directed toward the trailing surface, the flow turning the front corner of rib is pushed toward the trailing surface, and stays attached on the rib B face.

In Figs. 6(*a*)–6(*d*), the streamwise component of vorticity and temperature field are presented in a time sequence. The various walls of the duct are labeled as LW: leading wall, TW: trailing wall, LSW: left-side wall, and RSW: right-side wall. Starting time instant t_0 is arbitrary and the time gap T is equal to 150 time steps (or 0.15τ, where τ is the flow through time period). A key conclusion from these pictures is the important role of coherent structures on the scalar mixing and therefore on the heat transfer. The vorticity field near the trailing surface is considerably stronger (more structures, higher magnitudes) than along the leading surface, and therefore along the trailing surface scalar mixing is greater, the flowfield is destabilized to a greater extent, and the thermal gradients and the heat transfer rates are greater. The accumulation of coolant (blue temperature contours) closer to the trailing wall is a direct consequence of Coriolis forces in this plane directing the flow from the leading to the trailing surface. This is seen in Fig. 6 along with the three-dimensional streamwise vorticity field resulting from the breakdown of the separating shear layer and the near-wall boundary layer. Counter-rotating vortex pairs are consistently observed near the trailing surface (shown by arrows), and its dynamics is seen to play an important role in the large scale mixing of the core coolant fluid. The vortex pair entrains the surrounding core fluid (blue) and mixes this with the near wall fluid (red) resulting in lower temperatures (green) and higher thermal gradients near the trailing wall. Contrast this with the region near the leading wall where the temperature contours are primarily red and yellow indicating elevated temperatures and lower thermal gradients or heat transfer. Further, along the leading wall, the vortices are accumulated primarily around the center. This results in growth of thermal plumes around the corner of the leading wall due to the lack of mixing in these regions. These plumes appear as fingers penetrating into the coolant core. At time t_0+T [Fig. 6(*b*)], the counter-rotating vortex pair near the TW has intensified and penetrates further into the coolant core. At time t_0+2T [Fig. 6(*c*)] another counter-rotating pair near the left-side wall can be seen, and correspondingly enhances the mixing in this region. At time t_0+4T [Fig. 6(*d*)], vortices near the trailing wall left corner have penetrated upward resulting in the growth of a thermal boundary layer on the left-side wall, and enhanced mixing in this region (see corresponding image on the right). The counter-rotating vortex on the center of the trailing wall has diminished in strength but is larger in size.

Attention is next turned to the dynamics of spanwise vorticity and temperature field on a cross-section plane through the center of duct at $Y/D=0.5$ [Fig. 7(*a*)–7(*d*)]. In this time sequence, the time gap is 375 time steps ($=0.375\tau$). The temperature contours do not exhibit periodicity across one inter-rib module, and evidence of vortical structures with streamwise length of nearly half the inter-rib distance can be observed. These facts indicate that imposition of streamwise periodicity over one inter-rib module is inappropriate (as done in the majority of the reported LES studies for ribbed ducts). Most of the vortices shed from ribs on trailing

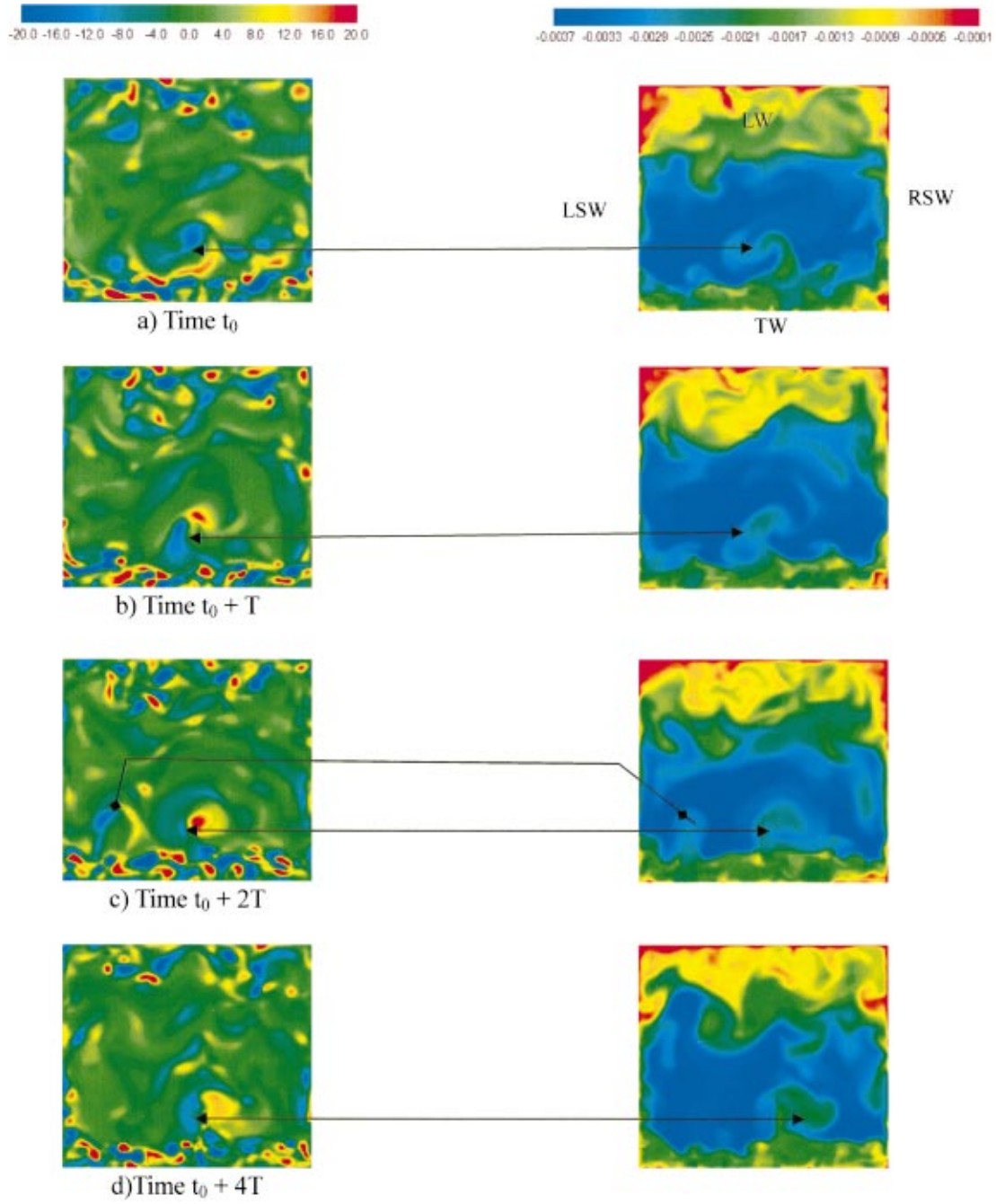

Fig. 6 Time sequence of streamwise vorticity (left) and temperature field (right) at $Z/D=1.0$. Temperature field: red is 1 and blue is 0. Arrows show locations of counter-rotating vortex pairs.

wall remain close to the wall due to Coriolis body force (directed from leading to trailing wall on this plane). Vortices that reach the core of the duct enhance mixing of scalar field there. Ribs on the leading wall generate spanwise vorticity in the opposite sense and high-temperature streaks in the vicinity of leading edge ribs indicate low heat transfer rates. Temperature field distribution shows the presence of more coolant closer to the trailing wall, resulting in larger temperature gradients and heat transfer rates. To correlate the role of coherent structures in the mixing process, a set of vortical structures shed by the rib is shown encircled, and in these regions the temperature contours consistently exhibit greater mixing between the core fluid and the near-wall fluid. Since the footprint of the vortical structures are visible in the temperature contours, it is conjectured that the dominant contribution to the mixing process is the entrainment induced by the large scale structures. Also indicated by a rectangular box in Fig. 7 is the development of the interface of the coolant flow as it passes through the channel. This convoluted interface is typical of a mixing layer and jet, and reflects the role of large scale dynamics in the mixing process. In addition to shear layer separation past the ribs, these dynamics are also potentially influenced by rotation induced secondary flows, centrifugal-buoyancy, and shear layer curvature.

To illustrate the influence of coherent structures generated by ribs on the leading and trailing wall heat transfer, three instantaneous snapshots (t_1 through t_3) of the Y component of vorticity are presented at the centerplane $Y/D=0.5$ (Fig. 8). Also, the corresponding non-dimensional instantaneous heat flux is presented along the trailing surface centerline ($X/D=0.0$; figures on the

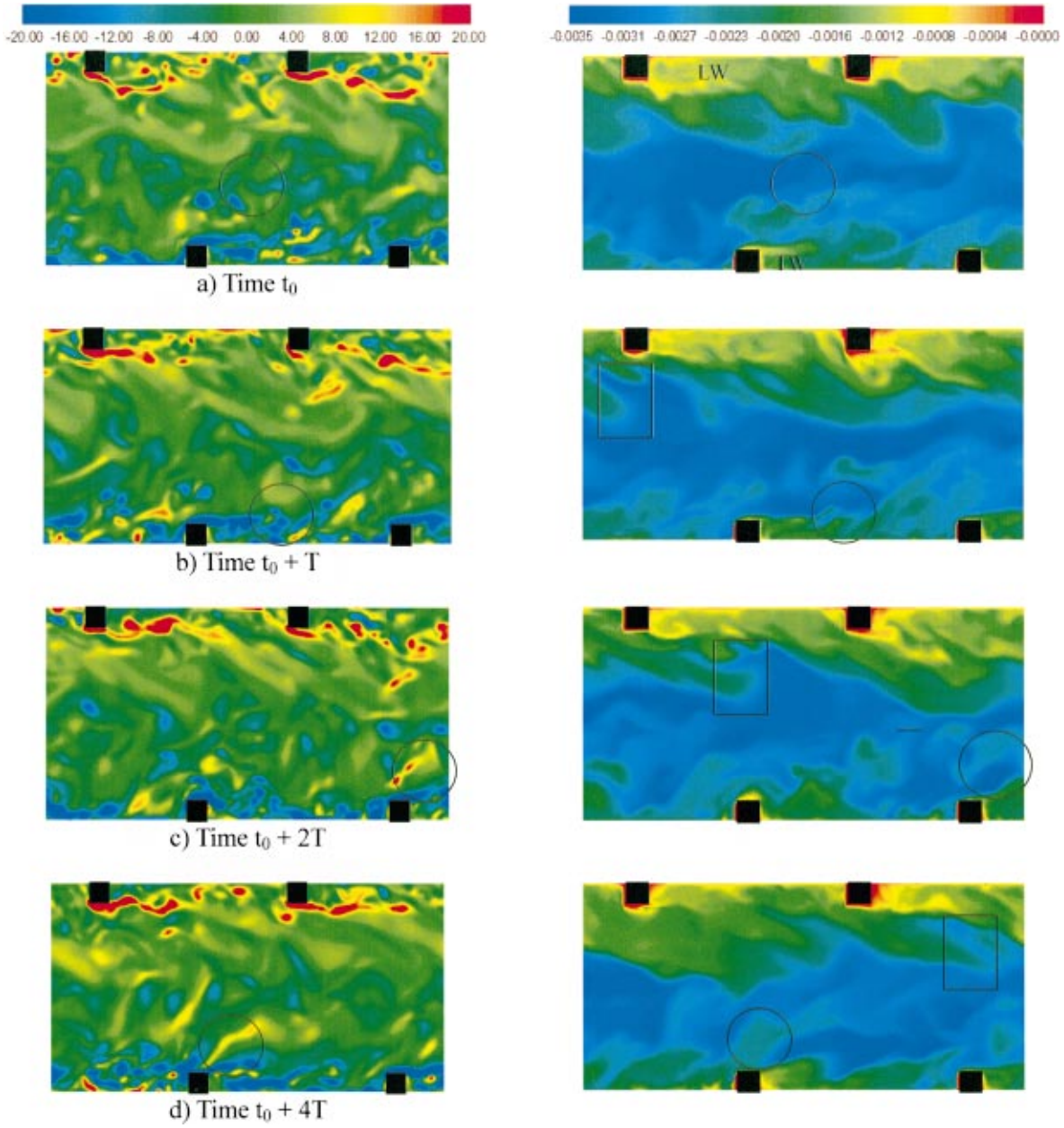

Fig. 7 Time sequence of vorticity dynamics and temperature field on cross-sectional plane at $Y/D=0.5$. Spanwise vorticity (left) and temperature field (right). Arrows on the snapshots track vortices and entrainment interface of scalar field.

right) and along the leading surface centerline ($X/D=1.0$; figures on the left). Peak heat transfer rates at trailing wall are about 2–3 times than that on leading wall. The heat transfer between the ribs in a geometrically periodic module along the leading wall is ''in phase'' with the adjacent geometrically periodic module, and the time variations in these profiles are relatively small. However, along the trailing wall, the heat transfer rates in successive inter-rib modules do not exhibit periodicity, and contains spatial modes larger than the pitch of periodic module. This observation further supports the argument for using computational domains longer than that suggested by geometric periodicity. Time-dependent calculations performed for only one geometric pitch module are likely to produce inaccurate evolutionary dynamics of coherent structures and their influence on unsteady heat transfer. To date, most of the unsteady computational simulations for the configuration of interest are performed in geometrically periodic domains using one rib-pitch as the streamwise periodic length (e.g., Murata and Mochizuki [18,19]).

Time-averaged results show that the peak heat transfer coefficient downstream of the rib is in the vicinity of the reattachment point (nearly six-rib heights), and the peak heat transfer coefficient one rib height upstream is due to the corner eddy. The temporal variations in the heat flux along the leading surface indicate that the upstream peak heat flux magnitude is the highest, and remains fairly steady in magnitude and location, while downstream the heat flux plateaus beyond two-rib heights, and fluctuations in magnitude spatially and temporally are relatively small. These fluctuations are associated with the streamwise migrations of the near-wall vortical structures. Near the trailing wall, the spatial and temporal fluctuations of the heat flux are more significant due to the greater unsteadiness in the separating shear layer and the more intense vortical activity along the trailing wall. In the first inter-rib module on the trailing wall, the peak magnitude associated with the corner vortex (immediately upstream of the first rib) changes by a factor of nearly 2 with time (compare t_1 with t_3), while the location of the peak associated with the reat-

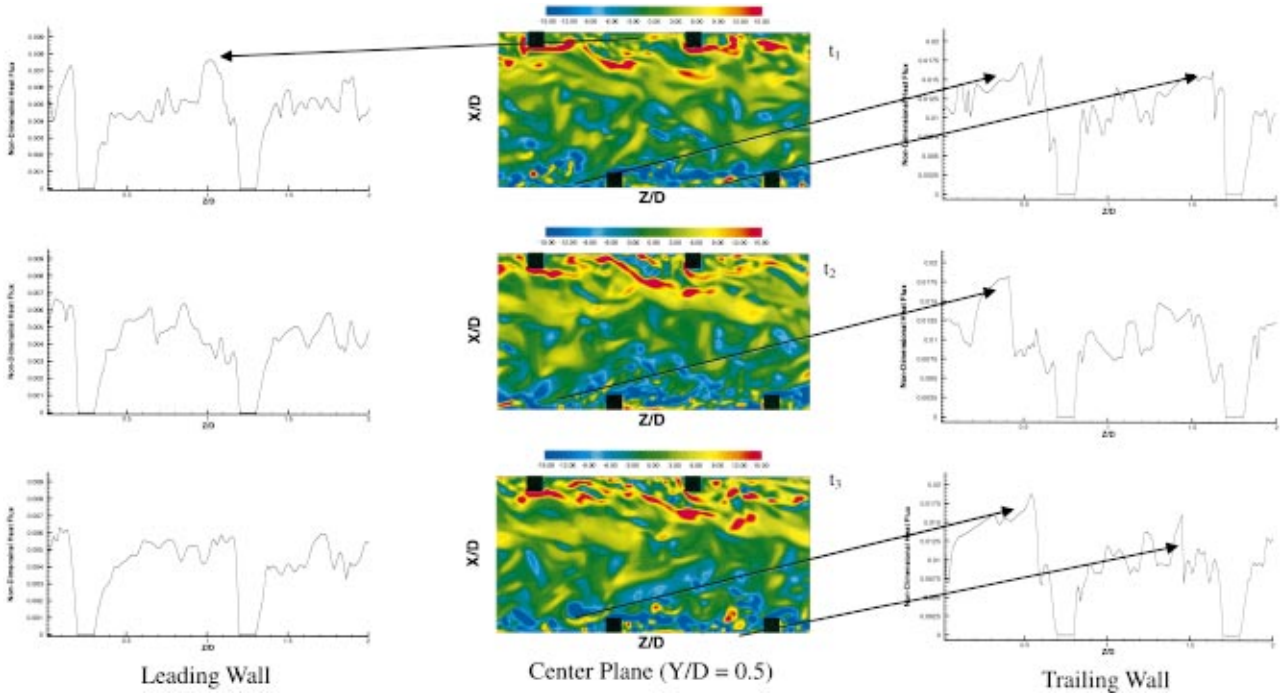

Fig. 8 Influence of vortical structures on the near wall heat transfer in rotating ribbed duct. (Note: range of nondimensional heat flux on leading and trailing wall is different in this figure).

tachment point (in the first inter-rib module) moves around from two-rib heights upstream (at t_3) to nearly four-rib heights upstream (at t_2).

Temperature signals are presented in Fig. 9(*a*) for two stations, one near the leading wall and the other near the trailing wall, along the center plane ($Y/D=0.5$) midway between the ribs on each wall. To provide a measure of the temperature fluctuations, the temperature values have been converted into dimensional numbers assuming inlet coolant bulk temperature of 800°F and metal wall temperature of 2500°F. These assumed temperatures are only representative and do not correspond to any specific configuration. The trailing wall temperature shows lower temperature levels (due to higher heat transfer coefficients shown in Fig. 8), high frequency variation as well as larger excursions from its mean value (due to greater vortical activity shown in Fig. 6) as compared to the leading wall temperatures. The corresponding representation in terms of probability distribution function shows a bimodal distribution on the trailing wall while near the leading wall a unimodal distribution is obtained and does not exhibit large variations [Fig. 9(*b*)].

The instantaneous temperature field on a plane close to the trailing surface along with the wall-normal component of vorticity

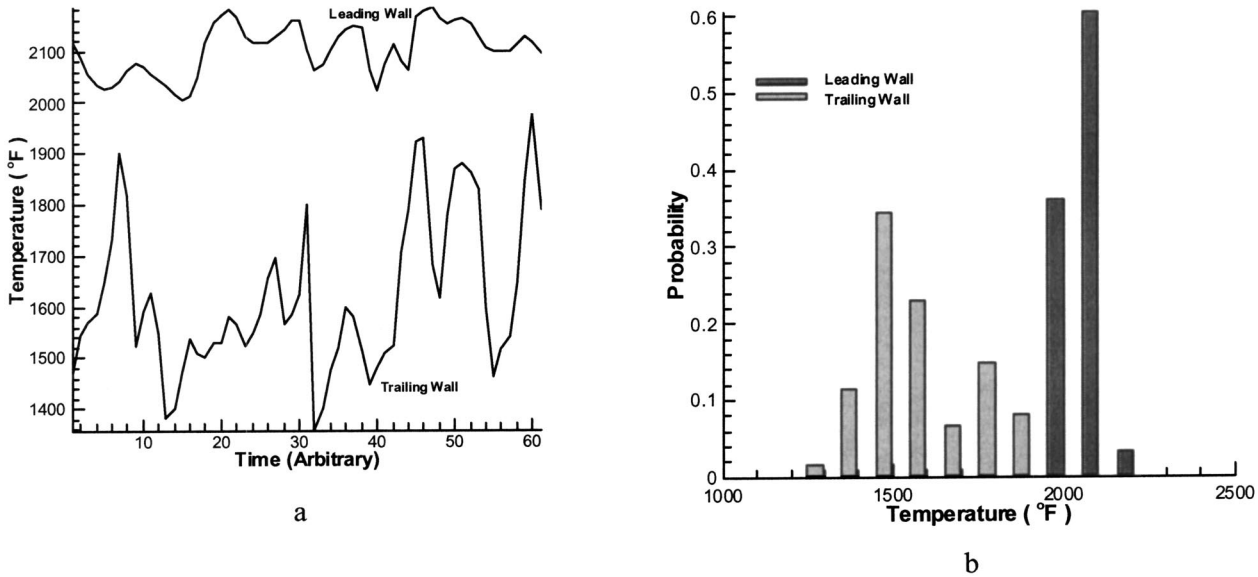

Fig. 9 (*a*) Temperature signals around probe stations just above the walls between the ribs along the centerplane (*Y/D* =0.5). (*b*) Corresponding probability distribution function.

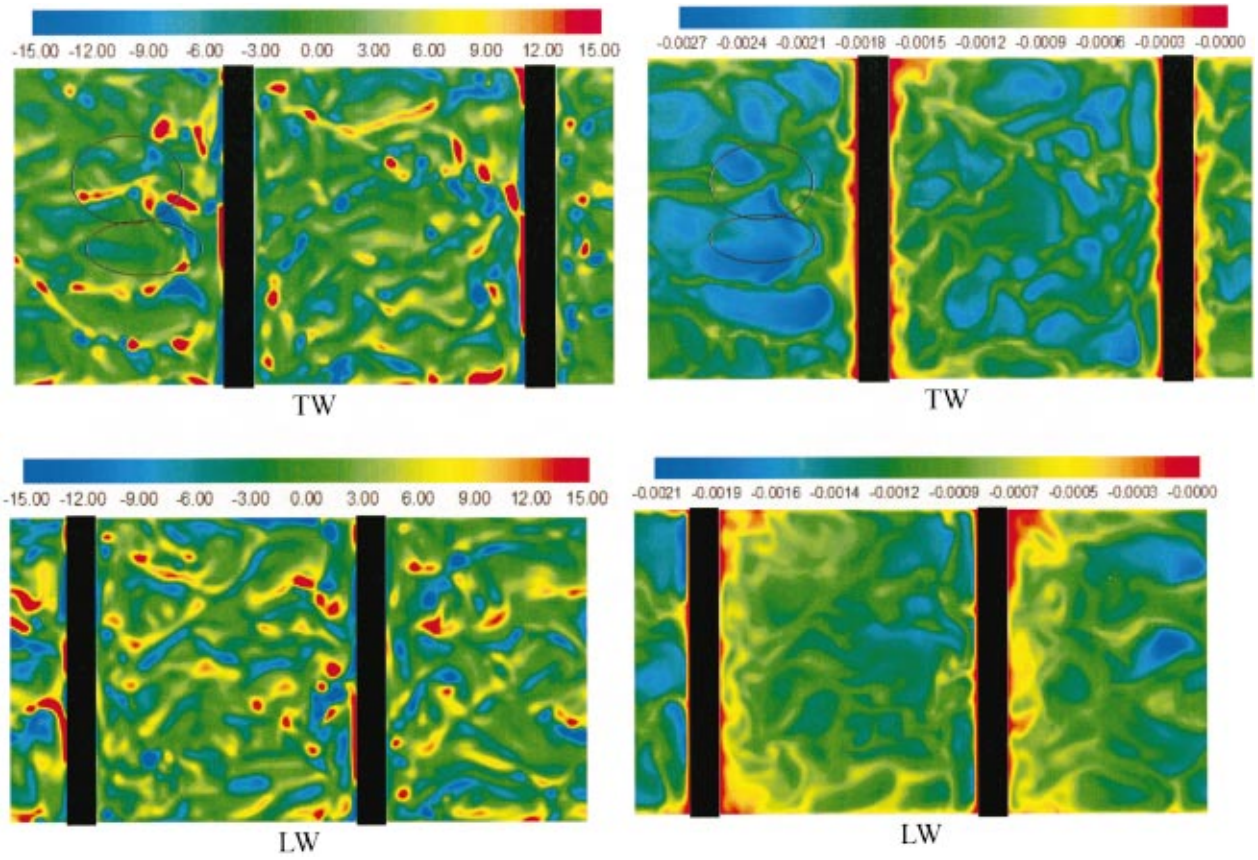

Fig. 10 Vorticity dynamics and temperature field over trailing wall at $X/D=0.125$ (top row) and leading wall at $X/D=0.975$ (bottom row), wall-normal vorticity (left) and temperature field (right)

are shown in Fig. 10 (top row) while the corresponding plots for the leading surface are shown in Fig. 10 (bottom row). These temperature contours are inversely proportional to the Nusselt number distributions. As may be expected, the trailing surface regions exhibit larger patches of cold spot (high Nusselt number) compared to the leading surface. The low temperature streaks are correlated not only with the streamwise vorticity (as shown earlier in Fig. 6), but appear to show some correlation with the wall-normal vorticity along the trailing surface (see encircled regions).

In an attempt to explain the flow physics better, coherent structures are extracted here using positive iso-surfaces of the Laplacian of the pressure field (Wray and Hunt [30]; Tanaka and Kida [31]; Dubief and Delcayre [32]). Since the vortex cores are associated with strong vorticity and local pressure minima, it can be readily shown that positive surfaces of the Laplacian of pressure $[p_{,kk}=(\omega_i\cdot\omega_i)/2\text{-}S_{ij}\cdot S_{ji}]$ can be used to identify coherent structures. For incompressible flows, $p_{,kk}$ is also directly related to the second invariant of the velocity gradient tensor. In Fig. 11, a time sequence of such structures (at t_1, t_2, and t_3) is presented along the trailing surface, while in Fig. 12, a single snapshot at t_2 is shown along the leading surface. The higher concentration of vortical structures near the trailing wall (also seen earlier in Fig. 6) increases the mixing and heat transfer along this wall significantly (Fig. 8). The shear layer that separates from the ribs is initially oriented in the spanwise direction parallel to the ribs in the form of roller vortices. The roller vortices begin to form immediately upstream of the rib, and are inherently three-dimensional structures coming off the rib. These vortices move downsteam, and reorient and align in the flow direction into braids. The roller vortices are mostly converted into braid vortices within a pitch length. Due to the influence of Coriolis forces, these vortices tend to accumulate close to the centerplane in the form of braids (streamwise oriented coherent structures). As the vortices are transported downstream. They are distorted to result in arch or hairpin shape vortical structures. As seen in Fig. 12, upstream of the first rib, due to the influence of Coriolis forces, the coherent braidlike structures converge toward the spanwise centerplane and break up into smaller structures in front of the rib. Moreover, some smaller vortices are also seen beneath these large structures. These structures are produced primarily at the wall and evolve under the influence of the induced flow field of the larger structures. The size of the coherent structures can be of the order of a rib-pitch (see structure marked A in Fig. 11 which extends nearly half pitch length in the streamwise direction and half pitch length in the transverse direction). Therefore, most of the single rib-pitch module calculations cannot capture such large energy containing scales accurately. These coherent structures must be resolved in a larger computational domain. Evolution of these structures on leading and trailing wall results in migration of ''hot-streaks'' on walls, entrainment of coolant from the duct core and mixing of scalar field in the core of these vortices.

To track the evolution of specific structures, in Fig. 11, three specific structures are identified as A, B, and C, and their evolution at three time instances t_1, t_2, and t_3, is shown. At time $t=t_1$, the roller vortex A has migrated towards the second rib and the arch-shaped head is distorted by the adverse pressure gradient in front of the rib. Coherent structure ''B'' has convected downstream while growing in size. Inception of roller vortex ''C'' on the first rib can be seen. At time $t=t_2$, the roller vortex ''A'' is moving over the second rib on the trailing wall. The influence of the rib can be seen in the deformation of the coherent structure. At this time instance, there are two pairs of roller vortices after the first rib on the trailing wall separated by the braid vortices around the centerplane. Roller vortex ''B'' is reoriented by the flow to

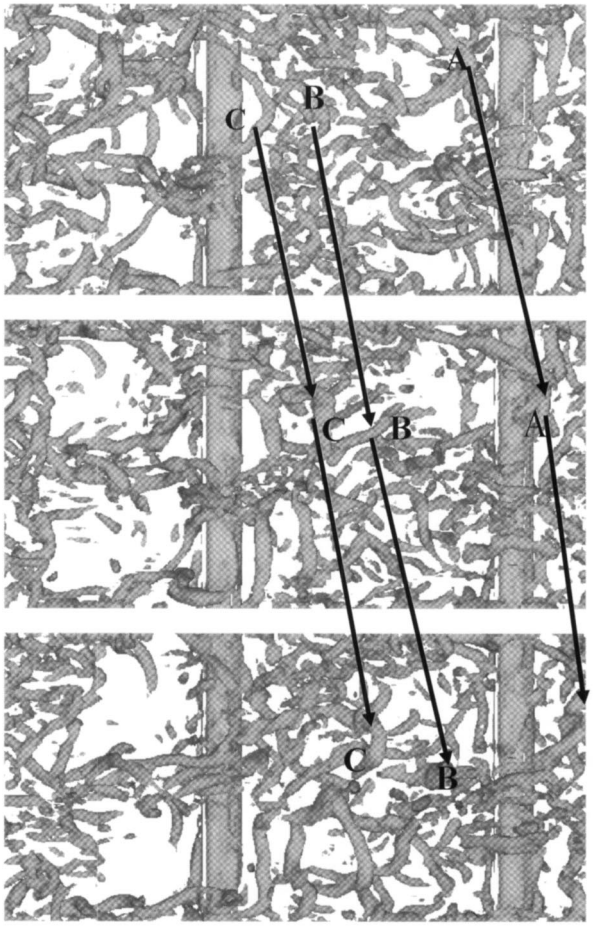

Fig. 11 Coherent structures over the trailing wall—three time instances

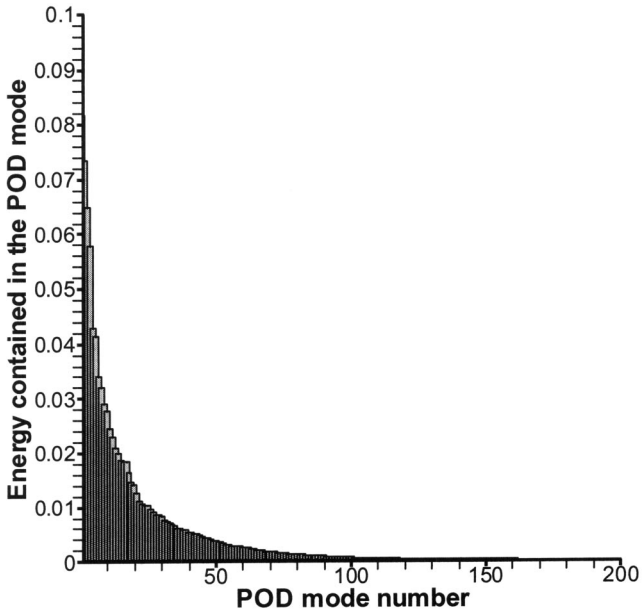

Fig. 13 Energy distribution in the POD modes calculated from 200 snapshots

align in streamwise direction. Coherent structure ''C'' is growing in size while migrating in the streamwise direction. At time $t = t_3$, the roller vortex ''A'' has left the computational domain while further disintegrating due to stretching by the flow. Roller vortex ''B'' has grown in size, has aligned with the flow, and merges into the braids along the centerplane over the second rib. Roller vortex ''C'' is around the midway between the ribs and a spanwise wavy instability has distorted the structure into an arch shape. This instability will eventually break it into smaller vortices. The dynamics near the leading wall are not substantially different, and therefore only a single snapshot is shown in Fig. 12. Clearly, the influence of these structures on mixing of coolant fluid (near duct core) and heated fluid (near the wall) will determine the unsteady heat transfer over the duct surfaces (as seen earlier in Figs. 6–8).

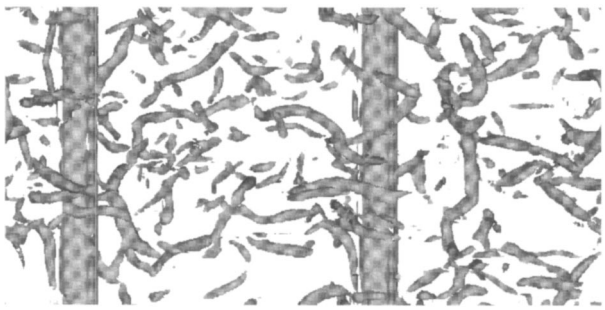

Fig. 12 Coherent structures over the leading wall—one time instance

Proper Orthogonal Decomposition. To analyze the low dimensionality of this system, proper orthogonal decomposition (POD) is applied on two hundred snapshots from the flow field. POD is a projection of turbulent fields on an optimal basis with some structure to these underlying flowfields. The optimality lies in the fact that for a given number of modes, the POD modes capture the most amount of ''energy'' of the turbulent fields. Mathematically, one solves an eigenvalue problem for the covariance or autocorrelation matrix. This matrix is constructed using method of snapshots (Holmes et al. [33], Sirovich [34]). The eigenvectors would then be POD modes with eigenvalues representing the amount of ''energy'' captured by the respective mode. Clearly, as shown in Fig. 13, the first 75–80 modes capture almost 99% of the total turbulent energy.

The first two POD modes shown in Fig. 14 identify the most energetic flow events. The top row in Fig. 14 shows the velocity components for the first mode while the lower row shows the velocity components for the second mode. As explained earlier, these modes correspond to the first two eigenvectors when arranged with decreasing magnitude of eigenvalues (or ''energy''). The energetic modes for W, the streamwise velocity component, confirms that flow reattachment on the trailing surface (red region) and separation (blue region) on the leading and trailing surfaces are clearly the dominant events. The U modes (wall-normal velocity component) confirm this observation, but also indicate high values of the second mode near the trailing surface reflecting impingement on the upstream face of the rib, and the upward deflection of coherent structures by this face. The importance of this upward deflection was evident in Fig. 7 in the form of the counter-rotating vortex pair which penetrated into the core coolant and induced large-scale mixing between the core-coolant and the hot near-wall fluid. The spanwise velocity modes (V) indicate that there are considerable spanwise movement of the flow and three dimensionality associated with reattachment (and breakup of coherent structures) and shear layer separation upstream of the rib (inducing spanwise instability and breakup of roller vortices seen in Fig. 12).

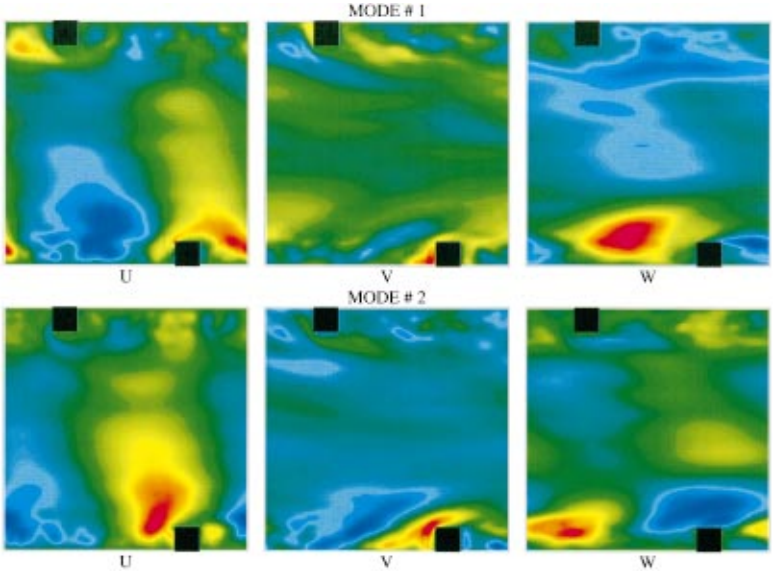

Fig. 14 Velocity components of the first two POD modes (top row: mode 1, bottom row: mode 2) extracted from 200 snapshots for single module flow fields

No attempt is made here to construct a low-dimensional system emulating the dynamics of the Navier-Stokes system. This is deferred for future work.

Concluding Remarks

Large eddy simulations are performed for a rotating square duct with normal rib turbulators. The Coriolis force as well as the centrifugal buoyancy parameter has been included in this study. A direct approach is presented for the unsteady calculation of nondimensional temperature field in periodic domains with UWT boundary conditions. The results show that large scale vortices play a major role in the mixing between the core fluid and the near-wall heated fluid. The temperature field is driven by the large-scale mixing, is inherently unsteady, and contains low frequency mode with long time periods. To resolve the low frequency modes and to better understand coherent structure dynamics, simulations are performed in a computational domain consisting of two inter-rib modules. Time sequences of vorticity components and temperature fields are presented to understand the unsteady flow physics and heat transfer processes. Along the leading surface the spatial and temporal fluctuations of the temperature and velocity field are small, while along the trailing surface significant fluctuations in the velocity and temperature field with a bimodal temperature distribution is observed. The instantaneous heat flux distribution at the trailing wall indicates the lack of periodicity in successive inter-rib modules, and significant spatial migration of the peaks with time indicating temporal variations of the reattachment points downstream and separation points upstream of the rib. Along the leading surface inter-rib modules show reasonable periodicity in the heat flux profiles and muted dynamics. Coherent structures are extracted using a simple pressure Laplacian criterion. It is shown that as the flow separates past the rib the flow structures initially evolve as roller vortices parallel to the rib, and then are reoriented as braid vortices parallel to the streamwise flow direction. Proper orthogonal decomposition (POD) of 200 snapshots indicates a low dimensionality of this system. Almost 99% of turbulent energy can be captured by first 80 POD modes. The first two most energetic modes are related to dynamical events of flow impingement on the front face of the trailing rib, flow separation and reattachment.

Acknowledgments

This work was supported by a grant from the South Carolina Institute of Energy Studies under the Department of Energy's Advanced Gas Turbine Systems Research (AGTSR) and High Efficiency Engine Technology (HEET) programs. Their support is gratefully acknowledged.

Nomenclature

Bo = Buoyancy parameter
D = Hydraulic diameter
Nu = Nusselt number
p = Pressure field divided by constant density
Pr = Prandtl number ($=0.71$)
q_j = Subgrid scale (SGS) scalar flux vector
r = Radial distance from rotation axis
Re = Reynolds Number
Ro = Rotation number
T_b = Coolant bulk temperature (dimensional)
T_w = Wall temperature (dimensional)
U_i = Filtered velocity field
X = Vertical direction (normal to ribbed surfaces)
Y = Spanwise direction (parallel to the ribs)
Z = Streamwise direction (periodic)

Greek:

τ_{ij} = Subgrid scale (SGS) stress tensor
Θ = Nondimensional temperature

References

[1] Morris, W. D., 1981, *Heat Transfer and Fluid Flow in Rotating Coolant Channels*, Research Studies Press, Hertfordshire, UK.
[2] Wagner, J. H., Johnson, B. V., Graziani, R. A., and Yeh, F. C., 1992, "Heat Transfer in Rotating Serpentine Passages with Trips Normal to the Flow," ASME J. Turbomach., **114**, pp. 847–857.
[3] Morris, W. D., and Rahmat-Abadi, K. F., 1996, "Convective Heat Transfer in Rotating Ribbed Tubes," Int. J. Heat Mass Transfer, **39**, pp. 2253–2266.
[4] Yamawaki, D., Obi, S., and Masuda, S., 2002, "Heat Transfer in Transitional and Turbulent Boundary Layers with System Rotation," Int. J. Heat Fluid Flow, **23**, pp. 186–193.
[5] Acharya, S., and Zhou, F., 2001, "Flow and Heat Transfer in Dimpled Two-pass Channel, in Heat Transfer in Gas Turbine Systems," Ann. N.Y. Acad. Sci., **934**, pp. 424–431.
[6] Hibbs, R., Acharya, S., Chen, Y., Nikitopoulos, D., and Myrum, T., 1998,

''Heat Transfer in a Two-Pass Internally Ribbed Turbine Blade Coolant Channel with Cylindrical Vortex Generators,'' ASME J. Turbomach., **120**, pp. 724–734.
[7] Zhou, F., Lagrone J., and Acharya, S., 2004, ''Internal Cooling in 4:1 AR Passages at High Rotation Numbers,'' Paper no. GT2004-53501, IGTI Turbo Expo, Vienna.
[8] Han, J. C., and Dutta, S., 2001, ''Recent Developments in Turbine Blade Internal Cooling, in Heat Transfer in Gas Turbine Systems,'' Ann. N.Y. Acad. Sci., **934**, pp. 162–178.
[9] Bredberg, J., 1997, *Turbine Blade Internal Cooling*, Chalmers University, Goteborg.
[10] Iacovides, H., and Launder, B. E., 1995, ''Computational Fluid Dynamics Applied to Internal Gas-Turbine Blade Cooling: A Review,'' Int. J. Heat Fluid Flow, **16**, pp. 454–470.
[11] Naimi, M., and Gessner, F. B., 1997, ''Calculation of Fully Developed Turbulent Flow in Rectangular Ducts with Two Opposite Roughened Walls,'' Int. J. Heat Fluid Flow, **18**, pp. 471–481.
[12] Iacovides, H., 1998, ''Computation of Flow and Heat Transfer Through Rotating Ribbed Passages,'' Int. J. Heat Fluid Flow, **19**, pp. 393–400.
[13] Bonhoff, B., Parniex, S., Leusch, J., Johnson, B. V., Schabacker, J., and Bolcs, A., 1999, ''Experimental and Numerical Study of Developed Flow and Heat Transfer in Coolant Channels with 45 Degree Ribs,'' Int. J. Heat Fluid Flow, **20**, pp. 311–319.
[14] Iacovides, H., and Raisee, M., 1999, ''Recent Progress in the Computation of Flow and Heat Transfer in Internal Cooling Passages of Turbine Blades,'' Int. J. Heat Fluid Flow, **20**, pp. 320–328.
[15] Saidi, A., and Sunden, B., 2001, ''On Prediction of Thermal-Hydraulic Characteristics of Square-Sectioned Ribbed Cooling Ducts,'' ASME J. Turbomach., **123**, pp. 614–620.
[16] Hermanson, K., Parneix, S., Von Wolfersdorf, J., and Semmler, K., 2001, ''Prediction of Pressure Loss and Heat Transfer in Internal Cooling Passages,'' Ann. N.Y. Acad. Sci., **934**, pp. 448–455.
[17] Jang, Y.-J., Chen, H.-C., and Han, J.-C., 2001, ''Flow and Heat Transfer in a Rotating Square Channel with 45° Angled Ribs by Reynolds Stress Turbulence Model,'' ASME J. Turbomach., **123**, pp. 124–132.
[18] Murata, A., and Mochizuki, S., 2000, ''Large Eddy Simulation with a Dynamic Subgrid-Scale Model of Turbulent Heat Transfer in an Orthogonally Rotating Rectangular Duct with Transverse Rib Turbulators,'' Int. J. Heat Mass Transfer, **43**, pp. 1243–1259.
[19] Murata, A., and Mochizuki, S., 2001, ''Effect of Centrifugal Buoyancy on Turbulent Heat Transfer in an Orthogonally Rotating Square Duct with Transverse or Angled Rib Turbulators,'' Int. J. Heat Mass Transfer, **44**, pp. 2739–2750.
[20] Pallares, J., Grau, F. X., and Davidson, L., 2001, ''A Model for Estimating Three-Dimensional Boundary Layers in Rotating Duct Flow at High Rotation Rates,'' *2nd International Symposium on Turbulence and Shear Flow Phenomena*, Vol. **1**, KTH-Stockholm, pp. 359–364.
[21] Roclawski, H., Jacob, J. D., Yang, T., and McDonough, J. M., 2001, ''Experimental and Computational Investigation of Flow in Gas Turbine Blade Cooling Passages,'' AIAA paper 2925.
[22] Miyake, Y., Tsujimoto, K., and Nagai, N., 2002, ''Numerical Simulation of Channel Flow with a Rib-Roughened Wall,'' J. Turbul., **3**, 35.
[23] Saha, A., and Acharya, S., 2004, ''Unsteady Computations for Flow and Heat Transfer in 1:1, 4:1, 1:4 AR Ribbed Coolant Passages with Rotation,'' ASME paper No. GT2004-53986.
[24] Patankar, S. V., Liu, C. H., and Sparrow, E. M., 1977, ''Fully Developed Flow and Heat Transfer in Ducts Having Streamwise-Periodic Variations of Cross-Sectional Area,'' ASME J. Heat Transfer, **99**, pp. 180–186.
[25] Wang, G., and Vanka, S. P., 1995, ''Convective Heat Transfer in Periodic Wavy Passages,'' Int. J. Heat Mass Transfer, **38**, pp. 3219–3230.
[26] Moin, P., Squires, K., Cabot, W., and Lee, S., 1991, ''A Dynamic Subgrid-Scale Model for Compressible Turbulence and Scalar Transport,'' Phys. Fluids A, **3**(11), pp. 2746–2757.
[27] Vreman, B., Guerts, B., and Kuerten, H., 1994, ''On the Formulation of the Dynamic Mixed Subgrid Scale Model,'' Phys. Fluids A, **6**, pp. 4057–4059.
[28] Tyagi, M., and Acharya, S., 2004, ''Large Eddy Simulations of Turbulent Flown in Complex and Moving Rigid Geometries With the Immersed Boundary Method,'' Int. J. Numer. Methods Fluids, (to be published).
[29] Tyagi, M., 2003, ''Large Eddy Simulation of Turbulent Flows in Complex Geometries,'' Ph.D. thesis, Mechanical Engineering Department, Louisiana State University.
[30] Wray, A. A., and Hunt, J. C. R., 1989, ''Algorithms for Classification of Turbulent Structures, Topological Fluid Mechanics,'' *Proceedings of the IUTAM symposium*, H. K. Moffat and A. Tsinober, eds., Cambridge University Press, Cambridge, UK, pp. 95–104.
[31] Tanaka, M., and Kida, S., 1993, ''Characterization of Vortex Tubes and Sheets,'' Phys. Fluids A, **5**, pp. 2079–2082.
[32] Dubief, Y., and Delcayre, F., 2000, ''On Coherent-Vortex Identification in Turbulence,'' J. Turbul., **1**, pp. 1–22.
[33] Holmes, P., Lumley, J. L., and Berkooz, G., 1996, *Turbulence, Coherent Structures, Dynamical Systems and Symmetry*, Cambridge University Press,
[34] Sirovich, L., 1987, ''Turbulence and the Dynamics of Coherent Structures, Part I–III,'' Q. Appl. Math., **XLV**, pp. 561–590.

Experimental Investigation of Flow Structure and Nusselt Number in a Low-Speed Linear Blade Passage With and Without Leading-Edge Fillets

G. I. Mahmood
R. Gustafson
S. Acharya

Turbine Innovation and Energy Research (TIER) Center,
Mechanical Engineering Department,
Louisiana State University,
Baton Rouge, LA 70803

The potential of contouring the leading edge of a blade to control the development of the secondary flows in the blade passage and to reduce the thermal loading to the end wall is investigated experimentally. Fillets placed at the junctions of the leading edge and the end wall are used for contouring. Four different types of fillet profiles are tested in a low-speed linear cascade a Reynolds numbers of 233,000 based on the inlet velocity. Images of instantaneous smoke flow patterns show a smaller horseshoe vortex along the leading edge with the fillets. In the passage, the fillets cause the passage vortex to be located closer to the suction surface. Upstream of the throat, the normalized axial vorticity values for the passage vortex and the turbulence intensity levels are smaller with the fillets compared to the baseline. For the leading-edge fillet with a concave profile, the end-wall Nusselt number distributions show significant reductions compared to the baseline.
[DOI: 10.1115/1.1865218]

Introduction

Secondary flows in turbomachinery blade passages are responsible for increased aerodynamic losses, and increased thermal loading on the end wall (EW) as they transport higher temperature gases from the midspan regions to the EW regions. The horseshoe vortex formed at the leading edge, combined with the pressure gradients in the blade/vane passages, lead to a complex passage vortex structure. Flow visualization studies by Goldstein and Spores [1], Langston et al. [2], Sieverding and Bosche [3], and Wang et al. [4] indicate that the pressure-side leg of the horseshoe vortex is a dominant constituent of the passage vortex system. Reducing the size and strength of the passage vortex is expected to contribute to a reduction in the aerodynamic loss, and in reducing the fluid mixing between the core midspan (where the temperature profile peaks) and the near-wall regions. The reduced mixing is expected to decrease the heat transfer to the EW. Various modifications proposed to control the secondary flows include: fillets employed at the junction of the blade leading edge and EW, contoured EW profile, and coolant film injection through shaped holes in the EW.

Several studies have been reported in linear blade cascades for developing the basic understanding of the secondary flow structures and heat transfer in the blade passage. Using the naphthalene sublimation technique, Häring et al. [5] and Goldstein et al. [6] show the effect of laminar-to-turbulent boundary layer transition and the passage vortex system on the heat transfer on the blade-suction surface. Yamamoto [7] compares measured Stanton number and pressure loss, and Hermanson et al. [8] provide numerical comparison of Stanton number between the blade and the vane passages. They observe higher Stanton numbers in the blade passage than in the vane passage because of the larger turning and the influence of the passage vortex in the blade passage. Graziani et al. [9] apply different inlet boundary layer thicknesses and measure the influences of the passage vortex on Stanton numbers and pressure gradients in the blade cascade passage. Other notable studies include Gallus et al. [10], Hah [11], and Gregory-Smith and Cleak [12], who provide in-passage and exit-plane flow structures in the blade cascades.

Studies have also been reported that determine the flow field and heat transfer around airfoils in the presence of fillets placed at the junction of the stagnation region and EW. Davenport et al. [13] find that leading-edge fillets do not prevent the formation of the horseshoe vortex, but increase the distortion of the boundary layer thickness around a wing-body junction. Use of fairings and strakes at the nose of a symmetric wing-body junction to reduce horseshoe vortex structures is proposed by Simpson [14]. Sauer et al. [15] show that the total pressure loss is reduced considerably when the blade leading edge near the EW is modified with a bulb profile. Zess and Thole [16] propose some design parameters for leading-edge fillets and show that an asymmetric elliptical fillet with height and length equal to the incoming boundary layer thickness and twice the incoming boundary layer thickness, respectively, reduces secondary flows, vorticity, and turbulent kinetic energy. Shih and Lin [17] simulate secondary flows and heat transfer in a vane passage with two types of leading-edge fillets and inlet swirl. Their results show reduction of total pressure loss across the passage as well as reduced heat transfer coefficients both on the vane and EW when fillets are employed without inlet swirl. However, they did not evaluate specific mechanisms responsible for the improved pressure losses and heat transfer coefficients due to the fillets. A computational optimization of a fillet profile is performed by Lethander et al. [18] for a vane passage. They conclude that the optimized fillet reduces the intensity of secondary flows by accelerating flows near the EW region. Recent results with leading-edge bulbs and fillet [19,20] in a linear blade cascade show a decrease in the near-wall total pressure loss at the exit plane with the fillet.

The present investigation studies the effects of four different types of fillets on the secondary flow structures and Nusselt numbers in the passage of a low-speed linear blade cascade. The blade profile is two-dimensional and represents the hub-side section of a GE-E^3 first stage blade. Flow visualization, velocity, pressure, and Nusselt number measurements in the passage are made with the fillets, and are then compared with the measured baseline data.

Contributed by the Heat Transfer Division of ASME for publication in the JOURNAL OF HEAT TRANSFER. Manuscript received April 7, 2004; revision received November 12, 2004. Review conducted by: P. M. Ligrani.

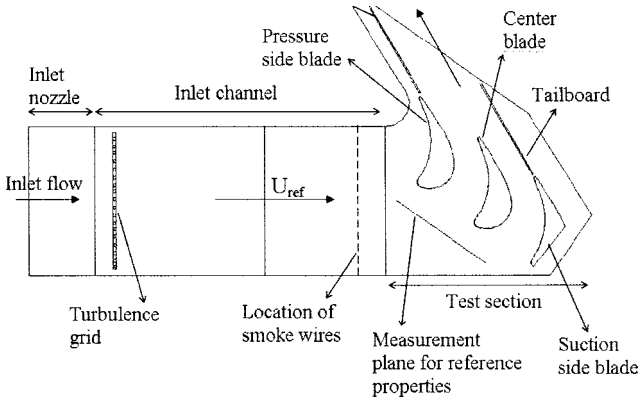

Fig. 1 Schematic of the experimental test facility

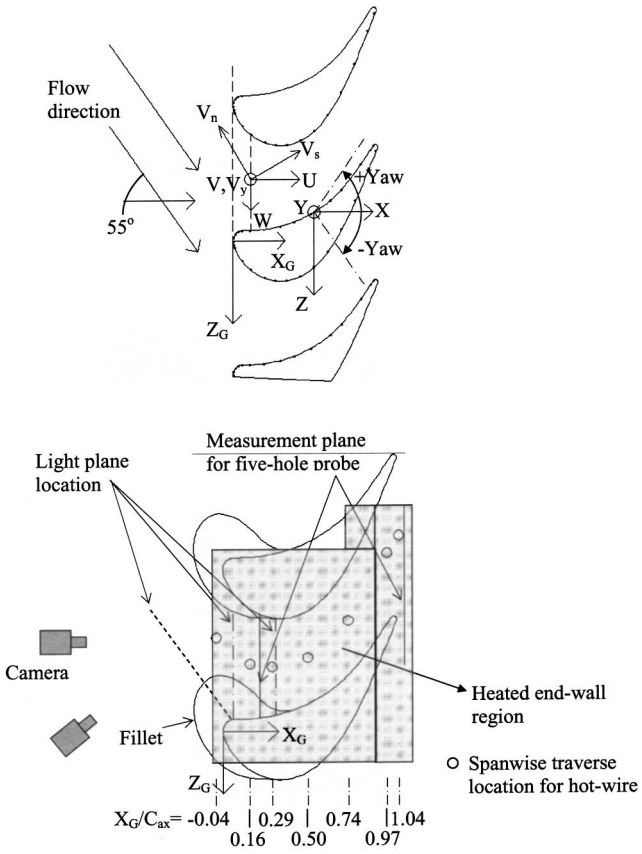

Fig. 2 Coordinate system and measurement locations employed in the test section

This is the first experimental study in which the effects of different fillet profiles on the EW heat transfer have been studied.

Experimental Setup and Techniques

1 Linear Cascade Facility. Measurements are made in a low-speed wind tunnel shown schematically in Fig. 1. The wind tunnel houses a linear cascade test section accommodating three two-dimensional GE-E^3 blades [21] that form two blade passages. The facility operates in an open-circuit suction mode with a 3.73 kW duct fan blower drawing in air from the laboratory. The ambient air enters the inlet channel of aspect ratio 1.36:1 through a two-dimensional nozzle of contraction ratio 3.4:1, and then flows through the test section. The height of the channel is the same as the blade span and thus allows no clearance between the blade tip and the EW. The four walls of the inlet channel and the two side walls of the test section have cut out slots that allow bleed suction of the boundary layer as well as control of the stagnation line on the blade leading edge. The tailboards, pivoted at the trailing edges of the two side blades in the test section, are adjustable with external lead-screws. The tailboard adjustments enable equal mass flow rate in the two passages. A passive turbulence grid made of cylindrical rods of diameter 12.20 mm is positioned in the channel just downstream of the nozzle and 4.2C upstream of the center blade. The removable top EW of the test section has either machined slots for automated traverse of five-hole and hot-wire anemometer probes or window sections with zinc selenide windows for infrared camera measurements of the EW and blade temperatures. The unused slots and holes are either masked with tape or filled in with foam weather strips to prevent any air leakage from outside.

Figure 2 shows the coordinate systems and slot positions employed in the measurements. (X_G, Z_G) coordinates refer to the global coordinate system originated at the farthest upstream position on the center blade. The local coordinates (X, Y, Z) originate on the pressure side of the center blade and are parallel to the global coordinate system. The velocity components (U, V, W) are parallel to (X, Y, Z), while (V_s, V_n, V_y) are components of the streamline velocity vector.

The blade coordinates and passage dimensions are based on the hub-side section of the high-pressure first stage GE-E^3 blade and on the annular passage geometry for the E^3 engine [21]. The cascade configurations employed for the measurements are scaled up ten times the actual geometry, and are provided in Table 1. A flow speed of 10.26 m/s is employed during the flow and heat transfer measurements. Reynolds numbers in Table 1 are based on the actual blade chord length and inlet streamwise velocity. The blades are oriented at a zero-degree angle of attack to the flow. As shown in Fig. 1, a portion of the suction side of the outer blade is removed to widen the gap between the suction surface of this blade and the side wall, and therefore the air flows freely on both sides of the outer blade without any significant flow blockage or any reverse flow. The blade profile has machined slots along the span that accommodate 1.65-mm-diameter steel tubes fitted with 0.30-mm-diameter pressure tap holes. The bottom EW surface of the test section and the center blade are instrumented with thermocouples and Kapton™ encapsulated foil heaters. Figure 2 shows the EW surface area covered by the heater. The flow side of the heater is covered with 0.10 mm thick copper foil. The copper surface is painted flat black for maximum emissivity during the infrared thermal imaging. Thermocouples are positioned at select locations below the heater surface, and are attached to the heater surfaces with double sided tape. The heater-thermocouple assembly is firmly glued to the bottom surface of the test section, and the pressure exerted by the blade weight and the top EW provides intimate contact between the heater element, the thermocouple and the bottom end wall.

2 Fillet Profiles and Fabrication. Measurements are obtained with four different leading-edge fillets. All the fillets are manufactured using a three-dimensional stereo lithography sys-

Table 1 Cascade test section parameters

Actual chord length C (cm)	35.86
Axial chord length C_{ax} (cm)	30.36
Aspect ratio (true chord length to blade span) C/S	0.78
Solidity ratio (true chord length to blade pitch) C/P	1.23
Stagnation temperature $T_{o,in}$ (K)	302
Stagnation pressure $P_{o,in}$ (Pa)	1.013×10^5
Flow inlet angle (degrees)	0
Average streamwise velocity upstream U_{ref} (m/s)	10.26
Inlet Reynolds number Re_{in}	233,000
Upstream streamwise turbulence intensity	4.0%

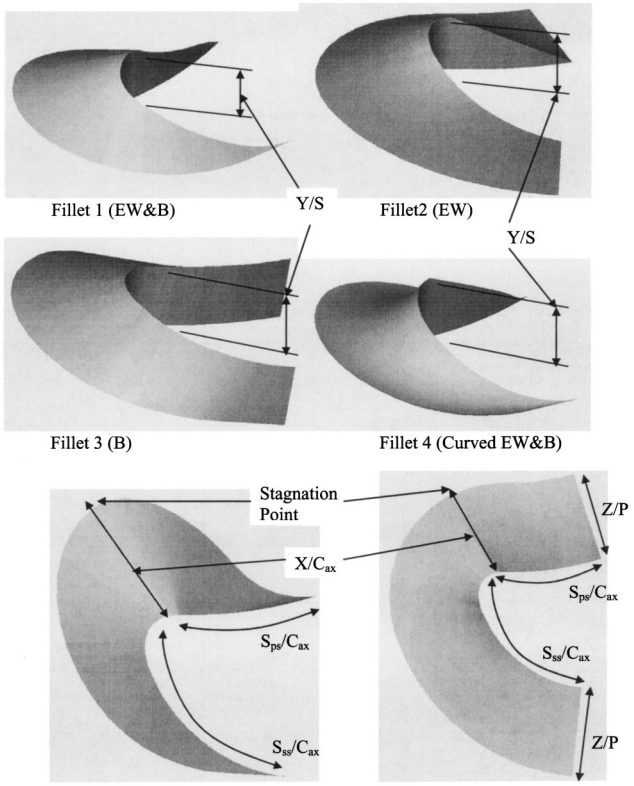

Fig. 3 Profile geometry and shape of the four types of fillets

tem. The profiles of the fillets are selected based on the work reported in [15–18]. The fillets are attached to the junction of the blade leading edge and the bottom end wall. No fillets are employed at the junction of the top wall and blade leading edge. The profile geometry and the shape of the fillets employed in the present experiments are shown in Fig. 3 and Table 2. The highest point of the fillet is located on the stagnation line of the blade (B) and has the same height as the boundary layer thickness of the incoming flow. As shown in Fig. 3, the edge along the outer periphery of the bottom section of the fillet is elliptical, and extends more on the blade-suction side than on the pressure side making the profile asymmetric. Thus, the profile of the ellipse is different on either side of the stagnation line, but both profiles have the same curvature where they meet along the plane extending from the stagnation line (at zero-degree angle of attack). The surface profile of fillets 1(EW&B), 2(EW), and 3(B) varies linearly in the direction normal to the blade surface, whereas the profile height of the fourth fillet (curved EW&B) is defined on a concave circular arc in a direction normal to the blade surface. The notation used to represent the fillets describes how the fillets are blended to the end-wall or blade surface. Thus, fillet 1 (EW&B) blends simultaneously toward the end wall and the blade, fillet 2 (EW) blends to the end wall only, fillet 3 (B) blends to the blade only, and fillet 4 (curved EW&B) again blends both to the end wall and the blade.

3 Flow Visualization. Smoke is used to obtain the instantaneous qualitative flow structure in the blade passage. The smoke in the channel is generated by applying coats of toy train liquid smoke on smoke wires (diameter 0.051 cm), which are then heated by passing controlled dc current through them. Nine wires are located about $1.5C$ upstream of the center blade stagnation line and span across the width of the inlet channel, as shown in Fig. 1. When air flows through the channel, plane sheets of white smoke are generated from the wires that are placed both inside and outside the boundary layer upstream of the blade passage. As the sheets of smoke approach the passage, they are convoluted according to the shape and size of the secondary flows. A plane sheet of light generated with a 1000 W theatrical lamp illuminates the smoke patterns inside the passage. The channel walls are made of acrylic and are transparent to the light and the camera sensor. A trip wire of diameter 1.30 mm is placed on the bottom wall $4.7C$ upstream of the center blade to trip the boundary layer.

The flow visualization pictures are recorded using a SONY DFW-V500 digital video camera, and image capturing software provided by the camera manufacturer, at a frame rate of 33 Hz with 640×480 lines of resolution. Instantaneous images of the recorded movie are then captured with the commercial software Ulead VideoStudio™ 4.0SE Basic and further enhanced in Adobe Photoshop™ v8.10. The relative positions of the camera and light plane where the smoke flow pattern is illuminated are shown in Fig. 2. The relative position of the camera changes with the location of the light plane since the camera is focused approximately normal to the light planes. However, the camera position remains the same when images are captured in a plane for the baseline (without fillet) case and the four filleted cases. The images are obtained for an inlet bulk flow velocity of 0.80 m/s, which provides a Reynolds number of 18,200.

4 Flow Structure Measurement. Flow structure is measured with a subminiature five-hole pressure probe of tip diameter 1.30 mm and a two-wire constant temperature (or hot-wire) anemometer. The five-hole pressure probe is calibrated in the inlet channel of the test facility for yaw and pitch angles between $+30°$ and $-30°$ at a streamwise velocity of 10.26 m/s. The detail construction and calibration of the five-hole pressure probe is provided in Ligrani et al. [22,23]. Pressure signals from the tubes of the five-hole probe are obtained in a HP3497A data acquisition control unit through Omega differential transducers. The converted voltage signals from the data acquisition unit are finally processed in a Dell Dimension 2100 desktop PC. The calibration curves for the transducers and five-hole probe are applied to the voltage signals to deduce the local total pressure, static pressure, and velocity components of the flow. The pressure and velocity are determined after spatial resolution and downwash corrections [23] because of the finite tip diameter of the probe. The sensors, calibration stand, signal conditioners, data acquisition unit, and data processing software for the hot-wire anemometer are all purchased through TSI. Both the five-hole and hot-wire probes are traversed in a plane through the top-wall slots shown in Fig. 2

Table 2 Fillet parameters

Fillet name	Description	$(Y/S)_{\max}$	$(X/C_{ax})_{\max}$	s_{ss}/C_{ax}	s_{ps}/C_{ax}
Fillet 1 (EW&B)	Blends into the end wall and blade wall with a linear profile	0.10	0.299	0.566	0.322
Fillet 2 (EW)	Blends into the end wall only with a linear profile	0.10	0.299	0.566	0.322
Fillet 3 (B)	Blends into the blade wall with linear profile	0.10	0.299	0.566	0.322
Fillet 4 (Curved EW&B)	Blends into the end wall and blade wall with a curved profile	0.10	0.299	0.566	0.322

with the Unislide two-axis motorized traverse and Velmex Inc. stepper motor controller. The sampling rate at which data is acquired and time averaged is 20 Hz over a 40 s period for the five-hole probe, and 5 kHz over 1.60 s for the hot-wire anemometer. Static pressure on the blade profile is measured with the pressure tap fitted steel tubes located in the grooves on the blade profile. The tubes are mounted flush with the blade profile and do not obstruct the flow. Rubber tubes connect the steel tubes to a Validyne differential transducer which, in turn, is connected to a HP3497A data acquisition unit controlled by a Dell desktop PC.

The probe is traversed in the pitch direction at each span location starting from the bottom EW to the midspan at $X_G/C_{ax}=0.16$ and $X_G/C_{ax}=1.04$. The nearest data location in the spanwise direction is 4.0 mm above the EW; any closer position of the probe tip to the EW influences the flow structure in the gap between the probe body and the EW. For the same reason, data measurements very near to the blade surface are avoided. The probe tip is oriented along the average inviscid streamwise direction between the blades to minimize the yaw-pitch angle corrections.

5 Heat Transfer Measurement. Thermocouple and infrared signature of the heated EW provide the temperature measurements. The blades are not heated and the blade surfaces can be considered to be adiabatic. The leading-edge fillets are not instrumented with the heater and thermocouples, and thus no temperature data are measured on the fillet surface. The foil heaters on the EW provide a constant heat flux boundary condition in the test section, while the outside of the EWs are insulated with plywood. As shown in Fig. 2, heating of the bottom EW surface starts at $0.063C_{ax}$ upstream of the blade passages. Infrared images are obtained with a Raytheon Radiance HS 2012 model camera at a frame rate of 33.3 Hz. The camera views the bottom EW through a zinc-selenide window located on the channel top wall. Seven such window locations on the top wall are used and provide the coverage needed to image most of the EW between the center blade and the pressure-side blade. Images from the camera are transferred to a desktop PC through an image grabbing PCI board and ImageDesk™ v.2.1 software over a 5 s period. The recorded images are in a gray-scale form with 12 bit/pixel and 256×256 pixel resolution. The dimension of each imaged field of view is about 14 cm by 14 cm, and the corresponding pixel resolution is 0.5 mm by 0.5 mm. The pixel gray-scale values in the time-averaged image are then converted to local Nusselt numbers by applying the in situ calibration, and an energy balance that accounts for heat losses through the bottom wall. The in situ calibration procedure uses the measured thermocouple temperatures logged in with a HP3497A data acquisition unit. The spatial locations of the pixels are calibrated using the predefined coordinates of thermocouple in an image field. Temperature measurements with the thermocouples and the infrared images at the same position of the camera are then obtained simultaneously. Pixel gray-scale values at the thermocouple locations and thermocouple temperatures then provide a calibration of the infrared images. In each time-averaged image, corresponding to a top-wall window position, 8 to 12 calibration data points are available. Sargent et al. [24] and Mahmood et al. [25] provide additional details on infrared thermography and in situ calibration technique. The Nusselt number data in an image field are combined with the Nusselt numbers in the adjacent image field to provide the surface distribution of Nusselt numbers in the blade passage. Nu data in the overlapping region of the adjacent image fields are averaged while combining two such image fields. All the measurements are obtained when the test section reaches steady state and temperature varies within $\pm0.1°$C.

The Nusselt number is determined from the following equations with the blade actual chord as the length scale and passage inlet average temperature as the reference temperature.

Table 3 Upstream boundary and reference properties

Average upstream reference velocity U_{ref} (m/s)	10.26
Average reference static pressure (below atmospheric) $P_{stat,0}$ (Pa, gage)	121.9
Average reference total pressure (below atmospheric) $P_{tot,0}$ (Pa, gage)	60.5
Boundary layer thickness δ (mm)	46.0
Displacement thickness $\delta1$ (mm)	8.4
Momentum thickness $\delta2$ (mm)	6.6

$$\mathrm{Nu}=\frac{q''_{conv}C}{(T_{wall}-T_{in})k_{air}} \tag{1}$$

$$q''_{conv}=(VI-Q_{cond})/A_{heater} \tag{2}$$

The air properties are measured at the reference inlet temperature. Wall temperature T_{wall} is obtained from the thermocouples and calibrated pixel gray-scale values in the infrared image field. The convective wall flux in Eq. (1) is determined after subtracting conduction heat loss from the total power input to the foil heater. Voltage and current measurements in Eq. (2) provide the total power supplied to the heater. The conduction loss Q_{cond} in the EW region is measured based on one-dimensional conduction through the EW acrylic surface. To measure the conduction heat loss, the EW heater surface is covered with three layers of thermocouple-embedded Styrofoam™ insulation. The heater is then powered up with no air flow inside the channel. When the heater temperature reaches steady state, the heat loss through the Styrofoam™ insulation measured from the temperature differences between the insulation layers is subtracted from the total power input in the heater. The energy balance then determines the conduction loss through the acrylic EW and plywood insulation layer outside to the atmosphere. Since this conduction loss is de-

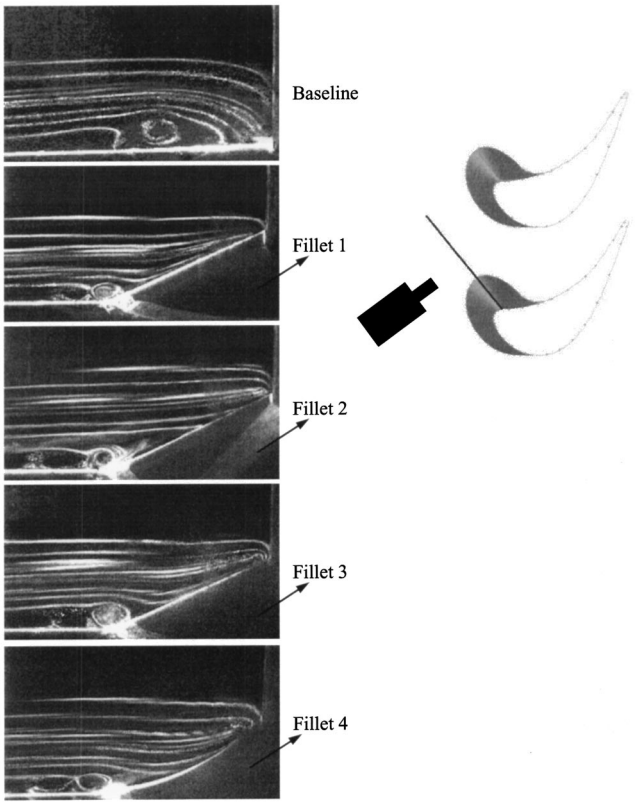

Fig. 4 Flow visualization images of secondary flows in the stagnation-line plane with and without fillets

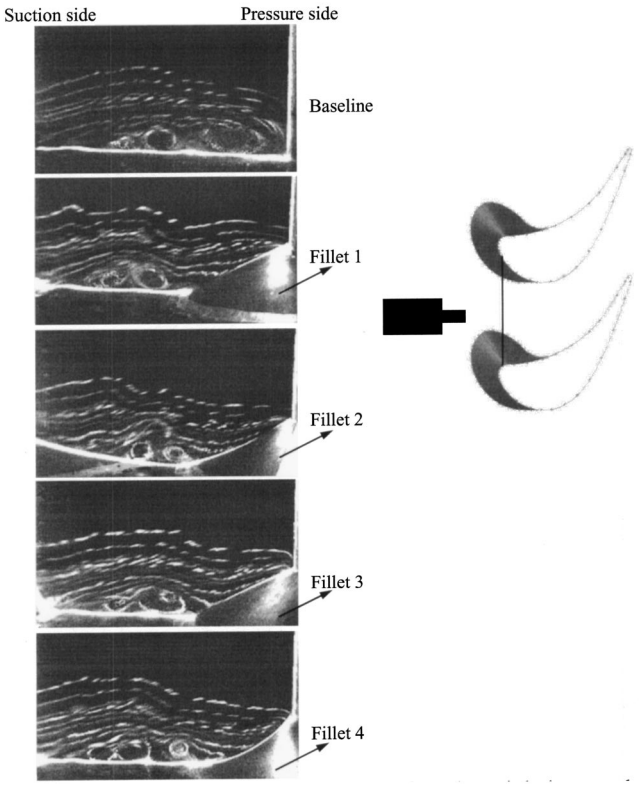

Fig. 5 Flow visualization images of secondary flows in a pitchwise normal plane at $X_G/C_{ax}=0.05$ with and without fillets

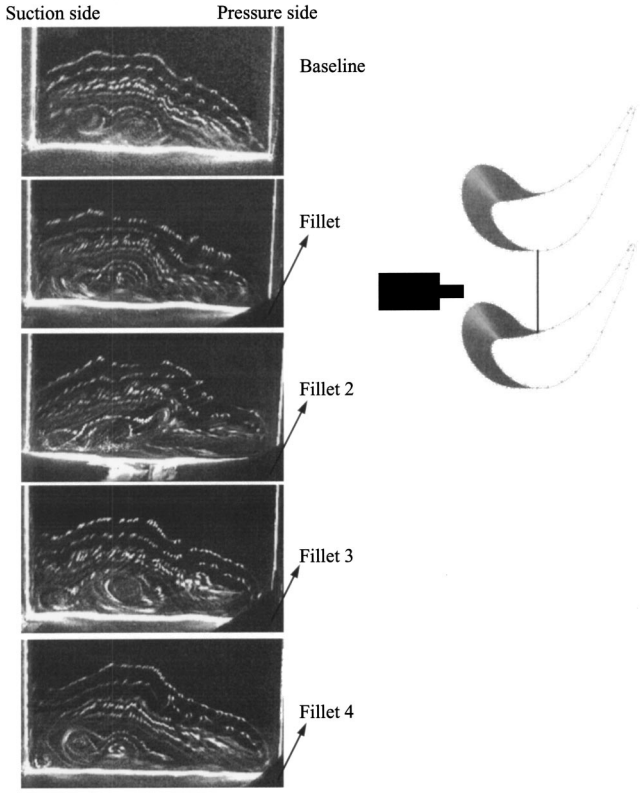

Fig. 6 Flow visualization images of secondary flows in a pitchwise normal plane at $X_G/C_{ax}=0.285$ with and without fillets

pendent upon the temperature difference between the heater and outside atmosphere, the above-mentioned energy balance is performed for different heater temperatures on the end-wall. The functional dependence of the conduction loss on the temperature difference between the heater and ambient air then provides a measure of conduction loss during the Nu measurements. The conduction heat loss from the EW during Nu measurements is generally within 3.0% of the total heater power. The blades are made of solid wood and any conduction loss through the blade material is neglected. Radiation loss to the surrounding is assumed to be negligible as the wall temperature varies between 35 and 55°C, and hence, is not accounted for in the Nu computation.

6 Uncertainty Estimates. Uncertainties in the measured data are estimated according to the methods in Holman [26] and Moffat [27], and presented here based on a 95% confidence level. Uncertainty in the total pressure near the EW is 3.0% and away from the EW in the inviscid flow region is 6.0%. Static pressure

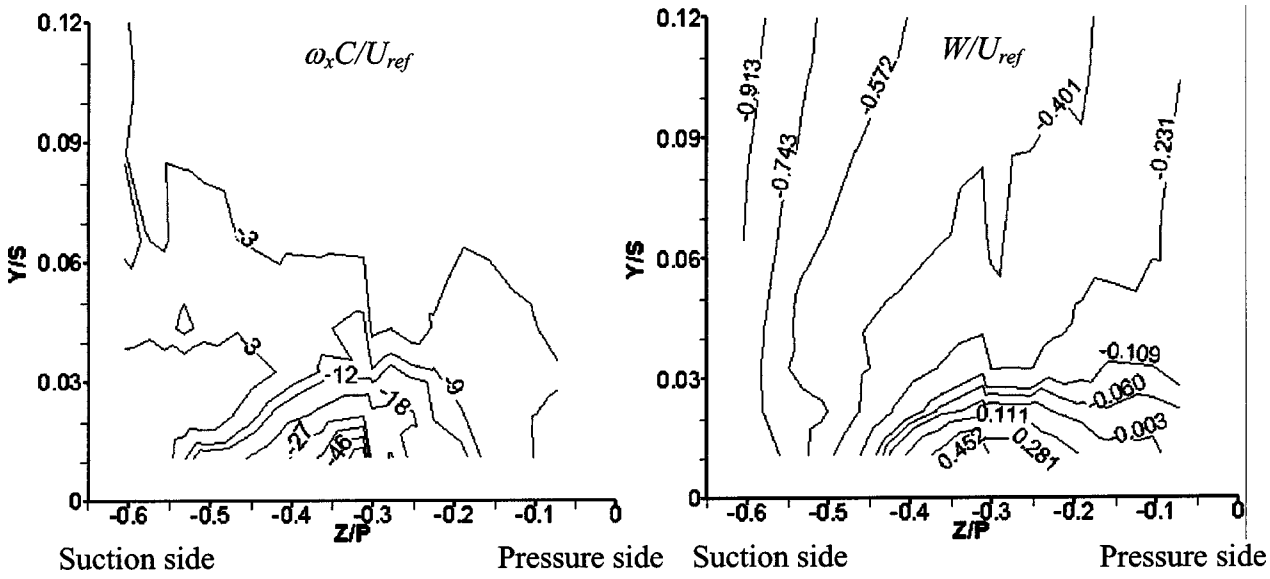

Fig. 7 Normalized axial vorticity $\omega_x C/U_{ref}$ and pitchwise velocity W/U_{ref} in a pitchwise normal plane at $X_G/C_{ax}=0.215$ for the baseline

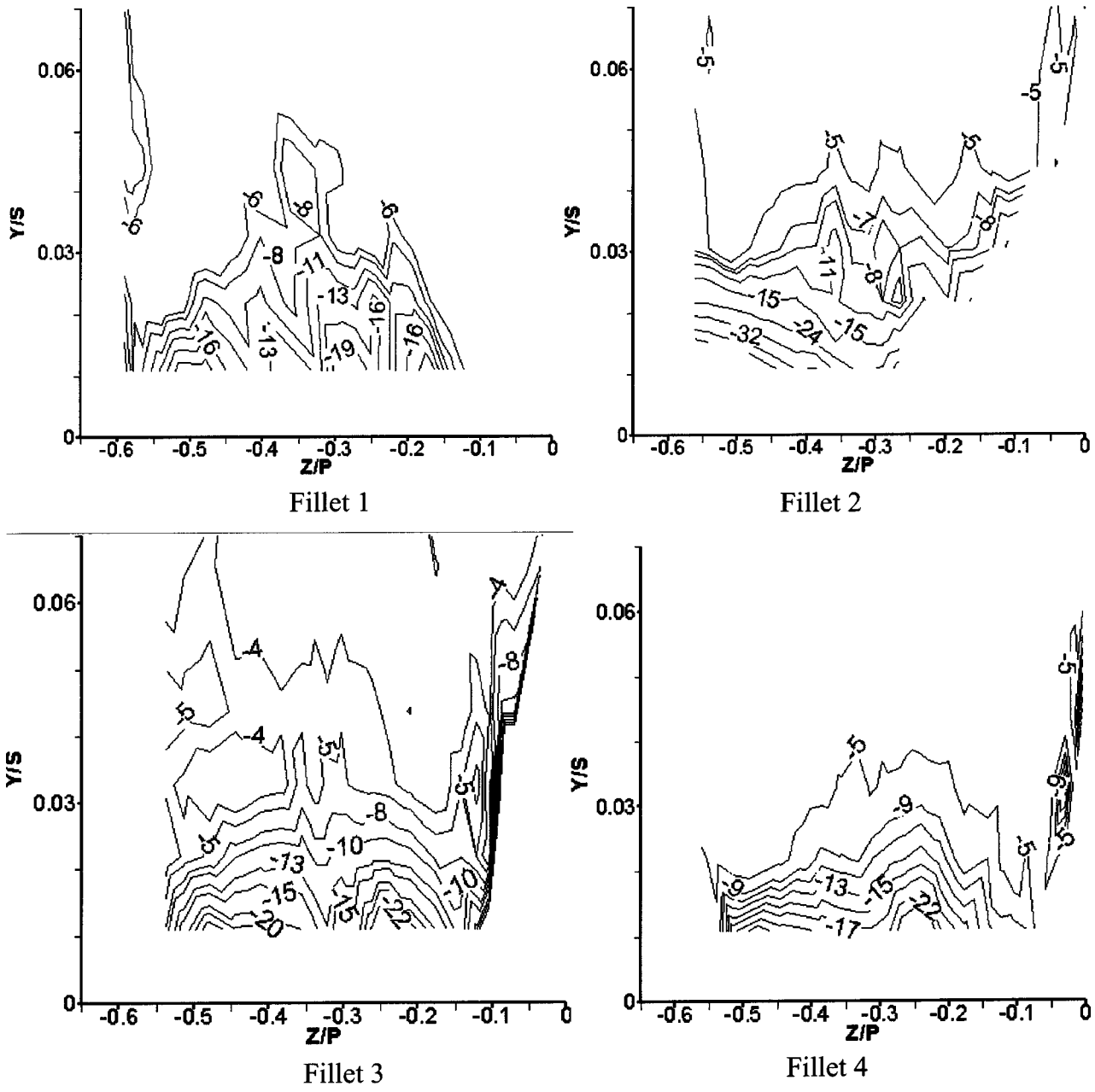

Fig. 8 Normalized axial vorticity component $\omega_x C/U_{ref}$ in a pitchwise normal plane at $X_G/C_{ax}=0.215$ with fillets

has uncertainties of 4.0% and 7.0% near the trailing edge and leading edge, respectively. Streamwise velocity varies approximately within ± 0.40 and ± 0.20 m/s near the EW and in the inviscid region, respectively. The corresponding uncertainties are 10.0% and 5.0%. The maximum uncertainties in the thermocouple temperature and heat flux are 0.75% and 6.5%, respectively. The uncertainty in pinpointing the thermocouple location during the in situ calibration contributes the most in the uncertainty of EW Nusselt numbers. EW Nu uncertainties near the inlet and passage throat area are 6.9% and 6.3%, respectively.

Experimental Results and Discussions

The upstream boundary conditions and the reference quantities used to normalize the data are presented in Table 3. The upstream data are measured in a plane located 100 mm upstream of the inlet plane of the blade passage. Both the hot-wire anemometer and the five-hole pressure probe are used to measure the upstream conditions, and the mean velocities with the two measurement techniques agree quite well with each other. Reference quantities in Table 3 are the ensemble averages of the data measured in this plane. Since the cascade operates in a suction mode, the pressures measured are below atmospheric pressure. The boundary layer properties in the table are estimated by numerically integrating the measured velocity data using the MATLAB function "trapz.m."

1 Instantaneous Secondary Flow Structures. Instantaneous images from smoke flow visualization are obtained in three planes: the stagnation-line plane (the plane parallel to the zero-degree angle of attack and going through the center blade stagnation line) and two parallel planes inside the passage between the center blade and the pressure-side blade. The planes inside the passage are parallel to the inlet plane and located at the axial distances $X_G/C_{ax}=0.05$ and 0.285. Figures 4 to 6 present snapshot images of secondary flow patterns in these three planes for the baseline case, and when the leading edge are contoured with the fillets. The locations of the light plane and the camera view are also shown in the figures.

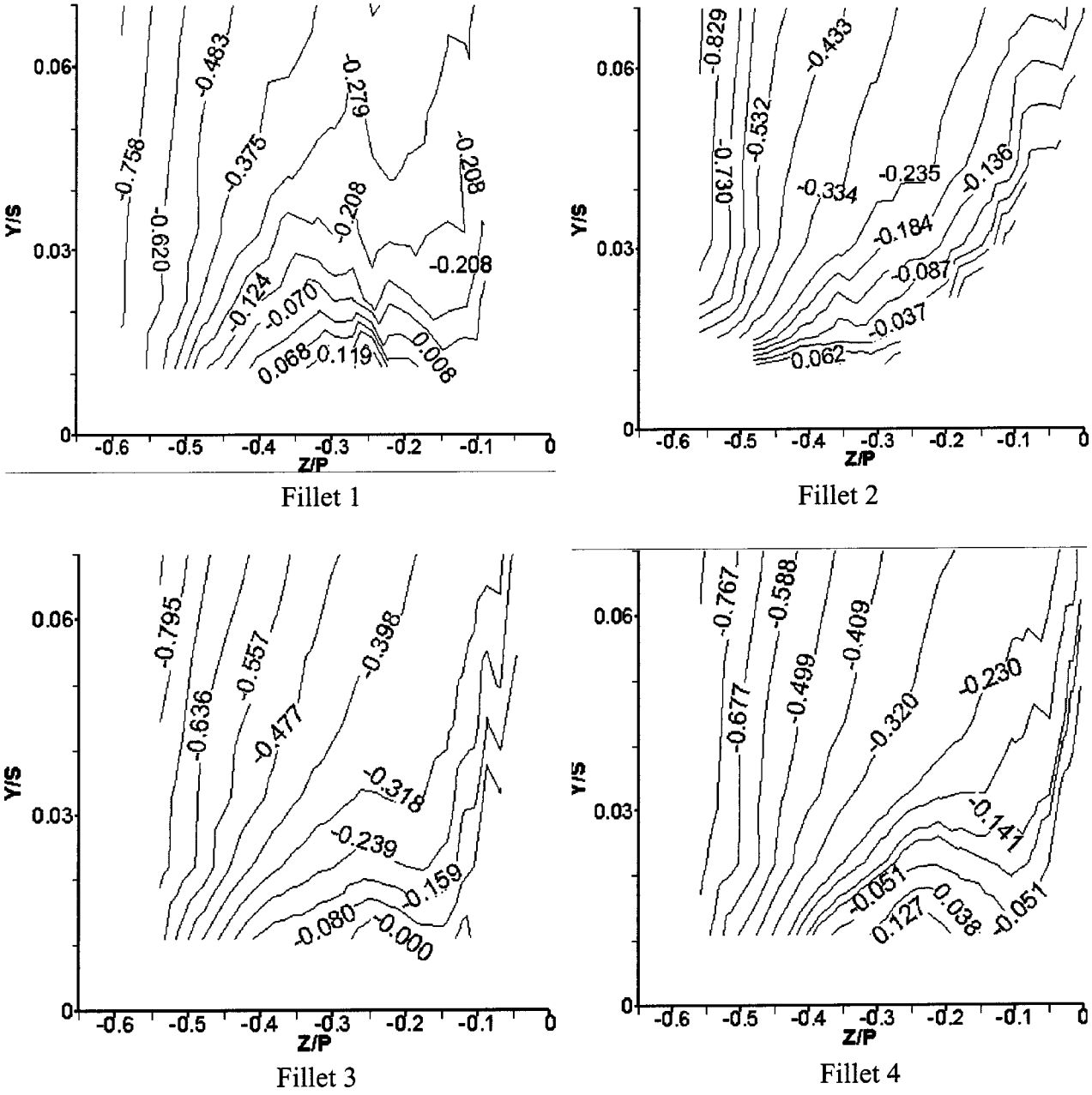

Fig. 9 Normalized pitchwise velocity component W/U_{ref} in a pitchwise normal plane at $X_G/C_{ax}=0.215$ with fillets

In Fig. 4, all the images show a clear structure of the horseshoe vortex. The horizontal bright white line at the bottom of each image is the location of the EW and the wedge-shaped object is the fillet location. The top horizontal smoke line in the images is located about 55 mm above the EW. When the sizes of the horseshoe vortex patterns in Fig. 4 are compared, it is clearly evident that the vortex patterns are smaller for the fillets than for the baseline. As the boundary layer moves up the fillet surface along the stagnation-line plane, the flow area in the blade-span direction is reduced leading to the boundary layer fluid being displaced away from the stagnation-line plane to maintain mass conservation. Therefore, the reduction in the size of the horseshoe vortex can be considered to be a consequence of the displacement of the boundary layer fluid away from the stagnation location. Further, the fillets introduce a pressure gradient in the direction from the fillet leading edge to the blade leading edge, which is counter to the adverse pressure gradient on the blade/fillet leading edge that drives the horseshoe vortex. Thus, the presence of the fillet reduces the size of horseshoe vortex in the leading-edge region. In addition, immediately behind the visible horseshoe vortex in the images of Fig. 4, smoke traces indicating the development of a secondary vortex is visible. The apparent shape and size of this second structure is about the same as the primary horseshoe vortex shape and size. The two structures merge into one periodically, as has also been shown in [4]. The primary vortex structure for the baseline unfilleted case is at least twice the size observed for the filleted cases.

Figure 5 presents the instantaneous structures of the pressure-side leg of the horseshoe vortices in the pitchwise Y-Z plane at $X_G/C_{ax}=0.05$. The pressure side of the passage is located on the right side of each image, and its outline along with that of the EW can be seen in the images. A pair of distinct vortex roll-up in the clockwise rotation is visible for all cases. Due to the pitchwise displacement of the flow by the fillets, the location of the vortex pair is farther from the pressure side for the filleted cases compared to the baseline. The location of these vortex structures also

depends on the strength of the crossflow near the EW since the crossflow from the pressure to suction side sweeps the structures towards the suction side. The right-side vortex of the pair represents the primary horseshoe vortex in the stagnation-line plane. In general, the size of this primary pressure-side vortex is smaller for the filleted cases (consistent with the size of the structures in the stagnation-line plane) compared to the baseline. Fillets 1, 2, and 4, where the fillets blend into the EW, show a smaller structure than fillet 3, where the fillet blends only to the blade. The second vortex on the left of the pair is also smaller for the filleted cases. As noted earlier, the vortex structures do exhibit some periodic unsteadiness, with the two vortex structures periodically merging into a single structure. This is also observed in the pair of pressure-side vortices in Fig. 5.

Figure 6 presents flow visualization images in the pitchwise plane at $X_G/C_{ax}=0.285$. The main flow direction is into the plane of the images, and the right and left edges of the images correspond to the pressure and suction sides of the passage, respectively. The full passage is shown, and the surfaces corresponding to the pressure and suction sides can be seen in the images. As the location of the image plane is further downstream, the passage vortices are now located closer to the suction side, driven there by the crossflow pressure gradients from the pressure side to the suction side. While there are essential differences in the vortex structures for the various cases, at this axial location, the size of the structures appear to be comparable. However, the locations of the passage vortices appear to be nearer to the suction side for the filleted cases than for the baseline.

From the images shown in Figs. 4–6, it would appear that the fillets reduce the size of the passage vortex structures near the leading edge, and upstream of the throat. However, downstream of $X_G/C_{ax}=0.285$, the passage vortex structures appear to have grown to comparable sizes, and the main role of the fillets, from the smoke visualization, appears to be a shift of the structures toward the suction surface. It should be noted that these flow visualizations are done at lower Reynolds numbers than those of the five-hole probe and heat transfer measurements, and therefore provide only a qualitative measure of the effects of the fillets.

2 Time-Averaged Secondary Flow Structures. Time-averaged flow structures are measured at an inlet velocity of 10.26 m/s using a five-hole probe and a hot-wire anemometer. This section presents measurements of axial vorticity, mean pitchwise velocity, total pressure loss coefficients, streamwise turbulence intensity, and streamwise velocity. Figure 7 presents normalized axial vorticity and pitchwise velocity near the EW region in a pitchwise normal plane (Y-Z plane) at $X_G/C_{ax}=0.215$ for the baseline. These measurements are derived from the five-hole probe data. Location $Z/P=0.0$ (right side of the plot) corresponds to the pressure side, while the left side of the plot corresponds to the suction side of the passage at that location. Vorticity ω_x is computed from the velocity components W and V in this plane. The magnitudes of the normalized vorticity just above the EW region are high because of the passage vortex (primarily the pressure side leg of the horseshoe vortex). The negative W/U_{ref} magnitudes in Fig. 7 correspond to the cross flow from the pressure to the suction side. It is clearly seen that just above the EW these magnitudes are positive indicating a reverse flow region because of the passage vortex.

Figures 8 and 9 show the normalized axial vorticity and pitchwise velocity for the filleted cases at the same locations as in Fig. 7. The locations $Z/P=0.0$ and -0.65 again correspond to the pressure and suction sides, respectively. No data are presented near the junction of the blade and EW because of the presence of fillet profiles. When $\omega_x C/U_{ref}$ magnitudes near the EW in the region $-0.45<Z/P<-0.15$ and $Y/S<0.03$ are compared, the baseline values vary between -9 and -50, while the data for filleted cases generally vary between -8 and -27. Thus, the fillets weaken the passage vortex structure at this location. Comparing the various fillet cases with each other, it can be seen that

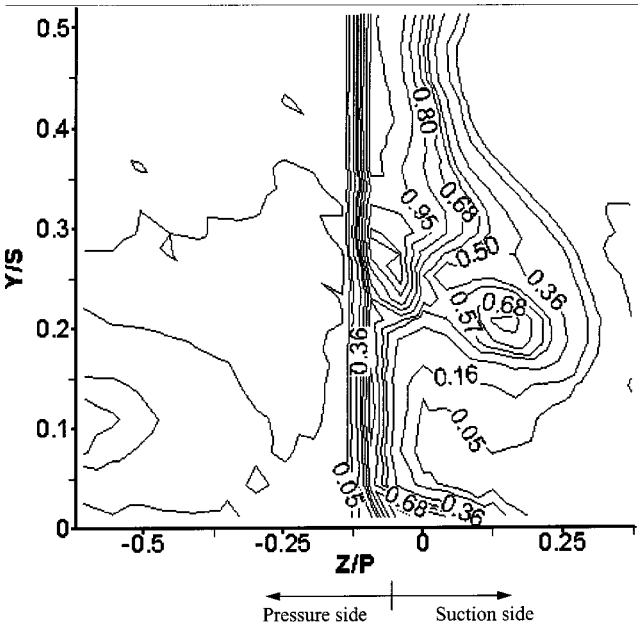

Fig. 10 Total pressure loss coefficient $C_{pt,loss}$ in a pitchwise normal plane at $X_G/C_{ax}=1.071$ for the baseline

the magnitudes for fillet 2 are slightly higher than for other fillets. With fillets 1, 3, and 4, the peak vorticity magnitude exhibits a reduction of nearly 50% over the baseline case.

The magnitudes of the pitchwise cross flow W/U_{ref} for the fillets in Fig. 9 are different from those for the baseline, especially near the EW between $Y/S=0.0$ to 0.03, and confirm the observations made in the vorticity plots in Fig. 8. In this region, the reverse flow region (with $W/U_{ref}>0.0$ near the EW) is smaller with the fillets than for the baseline, again indicating a weaker and smaller passage vortex structure with the fillets. The crossflow velocities from the pressure side to the suction side, with $W/U_{ref}<0.0$ in the near-wall region ($Y/S<0.03$), have higher magnitudes for the filleted cases than for the baseline (close to the pressure side). This is a consequence of the physical deflection of the flow by the fillets on the pressure side. These negative magnitudes are particularly the highest for fillet 3 followed by fillet 4, among all the configurations.

Figures 10 and 11 present total pressure loss coefficients for the baseline and filleted cases, respectively, in the pitchwise normal plane at $X_G/C_{ax}=1.071$, which is located just downstream of the exit plane of the blade passage. The loss coefficient is computed from the five-hole probe total pressure measurements using the following equation:

$$C_{pt,loss}=\frac{P_{\text{tot},0}-P_{\text{tot}}}{0.5\rho U_{ref}^2} \tag{3}$$

In Fig. 10, the high magnitude of the loss coefficients in the suction-side region between $Z/P=0.05$ to 0.25 and $Y/S=0.15$ to 0.30 is associated with the passage vortex. According to Wang et al. [4], the passage vortex, which is dominated by the clockwise-rotating horseshoe leg on the pressure side, is strengthened by the crossflow and the incoming boundary layer, and lifts away from the EW somewhere in the middle of the passage. Figure 11 shows that the center location of the passage vortex (identified by the eye of the contours associated with the passage vortex) for the filleted cases is about $0.02S$ to $0.025S$ (or 9.0 to 11.0 mm) above the center location for the baseline passage vortex. The stronger end-wall cross-flow in the passage with the fillets (see Figs. 7 and 9) lifts the passage vortex higher than the location of the baseline passage vortex. Except for fillet 1, no reduction in the pressure loss coefficient is seen with the fillets at this location.

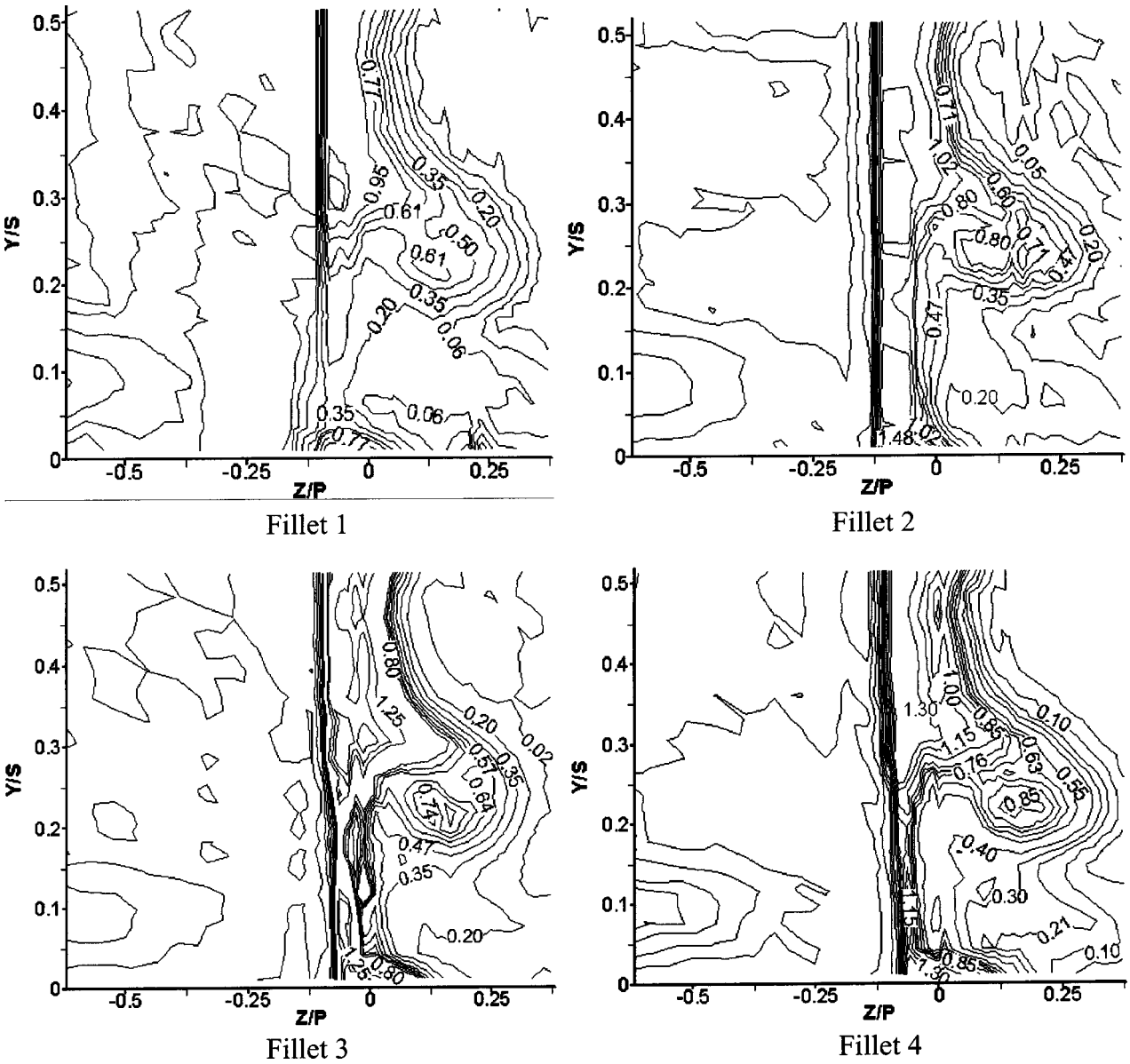

Fig. 11 Total pressure loss coefficient $C_{pt,loss}$ in a pitchwise normal plane at $X_G/C_{ax}=1.071$ with the fillets

Rather, for fillets 3 and 4, they are higher, presumably a consequence of the stronger pitchwise velocity (W/U_{ref}) near the fillets on the pressure side observed for these two cases (see Fig. 9). Note also in Figs. 10 and 11, the loss contour magnitudes are very high in the small region between $Z/P=-0.06$ and 0.06, and below $Y/S=0.04$. This is the EW-blade junction region immediately downstream of the blade trailing edge. The corner vortices are responsible for the high contour values in this region.

The effects of the crossflow with the fillets are further evident in the streamwise turbulence intensity and streamwise normalized velocity distributions in Figs. 12 and 13, respectively. The data in the figures are presented along the pitchwise line located at the middle of the passage at different axial locations. In Fig. 12, turbulence intensity values from $Y/S=0.0$ to 0.10 and from $X_G/C_{ax}=0.16$ to 0.50 are high in general because of the boundary layer and passage vortex system. The high values then lifts up to the locations between $Y/S=0.08$ and $Y/S=0.17$ further downstream at $X_G/C_{ax}=0.97$ as the passage vortex system lifts away from the EW region. It can also be seen that in these high turbulence intensity regions, the values are higher for the baseline than for the fillets. This indicates a more turbulent boundary layer for the baseline case than for the filleted cases, for which, as indicated by Kang and Thole [28], the EW region flow deviates less from the direction of midspan streamlines, resulting in smaller pitchwise velocity. This is consistent with the weaker crossflows in the EW regions with the fillets than for the baseline (as seen earlier in Figs. 7 and 9). The lower turbulence intensity for the filleted cases is likely to have a beneficial impact on the EW heat transfer.

Figure 13 shows the streamwise velocity distribution at two axial chord locations ($X_G/C_{ax}=0.29$ and 0.50). Boundary layer effects appear to extend up to 10%–15% of the blade span. No significant effects of the fillets are seen since these effects are primarily confined to the EW region, and influence the secondary flows to a greater extent.

Figure 14 shows the static pressure coefficient distributions along the blade surface with and without fillets at the spanwise location $Y/S=0.33$. The C_p coefficients are determined from the difference of measured reference static pressure and surface static pressure normalized by the reference dynamic head. The blade surface coordinate $s/C=0.0$ is located at the suction-side trailing edge. As shown, the C_p distributions are the same with and without the fillets. This illustrates the fact that the pressure distribu-

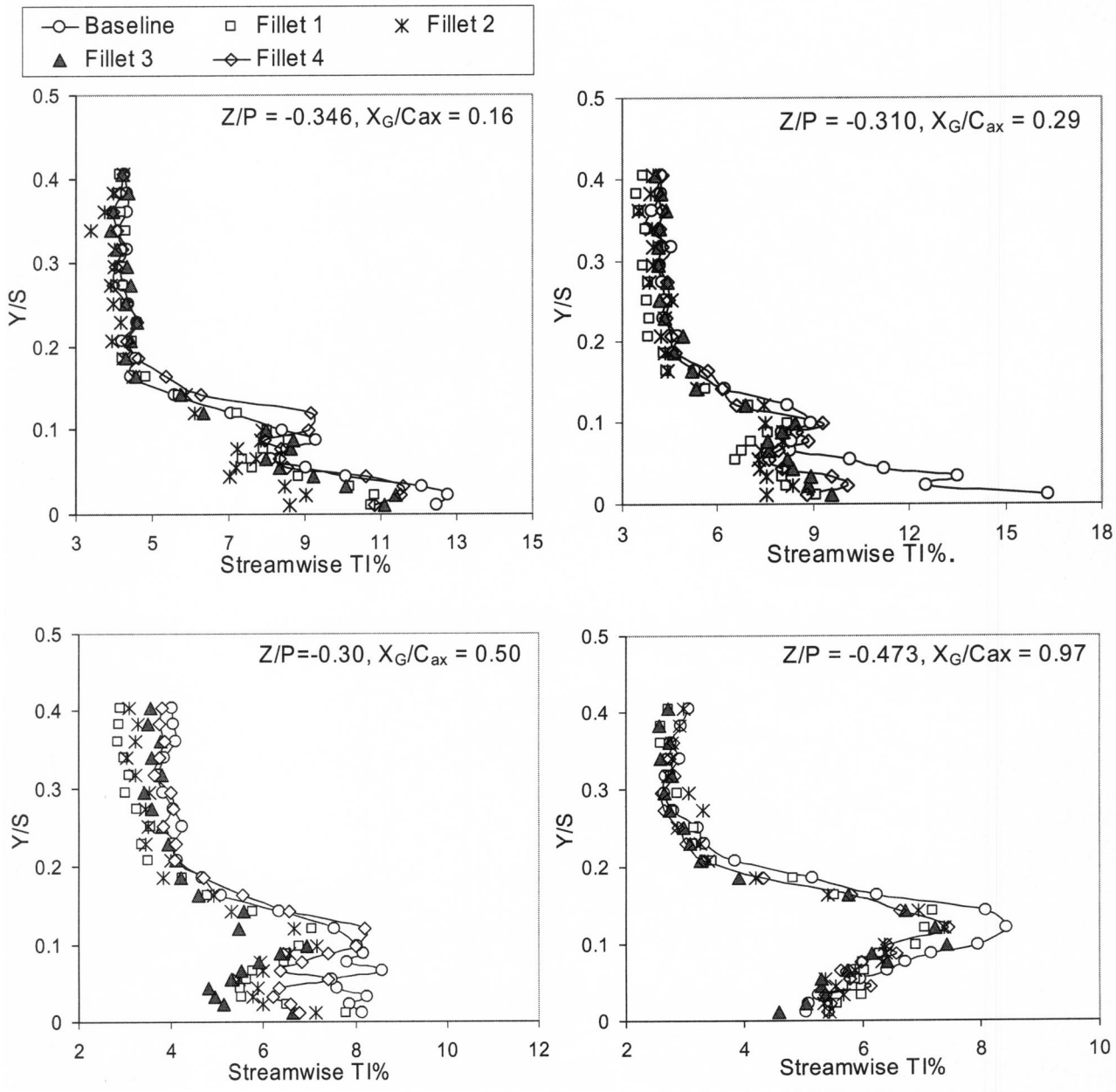

Fig. 12 Streamwise turbulence intensity distribution in spanwise direction at pitchwise passage middle position and at different axial locations with and without fillets

tions on the blade surface at 33% span are unaffected when the fillets are employed. However, the overall blade loading was not measured, and is an issue that needs to be considered by the turbine designer.

3 Nusselt Numbers. Nusselt numbers on the EW and blade surface are measured with constant heat flux boundary condition and for an inlet velocity of 10.26 m/s. All other conditions in the channel are as same as for the time-averaged flow measurements. Figures 15 to 19 show the Nusselt number distributions on the EW for the baseline and fillets. No data are presented on the fillet surface as the fillets are not heated. Nusselt numbers are generally high in the region between $X_G/C_{ax}=0.0$ and $X_G/C_{ax}=0.20$ because of the thermally developing flow in this region since the heating of the EW begins at $0.063C_{ax}$ upstream of the passage inlet. The peak Nu values move towards the suction side of the passage as the passage vortex system migrates toward this side. The Nu values initially decay due to the thermal development, and reduction of turbulence intensities (see Fig. 12). However, as the flow accelerates toward the throat region, Nusselt numbers increase again, and Nu values in excess of 1000 are noted in the vicinity of $X_G/C_{ax}=0.9$. When Nu values for the baseline are compared with those obtained with fillets (Figs. 16–19), Nusselt numbers are clearly smaller with the fillets from the inlet until about $X_G/C_{ax}=0.50$. This is primarily because of the reduction in the size and strength of the pressure-side leg of the horseshoe vortex with the fillets, as seen earlier in the measurements of the axial vorticity and the pitchwise velocity component (Figs. 7–9), and in the flow visualization images (although these were taken at a lower Re, but depict qualitative behavior). The Nusselt number reduction is substantial in certain regions. For example, for fillets 2 and 4, the reductions are in the range of 25%–35%. Downstream of the location $X_G/C_{ax}=0.75$, Nusselt numbers are much closer to each other for the various cases (within 10%–15%), and only fillet 4 shows consistently lower heat transfer compared to

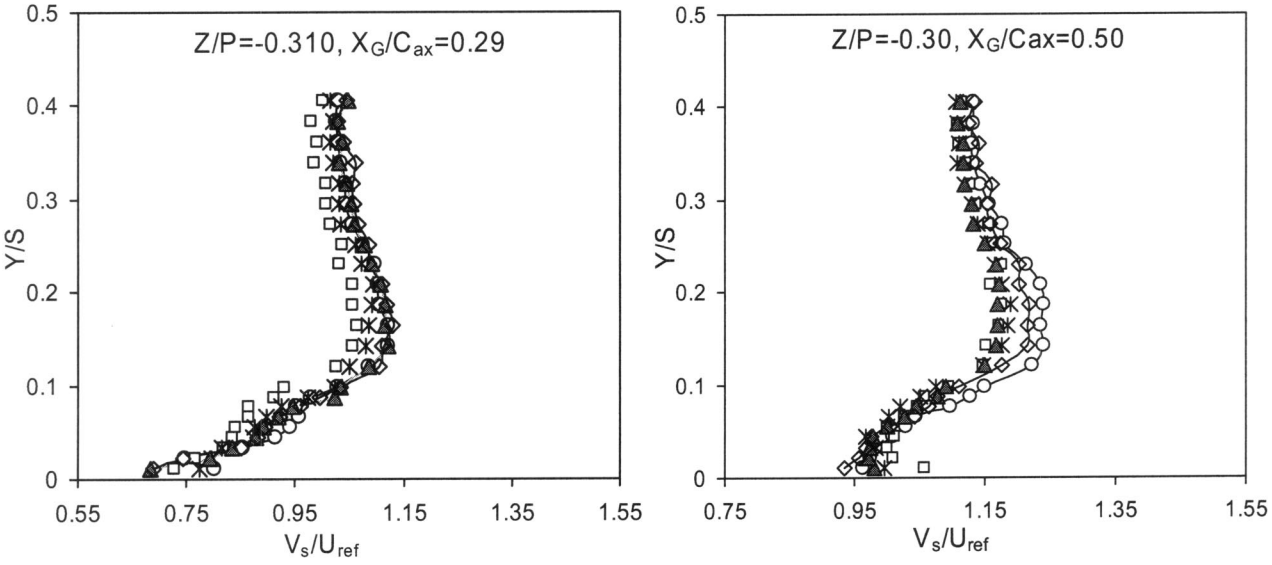

Fig. 13 Streamwise normalized velocity V_s/U_{ref} distribution in spanwise direction at pitchwise passage middle position and at difference axial locations with and without fillets. Legends for the symbols are shown in Fig. 12.

the baseline. In fact, the Nusselt numbers are slightly higher for the fillets 1, 2, and 3 compared to Nu for the baseline case and fillet 4 (which shows the lowest Nu values consistently). As noted earlier, with increasing downstream distances, the passage vortex structures become comparable in size (Fig. 6) for all the cases, and the turbulence intensities also become comparable (Fig. 12). Therefore, some of the beneficial effects of the fillet are lost downstream of the throat region.

Figure 20 presents the local Nu distributions in the pitchwise direction at different axial locations. The plotted data is extracted from the results in Figs. 15 to 19 to enable a more direct comparison between the various cases. As shown in Fig. 20, Nusselt numbers are significantly higher for the baseline at $X_G/C_{ax}=0.202$ across the entire pitch, and at $X_G/C_{ax}=0.453$ near the suction side compared to the Nu for the fillets at the same locations. Nu data for the fillets near the pressure side at $X_G/C_{ax}=0.202$ are not presented because the fillets are not heated. Among the fillets, fillet 3 produces much higher Nu values than any other fillets across the entire pitch at $X_G/C_{ax}=0.453$. Fillet 3 also produces higher Nu than the baseline near the pressure side at this axial location due to the stronger crossflow. In the axial location $X_G/C_{ax}=0.881$ in Fig. 20, the Nusselt numbers are higher for fillets 1, 2, and 3 than for the baseline and fillet 4. However, the Nu distribution for fillet 4 is still lower at this location relative to the baseline. Note also that the Nu value increases near the pressure side for all the configurations at $X_G/C_{ax}=0.881$ due to the pressure-side corner vortex.

Figure 21 compares the pitchwise-averaged Nu distributions in the axial direction between the baseline and the filleted cases. To compute the average Nu at a given X_G/C_{ax} location in this figure,

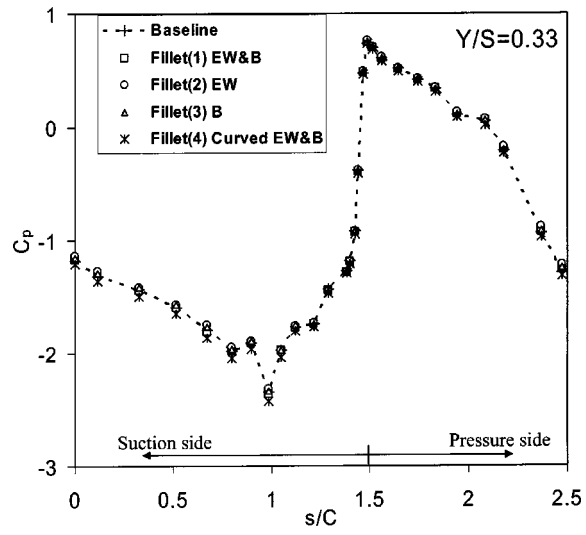

Fig. 14 Surface static pressure coefficient C_p distributions along the blade surface at $Y/S=0.33$ with and without the fillets

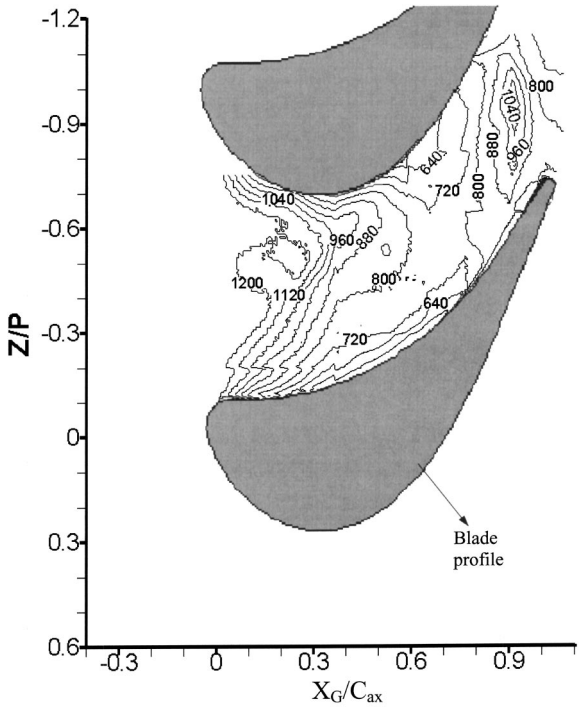

Fig. 15 EW Nusselt number distributions for baseline

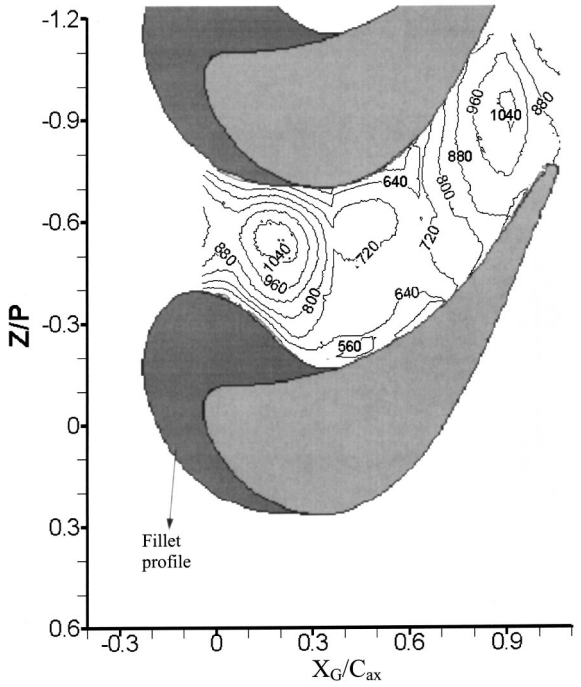

Fig. 16 EW Nusselt number distributions for fillet 1 (EW&B)

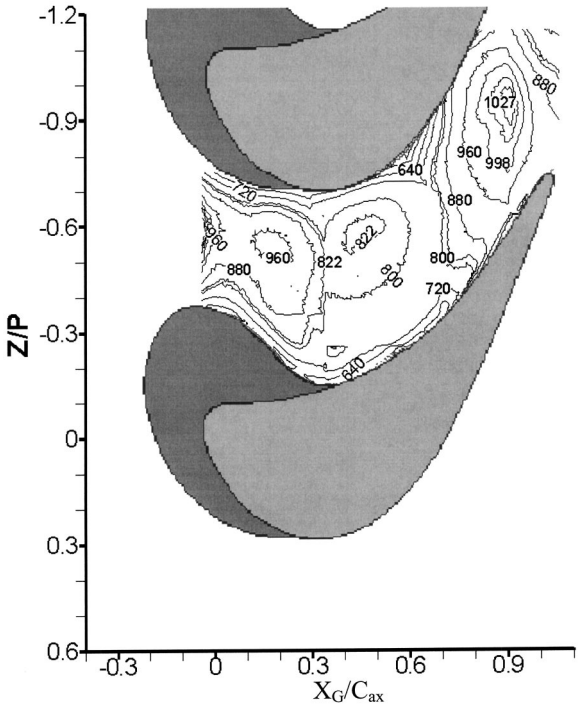

Fig. 18 EW Nusselt number distributions for fillet 3 (B)

local data along the pitchline at that X_G/C_{ax} location are averaged. Note that in the region covered by the fillets, there are no heat transfer data over the filleted region itself. The baseline average Nu values are much higher from $X_G/C_{ax}=0.0$ to 0.25 compared to the average Nu values for the filleted cases because of the weaker and smaller passage vortex structures, as mentioned before. In this region, fillet 2 shows the lowest average Nu values. Between $X_G/C_{ax}=0.35$ and $X_G/C_{ax}=0.60$ the average Nu values are about 10% to 20% smaller for fillets 1, 2, and 4 than the average Nu for the baseline. Downstream of $X_G/C_{ax}=0.75$, the average Nu values are higher for fillets 1, 2, and 3 than for the baseline and fillet 4, as noted earlier in presenting the local results. In general, the average Nu values are consistently lower for the fillet 4 relative to the baseline, while the fillet 3, which shows the worst performance overall, lower Nu relative to the baseline are observed only upstream of $X_G/C_{ax}=0.50$.

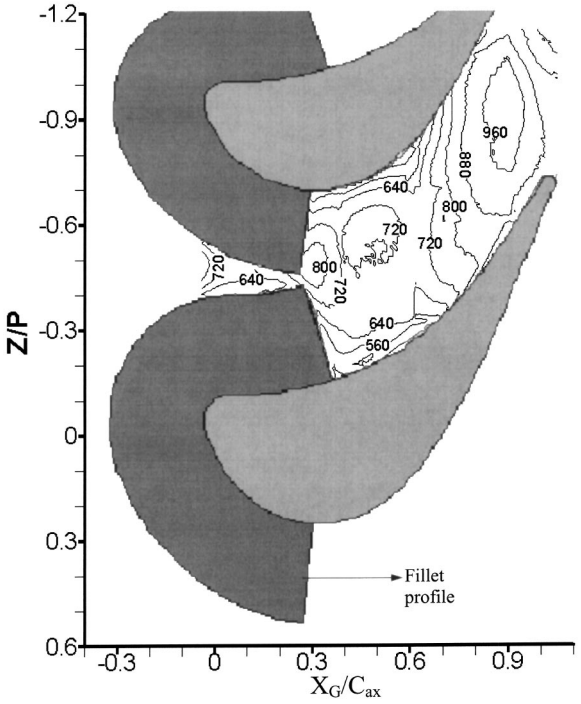

Fig. 17 EW Nusselt number distributions for fillet 2 (EW)

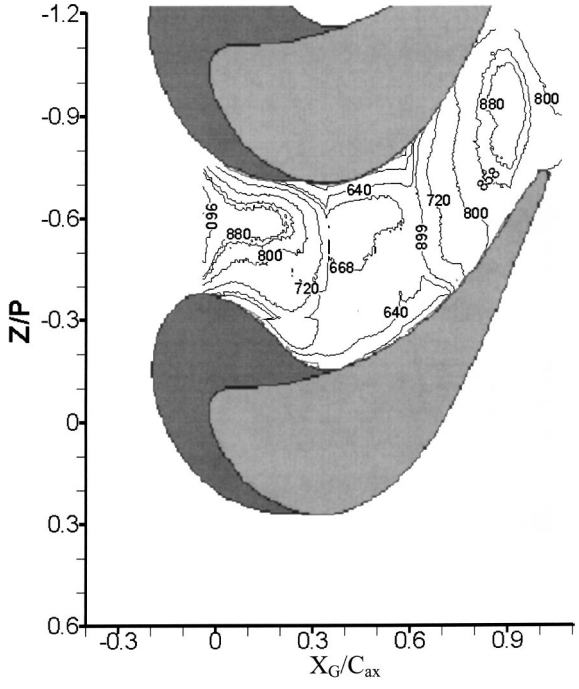

Fig. 19 EW Nusselt number distributions for fillet 4 (curved EW&B)

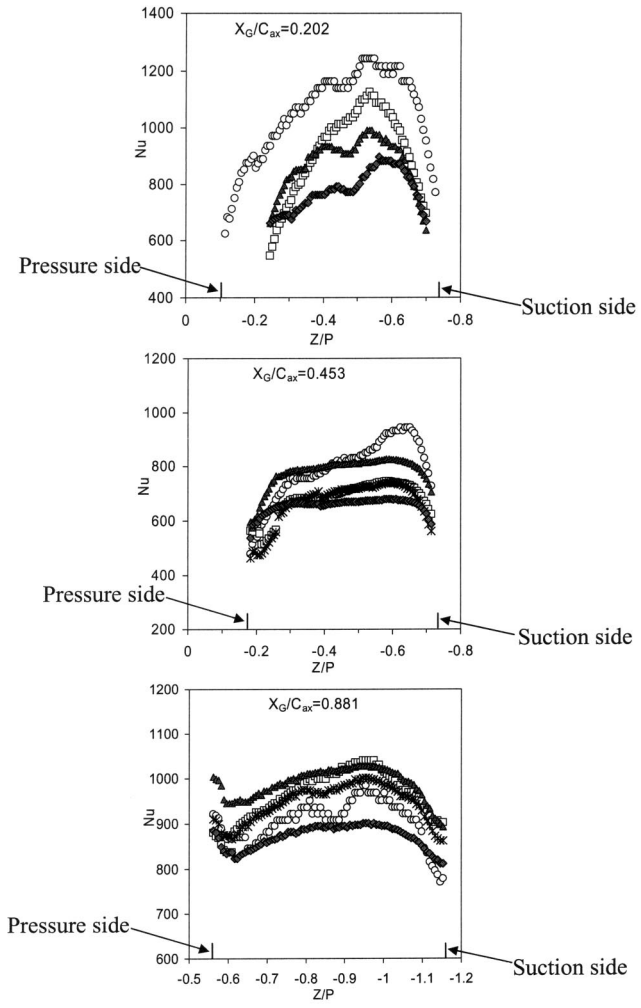

Fig. 20 EW Nu distributions in pitchwise direction and at different axial locations for baseline and fillets. Symbol legends are shown in Fig. 21.

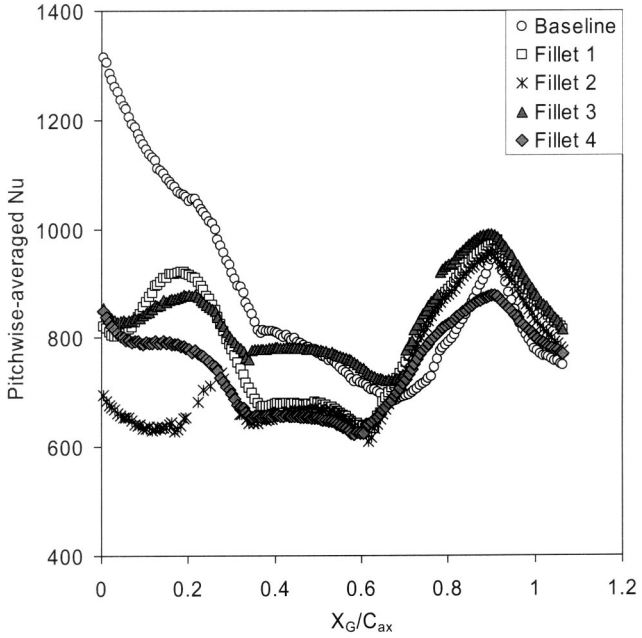

Fig. 21 Pitchwise-averaged EW Nusselt number distributions in axial direction for baseline and fillets

Summary and Conclusions

Experimental results are presented on flow structures and Nusselt numbers in a linear blade passage with and without leading-edge fillets. Four different fillet profiles are studied: fillet 1 (EW&B) blends the linear profile simultaneously toward the end wall and the blade, fillet 2 (EW) blends the linear profile to the end wall only, fillet 3 (B) blends the linear profile to the blade only, and fillet 4 (curved EW&B) blends a concave circular curved profile both to the end wall and the blade. The objective of the study is to explore the potential of the different fillet profiles in reducing the secondary flow structures and Nusselt numbers on the end wall. Instantaneous flow visualization images show smaller horseshoe vortex structures in the stagnation region with the leading-edge fillets compared to the horseshoe vortex structure for the baseline case. In the passage region, the secondary vortex structures are smaller in size near the leading edge, but the structures become comparable in size as the throat region is approached. The flow structure measurements (five-hole probe and hot-wire anemometry) also show smaller magnitudes of near-wall vorticity and lower positive values of pitchwise velocity in the region between the leading edge and the throat, indicating weaker passage vortex structures in this region. The EW Nusselt numbers are therefore generally lower for the filleted cases upstream of the throat, while further downstream the Nusselt numbers for the various cases are closer to each other, with only fillet 4 consistently showing the lowest heat transfer to the end wall. Total pressure loss coefficients in a pitchwise plane just downstream of the exit plane indicate no reductions in the total loss profile, but show that the fillets shift the passage vortex upwards by about $0.02S$ to $0.025S$. Turbulence intensity magnitudes at different axial locations indicate that the fillets reduce the turbulence intensity in the near wall regions upstream of the throat. This mechanism also contributes to the lower EW heat transfer observed upstream of the throat.

Acknowledgments

This work was supported by a grant from the DOE-University Turbine System Research (UTSR) program. Their support is gratefully acknowledged.

Nomenclature

A_{heater} = heater area exposed for convection
C = actual chord length of scaled up blade profile
C_{ax} = axial chord length of the scaled up blade profile
C_p = static pressure coefficient on blade surface
$C_{pt,loss}$ = total pressure loss coefficient
I = measured current through heater
Nu = Nusselt number
P = blade pitch
$P_{o,in}$ = stagnation pressure on blade surface
$P_{stat,0}$, $P_{\mathrm{tot},0}$ = average static and total gage pressure in reference plane, respectively
P_{tot} = measured total gage pressure
Q_{cond} = conduction heat loss
Re_{in} = Reynolds number, defined as $\mathrm{Re}_{in}=\rho U_{ref}C/\mu_{air}$
S = span of the scaled-up two-dimensional blade
T_{in}, $T_{o,in}$ = average temperature and stagnation temperature in reference plane, respectively
T_{wall} = surface temperature
U, V, W = velocity components in (X,Y,Z) coordinate system
U_{ref} = average streamwise velocity in reference plane

V_s, V_n, V_y = velocity components in streamline coordinate system
X, Y, Z = Cartesian coordinate system
k_{air} = thermal conductivity of air
q''_{conv} = convective heat flux
s = blade coordinate referring to distance on blade surface

Greek Symbols

δ, $\delta 1$, $\delta 2$ = properties related to boundary layer thickness [$\delta 1 = \int_0^{s/2}(1-u\rho_{ref})dy/u_{S/2}\rho_{ref}$, $\delta 2 = \int_0^{s/2}u\rho_{ref}(1-u/u_{s/2})dy/u_{S/2}\rho_{ref}$]
μ = dynamic viscosity
ρ = air density
ω = vorticity

Subscripts

G = global coordinate
air = properties related to air
ax = quantity related along X or axial direction of blade
max = maximum quantity
o, ref = reference quantity
$stat$, tot = static and total quantities, respectively
ss, ps = blade-suction side and pressure side, respectively
x = quantity in X direction

References

[1] Goldstein, R. J., and Spores, R. A., 1988, ''Turbulent Transport on the Endwall in the Region Between Adjacent Turbine Blades,'' ASME J. Heat Transfer, **110**, pp. 862–869.
[2] Langston, L. S., Nice, M. L., and Hooper, R. M., 1977, ''Three-Dimensional Flow Within a Turbine Cascade Passage,'' ASME J. Eng. Power, **99**, pp. 21–28.
[3] Sieverding, C. H., and Bosche, V. P., 1983, ''The Use of Colored Smoke to Visualize Secondary Flows in a Turbine-Blade Cascade,'' J. Fluid Mech., **134**, pp. 85–91.
[4] Wang, H. P., Olson, S. J., Goldstein, R. J., and Eckert, E. R. G., 1997, ''Flow Visualization in a Linear Turbine Cascade of High Performance Turbine Blades,'' ASME J. Turbomach., **119**, pp. 1–8.
[5] Häring, M., Böles, A., Harasgama, S. P., and Richter, J., 1995, ''Heat Transfer Measurement on Turbine Airfoils Using the Napthalene Sublimation Technique,'' ASME J. Turbomach., **117**(3), pp. 432–439.
[6] Goldstein, R. J., Wang, H. P., and Jabbari, M. Y., 1995, ''The Influence of Secondary Flows Near the Endwall and Boundary Layer Disturbance on Convective Transport from a Turbine Blade,'' ASME J. Turbomach., **117**(4), pp. 657–665.
[7] Yamamoto, A., 1987, ''Production and Development of Secondary Flows and Losses in Two Types of Straight Turbine Cascades: Part 2- A Rotor Case,'' ASME J. Turbomach., **109**(2), pp. 194–200.
[8] Hermanson, K., Kern, S., Picker, G., and Parneix, S., 2002, ''Predictions of External Heat Transfer For Turbine Vanes and Blades With Secondary Flowfields,'' *Proc. ASME Turbo Expo*, ASME, New York, GT-2002-30206.
[9] Graziani, R. A., Blair, M. F., Taylor, J. R., and Mayle, R. E., 1980, ''An Experimental Study of Endwall and Airfoil Surface Heat Transfer in a Large Scale Turbine Blade,'' J. Eng. Power, **102**(2), pp. 257–267.
[10] Gallus, H. E., Zeschky, J., and Hah, C., 1995, ''Endwall and Unsteady Flow Phenomena in an Axial Turbine Stage,'' ASME J. Turbomach., **117**, pp. 562–570.
[11] Hah, C., 1984, ''A Navier-Stokes Analysis of Three-Dimensional Turbulent Flows Inside Turbine Blade Rows at design and Off-Design Conditions,'' J. Eng. Gas Turbines Power, **106**, pp. 421–429.
[12] Gregory-Smith, D. G., and Cleak, J. G. E., 1992, ''Secondary Flow Measurements in a Turbine Cascade with High Inlet Turbulence,'' ASME J. Turbomach., **114**(1), pp. 173–183.
[13] Davenport, W. J., Agarwal, N. K., Dewitz, M. B., Simpson, R. L., and Poddar, K., 1990, ''Effects of a Fillet on the Flow Past a Wing-Body Junction,'' AIAA J., **28**(12), pp. 2017–2024.
[14] Simpson, R. L., 2001, ''Junction Flows,'' Annu. Rev. Fluid Mech., **33**, pp. 415–443.
[15] Sauer, H., Müller, R., and Vogeler, K., 2001, ''Reduction of Secondary Flow Losses in Turbine Cascades by Leading Edge Modifications at the Endwall,'' ASME J. Turbomach., **123**, pp. 207–213.
[16] Zess, G. A., and Thole, K. A., 2001, ''Computational Design and Experimental Evaluation of Using a Leading Edge Fillet on a Gas Turbine Vane,'' *Proc. ASME Turbo Expo*, ASME, New York GT-2001-0404.
[17] Shih, T. I-P., and Lin, Y.-L., 2002, ''Controlling Secondary-Flow Structure by Leading-Edge Airfoil Fillet and Inlet Swirl to Reduce Aerodynamic Loss and Surface Heat Transfer,'' *Proc. ASME Turbo Expo*, ASME, New York, GT-2002-30529.
[18] Lethander, A. T., Thole, K. A., Zess, G., and Wagner, J., 2003, ''Ortimizing the Vane-Endwall Junction to Reduce Adiabatic Wall Temperatures in a Turbine Vane Passage,'' *Proc. ASME Turbo Expo*, ASME, New York, GT-2003-38939.
[19] Becz, S., Majewski, M. S., and Langston, L. S., 2003, ''Leading Edge Modification Effects On Turbine Cascade Endwall Loss,'' *Proc. ASME Turbo Expo*, ASME, New York, GT-2003-38898.
[20] Becz, S., Majewski, M. S., and Langston, L. S., 2004, ''An Experimental Investigation of Contoured Leading Edges for Secondary Flow Loss Reduction,'' *Proc. ASME Turbo Expo*, ASME, New York GT-2004-53964.
[21] Timko, L. P., 1990, ''Energy Efficient Engine High Pressure Turbine Component Test Performance Report,'' Contract Report for NASA, Report No. NASA CR-168289.
[22] Ligrani, P. M., Singer, B. A., and Baun, L. R., 1989, ''Miniature Five-hole Pressure Probe for Measurement of Three Mean Velocity Components in Low-Speed Flows,'' J. Phys. E, **22**, pp. 868–876.
[23] Ligrani, P. M., Singer, B. A., and Baun, L. R., 1989, ''Spatial Resolution and Downwash Velocity Corrections for Multiple-Hole Pressure Probes in Complex Flows,'' Exp. Fluids, **7**, pp. 424–426.
[24] Sargent, S. R., Hedlund, C. R., and Ligrani, P. M., 1998, ''An Infrared Thermography Imaging System For Convective Heat Transfer Measurements in Complex Flows,'' Meas. Sci. Technol., **9**(12), pp. 1974–1981.
[25] Mahmood, G. I., Hill, M. L., Nelson, D. L., Ligrani, P. M., Moon, H.-K., and Glezer, B., 2001, ''Local Heat Transfer and Flow Structure On and Above a Dimpled Surface in a Channel,'' ASME J. Turbomach., **123**(3), pp. 115–123.
[26] Holman, J. P., 2001, *Experimental Methods for Engineers*, 7th ed., McGraw Hill, New York, Chap. 3, pp. 51–77.
[27] Moffat, R. J., 1988, ''Describing the Uncertainties in Experimental Results,'' Exp. Therm. Fluid Sci., **1**(1), pp. 3–17.
[28] Kang, M. B., and Thole, K. A., 2000, ''Flowfield Measurements in the Endwall Region of a Stator Vane,'' ASME J. Turbomach., **122**, pp. 458–466.

Turbulent Transport in Film Cooling Flows

Atul Kohli
400 Main Street, M/S 165-16,
Pratt & Whitney,
East Hartford, CT 06108

David G. Bogard
Mechanical Engineering Department,
University of Texas,
Austin, TX 78712

This experimental study was performed on a single row of round holes with a 35° surface angle, representing film cooling geometry commonly used in turbine engines. Simultaneous velocity and temperature measurements were made using a cold-wire in conjunction with a LDV. The experimentally determined cross correlations provide a direct indication of the extent of turbulent transport of heat and momentum in the flow, which in turn governs dispersion of the film cooling jet. Actual engine environments have elevated mainstream turbulence levels that can severely reduce the cooling capability of film cooling jets. Clearly, the turbulent transport for very high mainstream turbulence is expected to be markedly different than that with low mainstream turbulence, and would improve our understanding of the mechanisms involved in the dispersion of film cooling jets. Experimental cross-correlation data was obtained for two vastly different freestream turbulence levels (0.6% and 20%) in this study. For this purpose, eddy diffusivities for momentum and heat transport were estimated from the measured data. These results will help develop new turbulence models and also explain why gradient diffusion based models do not give good predictions relative to experimental results.
[DOI: 10.1115/1.1865221]

Introduction

Over the last few decades, a lot of research has been focused on film cooling of gas turbine blades. Most of the experimental work done in this area has concentrated on improving film cooling effectiveness by changing geometrical parameters, without much attention to a description of the flowfield. As a result, there is a fundamental lack of understanding of the mechanisms governing the transport of heat and momentum in the film cooling process. Better understanding of these mechanisms is essential in order to improve modeling capabilities of the film cooling process, and will lead to concepts for reducing dispersion of film cooling jets and improving effectiveness. Current numerical and analytical film cooling models are unable to make good effectiveness predictions especially near the injection location [1]. This suggests that transport mechanisms present near the injection location are different from those in the far-field region and are not being modeled correctly.

Although most film cooling literature consists of surface measurements, there are a few studies that have attempted to document the turbulent transport of momentum in film cooling flows by making field measurements. Mean and turbulent velocity components were measured in [2] using triple-wire probes for a jet injecting at 90° to the mainstream with velocity ratios VR=0.5, 1, and 2. It was found that the turbulent kinetic energy and the $\overline{uv}$ shear stress were closely related to the mean streamwise velocity gradient normal to the wall.

Turbulence measurements of film cooling jets for a density ratio DR=2, was first reported in [3]. In this study, detailed three-component LDV measurements were made of mean and turbulence quantities for film cooling jets for a row of round holes inclined at 35°. The hydrodynamics of the film cooling jet were evaluated in terms of mean velocity profiles and contours of turbulence intensities, Reynolds shear stresses and correlation coefficients. An important finding of this study was the correspondence between the turbulence stresses and the mean velocity gradient. The local streamwise velocity gradient normal to the wall dictated the production of shear stress and this implied that mean field closure models could be applied.

Contributed by the Heat Transfer Division for publication in the JOURNAL OF HEAT TRANSFER. Manuscript received March 24, 2004; revision received October 28, 2004. Review conducted by: P. M. Ligrani.

Eddy diffusivity measurements in the wall-normal and lateral directions using triple-wire anemometry were reported in [4] for a film cooling flow. Results showed that momentum transport in the lateral direction was greater than that in the wall-normal direction.

Fluctuating temperature measurements are reported in [5,6] for a typical film cooling flow with low and high freestream turbulence (20% turbulence intensity). Analysis of pdf's and spectra of the fluctuating temperature indicated that for low freestream turbulence the coolant dispersion is primarily due to large scale turbulent structures generated by the shear layer between the mainstream and the coolant jet. However, for high freestream turbulence, turbulent structures in the freestream turbulence dominated.

As indicated above, there have been previous studies of the turbulent velocity field associated with film cooling flows, and of turbulent fluctuating temperature fields associated with film cooling flows. However, there have been no previous studies in which simultaneous velocity and temperature fluctuation measurements have been made. These measurements are necessary to determine the turbulent transport of heat in a film cooling flow field.

In current Reynolds Averaged Navier-Stokes (RANS) type numerical predictions the local generation of turbulence is controlled mainly via the local velocity gradients and routinely use turbulence models that make the assumption of isotropic turbulence. Most turbulence models also use a turbulent Prandtl number value of $Pr_t \sim 1$ based on the Reynolds analogy. The results of this study can be used to check the validity of these assumptions and provide a database for development of new turbulence models that are appropriate for film cooling flows.

Experimental Facilities and Instrumentation. This study was performed in a recirculating boundary layer wind tunnel with a test section that was 0.13 m high, 0.6 m wide, and 1.8 m long, and has been described in [7]. Liquid nitrogen was used to cool a secondary flow loop for the film cooling flow to achieve a density ratio of DR=1.05. A unique turbulence generator that used two opposing rows of jets in crossflow with the mainstream to generate turbulence levels of TL=20% with a length scale of $\Lambda_x/D=3$ near the injection location was used in this study. Details of this turbulence generator and characterization of the freestream turbulence can be found in [8]. The turbulence level in the test section without the turbulence generator in operation was TL=0.6%.

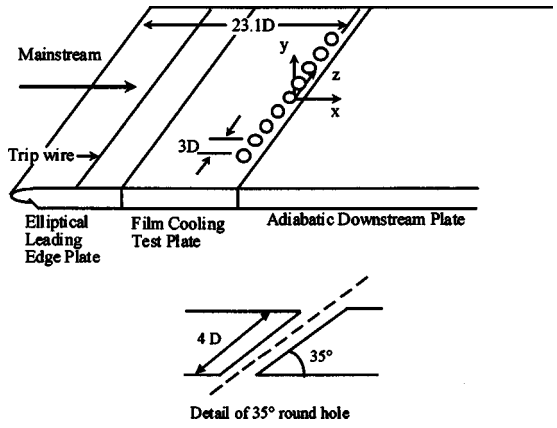

Fig. 1 Schematic of test section and cooling hole geometry [5]

The test section (see Fig. 1) consisted of three separate sections: an elliptical leading edge plate, followed by a film cooling hole plate, downstream of which was an adiabatic plate. For this study, a single row of nine round holes inclined at 35° was used. The holes had a diameter of $D=11.1$ mm, were spaced $P/D=3$ apart, and had a length $L/D=4$, representative of actual gas turbines. The hole inlets and exits were sharp edged, and the interiors were aerodynamically smooth. The coordinate origin was fixed at the trailing edge of the central hole. To minimize conduction losses, the film cooling hole plate was made out of extruded polystyrene foam that had a thickness of 2.54 cm. The adiabatic plate comprised of 1.27-cm-thick polystyrene foam glued on to a 1.27 cm fiberglass composite (EXTREN) sheet for structural rigidity. A 15 cm layer of Corning™ fiber glass insulation was installed below the adiabatic plate to reduce backside conduction losses.

For the experiments in this study, the mainstream velocity was maintained at $U_\infty=10.0$ m/s, for both the low and high freestream turbulence cases. For the low freestream level, an approach turbulent boundary layer was obtained by tripping the flow using a 0.8 mm trip wire, $9D$ from the leading edge, as shown in Fig. 1. For low freestream turbulence at the leading edge of the holes, the boundary layer parameters were $\delta^*/D=0.1$, $\mathrm{Re}_\theta=420$ and $H=1.66$. For this study, the jet was cooled to obtain a density ratio of DR=1.05. Although this density ratio is not representative of that in the actual turbine environment, as shown in [9], similar thermal fields occur for a wide range of density ratios when the jet-to-mainstream momentum flux ratio (I) is matched. This was further confirmed in [5] by comparing the mean thermal field at DR=1.05 with previous measurements at DR=1.6. All measurements in this study were made using a momentum flux ratio of $I=0.16$ for the film cooling jets, with corresponding mass flux ratio of $M=0.40$ and velocity ratio of VR=0.38.

The simultaneous temperature and velocity measurements reported in this study were made using a cold-wire in conjunction with a LDV. The cold-wire was constructed using an etched Wollaston wire of length $l=0.6$ mm and diameter $d=1.5$ μm. It had a frequency response of 2.6 kHz and was operated at a very low current of $i=25$ mA to avoid sensitivity to velocity. Details of its construction and validation of the fluctuating temperature measurements can be found in [5]. The cold-wire was powered using a TSI model 1050 anemometer operating in constant current mode. For signal conditioning of the analog voltage output from the anemometer, a Stanford Research Systems Inc. model SR640 low-pass filter was used. Cold-wire data were digitized using a sixteen-bit analog-to-digital card, model NB-MIO-16XL, made by National Instruments. For the simultaneous measurements, the data acquisition was triggered by the LDV, and the analog data was acquired within 30 μs of the LDV data. A backscatter LDV system, TSI model 9100-10, was operated as a two-component system for the velocity measurements. The LDV system used a 3 W argon ion laser, a 3.75× beam expander, a 450 mm focusing lens, frequency shifters, and TSI 1990 counter signal processors. A 10 μs coincidence window was used for the velocity measurements using two signal processors. The LDV was mounted on a traverse system that allowed travel in three directions with a resolution of 2 μm. The velocity data were acquired using a Macintosh II computer and a digital input board, National Instruments model NB-DIO-32F. To remove bias of the LDV measurements towards higher velocities, residence time weighting was used on all data.

Simultaneous temperature and velocity measurements were made on the jet centerline at $x/D=-1.75$, -1, -0.5, 0, 1, 3, 6, and 10. The vertical measurement locations were performed at $y/D=0.1$, 0.2, 0.3, 0.4, 0.5, 0.7, 1, 1.5, 2, 2.5, and 3. In addition to profiles on the jet centerline, lateral measurements were made at $z/D=0.2$, 0.4, 0.7, 1, and 1.5 at $x/D=-0.5$, 0, 1, and 3. As shown in [3], the $\overline{uv}$ shear stress dominated over the other shear stress components especially for the low VR conditions. While this was true for all regions of the flow, it is especially true at the jet centerline where $\overline{uw}$ and $\overline{vw}$ are zero because of the symmetry condition. Therefore, only the centerline measurements results are discussed in this paper.

The experimentally measured temperature-velocity products in this study, along with the temperature and velocity fields, allowed estimation of the eddy viscosity and diffusivity. For example, the eddy viscosity defined as $\varepsilon_m=\overline{uv}/(dU/dy)$, was estimated using $\overline{uv}$ and the slope of the velocity profile, which was obtained from a three-point second-order accurate scheme for unequally spaced points [10].

The uncertainty of the above results was obtained using repeatability measurements at $x/D=3$ and $y/D=0.5$, where very high turbulence levels and sharp velocity gradients exist. The turbulent heat fluxes and shear stress also showed peak values at this location. Therefore, the precision uncertainties at this location provide an upper bound for the uncertainty. The uncertainty was less than ±0.0005 for the temperature-velocity products ($\overline{uv}^*$, $\overline{ut}^*$, and $\overline{vt}^*$) and it was less than ±0.01 for the correlation coefficients (R_{uv}, R_{ut}, and R_{vt}). Using sequential perturbation, uncertainty in the calculation of eddy viscosity and eddy diffusivity was estimated at 11%.

Validation of Temperature-Velocity Measurements. Simultaneous temperature-velocity measurements are difficult to make and the few studies with such measurements have been limited mainly to boundary layer flows. Almost all of them have used a cold-wire with a hot-wire, requiring correction of velocity measurements for temperature changes. Note that in the present study, these measurements were made using a cold-wire in conjunction with a LDV. Since LDV measurements are not affected by temperature fluctuations, no corrections are required for velocity data and flow disturbances associated with the previous methods are also avoided.

Using an LDV for the velocity measurements required that the flow be seeded with particles. Selection of appropriate particles is critical because the cold-wire has to survive in the seeded flow. Seed particles also tend to stick to the cold-wire and cause a decrease in the frequency response and drift of calibration. Several different seed particles were tested [11] and it was determined that filtered incense smoke particles were acceptable for seeding the flow. The same technique was used for the measurements done in this study. Even though the smoke was filtered, tar particles deposited on the cold-wire with time and were removed by switching to the hot-wire mode with an overheat ratio of OH=1.6. This procedure vaporized the tar from the wire and was implemented at every measurement location. As reported in [12], this burning process shifted the calibration curve, but its slope (dV/dT) remained the same.

One other important aspect of simultaneous measurements is the alignment of the temperature and velocity sensors. In the studies using a triple-wire configuration [13,14], a typical separation

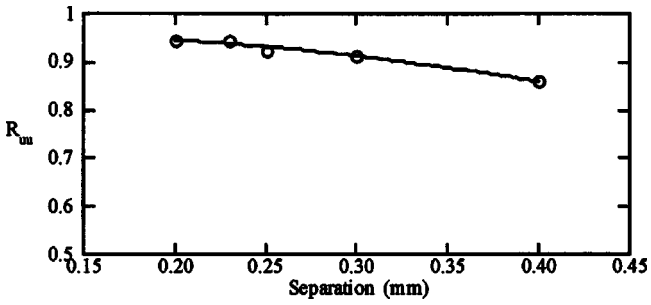

Fig. 2 R_{uu} variation with distance between LDV and cold-wire

between the two sensors has been about 1 mm. In the present study, a separation of 0.2 mm was achieved by using the U-shaped cold-wire. To verify that the two measurement points were close enough that they could be regarded as simultaneous point measurements, cross correlations between the LDV and the temperature sensor operating as a hot-wire sensitive to the U velocity were measured. The R_{uu} correlation was measured for different separation distances between the LDV and the temperature probe. As shown in Fig. 2, a relatively constant correlation coefficient of $R_{uu} \sim 0.95$ was measured when the separation was less than 0.25 mm. This is very close to the ideal value of $R_{uu}=1$, and the slight difference could be because of the hot-wire's sensitivity to the vertical component of velocity. The correlation coefficient decreased rapidly when the spacing was increased further. For all the simultaneous temperature velocity measurements done in this study, a separation distance of 0.2 mm was used.

In order to validate simultaneous temperature-velocity measurements, correlation coefficients were measured in a thermal boundary layer with a constant heat-flux wall boundary condition. Figure 3 shows the measured profiles for the temperature-velocity correlations along with experimental data from Chen and Blackwelder [13] and Subramanian and Antonia [14]. The data from the present study are lower than that in [13], but this may be attributed to the frequency response of the cold-wire used in [13], which was only 350 Hz, and thus only large-scale eddies were detected. A relatively constant value of $R_{vt}=0.4$ was reported by [15] across the boundary layer. The R_{ut} data of [14] does not follow the trends shown by the other studies, showing a relatively constant value for the correlation coefficient across the boundary layer. It should be noted that [14] used hot-wires with $l/d \sim 200$

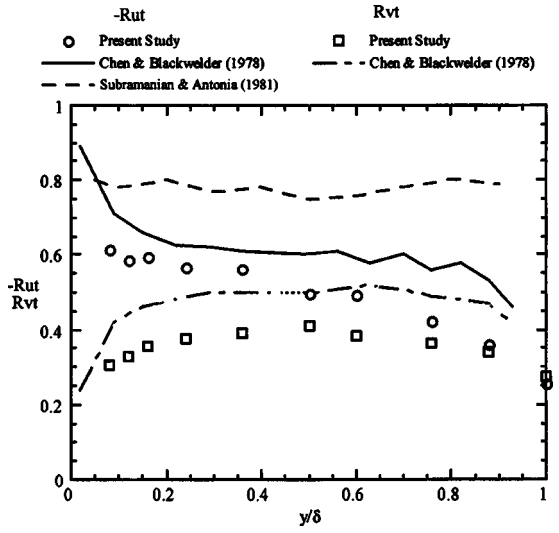

Fig. 3 Temperature-velocity correlation coefficients for the standard thermal boundary layer

and report values for the rms velocity that were much lower than expected, suggesting that end effects contaminated their hot-wire measurements. In addition, thermal contamination of hot-wire signals would tend to increase the velocity-temperature correlations.

Background: Eddy Diffusivity Models. It is important to understand how film cooling flows are modeled in order to explain why they are not accurately described by current turbulence models. The crux of all turbulence models is estimating the transport of momentum due to turbulent motions, which for the Reynolds averaged Navier-Stokes equations refers to the Reynolds stress term: $-\overline{\rho u_i u_j}$. These correlations between velocity components are modeled using the assumption that they are directly proportional to the mean velocity gradients in the flow. This concept of a eddy viscosity (ε_m), which assumes that the turbulent stresses act like viscous stresses, was introduced by Boussinesq as

$$\varepsilon_m = \frac{-\overline{uv}}{\partial U/\partial y} \tag{1}$$

In a film cooling flowfield, the $\overline{uv}$ stress dominates and has been shown [2,3] to correspond well with the mean streamwise velocity gradient, dU/dy. This suggests that a gradient diffusion model should adequately predict momentum transport in a film cooling flowfield. The fact that film cooling models are unable to predict film effectiveness near the hole, implies that perhaps it is the transport of heat that is not modeled correctly.

Closure in the energy equation is achieved by modeling the velocity-temperature correlation using eddy diffusivity (ε_T), as

$$\varepsilon_{Ty} = \frac{-\overline{vt}}{\partial T/\partial y} \tag{2}$$

This is analogous to the modeling used for momentum transport, wherein the turbulent stresses are assumed to be directly proportional to the mean velocity gradients. As the temperature-velocity correlations have not been measured before in film cooling flow, it has not been verified whether such a gradient diffusion model can be expected to work.

In addition to the above assumptions most turbulence models use a fixed relation between the turbulent eddy viscosity and diffusivity defined by the turbulent Prandtl as

$$\mathrm{Pr}_t = \frac{\varepsilon_m}{\varepsilon_{Ty}} \tag{3}$$

Using the Reynolds analogy between momentum and heat transport, a majority of the turbulence models assume that $\mathrm{Pr}_t = 1$, or $\varepsilon_m = \varepsilon_T$. Another point to note is that most film cooling models use the assumption of isotropic behavior and use the same eddy diffusivity in all three directions: $\varepsilon_T = \varepsilon_{Tx} = \varepsilon_{Ty} = \varepsilon_{Tz}$. The $\overline{ut}$ and $\overline{vt}$ results from this study were used to test these assumptions.

Results With Low Freestream Turbulence

Contours of the normalized mean temperature field Θ presented in Fig. 4, shows the rapid dispersion of coolant along the centerline of the coolant jet. These contours show that by $x/D=5$ the coolant jet core temperature has been reduced by 50%. A major goal of this study was to obtain a better understanding of the physical mechanisms causing the rapid dispersion of the coolant jet in the region immediately downstream of the coolant holes.

Contours of the mean velocity field for this film cooling flow, presented in Fig. 5, show a low velocity region extending to $y/D=0.5$ downstream of the coolant hole. The mean temperature contours in Fig. 4 show that this low velocity region is coincident with the bulk of the low temperature region which identifies the coolant jet. Closely spaced mean velocity contour lines shown in Fig. 5 indicate a region of large velocity gradients above the coolant jet. The interface between the coolant jet and the mainstream was identified by using measurements of fluctuating temperature,

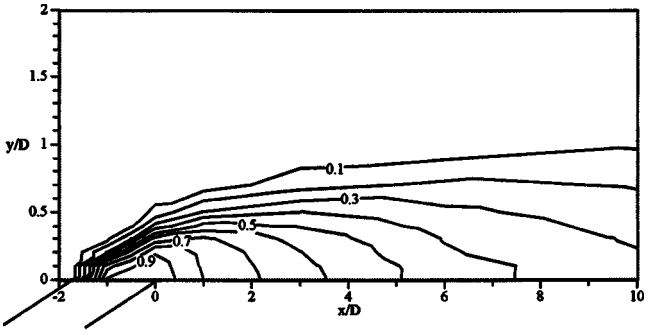

Fig. 4 Mean temperature contours (Θ) on jet centerline [5]

Θ'. The jet-mainstream interface line was defined by the locus of maximum Θ' as shown in Fig. 6. This jet-mainstream interface line is presented as a reference in all of the figures that follow.

Contours of the $\overline{uv}^*$ distribution on the centerline of the film cooling jet, shown in Fig. 7(*a*), showed that $\overline{uv}^*$ was generally negative, which is as expected due to the positive mean velocity gradients. As shown in Fig. 7(*a*), there were two regions where $-\overline{uv}^*$ had a local maximum. Over the hole, at $x/D=-1$, a region of high turbulent shear stress is found where the freestream first contacts the exiting jet. High velocity gradients occur in this region, which corresponds to the upstream edge of the jet, as the exiting jet is much slower than the freestream. The highest levels of turbulent shear stress in the flow are found downstream of the hole exit ($3<x/D<6$), at the interface between the jet and the freestream. These locations also correspond to regions where steep velocity gradients occur. In general, the turbulent shear stress maxima are coincident with large mean velocity gradients present in the flow.

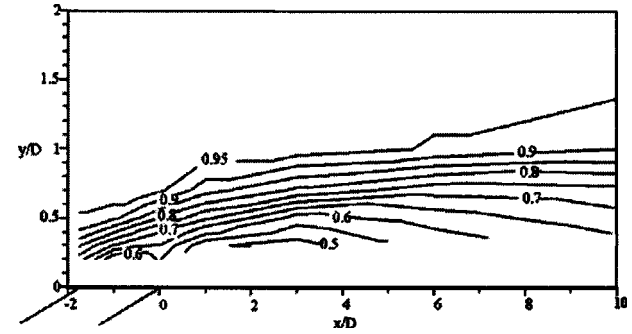

Fig. 5 Normalized mean streamwise velocity (U/U_∞) contours on jet centerline

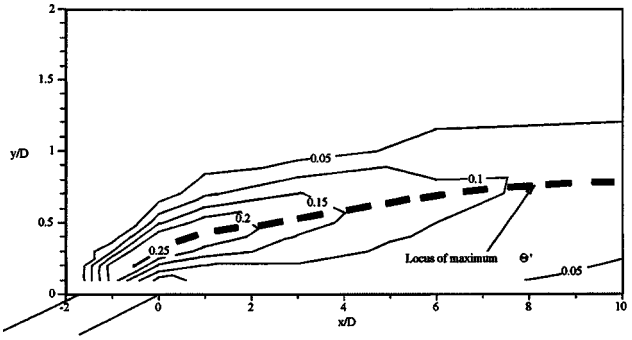

Fig. 6 Jet-mainstream interface defined using rms temperature contours (Θ') on jet centerline from [5]

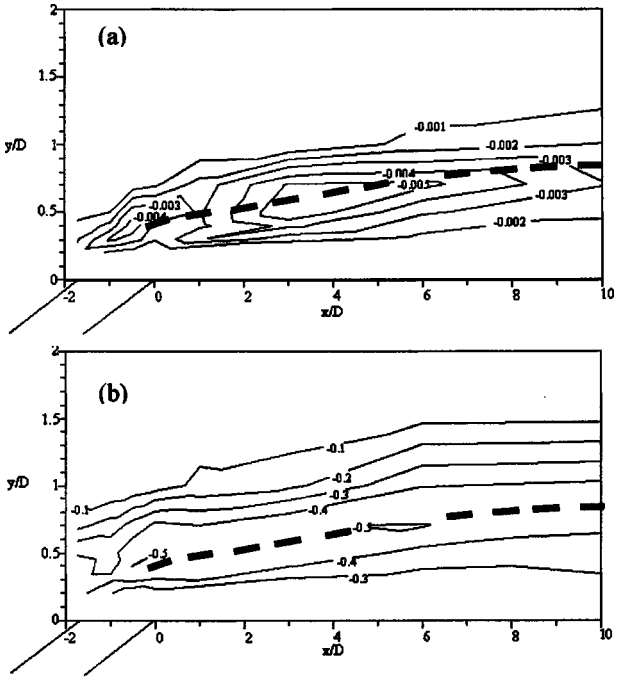

Fig. 7 (a) $\overline{uv}^*$ and (b) R_{uv} on centerline for low freestream turbulence

The turbulent mixing occurring at the jet-freestream interface is quite vigorous as indicated by the contour levels of $\overline{uv}^*=-0.005$. A better appreciation of the strength of this turbulent mixing can be obtained when compared to the peak value of $\overline{uv}^*\sim-0.002$ found in turbulent boundary layers and in turbulent jets [16].

While the above results indicate the magnitude of turbulent mixing occurring in the flow, the behavior of the correlation coefficient R_{uv} is also relevant. Figure 7(*b*) shows the contours for R_{uv}. In general, the jet-freestream interface shows correlation coefficients of $R_{uv}=-0.4$ with small regions showing a value of $R_{uv}=-0.5$. These levels of R_{uv} are similar to the levels that occur in turbulent boundary layers and turbulent jets [16]. In contrast to the $\overline{uv}^*$ contours, which had localized peak levels, R_{uv} was relatively constant along the length of the jet-freestream interface line.

In order to observe the correspondence between the velocity gradients and $\overline{uv}^*$ directly, the value of ε_m^* was calculated at each point of the measurement grid, and the resulting contours of ε_m^* are shown in Fig. 8. The values of ε_m^* ranged from $0.001\leqslant\varepsilon_m^*\leqslant0.008$. The value of ε_m^* is relatively constant in the core region of the film cooling jet which is similar to the constant ε_m^* distri-

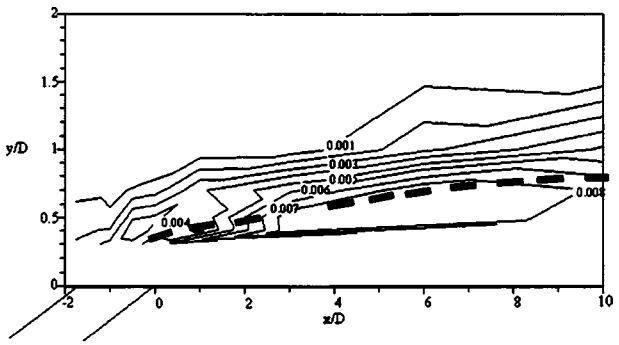

Fig. 8 Contours of ε_m^* for low freestream turbulence

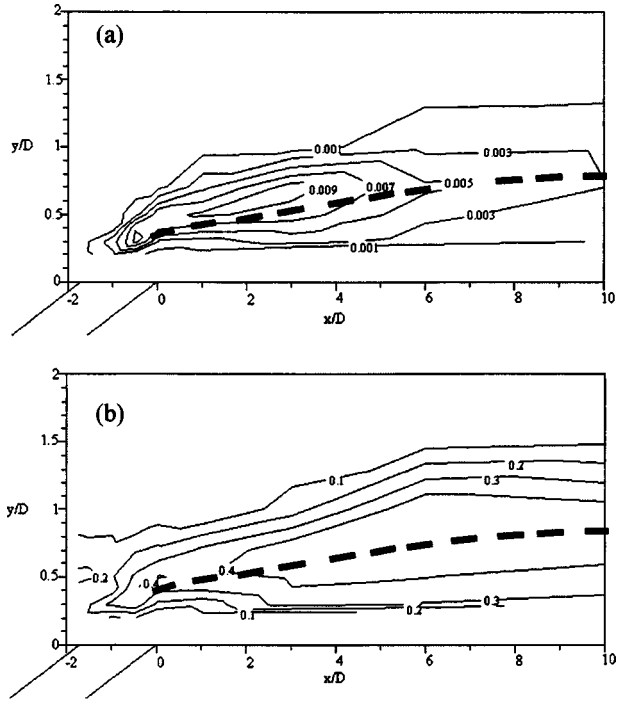

Fig. 9 (a) $\overline{ut}^*$ and (b) R_{ut} for low freestream turbulence

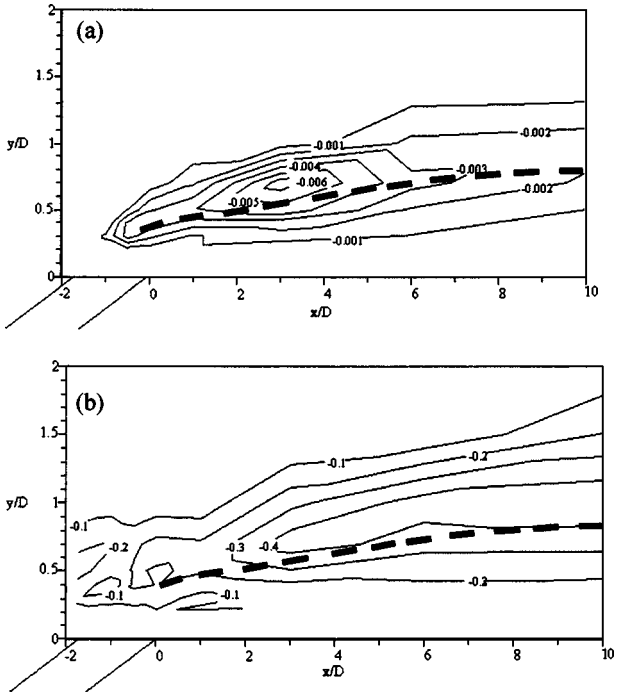

Fig. 10 (a) $\overline{vt}^*$ and (b) R_{vt} for low freestream turbulence

bution observed in the core of free jets. The magnitude of ε_m^* decreases with distance away from the jet-freestream interface.

The main thrust of this study was to provide a direct measure of the extent of turbulent thermal transport occurring in the flow to help explain the rapid thermal dispersion of the film cooling jet. Turbulent transport of thermal energy is proportional to the gradient of $\overline{ut}^*$ in the x (streamwise) direction, and to the gradient of $\overline{vt}^*$ in the y (wall normal) direction. The dispersion of the coolant jet is due primarily to the wall normal transport, i.e., due to gradients of $\overline{vt}^*$. However, measurements of $\overline{ut}^*$ and $\overline{vt}^*$ are presented in this paper since both $\overline{ut}^*$ and $\overline{vt}^*$ distributions are valuable for validating higher level CFD predictions such as large eddy simulation codes.

Contours of the $\overline{ut}^*$ product on the jet centerline, shown in Fig. 9(a), were positive with a localized peak of $\overline{ut}^* > 0.009$ centered about $x/D=2$ and on the jet-freestream interface line. The positive values for $\overline{ut}^*$ indicate that instantaneously higher velocities tend to correlate with higher temperatures, and vice versa. This can be attributed to higher velocities originating from the freestream, which was at the higher temperature, and lower velocities originating from the coolant jet, which was at the lower temperature. The peak level of $\overline{ut}^*$ was noticeably upstream of the location of the peak $\overline{uv}^*$ levels centered at about $x/D=4$. However, the peak level of $\overline{ut}^*$ occurred downstream of the maximum mean temperature gradients which occurred over the hole, i.e., $-2<x/D<0$.

Similar to the velocity correlation results, it is important to know the behavior of the temperature-velocity correlation coefficient. Contours of the correlation coefficient R_{ut} along the jet centerline, presented in Fig. 9(b), show maximum values of $R_{ut} > 0.4$ along the jet-freestream interface. These maximum R_{ut} levels were similar to the maximum R_{uv} values, but were smaller than the thermal boundary layer value of $R_{ut} \approx 0.6$.

Contours for $\overline{vt}^*$, which is a measure of the vertical turbulent transport of thermal energy, are shown in Fig. 10(a). These contours show that $\overline{vt}^*$ is generally negative; i.e., a correlation between high temperature fluid moving towards the wall and low temperature fluid moving away from the wall. This is consistent with turbulent eddies inducing high temperature mainstream fluid towards the wall and ejecting low temperature coolant away from the wall. A local peak value of $\overline{vt}^* > -0.006$ was found centered downstream of the hole at $x/D=3$, and slightly above the jet-freestream interface line. The peak level of $\overline{vt}^*$ was slightly above the peak value for $\overline{uv}^*$ and smaller than the peak $\overline{ut}^*$ values. Over the region $1<x/D<5$, there were significantly higher levels of $\overline{vt}^*$ immediately above the jet-freestream interface line than occurred farther downstream. This region of high turbulent transport may account for the 50% decrease in adiabatic effectiveness that occurs within $x/D<5$.

The variation of R_{vt}, the temperature-velocity correlation coefficient for the normal heat flux, is shown in Fig. 10(b). Highest values of $R_{vt}=-0.4$ were found at the jet-freestream interface beyond $x/D=2$. Therefore, the correlation between the vertical velocity and temperature is small when the jet is inclined to the freestream and increases when the jet becomes parallel to the wall. This causes the $\overline{vt}^*$ product to be small near the hole exit and to increase to a maximum at $x/D=3$. Along the jet-freestream interface line, the R_{vt} values remain constant at $R_{vt}=-0.4$ beyond $x/D=3$, similar to previously presented results for R_{uv} and R_{ut}.

As shown in Eq. (2), the $\overline{vt}^*$ term is modeled using the mean temperature gradients in the y direction. These values were used to calculate values of ε_{Ty}^* and the resulting contours are shown in Fig. 11. Comparing the distribution of ε_{Ty}^* with the earlier results for ε_m^* (Fig. 8), they are found to be distinctly different. At $x/D<0$, where the freestream first impacts the coolant jet, the values of ε_{Ty}^* peaked at 0.002, which was about a factor of 2 smaller than the values of ε_m^* at the same location. Consequently the turbulent Prandtl number in this region would have a value of $\mathrm{Pr}_t > 2$. Similar high values of Pr_t occurred in region near the wall. However, by $x/D=10$, in the region immediately above the jet-freestream interface line, contours show $\varepsilon_{Ty}^* > 0.008$ while for ε_m^* contours showed $\varepsilon_m^* < 0.004$. Consequently, in this region the turbulent Prandtl number would have a value of $\mathrm{Pr}_t < 0.5$. This factor of 4 variation in measured Pr_t shows the inadequacy of computational predictions using an assumed constant value for Pr_t.

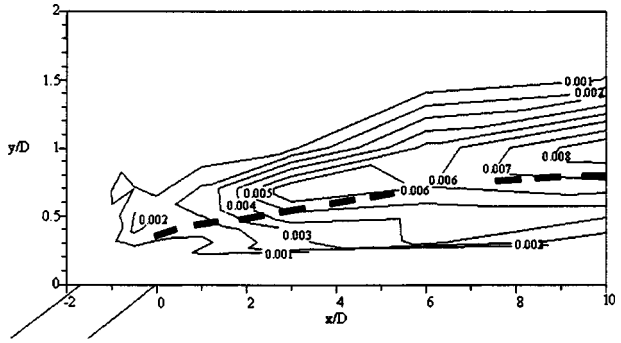

Fig. 11 Contours of ε^*_{Ty} for low freestream turbulence

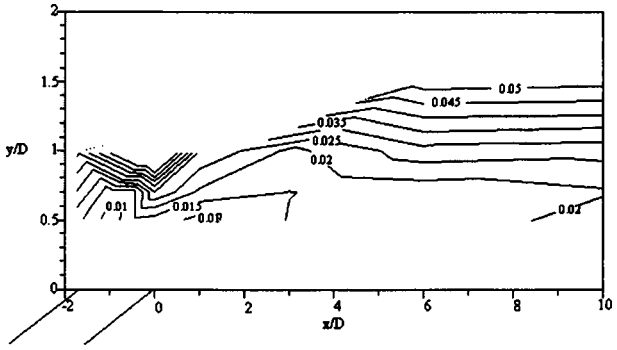

Fig. 13 Contours of ε^*_m for high freestream turbulence

Results With High Freestream Turbulence

The low freestream turbulence results showed that $\overline{ut}^*$ was much larger than $\overline{uv}^*$ and $\overline{vt}^*$, and all were high at the jet-mainstream interface. With the low freestream turbulence levels, the shear layer between the jet and mainstream was responsible for most of the turbulent stress and heat flux production. However, with high freestream turbulence, the whole flowfield, including the jet, was dominated by the freestream turbulence.

The $\overline{uv}^*$ contour levels for the high freestream turbulence results are shown in Fig. 12(*a*). Levels of high $\overline{uv}^*$ were found to extend to the maximum height measured of $y/D=2$ due to the large scale mixing of the freestream turbulence, which had an integral length scale of $\Lambda_x/D=3$, with the coolant jet. Maximum turbulent shear stress levels were found to be $\overline{uv}^*=-0.006$, which was similar to the levels found at the jet-mainstream interface for the low freestream turbulence case. A decrease in the levels is expected near the wall as the turbulence levels get damped. Clearly, the flowfield is dominated by the freestream turbulence and not by the jet-mainstream interaction as was the case with low freestream turbulence.

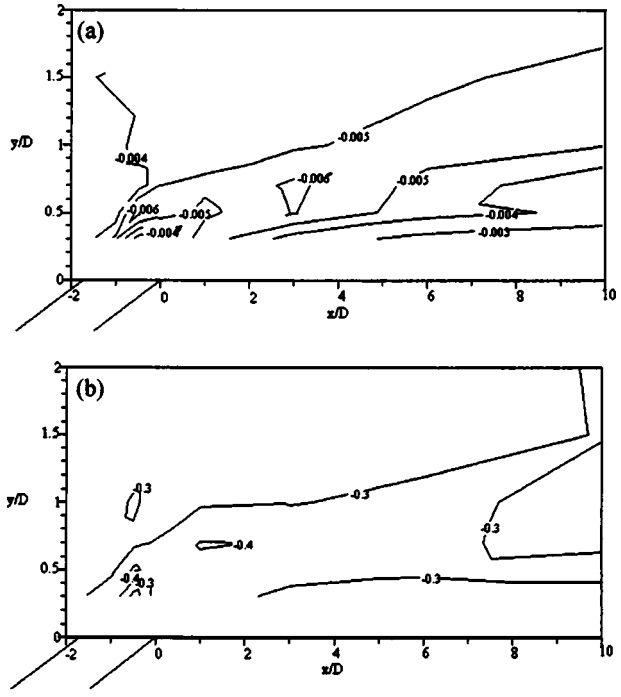

Fig. 12 (a) $\overline{uv}^*$ and (b) R_{uv} for high freestream turbulence

Results for the correlation coefficient R_{uv} on the jet centerline are shown in Fig. 12(*b*). These results shows a broad region encompassing the jet-freestream interaction line over which correlation coefficient was $R_{uv}>-0.3$. This is consistent with the $\overline{uv}^*$ levels being almost constant throughout this region. This is in contrast with the low freestream results, which showed high correlation coefficients ($-0.5\leqslant R_{uv}\leqslant -0.4$) at the jet-freestream interface and a quiescent freestream. Therefore, the high freestream turbulence causes a loss in the correlation coefficient at the jet-freestream interface. As the correlation coefficients are smaller, the higher $\overline{uv}^*$ levels are due to the higher turbulence levels present in the flow. The above results indicate that the freestream turbulence dominates over any coherent structures that might form at the jet-freestream interface.

The experimentally calculated values for ε^*_m are shown in Fig. 13. The magnitude of ε^*_m is much higher than that for low freestream turbulence, especially far away from the wall. This is due to the high $\overline{uv}^*$ occurring in regions with small velocity gradients. The increased momentum transport may be attributed to the large-scale eddies present in the flow. Any turbulence model used to simulate the flow has to account for this effect caused by the high freestream turbulence.

The results for the streamwise turbulent heat flux, $\overline{ut}^*$, on the jet centerline are shown in Fig. 14(*a*). Maximum values of $\overline{ut}^*=0.013$ were found that were significantly higher than the peak values of $\overline{ut}^*=0.009$ found with low freestream turbulence. Clearly, this enhanced turbulent transport would cause a more rapid dispersion of the film cooling jet. Another point to note is that the high turbulence levels in the freestream transport the cold jet fluid far into the freestream, which can be seen from the relatively higher location of the $\overline{ut}^*=0.001$ level.

The results for the correlation coefficient R_{ut} on the jet centerline are shown in Fig. 14(*b*). These contours indicate that the correlation coefficient has a peak value of $R_{ut}=-0.4$ similar to that for the low freestream results. However, the coefficient decays beyond $x/D=5$, while it remained at the higher levels for the low freestream turbulence case beyond $x/D=10$. This implies that the high freestream turbulence rapidly mixes out the jet reducing the R_{ut} correlation seen at the jet-freestream interface with low freestream turbulence. This combined with the rapid decay in the temperature rms levels due to high freestream turbulence causes the reduction observed in the $\overline{ut}^*$ levels for $x/D>6$.

Results for the $\overline{vt}^*$ product on the jet centerline are shown in Fig. 15(*a*). The maximum value is at $\overline{vt}^*=-0.011$, which is about twice as high compared to the peak value of $\overline{vt}^*=-0.006$ measured with low freestream turbulence. Therefore, the high freestream turbulence levels cause a very large enhancement of the vertical turbulent heat flux. With low freestream turbulence, the vertical heat flux was of the same order as that of the turbulent shear stress. However, with the addition of high freestream turbulence, the vertical turbulent heat flux is significantly enhanced,

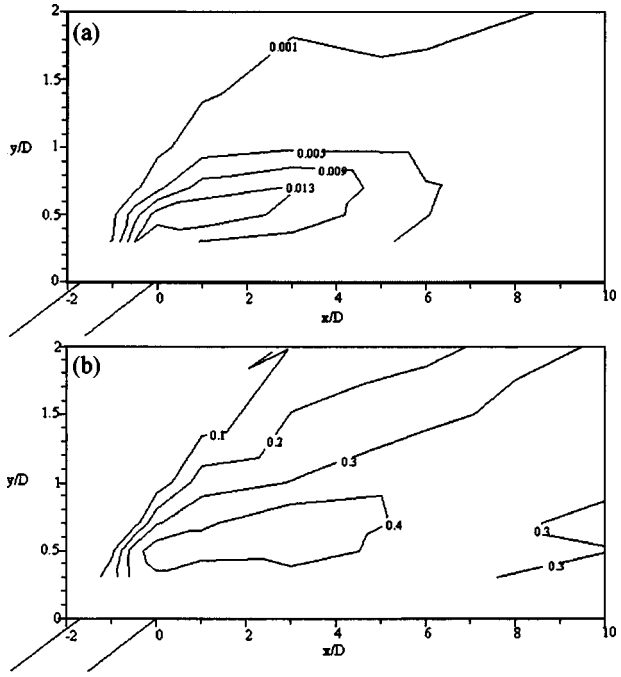

Fig. 14 (a) $\overline{ut}^*$ and (b) R_{ut} for high freestream turbulence

while the turbulent shear stress shows a marginal increase. This may be attributed to a more effective thermal transport by the large-scale eddies in the freestream than the momentum transport.

The higher $\overline{vt}^*$ levels in the flowfield imply that the vertical turbulent transport of heat is more vigorous with high freestream turbulence. The eddy diffusivity ε_{Ty}^* contours presented in Fig. 16 show much higher values compared to that for the low freestream turbulence case. This increase in ε_{Ty}^* shows the smaller effect that the mean temperature gradients have on thermal energy transport for the high freestream turbulence case. Instead, the transport is

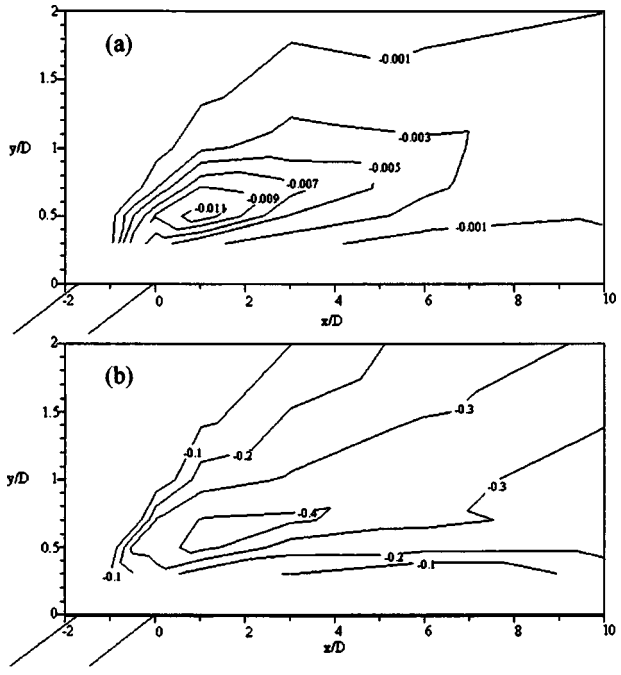

Fig. 15 (a) $\overline{vt}^*$ and (b) R_{vt} for high freestream turbulence

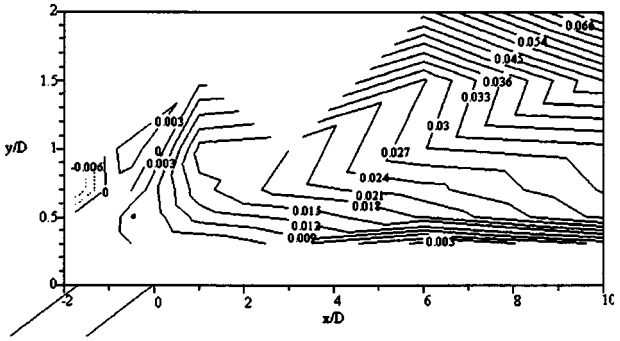

Fig. 16 Contours of ε_{Ty}^* for high freestream turbulence

driven mainly by the large-scale motions present in the flow. This large-scale eddy transport is damped by the wall as seen by the decreasing values of ε_{Ty}^* towards the wall.

Values of ε_{Ty}^* presented in Fig. 16 were generally slightly larger than values of ε_m^*, presented in Fig. 13, which were discussed previously. Comparison of the contour plots of ε_m^* and ε_{Ty}^* indicate that the turbulent Prandtl number for this flow would range from $\mathrm{Pr}_t = 0.9$ to 1.2. Hence the high freestream turbulence dominated flowfield results in relatively constant levels for turbulent Prandtl number.

Conclusions

Measurements of the $\overline{uv}$, $\overline{ut}$, and $\overline{vt}$, presented in this paper for a discrete hole film cooling flow give valuable insight into the physical mechanisms responsible for the rapid dispersion of coolant jets that occurs immediately downstream of the injection hole. Experiments were done for a single blowing ratio of $M = 0.4$ with low and high freestream turbulence. These are the first measurements of temperature velocity correlations in a film cooling flow field, and are a direct measure of the turbulent transport of thermal energy leading to the dispersion of the coolant jet. Besides the physical insight provided by these results, this study provides a valuable database for benchmarking numerical models used to predict the film cooling flowfield, including the effects of high freestream turbulence.

For low freestream turbulence conditions, measurements of $\overline{uv}$, $\overline{ut}$, and $\overline{vt}$, and the corresponding correlation coefficients R_{uv}, R_{ut}, and R_{vt}, showed that the maximum levels occurred along a line corresponding to the interface between the coolant jet and the freestream. Because of the low velocity of the coolant jet, there was a shear layer between the coolant jet and the higher velocity freestream along this interface line. Consequently, large mean velocity and mean temperature gradients occurred along this interface line. Maximum correlation coefficient levels along this interface line ranged from 0.4 to 0.5, which is similar to maximum correlation coefficient levels that occur in turbulent boundary layers and turbulent jets. Normalized turbulent shear stress $\overline{uv}^*$ and turbulent heat fluxes $\overline{ut}^*$ and $\overline{vt}^*$ were found to have localized peak values at distances that ranged from $x/D = 2$ to 4 downstream of the coolant hole. The magnitudes of these turbulent shear stresses and heat fluxes were a factor of two larger than typical values for turbulent boundary layers and jets. This may account for the strong dispersion of the coolant jet in this region.

The measured temperature and velocity correlations and mean velocity and temperature profiles were used to calculate distributions of eddy viscosity ε_m and diffusivity ε_{Ty}. These distributions were used to determine the spatial variation of turbulent Prandtl number Pr_t. Generally values of $\mathrm{Pr}_t \approx 2$ were found, but some regions of the flow had much lower values of $\mathrm{Pr}_t \approx 0.5$. This is an

important finding from this study, showing that the commonly assumed constant value of $Pr_t \approx 1$ would be completely inadequate.

For high freestream turbulence conditions, contours of $\overline{uv}$, $\overline{ut}$, and $\overline{vt}$ did not show the distinct maximum values along the jet-freestream interface line that were evident for the low freestream turbulence conditions. Furthermore, correlation coefficients R_{uv}, R_{ut}, and R_{vt} were reduced in magnitude. However, magnitudes of $\overline{ut}$ and $\overline{vt}$ were significantly higher than for the low freestream turbulence condition, reflecting the enhanced thermal transport that occurred with high freestream turbulence. Eddy viscosities and diffusivities were much larger for the high freestream turbulence than for the low freestream turbulence. This was attributed to increased transport by large scale turbulent eddies. Finally, the turbulent Prandtl numbers for the high freestream turbulence condition were relatively constant over the flowfield with a value of $Pr_t \approx 1$.

Nomenclature

D = diameter of film cooling hole
DR = density ratio $= \rho_c / \rho_\infty$
H = shape factor $= \delta^*/\theta$
I = momentum flux ratio $= (\rho_c U_c^2)/(\rho_\infty U_\infty^2)$
L = length of film cooling hole
LDV = Laser Doppler velocimeter
M = blowing ratio $= (\rho_c U_c)/(\rho_\infty U_\infty)$
P = pitch distance between cooling holes
Pr_t = turbulent Prandtl number (see Eq. (3))
R_{uu} = correlation coefficient $= \overline{uu}/(u_{rms} u_{rms})$
R_{uv} = correlation coefficient $= \overline{uv}/(u_{rms} v_{rms})$
R_{ut} = correlation coefficient $= \overline{ut}/(u_{rms} t_{rms})$
R_{vt} = correlation coefficient $= \overline{vt}/(v_{rms} t_{rms})$
Re_θ = momentum thickness Reynolds number
TL = turbulence level $= (u_{rms}^2 + v_{rms}^2)^{1/2}/U_\infty$
U = average velocity
VR = velocity ratio $= U_c/U_\infty$
d = diameter of cold wire
l = length of cold-wire
pdf = probability density function
t = fluctuating temperature
$\overline{ut}^*$ = normalized turbulent heat flux in x direction $= \overline{ut}/(U_\infty(T_c - T_\infty))$
$\overline{uv}^*$ = normalized shear stress $= \overline{uv}/(U_\infty)^2$
$\overline{vt}^*$ = normalized turbulent heat flux in y direction $= \overline{vt}/(U_\infty(T_c - T_\infty))$
x = axial coordinate
y = wall normal coordinate
δ = boundary layer thickness
δ^* = displacement thickness
ε_m^* = normalized eddy viscosity $= \varepsilon_m / DU_\infty$
ε_{Tx}^* = normalized eddy diffusivity $= \varepsilon_{Tx} / DU_\infty$
ε_{Ty}^* = normalized eddy diffusivity $= \varepsilon_{Ty} / DU_\infty$
η = adiabatic wall effectiveness $= (T_{aw} - T_\infty)/(T_c - T_\infty)$
Λ_x = integral streamwise length scale of mainstream
ρ = density
Θ = normalized mean temperature $= (T - T_\infty)/(T_c - T_\infty)$
Θ' = normalized fluctuation temperature $= t/(T_c - T_\infty)$

Subscripts

aw = adiabatic wall
c = coolant
rms = root-mean-square
∞ = mainstream

References

[1] Walters, D. K., and Leylek, J. H., 1997, "A Systematic Computational Methodology Applied to a Three-Dimensional Film-Cooling Flowfield," ASME J. Turbomach., **119**, pp. 777–785.
[2] Andreopoulos, J., and Rodi, W., 1984, "Experimental Investigation of Jets in a Crossflow," J. Fluid Mech., **138**, pp. 93–127.
[3] Pietrzyk, J. R., 1989, "Experimental Study of the Interaction of Dense Jets With a Crossflow for Gas Turbine Applications," Ph.D. thesis, The University of Texas at Austin, Austin, TX.
[4] Kaszeta, R. W., and Simon, T. W., 1999, "Measurement of Eddy Diffusivity of Momentum in Film Cooling Flows With Streamwise Injection," ASME paper No. 99-GT-37.
[5] Kohli, A., and Bogard, D. G., 1998, "Fluctuating Thermal Field in the Near Hole Region for Film Cooling Flows," ASME J. Turbomach., **120**, pp. 86–91.
[6] Kohli, A., and Bogard, D. G., 1998, "Effects of Very High Freestream Turbulence on the Jet-Mainstream Interaction in a Film Cooling Flow," ASME J. Turbomach., **120**, pp. 785–790.
[7] Kohli, A., 1996, "Experimental Investigation of the Jet-Mainstream Interaction in Film Cooling Flow With Different Freestream Condition," Ph.D. thesis, The University of Texas at Austin, Austin, TX.
[8] Thole, K. A., Bogard, D. G., and Whan-Tong, J. L., 1994, "Generating High Freestream Turbulence Levels," Exp. Fluids, **17**, pp. 374–380.
[9] Thole, K. A., Sinha, A. K., Bogard, D. G., and Crawford, M. E., 1992, "Mean Temperature Measurements of Jets With a Crossflow for Gas Turbine Film Cooling Application," *Rotating Machinery Transport Phenomena*, J. H. Kim and W. J. Yang, eds., Hemisphere Publishing Corp., New York.
[10] Chapra, S. C., and Canale, R. P., 1988, *Numerical Methods for Engineers*, 2nd ed., McGraw-Hill, New York.
[11] Thole, K. A., 1992, "High Freestream Turbulence Effects on the Transport of Heat and Momentum," Ph.D. thesis, The University of Texas at Austin, Austin, TX.
[12] Thole, K. A., and Bogard, D. G., 1994, "Simultaneous Temperature and Velocity Measurements," Meas. Sci. Technol., **5**, pp. 435–439.
[13] Chen, C. P., and Blackwelder, R. F., 1978, "Large-Scale Motion in a Turbulent Boundary Layer: A Study Using Temperature Contamination," J. Fluid Mech., **89**, Part 1, pp. 1–31.
[14] Subramanian, C. S., and Antonia, R. A., 1981, "Effect of Reynolds Number on a Slightly Heated Turbulent Boundary Layer," Int. J. Heat Mass Transfer, **24**, No. 11, pp. 1833–1846.
[15] Perry, A. E., and Hoffman, P. H., 1976, "An Experimental Study of Turbulent Convective Heat Transfer From a Flat Plate," J. Fluid Mech., **77**, Part 2, pp. 355–368.
[16] Pope, S. B., 2000, *Turbulent Flows*, Cambridge University Press, Cambridge, UK.

Film-Cooling Effectiveness on a Gas Turbine Blade Tip Using Pressure-Sensitive Paint

Jaeyong Ahn

Shantanu Mhetras

Je-Chin Han
M.C. Easterling Endowed Chair
e-mail: jchan@mengr.tamu.edu

Turbine Heat Transfer Laboratory, Department of Mechanical Engineering, Texas A&M University College Station, Texas 77843-3123

Effects of the presence of squealer, the locations of the film-cooling holes, and the tip-gap clearance on the film-cooling effectiveness were studied and compared to those for a plane (flat) tip. The film-cooling effectiveness distributions were measured on the blade tip using the pressure-sensitive paint technique. Air and nitrogen gas were used as the film-cooling gases, and the oxygen concentration distribution for each case was measured. The film-cooling effectiveness information was obtained from the difference of the oxygen concentration between air and nitrogen gas cases by applying the mass transfer analogy. Plane tip and squealer tip blades were used while the film-cooling holes were located (a) along the camber line on the tip or (b) along the tip of the pressure side. The average blowing ratio of the cooling gas was 0.5, 1.0, and 2.0. Tests were conducted with a stationary, five-bladed linear cascade in a blow-down facility. The free-stream Reynolds number, based on the axial chord length and the exit velocity, was 1,138,000, and the inlet and the exit Mach numbers were 0.25 and 0.6, respectively. Turbulence intensity level at the cascade inlet was 9.7%. All measurements were made at three different tip-gap clearances of 1%, 1.5%, and 2.5% of blade span. Results show that the locations of the film-cooling holes and the presence of squealer have significant effects on surface static pressure and film-cooling effectiveness, with film-cooling effectiveness increasing with increasing blowing ratio. [DOI: 10.1115/1.1909208]

Introduction

The concept of cooling a surface subjected to high mainstream temperatures by perforating the surface with several discrete holes and passing cold air (film cooling) through them is a popular technique used in several applications. The surface under test can be maintained at a cooler temperature due to formation of a thin protective film of relatively colder air on the surface. This technique has been successfully employed for cooling of gas turbine blades subjected to very high mainstream gas temperatures. A high and uniform film-cooling effectiveness on the blade surface will ensure superior performance and thermal fatigue life for the blade, thus making it an important parameter in its design.

Hot gases from the combustor enter the turbine, resulting in a significant heat load on the turbine components. One of the components more susceptible to thermal failure is the blade tip region because of its severe environment and difficulty in cooling. Large leakage flow occurs on the tip because of a high pressure differential from pressure to suction side. This leakage mass flow can be reduced by using a labyrinthlike recessed cavity also known as the squealer tip. Presence of film cooling on the tip further reduces heat transfer from the mainstream gas to the blade tip. A comprehensive compilation of the available cooling techniques used in the gas turbine industry has been encapsulated by Han et al. [1].

Experimental investigations performed in the general area of film cooling on a blade tip are limited, with very few papers available in open literature. Most recently, Kwak and Han [2,3] studied the local heat transfer distribution and film-cooling effectiveness using the hue-detection-based transient liquid-crystal technique on the blade tip for plane and squealer tip geometry. A GE-E^3, five-blade linear cascade was used similar to the one used in the present paper. They used three tip-gap clearances (1.0%, 1.5%, and 2.5% of blade span) along with three average blowing ratios (0.5, 1.0, and 2.0) for the coolant. Increasing blowing ratio increased film effectiveness, but overall heat transfer coefficients decreased. Their results also showed that the squealer geometry showed higher film-cooling effectiveness and lower heat transfer coefficients compared to the plane tip geometry because of its smaller leakage flow.

Film cooling on a blade tip was also studied by Kim et al. [4] and Kim and Metzger [5] by using a two-dimensional (2D) rectangular tip model used to simulate leakage flow between the tip and the shroud. Various film-cooling configurations were examined using a transient liquid-crystal technique, and the results for heat transfer coefficients and film-cooling effectiveness were reported.

There are many papers available in open literature that discuss heat transfer coefficients on the blade tip and near tip regions. Heat transfer coefficients on the blade tip and the shroud were measured by Metzger et al. [6] using heat flux sensors in a rotating turbine rig. Dunn and Haldeman [7] measured time-averaged heat flux at a recessed blade tip for a full-scale rotating turbine stage at transonic vane exit conditions. Their results showed that the heat transfer coefficient at the mid and rear portion of the cavity floor is of the same order as the blade leading-edge value. Bunker et al. [8] utilized a hue detection-based liquid-crystal technique to obtain local heat transfer distributions on the blade tip. They studied the effects of tip-gap clearance and free-stream turbulence intensity levels. Bunker and Baily [9] studied the effect of squealer cavity depth and oxidation on turbine blade tip heat transfer. Azad et al. [10,11] used a transient liquid-crystal technique to study heat transfer. They compared squealer tip and plane tip geometry and concluded that the overall heat transfer coefficients were lower for the squealer tip case. Heat transfer coefficient distributions for plane and squealer tip and near tip regions were presented by Kwak and Han [12,13]. By using a squealer tip, heat transfer was found to decrease on the tip and near tip regions. Azad et al. [14] and Kwak et al. [15] also investigated the heat transfer on several different squealer geometries. They found that a suction-side squealer tip gave the lowest heat transfer among all cases studied.

Investigations comparing a rotating and stationary shroud were performed by Mayle and Metzger [16]. They noted that the effect

Contributed by the Heat Transfer Division of ASME for publication in the JOURNAL OF HEAT TRANSFER. Manuscript recieved July 28, 2004. Final maunscript received October 20, 2004. Review conducted by Phillip M. Ligrani.

of shroud rotation could be neglected to measure the blade tip heat transfer over the entire range of parameters considered in the study. Heyes et al. [17] studied tip leakage flow on plane and squealer tips in a linear cascade and concluded that the use of a squealer tip, especially a suction-side squealer tip, was more beneficial than a flat tip. Local heat transfer coefficients on a turbine blade tip model with a recessed cavity (squealer tip) were studied by Yang and Diller [18] in a stationary linear cascade. Based on measurements at a single point on the cavity floor, they reported that heat transfer coefficients were independent of the tip-gap height.

Heat transfer coefficients and static pressure distributions of a large-scale turbine blade tip were measured by Teng et al. [19] in a low-speed wind tunnel facility using a transient liquid-crystal technique. Saxena et al. [20] investigated the effect of various tip-sealing geometries on blade tip leakage flow and heat transfer of a scaled-up HP turbine blade in a low-speed wind tunnel facility using a steady-state HSI-based liquid-crystal technique. They found that the trip strips placed against the leakage flow produce the lowest heat transfer on the tips compared to all the other cases. Mass transfer technique was used by Papa et al. [21] to study local and average mass/heat transfer distributions on a squealer tip and winglet-squealer tip in a low-speed wind tunnel. Jin and Goldstein [22,23] also used this technique on a simulated high-pressure turbine blade tip and near tip surfaces. They concluded that the average mass transfer from the tip surface was much higher than that on pressure- and suction-side surfaces.

Some numerical investigations have also been carried out to study heat transfer and film-cooling effectiveness on blade tip. Effects of tip clearance and casing recess on heat transfer and stage efficiency for several squealer blade tip geometries were predicted by Ameri et al. [24]. Numerical results for heat transfer and flow obtained by Ameri et al. [25] were compared to the experimental results from Bunker et al. [8] for a power-generation gas turbine. Ameri and Rigby [26] also calculated heat transfer coefficients and film-cooling effectiveness on turbine blade models.

Numerical techniques were also utilized by Yang et al. [27,28] to study flow and heat transfer past a turbine blade with plane and squealer tip. Film-cooling effectiveness for a flat and squealer blade tip with film-cooling holes on tip pressure side were predicted by Acharya et al. [29]. Effects of different hole locations on film-cooling effectiveness and heat transfer were predicted by Yang et al. [30]. Hohlfeld et al. [31] predicted film-cooling flow from dirt purge holes on a turbine blade tip. They found that the flow exiting the dirt purge holes helped in blocking the leakage flow across the gap. As the blowing ratio increased for a large tip gap, tip cooling increased only slightly, whereas film cooling on the shroud increased significantly.

Pressure-sensitive paint (PSP) has been widely used to measure local pressure distributions on a surface. Several papers are available in the literature that discuss the application of the PSP technique. Morris et al. [32] and McLachlan and Bell [33] discuss its applications to aerodynamics. Algorithms for image registration and reselection for PSP have been developed by Donovan et al. [34] and Bell and McLachlan [35]. Zhang and Fox [36], Zhang et al. [37], and Zhang and Jaiswal [38] conducted experimental work by applying the PSP technique to measure the local film-cooling effectiveness distribution on the flat plate, nozzle, and endwall region by using air and nitrogen as coolants.

The motivation for this study was to do a parametric investigation on the effect of blowing ratio, tip-gap clearance, and tip geometry on the pressure and the film-cooling effectiveness on the blade tip for plane as well as squealer geometry. Although the hue-detection-based transient liquid-crystal technique has been used by Kwak and Han [2,3] to study the detailed local film-cooling effectiveness, it is hindered by conduction effects near sharp edges, such as a film-cooling hole, resulting in relatively large errors in that region. Moreover, they used a blow-down facility where the flow needed some time (2.5 s) to reach the expected steady value and during that developing time, the unavoidable mainstream initial flow affected the blade tip initial temperature. Considering the high heat transfer coefficient and short experiment time, the error from the initial developing time can affect blade tip heat transfer and film-cooling effectiveness. However, the PSP technique is based on mass transfer analogy, no heating of the test section or coolant is required, and the tests are performed under steady flow conditions. Thus, conduction errors at the edges and initial temperature errors are avoided.

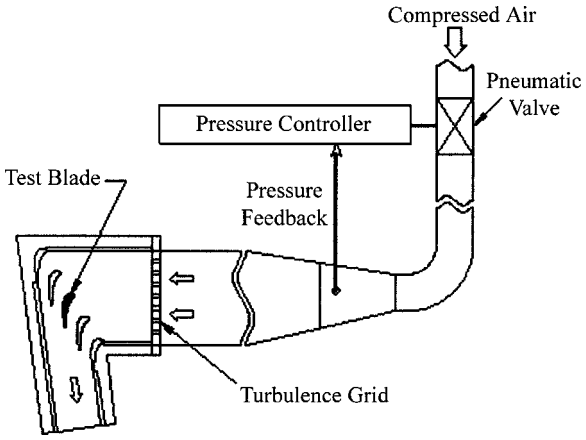

Fig. 1 Schematic of test section and blow-down facility

A scaled-up blade tip model of a first stage rotor blade (GE-E^3) of a modern aircraft gas turbine was used in a five-blade linear cascade with the center blade tip coated with PSP. The same test section and flow loop was used by Kwak and Han [2,3] but instead of PSP, the blade tip was coated with liquid crystal. Experiments were carried out to study pressure and effectiveness for plane and squealer blade tip for tip clearances of 1.0%, 1.5%, and 2.5% of blade span with the average blowing ratios of 0.5, 1.0, and 2.0. A row of seven film-cooling holes has been used on the blade tip camber line and pressure side as opposed to a row of 13 holes used by Kwak and Han [2,3]. Individual as well as combined effects of these two rows have been studied. The experimental results for pressure and effectiveness will aid future engineers to design more efficient turbine blades and help to validate CFD codes.

Experimental Setup

The test section consisted of a five-blade linear cascade with blade tip profiles placed in a blow-down loop. A schematic of the test section and the blow-down loop is shown in Fig. 1. Inlet cross section of the test section was 31.1 cm (width)×12.2 cm (height). A turbulence-generating grid (rectangular bar mesh type) with a porosity of 57% was placed before the inlet. Turbulence intensity was recorded 6 cm upstream of the middle blade (or 20.7 cm downstream of the grid) using a hot-wire probe. Turbulence intensity (Tu) at this location was found to be 9.7% due to the presence of the grid and turbulence length scales were estimated to be 1.5 cm, which is slightly larger than the grid bar size. The bottom and sides on the test section were machined out of 1.27 cm thick polycarbonate sheets, whereas a 1.27 cm thick acrylic plate was used for the top for better optical access to the blade tip. The top plate also acted as a shroud for the blades. A 12-bit, scientific-grade CCD (charge-coupled device) camera, which could maintain a constant CCD temperature (−15°C), was mounted above the test section and was used to record the images. Flow conditions in adjacent passages of the center blade were ensured to be identical by adjusting the trailing-edge tailboards for the cascade. A comprehensive discussion on the flow conditions, including

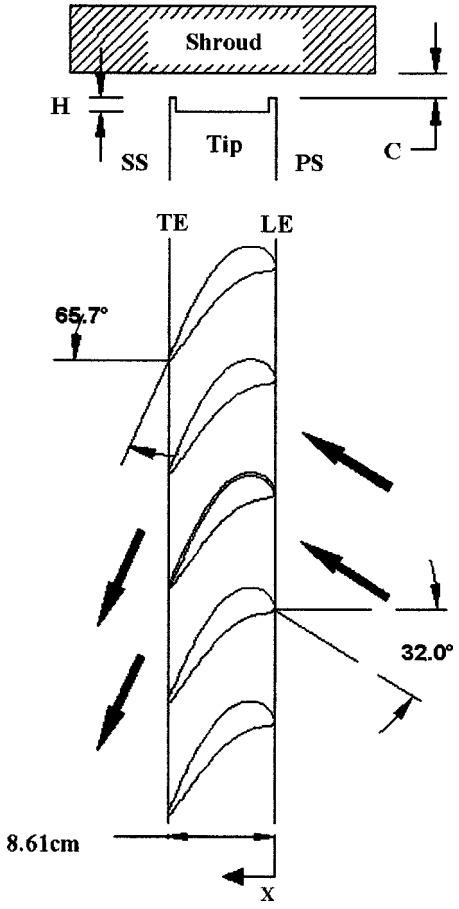

Fig. 2 Definition of blade tip and shroud

flow periodicity in the cascade and pressure distribution along the blade has been reported by Kwak and Han [12,13] and Azad et al. [10,11].

During the blow-down test, the cascade inlet air velocity and exit velocity were 85 and 206 m/s, respectively. The Reynolds number based on the axial chord length and exit velocity was 1.138×10^6. Overall pressure ratio (P_t/P) was 1.28 (where P_t is inlet total pressure and P is exit static pressure) and inlet and exit Mach numbers were 0.25 and 0.6, respectively. The pressure ratio and exit Mach number are slightly higher than those reported by Kwak and Han [12,13]. The blow-down facility could maintain steady flow in the cascade for about 40 s. Compressed air stored in tanks entered a high-flow pneumatic control valve, which could maintain steady flow by receiving downstream pressure feedback. The control valve could maintain a velocity within ±3% of desired value.

All five blades placed in the test section were made of aluminum. A 3X scaled model of the GE-E^3 blade was used with a blade span of 12.2 cm and an axial chord length of 8.61 cm. Since the blades were placed in a linear cascade, they were machined for a constant cross section for its entire span, corresponding to the tip profile of the actual GE-E^3 blade. Figure 2 shows the blade profiles, the inlet and exit angles for air, and the blade tip and shroud definitions. The middle blade was instrumented and was made in two sections. Figure 3 shows the film-cooling measurement blade. The lower portion of the blade was made of aluminum with one through hole for passage of the coolant air. The upper portion consisted of an aluminum rim with an internal cavity and an outer shell made of polycarbonate with low thermal conductivity. Seven film-cooling holes were provided for coolant to pass through on the airfoil pressure side and on the tip. Figures 4(*a*) and 4(*b*) show

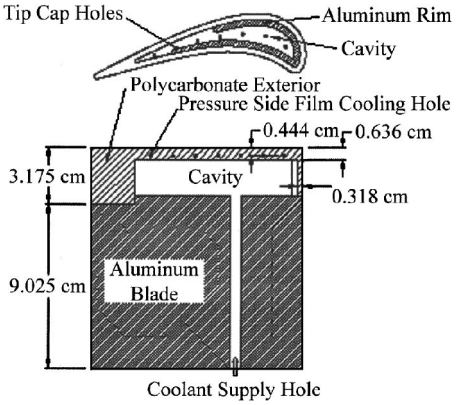

Fig. 3 Film-cooling measurement blade

the detailed geometry of the film-cooling holes and their orientation on the pressure side and on the blade tip for plane tip and squealer tip, respectively. Tip holes were drilled vertically along the camber line, whereas pressure-side holes were located 0.444 cm below the tip surface at an angle of 30° with respect to the airfoil pressure surface. Diameter (d) of all the film-cooling holes was 0.127 cm and distance between each hole was 1.27 cm ($10d$). The blade with squealer tip had a recess of 4.22% of blade span (0.508 cm).

This study was performed for three different tip gaps corresponding to 1.0%, 1.5%, and 2.5% of blade span (12.2 cm). The tip gaps thus obtained are 1.31, 1.97, and 3.29 mm, respectively. Gaskets of these thicknesses were prepared and placed on top of the side walls, the trailing-edge tailboards, and two outer guide blades to realize these tip gaps. These tip gaps were maintained on the middle three blades. Experiments were performed with three different blowing ratios (M) of 0.5, 1.0, and 2.0 for each tip gap. During testing, it was observed that actual velocity of the leakage flow and coolant air could vary with the location and mass flow rate of the coolant. For this reason, the blowing ratio was defined as $M=\rho_c V_c/\rho_m V_{\text{avg}}$. Here, V_{avg} and V_c are the averaged velocity

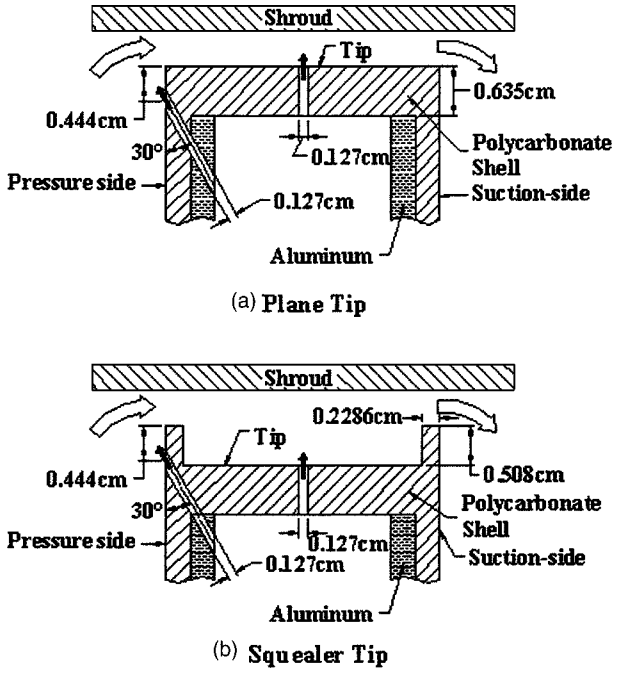

Fig. 4 Geometry of film-cooling holes

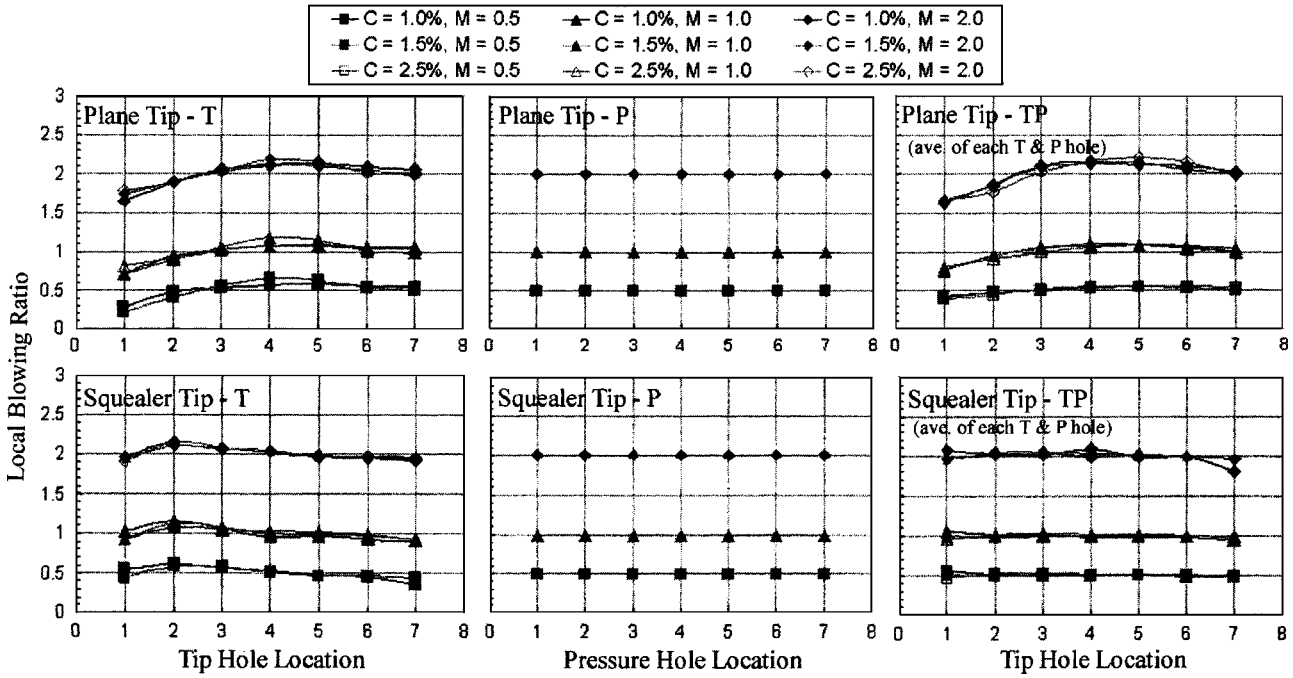

Fig. 5 Local blowing ratio for plane and squealer tip

of the cascade inlet and exit velocity and averaged coolant velocity, respectively, while ρ_m and ρ_c are the densities of mainstream and coolant air, respectively. If the density is same, the ratio is reduced to a velocity ratio.

To better explain the results for effectiveness, local blowing ratios through each of the seven holes on the tip and airfoil pressure side have been plotted in Fig. 5. Local blowing ratio was calculated by using the pressure differential for each hole. The static pressure in the cavity inside the blade was measured using three static pressure taps. The static pressure distribution was found to be uniform in the coolant cavity and was then compared to the static pressure distribution on the tip and pressure-side surfaces. The local pressure distribution for tip was found using PSP, whereas static pressure taps located at 97% of blade span were used to measure static pressure on the pressure side. The discharge coefficient, C_D was assumed to be the same for all the holes on a surface as it depends on the hole geometry. By knowing total mass flow rate of the coolant, discharge coefficient and pressure differential for each hole, the local blowing ratio, M_i was calculated. For the cases with tip and pressure-side injection, static pressures on the tip and pressure side were averaged for each hole location *i*.

From Fig. 5, for coolant injection for tip holes, the squealer tip shows a more uniform distribution of mass flux as compared to plane tip. The uniform distribution of coolant flow through pressure-side holes is mainly due to more or less constant static pressure on the airfoil pressure side. Since internal and external pressures for the pressure-side film holes are constant, the coolant flow rate is found to be uniform. The blowing ratio indicated for tip and pressure-side injection represents the average of the blowing ratio for each corresponding tip and pressure-side hole. The average blowing ratios thus obtained are similar to those for only tip injection, indicating a minor effect of pressure-side coolant injection.

Film-Cooling Effectiveness Measurement Theory and Data Analysis

Pressure-sensitive paint (PSP) was used to measure the film-cooling effectiveness on the blade tip. PSP is a photoluminescent material that emits light with intensity proportional to the surrounding partial pressure of oxygen. Any pressure variation on the PSP-coated surface causes emitting light intensity to change because of an oxygen-quenching process. A CCD camera measures this change of intensity. A calibration performed for intensity ratio to give pressure ratio gives pressure information. To measure the film-cooling effectiveness and to obtain the intensity ratio from PSP, four kinds of images are required. A reference image (with illumination, no mainstream flow, surrounding pressure uniform at 1 atm), an air image (with illumination and mainstream flow, air used as coolant), an air/nitrogen image (with illumination and mainstream flow, nitrogen gas used as coolant), and a black image (no illumination and no mainstream and coolant flow) to remove noise effects due to the camera.

Oxygen partial pressure information is obtained from the intensity ratio and calibration curve. This oxygen partial pressure information can be directly converted into static pressure distribution for the case with air coolant injection. Intensity ratio for air and air-nitrogen mixture is calculated using Eqs. (1) and (2), respectively,

$$\frac{I_{\text{ref}}-I_{\text{blk}}}{I_{\text{air}}-I_{\text{blk}}}=\text{func}((P_{O_2})_{\text{air}}) \quad or \quad \text{func}(P) \tag{1}$$

$$\frac{I_{\text{ref}}-I_{\text{blk}}}{I_{\text{mix}}-I_{\text{blk}}}=\text{func}((P_{O_2})_{\text{mix}}) \tag{2}$$

where I denotes the intensity obtained for each pixel for reference (ref), black (blk), air and air-nitrogen (mix) images and func(P) is the relation between intensity ratio and pressure ratio obtained after calibrating the PSP. $(P_{O_2})_{\text{air}}$ and $(P_{O_2})_{\text{mix}}$ are the partial pressures of oxygen on the test surface for air and air-nitrogen mixture images, respectively.

The film-cooling effectiveness can be expressed as a ratio of oxygen concentrations measured by PSP and is calculated using the following equation:

$$\eta=\frac{Co_{\text{air}}-Co_{\text{mix}}}{Co_{\text{air}}}=\frac{(P_{O_2})_{\text{air}}-(P_{O_2})_{\text{mix}}}{(P_{O_2})_{\text{air}}} \tag{3}$$

where Co_{air} and Co_{mix} are the oxygen concentrations of mainstream air and air-nitrogen mixture on the test surface, respec-

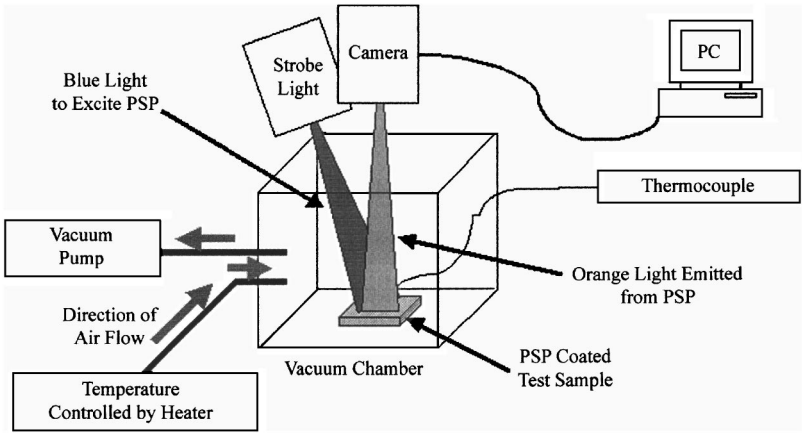

Fig. 6 Calibration setup for PSP

tively. By assuming the molecular weights of air and nitrogen as the same, effectiveness can be expressed as a ratio of partial pressures of oxygen due to proportionality between concentration and partial pressure.

The PSP-coated blade tip was illuminated by a strobe light fitted with an optical filter. Light emerging from this filter was blue light with a center wavelength of 460 nm and a bandwidth of 20 nm. A 12-bit scientific-grade CCD camera (high-speed Sensicam with CCD temperature maintained at −15°C using two-stage Peltier cooler) with an exposure time of 1 ms was employed to measure emitting light intensity. An optical 590 nm long pass filter was placed in front of the camera to record orange light emitting from the PSP. Optical filters were chosen to match the wavelengths for excitation (blue) and return (orange) signals for the PSP. Special care was taken in choosing the wavelength range of the filters to avoid any overlap of the ranges, so that the camera could detect only the excited light from PSP and not the reflected light from the light source. The camera and the strobe light were triggered at the same time by a 20 Hz trigger signal.

The PSP-coated blade tip surface was constructed by first coating the blade tip with enamel-based white paint and then layering it with PSP. Calibration for the PSP was conducted inside a vacuum chamber. Figure 6 depicts a schematic of the calibration setup. Air was removed from the chamber by a vacuum pump and the intensity from the PSP-coated test plate was recorded at different pressures ($P < P_{ref} = 1$ atm). Pressure was varied from 0 to 1 atm. The same optical components, strobe light, and camera were used in the calibration. There is a temperature dependency of PSP. However, if the intensity is normalized by that of the reference image (at 1 atm), the calibration curves, at different temperatures fall into one curve. Figure 7 shows the calibration curve of intensity ratio versus pressure ratio, which is found to be linear down to a ratio of 0.35. During testing, it was ensured that temperatures of mainstream air, coolant, and test section were the same, while taking reference, air, and nitrogen images to minimize uncertainty. Thermocouples (T-type) located upstream of the test section and in the coolant flow recorded temperatures of air and nitrogen gas. Experiments were conducted in an air-conditioned room (20°C) and temperatures of mainstream air, coolant air, and nitrogen gas were maintained at 20°C.

Coolant mass flow was set using a Rota-meter to a flow rate corresponding to the blowing ratio. A pneumatic valve was opened and the pressure controller was set to the desired flow rate for the mainstream air. A function generator was used to generate TTL trigger signal for camera and strobe light. The images were taken when the mainstream flow was fully developed, i.e., after the initial developing time for flow (~15 s). After the images were captured, the pneumatic valve was closed. The duration of a single experiment was about 30 s.

Images obtained from the camera were saved as TIF images, and a program created to calculate the average intensity value at each image pixel was executed. 200 images (10 s at 20 Hz) were captured for each case and the average pixel intensity was calculated from these images. Another program was used to convert the intensity magnitudes to partial pressure of oxygen and then to film-cooling effectiveness. Results obtained for each pixel were plotted as contour plots and are presented.

Uncertainty calculations were performed based on a confidence level of 95% and are based on the uncertainty analysis method of Coleman and Steele [39]. The uncertainty for effectiveness is estimated to be 7%, which arises due to an uncertainty of about 5% in the partial pressures of oxygen. This uncertainty is the result of uncertainties in calibration (4%) and image capture (1%). Uncertainties for very low effectiveness magnitudes may be higher. Uncertainties for the blowing ratios are estimated to be 4%.

Pressure Ratio Results

Local pressure ratio (P_t/P) distributions on plane and squealer tip for coolant injection through tip holes only (T case) for $C = 2.5\%$ are shown in Fig. 8. Pressure distributions for all cases were not included due to space restrictions. Typical distributions are displayed in Fig. 8. The inlet total pressure was 147.39 kPa, and the exit static pressure was 115.27 kPa.

Pressure Ratio Distributions for Plane Blade Tip. Pressure distributions help indicate the possible paths of the tip-gap leakage flow. For plane tip, the pressure ratio is higher near the tip pressure side (20–80% of chord region) indicating high leakage flow velocities on the tip. The pressure ratios near the leading edge of the blade are low, indicating lower velocities. Presence of

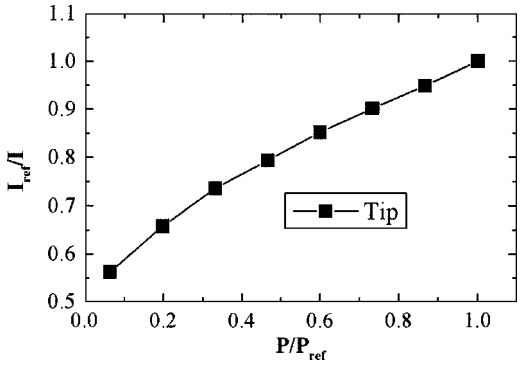

Fig. 7 Calibration curve for PSP

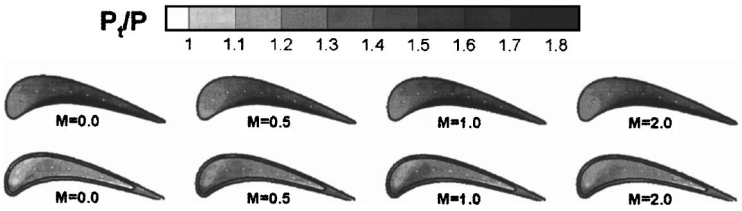

Fig. 8 Distributions of pressure ratio (P_t/P) for plane blade tip (top row) and squealer blade tip (bottom row) for coolant injection through tip holes only (T case) and $C=2.5\%$

film-cooling jets may result in a blockage effect, which might reduce the leakage flow through the tip gap. The plane tip pressure ratio distributions show slightly lower magnitudes with increasing blowing ratio, indicating the presence of this blockage effect.

Pressure Ratio Distributions for Squealer Blade Tip. Figure 8 also shows pressure ratio distributions for the squealer blade tip. The pressure ratio on the squealer surface inside the cavity is lower as compared to the plane tip, indicating lower velocities on the surface, suggesting the presence of a recirculation zone. The leakage flow reattaches at the base of the rim near the suction side and then the flow progresses toward the downstream pressure side of the cavity. Numerical simulation of the same geometry performed by Yang et al. [28] depicts flow path lines in the squealer tip, which correlate well with the experimental observations. High leakage flow occurs at about 15–35% of blade chord. For cases with squealer tip, the change in the pressure ratios with changing blowing ratio is muted. It can also be noted that pressure ratio distributions closely resemble the local heat transfer distributions [2,3] for both plane and squealer tip cases.

Film-Cooling Effectiveness Results

Film-Cooling Effectiveness Results for Plane Blade Tip Figure 9 shows film-cooling effectiveness distribution for plane blade tip. The first three rows in the figure include results for tip only (T) coolant injection, middle three rows for pressure side only (P) coolant injection, and the last three rows for tip (camber line) and pressure-side (TP) coolant injection. For each case, a set of three different tip gap clearances (C) of 1.0% (10), 1.5% (15), and 2.5% (25) are shown arranged columnwise. Results for blowing ratios of 0.5 (05), 1.0 (1), and 2 (2) for each tip-gap clearance are also presented row-wise in Fig. 9. Notations used in the figures are indicated by the numbers in parentheses above. Thus,

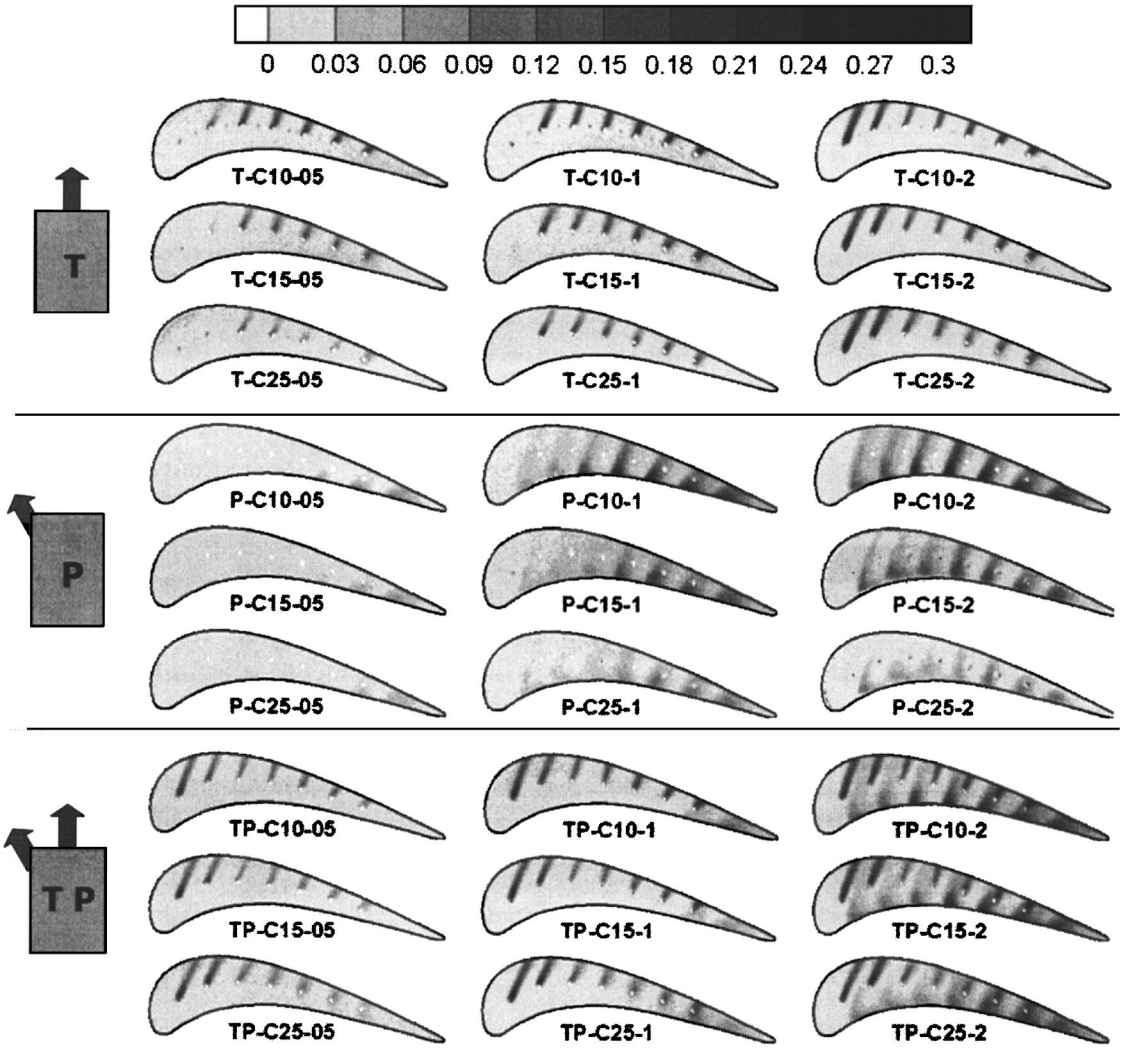

Fig. 9 Film-cooling effectiveness distribution on plane blade tip

TP-C15-2 corresponds to the case with coolant injection from tip as well as pressure side, for a tip-gap clearance of 1.5% and blowing ratio, $M=2$. Same notation has been used in all figures with plots of film-cooling effectiveness.

The maximum film-cooling effectiveness among all cases in Fig. 9 is about 0.3 with the maximum value occurring immediately downstream of the holes. As blowing ratio increases from $M=0.5$ to $M=2$, overall film-cooling effectiveness increases. This is due to higher mass flow rate of the coolant injected through the holes resulting in a larger film-covered area. The film-covered area extends further downstream with a more visible trace for film-cooling effectiveness as blowing ratio increases. The increase in magnitude is higher for tip holes (T and TP) closer to the leading and trailing edges as compared to midchord holes for higher blowing ratios ($M=1$ and 2), which can be attributed to smaller leakage flow in this region. The relatively lower increase in film-cooling effectiveness at 30–40% of chord region may be due to high leakage flow, which may dilute the injected coolant with the leakage flow. Besides, coolant injection at 90° to the blade tip surface is more prone to dilution with the mainstream flow, thus lowering effectiveness.

For TP cases, since number of film-cooling holes is double, the total mass flow rate was also set at two times that for T and P cases. Thus, average blowing ratio for each hole is maintained same for TP, T, and P cases. It should also be noted that the local static pressure measured on the pressure side at 97% of the blade span indicates that it is mostly constant over the region from where coolant is injected with local pressure ratio magnitudes increasing from 1.0 at the leading edge to 1.07 near the last hole. By comparing these ratios to local pressure ratios on the tip surface, the blowing ratio distribution for each corresponding tip and pressure-side hole can be approximated. It can be observed from Fig. 8 that the pressure ratio on the plane tip surface near the camber line is high with average values around 1.35, whereas for the squealer tip the pressure ratios are lower ($\sim$1.1). Thus, the pressure ratios for plane tip on the camber line are much higher as compared to near-tip pressure side (at 97% blade span), while for squealer tip, the pressure ratios are comparable. This indicates that for the plane tip for TP cases, relatively more coolant passes through the tip holes than pressure-side holes because of a higher pressure drop through the tip holes, resulting in higher blowing ratios for the tip holes. For the squealer blade tip for TP cases, the blowing ratios for tip and pressure-side holes are comparable due to similar surface static pressures on the tip and near-tip region. Thus, higher effectiveness on the tip surface due to tip holes for tip and pressure-side injection (TP) cases as compared to only tip injection (T) for the plane tip can be explained as the blowing ratios might be higher than the preset value.

For cases with coolant flow on the pressure side (P and TP), traces of the coolant on the blade tip can be observed more clearly with increasing blowing ratio. Due to high mainstream velocities on the pressure side, coolant injected through these holes can get diverted toward the trailing edge. Thus, effectiveness for the first two holes is almost negligible for blowing ratios of 0.5 and 1.0. For $M=2$ though, a trace is visible due to larger momentum of the coolant jet. The carrying over of the pressure-side coolant is higher for the holes near the midchord to trailing-edge region, resulting in higher film-cooling effectiveness. For both pressure-side and camber line coolant injection, almost uniform, high film-cooling effectiveness near the trailing edge is observed. A qualitative comparison with the results obtained by Kwak and Han [2] shows consistency between the two data sets. They performed tests for coolant injection using 13 holes each on the camber line and pressure side, whereas seven holes have been used in this study. Trends obtained for the coolant traces in both studies are similar, with the magnitudes in the present study slightly higher than those obtained by Kwak and Han [2].

Increasing tip gap from 1.0% to 2.5% of span generally shows a decreasing effect on the film-cooling effectiveness on the blade tip. Effectiveness due to the tip holes along camber line remains mostly constant, whereas that due to airfoil pressure-side holes shows an increasing trend with decreasing tip gap. Higher clearances between blade tip and shroud allow more leakage flow, which, in turn, may lead to dilution of the coolant.

Film-Cooling Effectiveness Results for Squealer Blade Tip Figure 10 shows film-cooling effectiveness distribution for squealer blade tip. The figure includes plots for T, P, and TP cases with different tip clearances and blowing ratios with the plots arranged in the same fashion as Fig. 9. The presence of a squealer tip reduces the leakage flow from pressure to suction side of the blade. The film-covered area for squealer tip is smaller as compared to plane tip. Moreover, trace of the coolant is oriented toward the trailing edge and pressure side for the holes on the camber line, whereas the trace in plane tip case is oriented toward suction side. This is because of the squealer rim, which induces a recirculation zone inside the cavity.

Film-cooling effectiveness increases with increasing blowing ratio. For the region from the midchord of the blade to the trailing edge in the cavity, the effectiveness is relatively higher due to the accumulation and recirculation of coolant. A noticeable trace can be detected on the trailing edge (TP), which is probably because of some carry over of the coolant over the rim from the pressure side.

Adding film-cooling holes on the pressure side (P and TP) has only a minor effect on the tip. The pressure-side rim of the squealer tip shows some traces of the coolant, while a stronger trace is visible on the trailing edge. The maximum value of film-cooling effectiveness is lower than 0.2 for cases with only pressure-side coolant injection. Results from a film-cooling effectiveness study performed by Kwak and Han [3] using a hue-detection-based transient liquid-crystal technique on a squealer blade tip show similar path lines for coolant flow. This indicates good consistency between the two methods. Their magnitudes for effectiveness on the tip cavity surface are higher mainly because of a larger number of holes (13), and, consequently, more coolant is supplied at the same blowing ratio.

Increasing tip gap shows increasing film-cooling effectiveness in the squealer cavity. This is opposite to that for the plane tip, which shows a decreasing trend. At smaller tip-gap clearance, the shroud may restrict the recirculation inside the cavity because the distance from the floor of cavity to the shroud is smaller than the width of cavity. On the other hand, at a larger tip-gap clearance, the recirculating vortex can be even stronger and can push the coolant to the tip surface.

Averaged Film-Cooling Effectiveness Results. Figure 11 shows the variation of averaged film-cooling effectiveness (%) for the plane and squealer blade tip for all cases. The averaged values are obtained by area averaging the effectiveness magnitudes for the projected tip area. Averaged effectiveness values show an increasing trend with increasing blowing ratios as observed for the contour plots. It can also be observed that results obtained for two sets of film cooling holes (TP case) do not necessarily show a cumulative effect for results with tip only (T case) injection and pressure side only (P case) injection. From Fig. 11, it is evident that pressure side only (P case) coolant injection has poor effectiveness for squealer tip as compared to plane tip.

Conclusions

A parametric study has been performed for film-cooling effectiveness on blade tip by using a plane tip and a squealer tip. Effects of coolant injection from tip, pressure side, tip and pressure side, blowing ratio, and tip-gap clearance have been studied. Major findings from the experimental results are listed below.

1. Increasing blowing ratio increases film-cooling effectiveness for tip for all cases. For pressure-side injection only (P), the increase in effectiveness is smaller for higher blowing ratios.

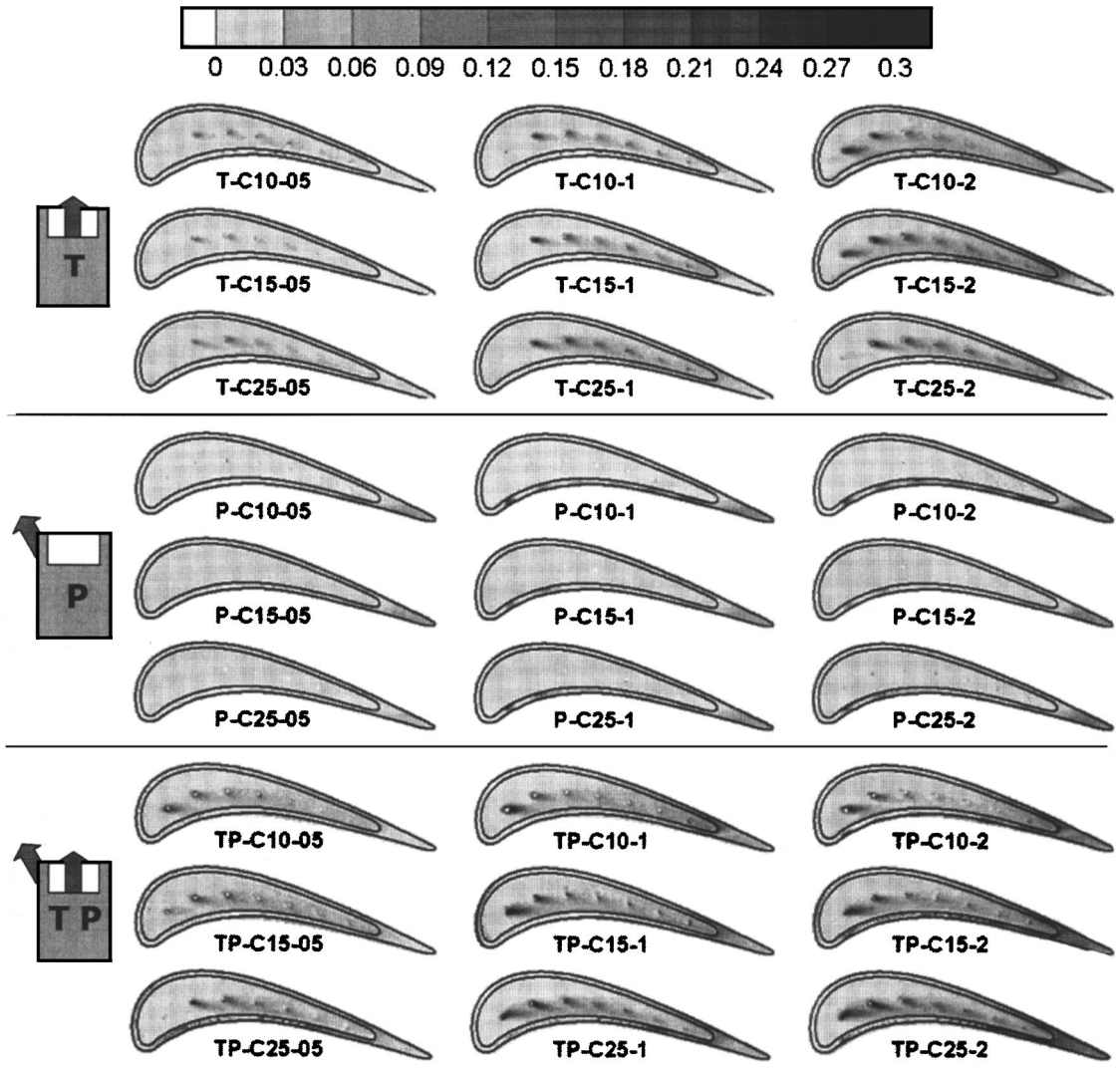

Fig. 10 Film-cooling effectiveness distribution on squealer blade tip

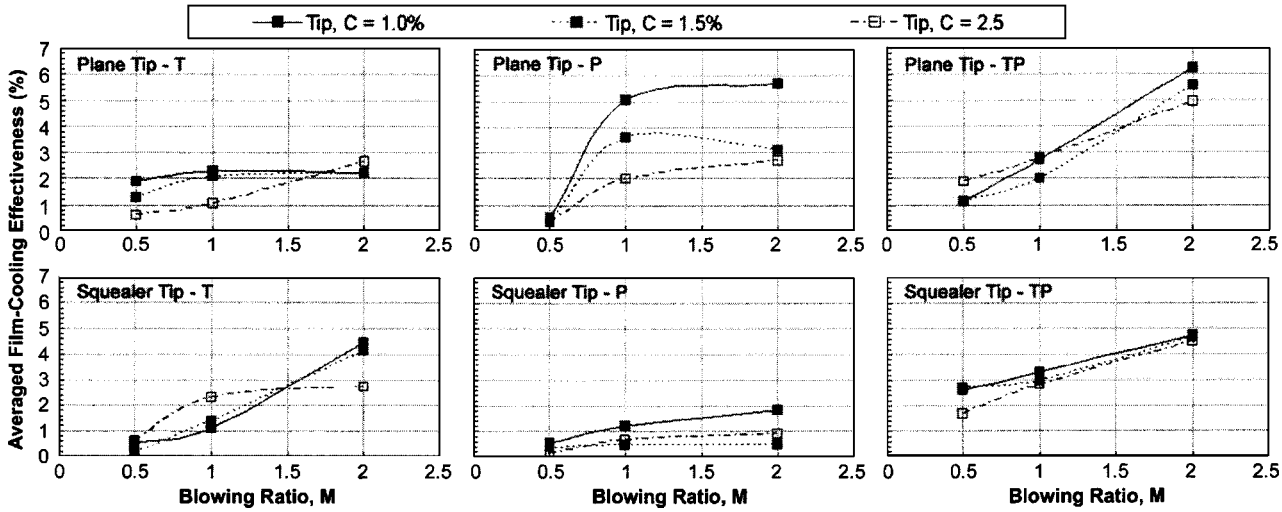

Fig. 11 Averaged film-cooling effectiveness for plane and squealer blade tip

2. Blade tip effectiveness is relatively unaffected by changes in tip-gap clearance.
3. For plane tip cases, the film-cooling effectiveness on blade tip is higher for the case with pressure-side injection (P) as compared to only tip (T) and tip and pressure-side injection (TP) except for the highest blowing ratio case ($M=2$).
4. For squealer tip cases, the film-cooling effectiveness on blade tip is higher for the case with tip and pressure-side injection as compared to only tip and only pressure-side injection.
5. For squealer tip cases, higher film-cooling effectiveness is observed due to accumulation between camber line and pressure side in the tip cavity.
6. Film-cooling effectiveness on the plane blade tip due to coolant injection from the pressure side of blade is significant, whereas for squealer tip, it is negligible.

Acknowledgment

This work was prepared with the partial support of the NASA Glenn Research Center, Solar Turbines, Inc., and State of Texas Advanced Technology Program.

Nomenclature

C = tip clearance gap
C_D = discharge coefficient
Co = oxygen concentration
C_x = axial chord length of the blade (8.61 cm)
d = diameter of film-cooling holes (0.127 cm)
i = film-cooling hole location on a surface from leading edge
I = pixel intensity for an image
M = average blowing ratio ($=\rho_c V_c/\rho_m V_{\text{avg}}$)
M_i = blowing ratio for ith hole ($=\rho_{c,i} V_{c,i}/\rho_m V_{\text{avg}}$)
LE = leading edge of the blade
P = local static pressure
P_t = total pressure at the cascade inlet
P_{O_2} = partial pressure of oxygen
PS = blade pressure side
TE = trailing edge of the blade
Tu = turbulence intensity level at the cascade inlet
x = axial distance (cm)
V_{avg} = averaged velocity of mainstream air at cascade inlet and exit
V_c = averaged velocity of coolant air from all film-cooling holes
α = thermal diffusivity of blade tip material (1.25×10^{-7} m^2/s)
η = local film-cooling effectiveness
ρ_c = density of coolant air
ρ_m = density of mainstream air

Subscript

air = mainstream air with air as coolant
mix = mainstream air with nitrogen as coolant
ref = reference image with no mainstream and coolant flow
blk = image without illumination (black)

References

[1] Han, J. C., Dutta, S., and Ekkad, S. V., 2000, *Gas Turbine Heat Transfer and Cooling Technology*, Taylor & Francis, New York.
[2] Kwak, J. S., and Han, J. C., 2002, "Heat Transfer Coefficient and Film-Cooling Effectiveness on a Gas Turbine Blade Tip," ASME Paper No. GT-2002-30194.
[3] Kwak, J. S., and Han, J. C., 2002, "Heat Transfer Coefficient and Film-Cooling Effectiveness on the Squealer Tip of a Gas Turbine Blade," ASME Paper No. GT-2002-30555.
[4] Kim, Y. W., Downs, J. P., Soechting, F. O., Abdel-Messeh, W., Steuber, G. D., and Tanrikut, S., 1995, "A Summary of the Cooled Turbine Blade Tip Heat Transfer and Film Effectiveness Investigations Performed by Dr. D. E. Metzger," ASME J. Turbomach., **117**, pp. 1–11.
[5] Kim, Y. W., and Metzger, D. E., 1995, "Heat Transfer and Effectiveness on Film Cooled Turbine Blade Tip Model," ASME J. Turbomach., **117**, pp. 12–21.
[6] Metzger, D. E., Dunn, M. G., and Hah, C., 1991, "Turbine Tip and Shroud Heat Transfer," ASME J. Turbomach., **113**, pp. 502–507.
[7] Dunn, M. G., and Haldeman, C. W., 2000, "Time-Averaged Heat Flux for a Recessed Tip, Lip, and Platform of a Transonic Turbine Blade," ASME J. Turbomach., **122**, pp. 692–697.
[8] Bunker, R. S., Baily, J. C., and Ameri, A. A., 2000, "Heat Transfer and Flow on the First Stage Blade Tip of a Power Generation Gas Turbine: Part 1: Experimental Results," ASME J. Turbomach., **122**, pp. 272–277.
[9] Bunker, R. S., and Baily, J. C., 2001, "Effect of Squealer Cavity Depth and Oxidation on Turbine Blade Tip Heat Transfer," ASME Paper No. 2001-GT-0155.
[10] Azad, G. M. S., Han, J. C., Teng, S., and Boyle, R., 2000, "Heat Transfer and Pressure Distributions on a Gas Turbine Blade Tip," ASME J. Turbomach., **122**, pp. 717–724.
[11] Azad, G. M. S., Han, J. C., and Boyle, R., 2000, "Heat Transfer and Pressure Distributions on the Squealer Tip of a Gas Turbine Blade," ASME J. Turbomach., **122**, pp. 725–732.
[12] Kwak, J. S., and Han, J. C., 2003, "Heat Transfer Coefficient on a Gas Turbine Blade Tip and Near Tip Regions," J. Thermophys. Heat Transfer, **17(3)**, pp. 297–303.
[13] Kwak, J. S., and Han, J. C., 2003, "Heat Transfer Coefficient on the Squealer Tip and Near Squealer Tip Regions of a Gas Turbine Blade," ASME J. Heat Transfer, **125**, pp. 669–677.
[14] Azad, G. M. S., Han, J. C., Bunker, R. S., and Lee, C. P., 2002, "Effect of Squealer Geometry Arrangement on a Gas Turbine Blade Tip Heat Transfer," ASME J. Heat Transfer, **124**, pp. 452–459.
[15] Kwak, J. S., Ahn, J., Han, J. C., Pang Lee, C., Bunker, R. S., Boyle, R., and Gaugler, R., 2002, "Heat Transfer Coefficients on Squealer Tip and Near Tip Regions of a Gas Turbine Blade With Single or Double Squealer," ASME Paper No. GT-2003-38907.
[16] Mayle, R. E., and Metzger, D. E., 1982, "Heat Transfer at the Tip of an Unshrouded Turbine Blade," *Proc. of 7th International Heat Transfer Conference*, Hemisphere, Washington, DC, pp. 87–92.
[17] Heyes, F. J. G., Hodson, H. P., and Dailey, G. M., 1991, "The Effect of Blade Tip Geometry on the Tip Leakage Flow in Axial Turbine Cascades," ASME Paper No. 91-GT-135.
[18] Yang, T. T., and Diller, T. E., 1995, "Heat Transfer and Flow for a Grooved Turbine Blade Tip in a Transonic Cascade," ASME Paper No. 95-WA/HT-29.
[19] Teng, S., Han, J. C., and Azad, G. M. S., 2001, "Detailed Heat Transfer Coefficient Distributions on a Large-Scale Gas Turbine Blade Tip," ASME J. Heat Transfer, **123**, pp. 803–809.
[20] Saxena, V., Nasir, H., and Ekkad, S. V., 2003, "Effect of Blade Tip Geometry on Tip Flow and Heat Transfer for a Blade in a Low Speed Cascade," ASME Paper No. 2003-GT-38176.
[21] Papa, M., Goldstein, R. J., and Gori, F., 2002, "Effects of Tip Geometry and Tip Clearance on the Mass/Heat Transfer From a Large-Scale Gas Turbine Blade," ASME Paper No. 2002-GT-30192.
[22] Jin, P., and Goldstein, R. J., 2002, "Local Mass/Heat Transfer on a Turbine Blade Tip," *9th International Symposium on Transport Phenomena and Dynamics of Rotating Machinery*, Honolulu, Feb. 10–14, HT-ABS-012, pp. 1–11.
[23] Jin, P., and Goldstein, R. J., 2002, "Local Mass/Heat Transfer on Turbine Blade Near-Tip Surfaces," ASME Paper No. 2002-GT-30556.
[24] Ameri, A. A., Steinthorsson, E., and Rigby, L. D., 1999, "Effects of Tip Clearance and Casing Recess on Heat Transfer and Stage Efficiency in Axial Turbines," ASME J. Turbomach., **121**, pp. 683–693.
[25] Ameri, A. A., and Bunker, R. S., 2000, "Heat Transfer and Flow on the First Stage Blade Tip of a Power Generation Gas Turbine: Part 2: Simulation Results," ASME J. Turbomach., **122**, pp. 272–277.
[26] Ameri, A. A., and Rigby, D. L., 1999, "A Numerical Analysis of Heat Transfer and Effectiveness on Film Cooled Turbine Blade Tip Models," NASA/CR 1999-209165.
[27] Yang, H., Acharya, S., Ekkad, S. V., Prakash, C., and Bunker, R., 2002, "Flow and Heat Transfer Predictions for a Flat-Tip Turbine Blade," ASME Paper No. 2002-GT-30190.
[28] Yang, H., Acharya, S., Ekkad, S. V., Prakash, C., and Bunker, R., 2002, "Numerical Simulation of Flow and Heat Transfer Past a Turbine Blade With a Squealer-Tip," ASME Paper No. 2002-GT-30193.
[29] Acharya, S., Yang, H., Prakash, C., and Bunker, R., 2002, "Numerical Simulation of Film Cooling on the Tip of a Gas Turbine Blade," ASME Paper No. 2002-GT-30553.
[30] Yang, H., Chen, H. C., and Han, J. C., 2004, "Numerical Prediction of Film Cooling and Heat Transfer With Different Film Hole Arrangements on the Plane and Squealer Tip of A Gas Turbine Blade," ASME Paper No. 2004-GT-53199.

[31] Hohlfeld, E. M., Christophel, J. R., Couch, E. L., and Thole, K. A., 2003, ''Predictions of Cooling Flow Dirt Purge Holes Along the Tip of a Turbine Blade,'' ASME Paper No. 2003-GT-38251.
[32] Morris, M., Donovan, J., Kegelman, J., Schwab, S., Levy, R., and Crites, R., 1995, ''Aerodynamic Applications of Pressure Sensitive Paint,'' AIAA Paper No. 92-0264.
[33] McLachlan, B., and Bell, J., 1995, ''Pressure-Sensitive Paint in Aerodynamic Testing,'' Exp. Therm. Fluid Sci., **10**, pp. 470–485.
[34] Donovan, J., Morris, M., Pal, A., Benne, M., and Crites, R., 1993, ''Data Analysis Techniques for Pressure- and Temperature-Sensitive Paint,'' AIAA Paper No. 93-0178.
[35] Bell, J., and McLachlan, B., 1993, ''Image Registration for Luminescent Paint Sensors,'' AIAA Paper No. 93-0178.
[36] Zhang, L. J., and Fox, M., 1999, ''Flat Plate Film Cooling Measurement Using PSP and Gas Chromatography Techniques,'' *Proc. Fifth ASME/JSME Joint Thermal Engineering Conf.*, San Diego, ASME, New York.
[37] Zhang, L. J., Baltz, M., Pudupatty, R., and Fox, M., 1999, ''Turbine Nozzle Film Cooling Study Using the Pressure Sensitive Paint (PSP) Technique,'' ASME Paper No. 99-GT-196.
[38] Zhang, L. J., and Jaiswal, R. S., 2001, ''Turbine Nozzle Endwall Film Cooling Study Using Pressure-Sensitive Paint,'' ASME J. Turbomach., **123**, pp. 730–738.
[39] Coleman, H. W., and Steele, W. G., 1989, *Experimentation and Uncertainty Analysis for Engineers*, Wiley, New York.

A Fully Implicit Hybrid Solution Method for a Two-Phase Thermal-Hydraulic Model

Vincent A. Mousseau[1]
Fluid Dynamics Group, T-3, M.S. B216,
Los Alamos National Laboratory,
Los Alamos, New Mexico 87545
e-mail: vmss@lanl.gov

This paper will present a hybrid solution algorithm for the two-phase flow equations coupled to wall heat conduction. The partial differential equations in the physical model are the same as in RELAP5. The hybrid solution algorithm couples two solution methods, the solution method currently employed by RELAP5 and an implicitly balanced solution method. The resulting hybrid solution method is both fast and accurate. Results will be presented that show when accuracy and CPU time are considered simultaneously that there are ranges when the hybrid solution algorithm is preferred over the RELAP5 solution method. © *2005 American Institute of Physics.* [DOI: 10.1115/1.1865223]

Introduction

This article is based on work presented at a conference in [1] and is a continuation of previous work on the accurate solution of the two-phase flow equations [2]. Both the mathematical model and the spatial discretization come directly from the RELAP5 code manual [3,4]. The purpose of this work is to investigate more accurate time integration methods applied to closure relations that are a function of the state of the fluid. Questions regarding spatial accuracy and correctness of the two-phase mathematical model are beyond the scope of this work. Many of the algorithmic details (such as the time discretization of the RELAP5 and of the fully implicit algorithms) that are presented in Ref. [2] will not be repeated here. The main difference between the results presented here and in [2] is related to the closure relations for the two-phase flow equations. In [2] the closure relations (friction and heat transfer coefficients) were assumed to be constants. In another recent work [5], a similar fully implicit algorithm was investigated employing the closure relations from COBRA/TRAC [6]. The results in terms of robustness were similar between [2] and [5], but there is only limited information on accuracy and efficiency in [5]. In this article, the closure relations will be a function of the vapor volume fraction as opposed to the constant closures used in [2], but the new closure relations are still simpler than the physically realistic closures employed in [5]. The purpose of this paper is to investigate the accuracy and efficiency of a fully implicit model with closure relations that depend on the state of the fluid.

The work in [2] is the result of many years of work with the Jacobian-free Newton-Krylov (JFNK) solution method [7]. The accuracy of JFNK's implicitly balanced approach compared to solution methods like the one employed by RELAP5 have been analyzed for nonequilibrium radiation diffusion, reduced magnetohydrodynamics equations, and the shallow water equations [8]. In all of these applications, the JFNK method provides higher accuracy for the same time step size. The idea of using a hybrid approach that couples two solution procedures has been documented for geophysical flows and magnetohydrodynamics in [9]. The basic ideas for the hybrid solution method are already well documented in [2,9], so many details will be left out of this article.

The nonlinear system of interest in this article will include water and steam flowing though a channel that is attached to a heat conducting solid slab. The slab is heated by a cosine-shaped source and is coupled to the two-phase flow in the channel through convective heat transfer (see Fig. 1).

This system is a very simplified version of a nuclear reactor. The heat source comes from nuclear fission and is conducted through a solid structure to be removed by the water-steam convection. The RELAP5 [3,4] code was designed to simulate the two-phase flow, heat conduction, and nuclear fission in a nuclear reactor. The numerical methods in RELAP5 are based on an operator splitting of the nuclear fission, the heat conduction, and the fluid flow. In addition, the fluid flow has further linearizations and operator splitting (the semi-implicit algorithm). The basic numerical methods in RELAP5 are still very similar to when the code was originally written in the mid 1970's. Because of the small memory and very slow computational speed of computers in the 1970's, these simplifications were required to make the simulations tractable.

The hybrid approach of this manuscript employs the operator split semi-implicit (OSSI) method that is the time integration algorithm of the RELAP5 code [3,4]. This OSSI method, which has problems with stability and accuracy, is used to provide a solution that is ''close'' to the correct answer. Given a good estimate of the solution from the OSSI method, the JFNK method [10,11], which is stable and accurate, quickly converges to the correct solution with only a small amount of computational work.

This hybrid approach has two main advantages. First, one can take advantage of the thirty years of investment in optimizing the OSSI method. Second, if the hybrid solution method contains the OSSI method, either one can be employed where appropriate.

The remainder of this article has the following layout. The mathematical model of the one-dimensional two-phase flow equations coupled to the two-dimensional nonlinear heat conduction equation is presented first. A brief discussion of the discretized equations follows. The closure models are presented in the next section. In the following section, the hybrid solution technique is briefly described. After this, results are presented for two test problems to demonstrate the accuracy and efficiency of this hybrid approach. Finally, conclusions are presented.

Mathematical Model

The partial differential equations presented in this section are taken directly from the RELAP5 computer code manual [3,4]. The model employed is a one-dimensional, six-equation, single pressure model with coupling to a two-dimensional, nonlinear heat conduction problem. In this model, both phases have their own mass, momentum, and energy conservation equations. The first two equations are the conservation of mass equation for the vapor phase,

[1]Telephone: (505)665-5891; fax: (505)665-5926.
Contributed by the Heat Transfer Division of ASME for publication in the JOURNAL OF HEAT TRANSFER. Manuscript received April 27, 2004; revision received December 23, 2004. Review conducted by: R. P. Roy.

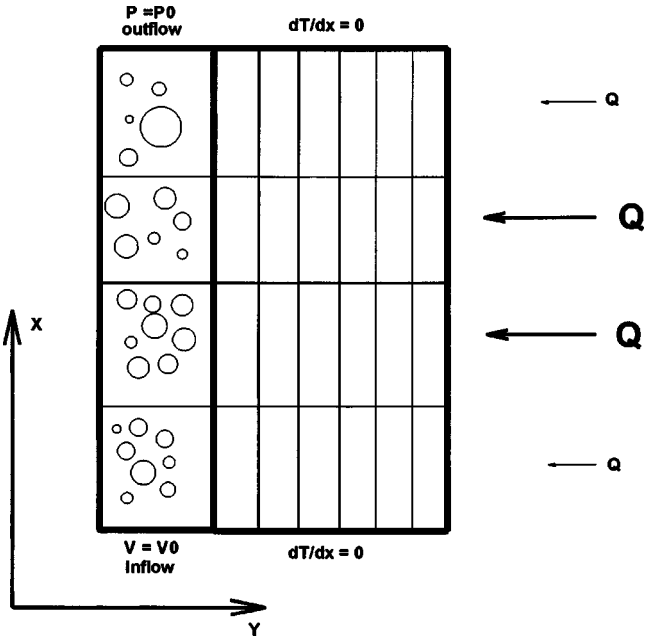

Fig. 1 Schematic diagram of the computational domain

$$\frac{\partial \alpha_g \rho_g}{\partial t} + \frac{\partial \alpha_g \rho_g v_g}{\partial x} = \Gamma_g , \tag{1}$$

and the conservation of mass in the liquid phase,

$$\frac{\partial \alpha_f \rho_f}{\partial t} + \frac{\partial \alpha_f \rho_f v_f}{\partial x} = -\Gamma_g . \tag{2}$$

The interfacial mass transfer is given by,

$$\Gamma_g = -\frac{H_{ig} a_i (T_s - T_g) + H_{if} a_i (T_s - T_f)}{h_g^* - h_f^*} . \tag{3}$$

This mass transfer model assumes that the properties of the interface are always at the thermodynamic saturation value associated with the pressure. The ''starred'' enthalpies in Eq. (3) are calculated from the vapor and liquid specific enthalpies and the vapor and liquid saturation specific enthalpies by,

$$h_g^* = \begin{cases} h_{gs}: & \text{if } \Gamma_g > 0, \\ h_g: & \text{otherwise,} \end{cases} \tag{4}$$

and,

$$h_f^* = \begin{cases} h_f: & \text{if } \Gamma_g > 0, \\ h_{fs}: & \text{otherwise.} \end{cases} \tag{5}$$

It is important to note that mass transfer is equal in magnitude and opposite in sign in Eq. (1) and Eq. (2).

This model has a conservation of momentum equation for the vapor phase,

$$\begin{aligned} &\alpha_g \rho_g \frac{\partial v_g}{\partial t} + \alpha_g \rho_g v_g \frac{\partial v_g}{\partial x} + \alpha_g \frac{\partial P}{\partial x} - \alpha_g \rho_g \boldsymbol{g} \\ &= -F_{wg} a_{wg} (\alpha_g \rho_g)^2 |v_g| v_g - F_i a_i |v_g - v_f| (v_g - v_f) \\ &\quad + \Gamma_g (v_i - v_g), \end{aligned} \tag{6}$$

and a conservation of momentum equation for the liquid phase,

$$\begin{aligned} &\alpha_f \rho_f \frac{\partial v_f}{\partial t} + \alpha_f \rho_f v_f \frac{\partial v_f}{\partial x} + \alpha_f \frac{\partial P}{\partial x} - \alpha_f \rho_f \boldsymbol{g} \\ &= -F_{wf} a_{wf} (\alpha_f \rho_f)^2 |v_f| v_f + F_i a_i |v_g - v_f| (v_g - v_f) \\ &\quad - \Gamma_g (v_i - v_f). \end{aligned} \tag{7}$$

The momentum losses due to wall and interfacial friction are given in terms of vapor and liquid wall area coefficients, vapor and liquid wall friction coefficients, and an interfacial friction coefficient. Here one notes that the interfacial friction has equal magnitude and opposite sign in Eq. (6) and Eq. (7). The terms that include mass transfer account for the momentum lost or gained by the mass appearing at the interfacial velocity.

This model also has two energy equations, one for conservation of energy in the vapor phase,

$$\begin{aligned} &\frac{\partial \alpha_g \rho_g U_g}{\partial t} + \frac{\partial \alpha_g \rho_g U_g v_g}{\partial x} + P \frac{\partial \alpha_g}{\partial t} + P \frac{\partial \alpha_g v_g}{\partial x} \\ &= H_{wg} a_{wg} (T_w - T_g) + H_{ig} a_i (T_s - T_g) \\ &\quad + H_{fg} a_i (T_f - T_g) + \Gamma_g h_g^* , \end{aligned} \tag{8}$$

and a second conservation of energy in the liquid phase,

$$\begin{aligned} &\frac{\partial \alpha_f \rho_f U_f}{\partial t} + \frac{\partial \alpha_f \rho_f U_f v_f}{\partial x} + P \frac{\partial \alpha_f}{\partial t} + P \frac{\partial \alpha_f v_f}{\partial x} \\ &= H_{wf} a_{wf} (T_w - T_f) + H_{if} a_i (T_s - T_f) \\ &\quad - H_{fg} a_i (T_f - T_g) - \Gamma_g h_f^* . \end{aligned} \tag{9}$$

The mathematical model includes a two-dimensional nonlinear heat conduction equation to represent conservation of energy in the solid wall,

$$\begin{aligned} &\frac{\partial e_w}{\partial t} - \frac{\partial}{\partial x} \mathrm{K} \frac{\partial T_w}{\partial x} - \frac{\partial}{\partial y} \mathrm{K} \frac{\partial T_w}{\partial y} - Q_{nw} \\ &= -[H_{wg} a_{wg} (T_w - T_g) + H_{wf} a_{wf} (T_w - T_f)]. \end{aligned} \tag{10}$$

Here the source term represents the energy imparted into the wall from nuclear fission. The wall energy is computed from,

$$e_w = \int_{T_0}^{T_w} \rho_w C_p dT_w . \tag{11}$$

It is important to note that in Eq. (10), the energy exchange with the liquid and vapor are equal in magnitude and opposite in sign in Eq. (8) and Eq. (9). Additionally, the areas between the wall and the vapor, and the wall and the liquid, are only nonzero in control volumes that are adjacent to the fluid. Similarly, the fission heat source is only nonzero in the cells adjacent to the opposite edge from the fluid (see Fig. 1).

Discrete Equations

The details of the discrete equations used for both the hybrid (JFNK) and the OSSI solution can be found in [2] and the complete details of the RELAP5 discrete equations can be found in [3,4] (note both of these documents are available on the web). The discrete form of the vapor momentum equation [Eq. (6)] will be given below.

The discrete equations are solved on a staggered mesh with the state variables (volume fraction, pressure, liquid and vapor energy) located at the cell centers (subscripts $j+1$ and j) and the liquid and vapor velocities are located at the cell faces (subscript $j+1/2$). For brevity, only the vapor momentum equation will be given in discrete form. The second order in time implicitly balanced discrete finite volume form of the vapor momentum equation used in the hybrid solution method is given by,

$$\frac{V(\overline{\alpha_g^{n+1/2}\rho_g^{n+1/2}})}{\Delta t}(v_g^{n+1}-v_g^n)+\frac{1}{2}F_{mg}^n+\frac{1}{2}F_{mg}^{n+1}=0, \quad (12)$$

where V is the volume of the fluid control volume and

$$F_{mg}^{n+1}=\Delta y(\overline{\alpha_g^{n+1}\rho_g^{n+1}})v_g^{n+1}(\widetilde{v_{g,j+1}^{n+1}}-\widetilde{v_{g,j}^{n+1}})+\Delta y\overline{\alpha_g^{n+1}}(P_{j+1}^{n+1}-P_j^{n+1})-V(\overline{\alpha_g^{n+1}\rho_g^{n+1}})\boldsymbol{g}+VF_{wg}\overline{a_{wg}^{n+1}}(\overline{\alpha_g^{n+1}\rho_g^{n+1}})^2|v_g^{n+1}|v_g^{n+1}+V\overline{\Gamma_g^{n+1}}(v_i^{n+1}-v_g^{n+1})+V(\overline{F_i a_i})^n|v_g^{n+1}-v_f^{n+1}|(v_g^{n+1}-v_f^{n+1}). \quad (13)$$

Since the vapor momentum equation is located at the cell face, the implied subscript in the discrete equations will be $j+1/2$, and only subscripts that are different from $j+1/2$ will be included. State variables that have been averaged to a cell face will have an overbar, and velocities upwinded to cell centers will have a tilde. The OSSI solution uses the following discrete form of the vapor momentum equation:

$$\frac{V(\overline{\alpha_g^n\rho_g^n})}{\Delta t}(v_g^{n+1}-v_g^n)+\Delta y(\overline{\alpha_g^n\rho_g^n})v_g^n(\widetilde{v_{g,j+1}^n}-\widetilde{v_{g,j}^n})+\Delta y\overline{\alpha_g^n}(P_{j+1}^{n+1}-P_j^{n+1})-V(\overline{\alpha_g^n\rho_g^n})\boldsymbol{g}+VF_{wg}\overline{a_{wg}^n}(\overline{\alpha_g^n\rho_g^n})^2|v_g^n|v_g^{n+1}+V\overline{\Gamma_g^n}(v_i^{n+1}-v_g^{n+1})+V(\overline{F_i a_i})^n|v_g^n-v_f^n|(v_g^{n+1}-v_f^{n+1}). \quad (14)$$

Comparing Eq. (12) and Eq. (14), one can see that Eq. (12) is a nonlinear equation that achieves second order in time accuracy by employing Crank-Nicolson temporal differencing. Equation (14) is a linear equation that has been linearized by a Picard linearization. An analysis of the truncation errors induced by Picard linearizations is given in [12].

Closure Equations

It should be stressed that these closure relations are representative and that no attempt has been made to compute ''accurate'' closure relations for the test problems. A significant amount of work is required to get the correct dependencies between the closure relations and the state variables. In addition, there is a significant amount of ''tuning'' of the closure relations to get them to match the empirical data that is available (see [3,4,6] for more details on flow regime maps). The closure relations presented here ignore the dependency on all of the state variables except for volume fraction. As a function of volume fraction, the friction and heat transfer coefficients have been given reasonable shapes with the correct limiting values as the volume fraction approaches zero and one.

These closure relations have been constructed in an attempt to have closure relations that depend on the state of the fluid as opposed to the constant closure relations that where employed in [2], but not a full flow regime as was employed in [5]. In addition there were differences between the model in this article and the model in [5]. These differences include a three-field model, switching between equations in the single-phase limits, and using an empirically verified set of closure relations. The three field effects will not be addressed in this article. To eliminate the difficulty of going to the single-phase limit, these closure relations have been designed so that they gradually approach the single-phase limit but remain two-phase. It is possible that closure relations constructed to match experimental data (such as the ones employed in [5]) may include discontinuities in state space. To eliminate the effects of these discontinuities on the numerical method, the closure relations constructed in this manuscript are smooth. The void dependency provides the nonlinear coupling between the state variables and the closure relations. However, the closure relations of this article do not include discontinuities and have not been designed to match any experimental data.

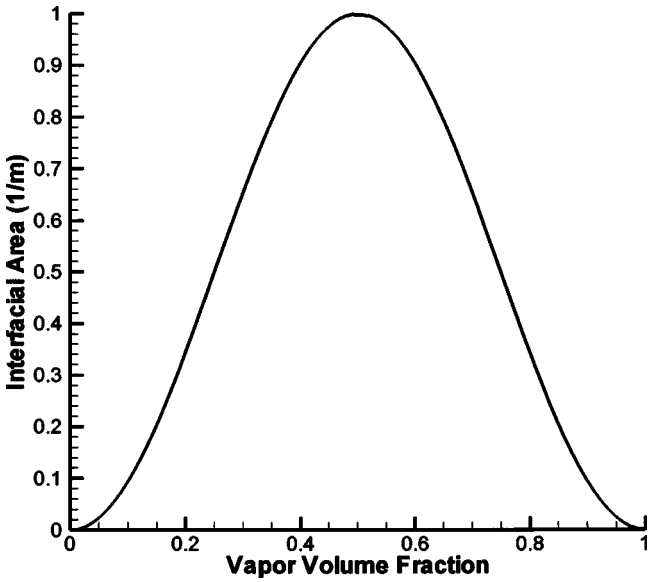

Fig. 2 Interfacial area versus vapor volume fraction

The interfacial area has been designed to prevent the interface mass transfer terms from driving the volume fraction greater than one or less than zero. To accomplish this the interfacial area is set to zero if the volume fraction is less than 0.001 or greater than 0.999. For simplification of nomenclature, we define a new normalized volume fraction that has the range 0 to 1 when the volume fraction has the range from 0.001 to 0.999:

$$\alpha_0=\frac{\alpha_g-0.001}{0.999-0.001}. \quad (15)$$

Given this normalized volume fraction, the interfacial area can now be expressed as,

$$a_i=\begin{cases}1+\sin[2\alpha_0-1/2]\pi: & \alpha_g\in[0.001,0.999],\\ 0: \quad \text{otherwise.}\end{cases} \quad (16)$$

A plot of this function is shown in Fig. 2. In this figure, one can see the interfacial area reaches a maximum at a volume fraction of one-half and goes to zero in the limits of high and low volume fractions. This interfacial area is then used as a multiplier of vapor and liquid interfacial heat transfer coefficients in the computation of the interfacial mass transfer.

The next closure relation to be addressed is the area between the wall and the vapor or liquid. These closure relations are designed to make the liquid area high when the vapor volume fraction is low and to make the vapor area high when the vapor volume fraction is high. It should be noted that as the vapor volume fraction approaches zero, all of the interactions with the wall take place with the liquid phase, and as the vapor volume fraction approaches one, all of the interactions with the wall take place with the vapor phase. The wall areas are given by the following two equations:

$$a_{wf}=\begin{cases}1+\sin[\alpha_0+1/2]\pi: & \alpha_g\in[0.001,0.999],\\ 0: & \alpha_g>0.999,\\ 1: & \alpha_g<0.001,\end{cases} \quad (17)$$

$$a_{wg}=1-a_{wf}. \quad (18)$$

Equation (17) and Eq. (18) are plotted in Fig. 3. These wall areas are used to compute the wall friction and the wall heat transfer. The interfacial area, wall liquid area, and the wall vapor area control interfacial mass transfer, wall friction, and wall heat transfer. The interfacial area has been designed to turn off mass transfer

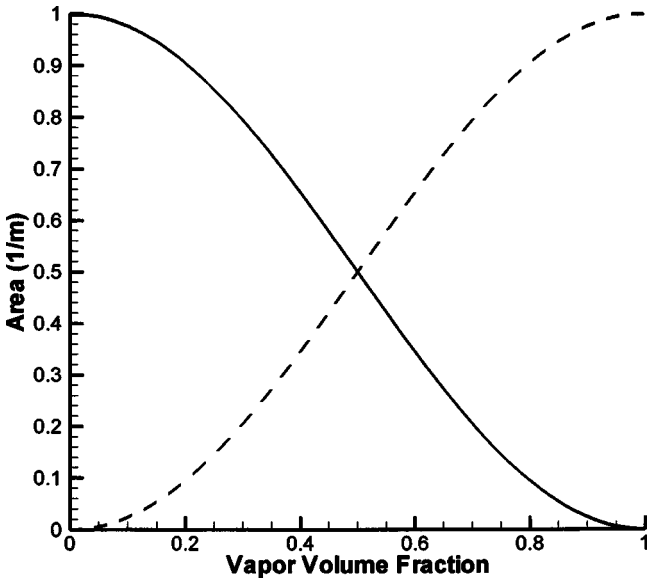

Fig. 3 Liquid (solid) and vapor (dashed) wall area versus vapor volume fraction

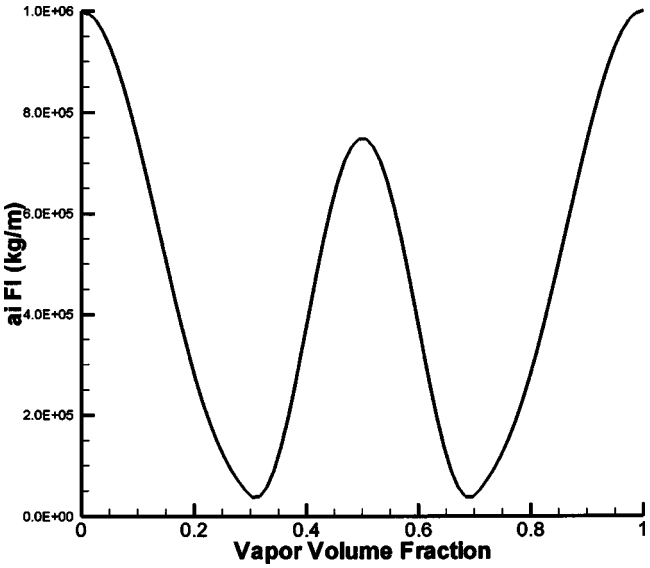

Fig. 4 Interfacial friction versus vapor volume fraction

as the vapor volume fraction approaches one and zero. This prevents the simulation from trying to condense the small amount of vapor present or from vaporizing the small amount of liquid present. This design keeps the simulation in the two-phase regime.

The last two closure relations have been designed to enforce thermal and mechanical equilibrium in the phase that is disappearing. To accomplish this, the interfacial friction needs to be high as the volume fraction approaches zero and one. In addition, the interfacial friction includes a local maximum at a volume fraction of one-half, which corresponds to the maximum in interfacial area at a volume fraction of one-half. Given these constraints, the interfacial friction can be expressed by the following four equations:

$$F_{i1}=\begin{cases}\frac{1}{8}[1+\sin\{2\alpha_0+1/2\}\pi]^3: & \alpha_g\in[0.001,0.999],\\ 1: \quad \text{otherwise},\end{cases} \tag{19}$$

$$\alpha_2=\frac{\alpha_g-0.3}{0.4}, \tag{20}$$

$$F_{i2}=\begin{cases}\frac{3}{8}[1+\sin\{2\alpha_2-1/2\}\pi]: & \alpha_g\in[0.001,0.999],\\ 1: \quad \text{otherwise},\end{cases} \tag{21}$$

$$a_iF_i=10^6(F_{i1}+F_{i2}). \tag{22}$$

To provide the local maximum at a volume fraction of one-half, a second normalized volume fraction [see Eq. (20)] had to be defined. Equation (22) is plotted in Fig. 4. It should be noted that Eqs. (16)–(18) define areas that are a function of volume fraction. These variable areas are then multiplied by constant coefficients to obtain the nonlinear effect into the interfacial mass transfer, wall heat transfer, and wall friction. In contrast, Eq. (22) defines the product of the area and the coefficient.

The last step in defining the closure relations is to provide a mechanism for driving the phase that is disappearing into thermal equilibrium with the dominant phase. Because the interfacial mass transfer is set to zero for values of volume fraction approaching zero and one, a simple contact heat transfer model is included to account for the energy transfer between phases. This interfacial heat transfer is independent of interfacial mass transfer. This model is designed to only be important as the volume fraction approaches the limits of zero and one. Given these constraints, the contact interfacial heat transfer is given by the following equation:

$$a_iH_{fg}=\begin{cases}10^5[1+\sin(\{2\alpha_0+1/2\}\pi)]^2: & \alpha_g\in[0.001,0.999],\\ 10^5: \quad \text{otherwise}.\end{cases} \tag{23}$$

Equation (23) is plotted in Fig. 5. Here one can see that the contact heat transfer is only large when the volume fraction is near zero and one. Again, it should be noted that Eq. (23) defines the product of the area times the coefficient.

It should be reiterated that these closure relations were formed in an attempt to include some of the nonlinear effects into the model. These closure relations are a first step beyond a constant closure model (like the one used in [2]) but is well short of a full flow regime map, as was employed in [5]. These simple relations are included to investigate the accuracy and efficiency of closure relations that depend on the state of the fluid. Three criteria were used for the development of these closure relations:

1. Their shape is a reasonable function of volume fraction
2. The shape is smooth

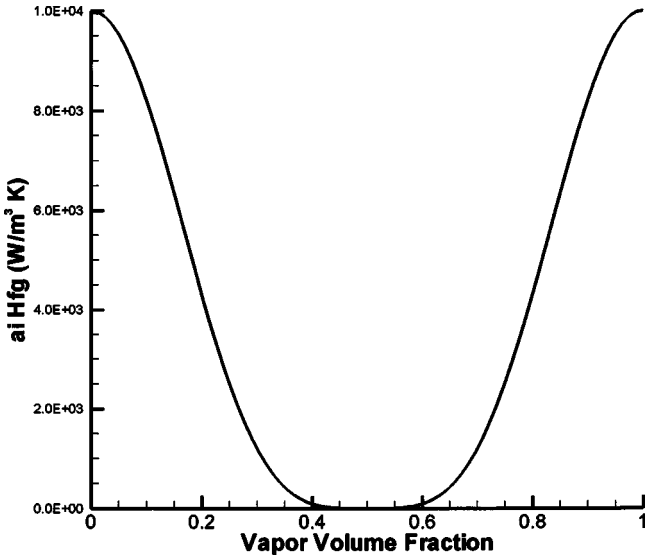

Fig. 5 Contact interfacial heat transfer (not associated with phase change) versus vapor volume fraction

3. The closure relations behave in a reasonable manner as the volume fraction approaches zero and one

Hybrid Solution Method

The hybrid solution method is a modified form of Newton's method. This hybrid method is sometimes called the physics-based preconditioned JFNK method [2,7,9]. Newton's method is designed to solve nonlinear systems of the form,

$$\mathbf{res}(\mathbf{x}) = 0, \tag{24}$$

where **res** is a vector function of the discretized form of Eqs. (1), (2), (6)–(10) and **x** is a vector of the state variables (volume fraction, pressure, wall temperature, liquid and vapor energy, and liquid and vapor velocity). Newton's method solves Eq. (24) iteratively by solving a sequence of linear problems defined by,

$$\mathbf{J}^k \delta\mathbf{x}^k = -\mathbf{res}(\mathbf{x}^k). \tag{25}$$

Here the matrix **J** is the Jacobian matrix and the superscript "k" is the Newton iteration. The (i,j) element of the Jacobian matrix is the derivative of the ith equation with respect to the jth variable or in equation form,

$$J(i,j) = \frac{\partial \mathrm{res}_i}{\partial x_j}. \tag{26}$$

Equation (25) is solved for the update vector and then the new Newton iteration value for **x** is computed from,

$$\mathbf{x}^{k+1} = \mathbf{x}^k + \omega\,\delta_{\mathbf{x}}^k. \tag{27}$$

The damping parameter (omega) is between zero and one and is chosen to keep the components of **x** in physically realizable space. This means that the volume fraction must be between zero and one and that the pressure, liquid and vapor energy, and wall temperature must all be positive. Note that the same damping value is applied to all of the updates. This iteration on **x** is continued until the nonlinear residual given by Eq. (24) is small relative to its value for the initial guess.

$$\|\mathbf{res}(\mathbf{x}^k)\|_2 < 10^{-8}\|\mathbf{res}(\mathbf{x}^0)\|_2. \tag{28}$$

If the Jacobian matrix is constructed analytically from Eq. (26) and Eq. (25) is solved exactly, then this is simply the traditional Newton's method for the solution of a nonlinear system of equations. In the rest of this section, modifications are presented to the basic Newton algorithm to improve its efficiency and storage.

The first modification is referred to as an inexact Newton's method [13]. The basic idea behind an inexact Newton's method is to only solve the linear system to a tight tolerance when the added accuracy improves the convergence of the Newton's iteration. This is accomplished by making the convergence of the linear residual proportional to the nonlinear residual or in equation form,

$$\|\mathbf{J}^k \delta\mathbf{x}_m^k + \mathbf{res}(x^k)\|_2 < 10^{-3}\|\mathbf{res}(\mathbf{x}^k)\|_2, \tag{29}$$

here the subscript m refers to the mth iteration of the linear solver. From Eq. (29), one can see that when the nonlinear residual is large the linear convergence criteria is loose and conversely when the nonlinear residual is small the linear convergence criteria is tight. The value 10^{-3} in Eq. (29) is chosen to try to minimize the CPU time while maintaining accuracy. For more details on the choice of this parameter, see Sec. 2.3.2 "Inexact Newton Methods" in [7] and the references contained in that section.

The linear solver used in this study is the Arnoldi-based GMRES [14] Krylov solver. The Krylov solver constructs the mth iteration from,

$$\delta\mathbf{x}_m^k = a_0\mathbf{r}_0 + a_1\mathbf{J}\mathbf{r}_0 + a_2\mathbf{J}^2\mathbf{r}_0 + \ldots + a_m\mathbf{J}^m\mathbf{r}_0, \tag{30}$$

where,

$$\mathbf{r}_0 = \mathbf{res}(\mathbf{x}^k).$$

It is important to note that in Eq. (30) the Jacobian matrix only shows up as the product of the Jacobian matrix and a vector. Therefore, if the action of the Jacobian matrix can be approximated, the Jacobian matrix itself is never required for the solution. Fortunately, the action of the Jacobian matrix [15] can be approximated by,

$$\mathbf{J}^k\mathbf{v} = \frac{\mathbf{res}(\mathbf{x}^k + \varepsilon\mathbf{v}) - \mathbf{res}(\mathbf{x}^k)}{\varepsilon}, \tag{31}$$

where,

$$\varepsilon = \frac{10^{-8}\|\mathbf{x}\|_1}{N\|\mathbf{v}\|_2}, \tag{32}$$

and N is the number of unknowns. If one employs Eq. (31), the work associated with forming the Jacobian matrix in Eq. (26) and the storage for the Jacobian matrix can be eliminated. If the number of Krylov iterations is small, this approximation saves both CPU time and storage for the nonlinear iteration. The optimization of the linear solution will be addressed next.

Because GMRES stores m vectors to construct the mth iteration, one needs to keep the number of Krylov iterations small to keep the storage and the CPU time for GMRES from becoming prohibitive. One way to keep the number of Krylov iterations small is to right precondition Eq. (25):

$$\mathbf{J}^k\mathbf{P}^{-1}\mathbf{P}\,\delta\mathbf{x}^k = -\mathbf{res}(\mathbf{x}^k). \tag{33}$$

The basic idea of preconditioning it to choose a preconditioner **P** such that the Jacobian matrix times the inverse of the preconditioner is an easier system to solve. The traditional approach to preconditioning is to construct the Jacobian matrix **J**, copy **J** into **P** and then approximately compute the inverse of **P**. By employing the Jacobian-free approximation of Eq. (31), this solution algorithm never computes the Jacobian matrix, so this traditional preconditioning approach is replaced with the physics-based preconditioning approach [2,7,9]. The physics-based preconditioning approach is based on the observation that the inversion of the Jacobian matrix is really a linearized time step and therefore the preconditioner can be any time stepping algorithm that solves the same equations. The time stepping algorithm employed in this study as the physics-based preconditioner is the OSSI solution method employed by RELAP5.

Therefore, the hybrid solution comes from employing the OSSI solution method to improve the JFNK method. In pseudocode form this is,

```
For each time step
  For each Newton iteration
    For each Krylov iteration
      Compute an OSSI solution
    End Krylov iteration
  End Newton iteration
End time step
```

In the hybrid solution algorithm, for each time step there are multiple Newton iterations and for each Newton iteration there are multiple Krylov iterations and for each Krylov iteration there is one call to the OSSI solution. Two effects are important for the hybrid algorithm to be effective.

1. Including the OSSI solution as a preconditioner in the Krylov linear solver must keep the number of Krylov iterations small
2. A significant increase in accuracy must be obtained by the Newton iteration

It should be noted that by simply turning off the Newton iteration and by turning off the Krylov iteration, one OSSI solution is computed per time step, and this is exactly the OSSI solution algorithm. Therefore, the OSSI solution method can be obtained from the hybrid solution method in a trivial manner.

Table 1 Input differences between the high velocity and low velocity test problems

Problem	Inflow velocity (m/s)	Flow area (m^2)
High velocity	0.4	0.049
Low velocity	0.1	0.196

It is important to note that for the hybrid method although there are no stability constraints on the time step because it is fully implicit. However, the time step size for this algorithm must still be controlled based on accuracy. The long-term efficiency of the hybrid algorithm depends on the time step control and the effectiveness of the preconditioner.

Results

This section will present results from an idealized representation of a nuclear reactor transient. The transient is a simplified model of a reactor SCRAM. In a SCRAM, the control rods are quickly inserted into the reactor to slow down the nuclear fission reaction. In the test problem, the nuclear fission power source is set to zero instantaneously. When the heat source is turned off, the water-steam advection cools the solid slab until it reaches thermal equilibrium with the fluid.

Two versions of this SCRAM transient will be presented that have the same mass flow rate, but different velocities. The constant mass flow rate is accomplished by varying the area of the flow channel. For the high velocity test problem the flow area is four times smaller than the low velocity test problem. This results in an inflow velocity that is four times higher for the high velocity test problem. The inputs that are different between the two simulations are given in Table 1.

To compress the two-dimensional temperature data from the wall into a single point that can be plotted as a function of time, a new variable will be defined which will be called the peak-clad temperature. The peak-clad temperature will be defined as the maximum temperature of the wall cells that are adjacent to the fluid (the first column of cells on the left side of the wall in Fig. 1).

Figure 6 presents the peak-clad temperature for both versions of the SCRAM problem (see Table 1). The transients are stopped when the peak-clad temperature drops to 80% of its range from full power to no power (2400 to 594 K for the low velocity test problem and 2016 to 740 K for the high velocity test problem). In the high velocity test problem, the maximum peak clad temperature is lower (2016 versus 2400 K) and the minimum peak-clad temperature is higher (740 versus 594 K) therefore the transient time is roughly half of the low velocity problem (64 versus 112 s).

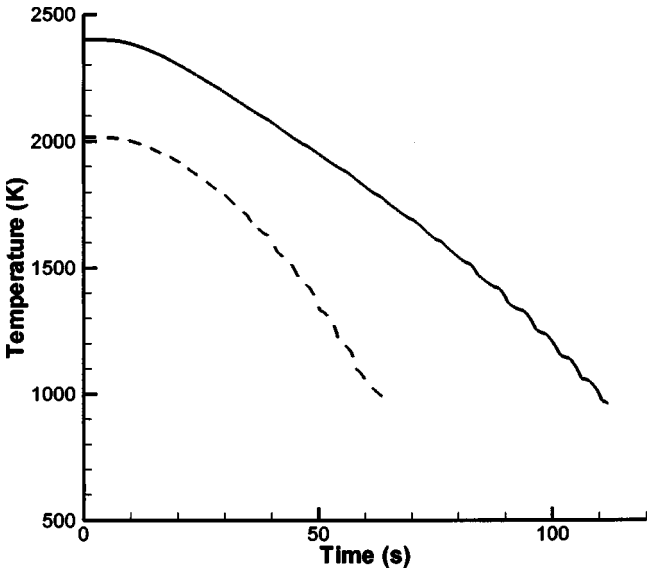

Fig. 6 Peak-clad temperature versus time for the high (dashed) and low (solid) velocity test problems

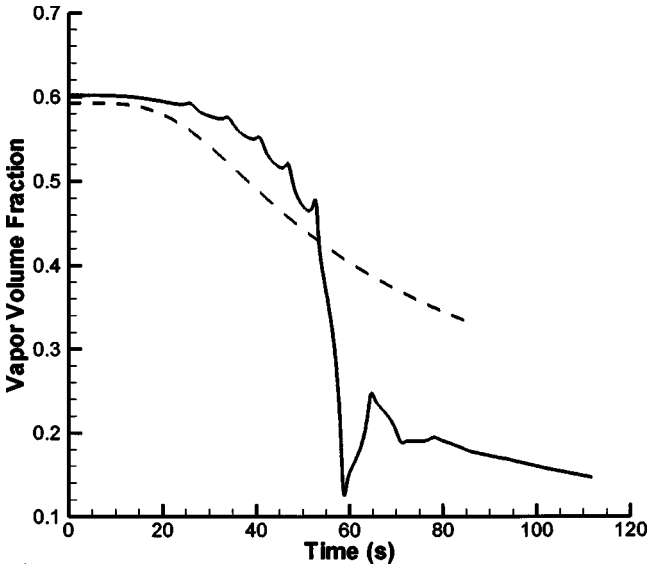

Fig. 7 Vapor volume fraction versus time for the constant closures (dashed) and the varaible closures (solid) at a location near the center of the domain

Closure Nonlinear Feedback Effects. A brief discussion will now be made about the impact of including the nonlinear feedback of the closure relations. In [2], constant closure relations were employed. Because of the constant closure relations, the solutions presented in [2] where smooth in both space and time. These smooth transients allowed the fully implicit solution of the hybrid method to obtain high levels of accuracy at large time steps. However, when the closure relations were made a function of vapor volume fraction, the solutions contained steep gradients in space. The propagation of these steep gradients in time restricted the size of an accurate time step. This effect has had a negative impact on the comparisons of the hybrid and OSSI solution methods.

Figure 7 shows a plot of vapor volume fraction as a function of time near the center of the one-dimensional domain (approximately 2.5 m). The plot includes data from the constant closure results presented in [2] as a dashed line and data from the closure relations that are a function of vapor volume fraction as a solid line. The constant closure relations result in a void fraction that is a smooth function of time while the variable closure relations exhibit significantly more structure with time.

Figure 8 shows a similar plot of vapor velocity (at approximately 2.5 m) as a function of time. Again the vapor velocity is a smooth function of time for the constant closure relations (dashed line) and the variable closure relations (solid line) show a more detailed structure as a function of time.

Figure 9 presents both the initial vapor volume fraction and the final vapor volume fraction for both the constant closure relations and the variable closure relations. The dashed lines (constant closure relations) show the smooth shape of both the initial vapor volume fraction (thin dashed line) and the final vapor volume fraction (thick dashed line). The smoothness of this transient lends itself to larger accurate time steps. The solid lines (variable closure relations) show very steep spatial gradients that are propagated as the solution evolves from its initial (thin solid line) to final (thick solid line) state.

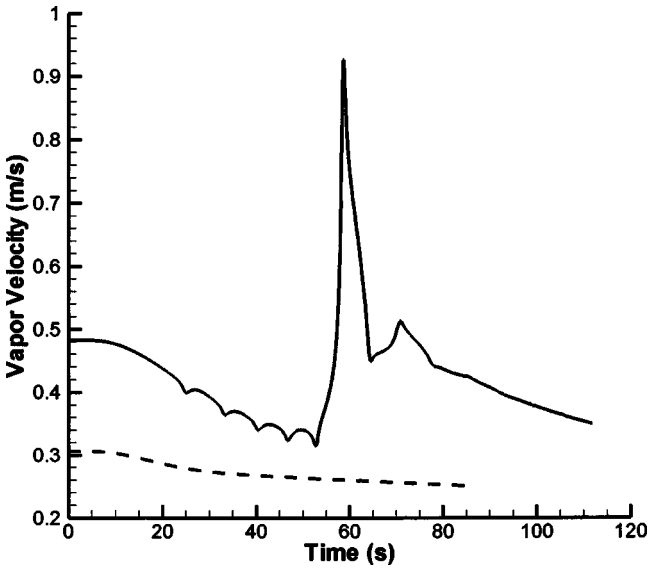

Fig. 8 Vapor velocity versus time for the constant closures (dashed) and the variable closures (solid) at a location near the center of the domain

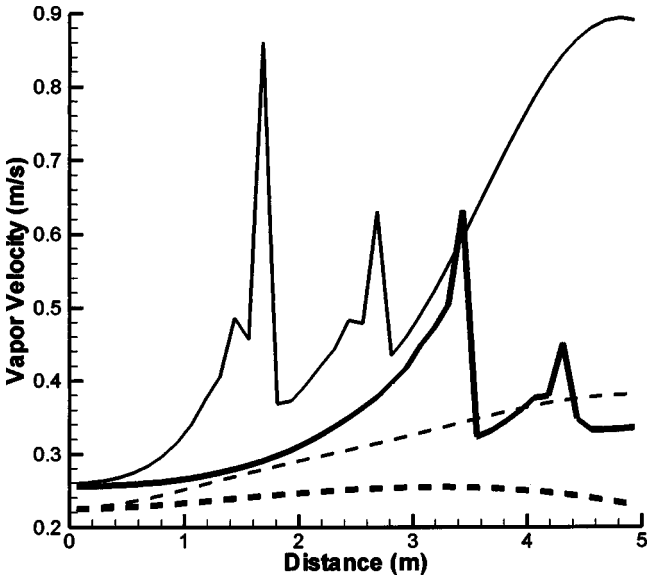

Fig. 10 Vapor velocity versus distance for the constant closures (dashed) and the variable closures (solid), thin lines initial, thick lines final

Figure 10 presents a similar plot for the vapor velocity. Once again the constant closure relations provide for small spatial gradients while the closure relations that depend on vapor volume fraction exhibit steep spatial gradients and structure that is propagated as the simulation evolves from its initial to final state. The nonlinear feedback between the vapor volume fraction and the interfacial mass, momentum, and energy exchange and wall momentum and energy exchange has had a dramatic effect on the solution evolution in space and time. This solution impact on the numerical method is one of the key differences between this article and [2].

Accuracy. Before presenting results about accuracy, a short discussion of error needs to occur. Because of the complexity of this nonlinearly coupled system of equations, there is no exact solution for the test problems. For this article, the ''exact'' solution will be a second order in time hybrid solution run at a time step ten times smaller than the smallest data presented on the plot. From this exact solution the vapor velocity is extracted. The vapor velocity was chosen since it is one of the most sensitive variables (see Fig. 8 and Fig. 10). The ''error'' is then computed from the following equation:

$$\text{error}=\left(\sum_{i=1}^{nx}\left[v_{g,i}-v_{g,i}^{e}\right]^{2}\right)^{1/2}. \tag{34}$$

Here the superscript e indicates the exact solution. In the results section the error will be plotted as a function of the material Courant number that is computed from,

$$\text{CFL}=\frac{v_{\max}\Delta t}{\Delta x}. \tag{35}$$

Here the maximum velocity is over both the liquid and vapor phase.

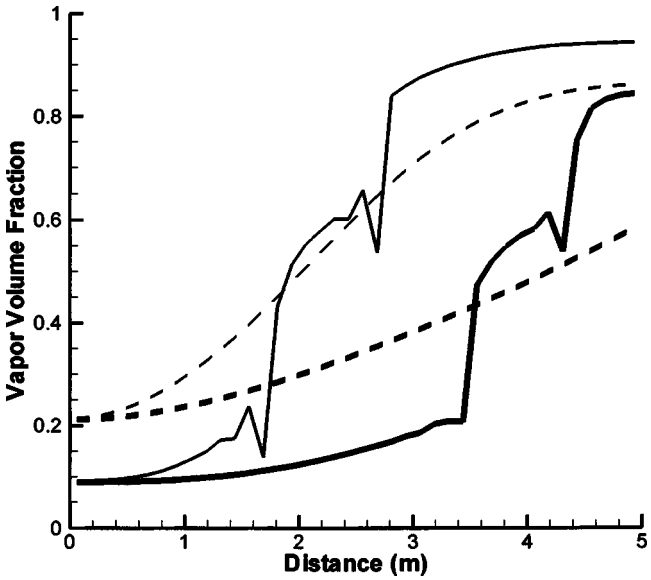

Fig. 9 Vapor volume fraction versus distance for the constant closures (dashed) and the variable closures (solid), thin lines initial, thick lines final

High Velocity Test Problem. Figure 11 presents a time step convergence study for the high velocity model problem. One can see for a given CFL number the error is always smaller for the second order in time hybrid solution than it is for the OSSI solution. In addition, the slope of the hybrid solution is second order for all of the data points.

The OSSI solution produced three data points (CFL $=1,1/2,1/4$) where the solution is clearly approximately two orders of magnitude larger than the three OSSI data points (CFL $=1/8,1/16,1/32$) that are first-order accurate in time. This catastrophic loss of accuracy is caused by unphysical oscillations in the solution. Researchers currently working with RELAP5 [16,17] have seen these types of oscillations. In both the NRC and DOE versions of RELAP5, work is currently underway to address this problem by improving the implicitness of the coupling between the fluid and the heat conduction. Additionally, a numerical technique called under-relaxation is employed in RELAP5 to help to smooth these types of oscillations [12].

For the single-phase Euler equations, the semi-implicit method addresses both the velocity and sound speed time scales and produces no oscillations in the solution up to a material Courant number of one. However, when the semi-implicit algorithm is applied to the physical model of this manuscript, there are now

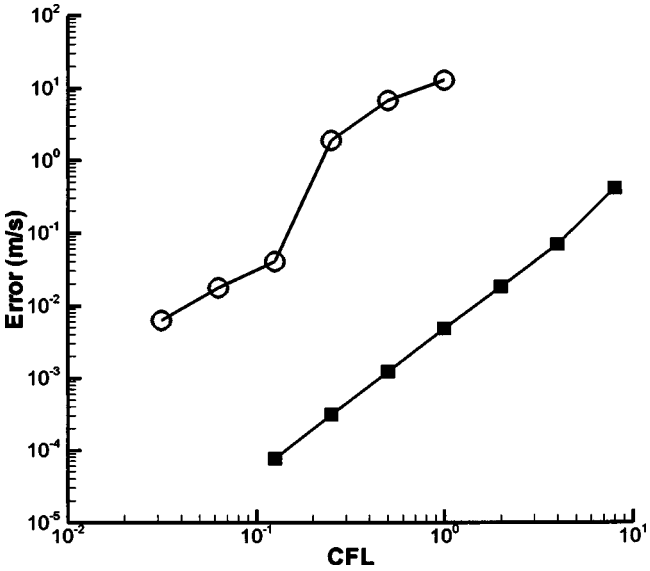

Fig. 11 High velocity test problem, error versus CFL number, squares hybrid, circles OSSI

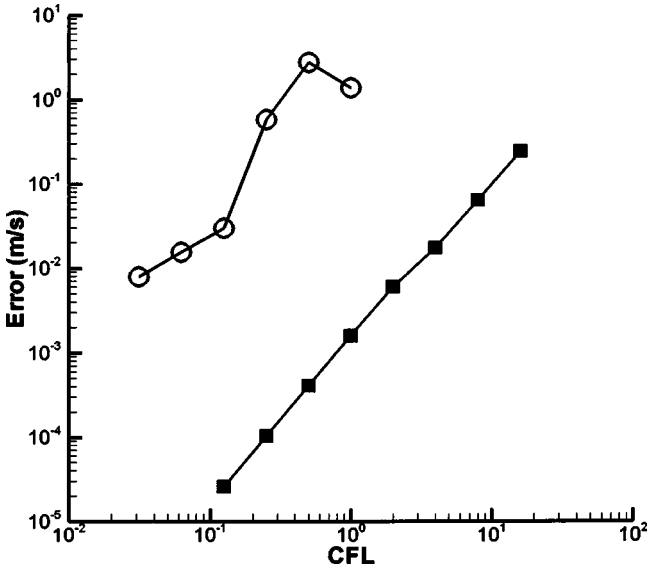

Fig. 13 Low velocity test problem, error versus CFL number, squares hybrid, circles OSSI

additional time scales associated with the exchange of mass, momentum, and energy between phases and with the exchange of momentum and energy between the individual phases and the wall. If the OSSI solution takes time steps too large to resolve these time scales, oscillations can occur. It should be noted that when the time step is made smaller, the unphysical oscillations are eliminated, and the slope of the OSSI solution is first order. Since the hybrid solution method solves all of the multiphase and heat conduction equations in a single system with all of the couplings (including the coefficients) implicit, the hybrid method does not experience these oscillations.

Figure 12 presents the same error points from Fig. 11, but in this figure the CPU time for the simulation is on the x axis. This simultaneous comparison of accuracy and CPU time will be referred to as an efficacy plot. This plot provides two clear pieces of information. A horizontal line determines how much CPU time is required to achieve a fixed level of accuracy. A vertical line determines how much accuracy can be obtained with a fixed amount of CPU time. Therefore, one can interpret these data to mean that for an error greater than 10^{-2} m/s or for a CPU time less than 100 s, the OSSI algorithm is the preferred solution method. For errors less than 10^{-2} m/s or CPU times greater than 100 s, the hybrid algorithm is the preferred solution method. If one needs to make a large number of runs where accuracy is not important (such as in a scoping study), the OSSI solution is a viable option. If one needs to make a few runs with a high level of accuracy, then the hybrid method is the better choice. However, since the hybrid solution contains both solution methods, both of these options are available.

Low Velocity Test Problem. Figure 13 presents a time step convergence plot for the low velocity test problem. This figure is very similar to Fig. 11. Again, the OSSI solution must take time steps at a CFL number of one eighth before the unphysical oscillations are removed.

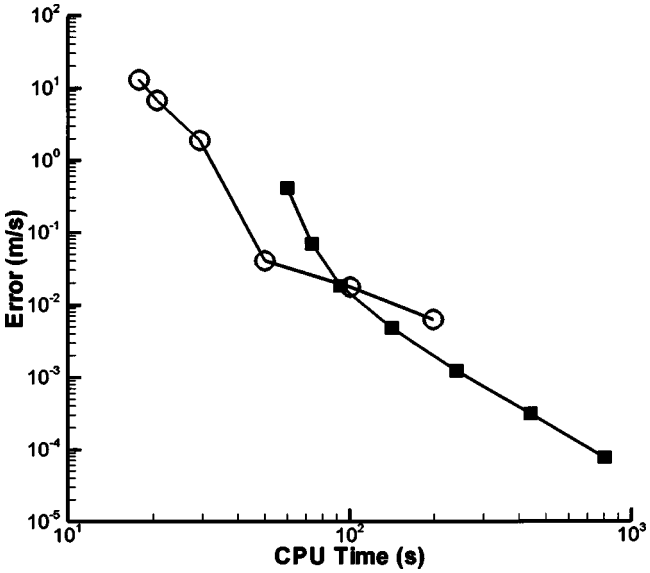

Fig. 12 High velocity test problem, error versus CPU time, squares hybrid, circles OSSI

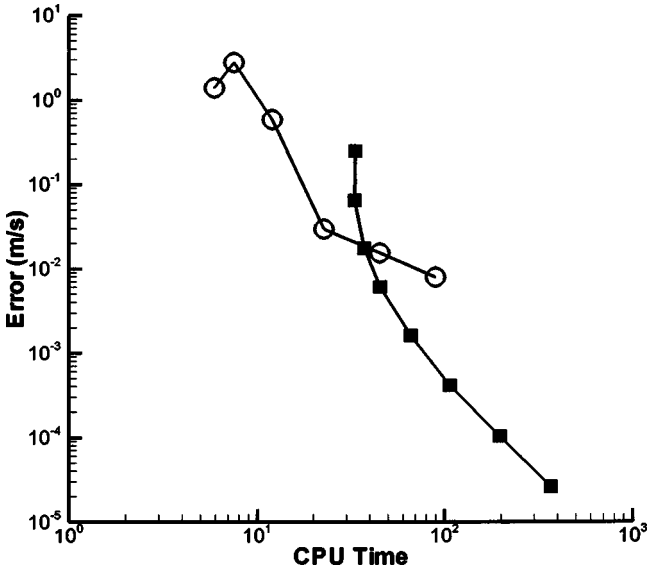

Fig. 14 Low velocity test problem, error versus CPU time, squares hybrid, circles OSSI

Figure 14 shows an efficacy plot that is similar to Fig. 12. Making the analysis similar to what was done for the high velocity problem, the OSSI solution is preferred for errors greater than 10^{-2} m/s and for CPU times less than 40 s. Recalling Fig. 6, which shows that the transient time for the low velocity test problem is longer than the high velocity test problem, it appears that as the transient time gets longer, the crossover point between the two solution method happens at a lower amount of CPU time.

Conclusions

Results have been presented for two variations of a simplified nuclear reactor SCRAM transient. In these two test problems the mass flow rates are the same but the velocities are different. Both simulations show that the hybrid solution is more accurate than the traditional OSSI solution for the same CFL number. This improved accuracy from the hybrid solution is due to the implicitly balanced solution and the second order in time integration scheme. This second-order accuracy is clearly present in the time step convergence plots. Results also show that for fast computer runs with a high error tolerance, the OSSI solution is preferred. For slower computer runs that require small error tolerances, the hybrid method is preferred. Since the hybrid solution algorithm presented in this manuscript contains the OSSI solution, it can provide a fast and accurate solution over a large range of problems.

In an attempt to resolve the accuracy and efficiency effects of the closure relations, closure relations that depend on the state of the fluid have been employed in this study as opposed to the constant closure relations in [2]. However, these closures are simpler than the ones employed in [5]. These simplified closure relations are used to determine the effect of the additional nonlinearity of the closure relations on the numerical algorithm. No attempt has been made to incorporate physically accurate closure relations like the ones employed in [5].

There is no reason to believe that closure relations that match the physics of two-phase flow will cause any difficulties with the numerical methods promoted in this article. However, it is important to note that closure relations that are discontinuous in the fluid properties and do not have the correct length and time scales for flow regime change could lead to difficulties in the numerical method. In addition, it is important for the closure relations to have the correct limits as the volume fraction approaches zero and one, so that the physics of phase appearance and disappearance is smooth.

The closure relations in this study increased the nonlinearity and caused a slight negative shift in the efficacy of the hybrid method relative to the traditional OSSI method. For the constant closure relations in [2] the hybrid method had higher efficacy for all of the test problems. In this study, there were ranges where the OSSI had higher efficacy and ranges where the hybrid method had higher efficacy. However, the accuracy and the robustness of the hybrid method were not negatively impacted by the nonlinearity of the closure relations. Future work will need to be done to determine if some of the difficulties in [5] were a result of discontinuities in the closure relations or from the discontinuities associated with switching between the single-phase equations and the two-phase equations.

Acknowledgment

This article has benefited from valuable conversations with Glen Mortensen, Richard Riemke, and Cesare Frepoli. This work was carried out under the auspices of the National Nuclear Security Administration of the U.S. Department of Energy at Los Alamos National Laboratory under Contract No. W-7405-ENG-36 (LA-UR-04-7078).

Nomenclature

C_p = specific heat ($J\,kg^{-1}\,K^{-1}$)
F_i = interfacial friction coefficient (kg)
F_{wf}, F_{wg} = wall friction coefficient ($m^3\,kg^{-1}$)
H = heat transfer coefficient ($W\,m^{-2}\,K^{-1}$)
P = pressure (Pa)
Q_{nw} = heat source from nuclear fission ($W\,m^{-3}$)
T = temperature (K)
U = specific internal energy ($J\,kg^{-1}$)
V = Volume (m^3)
a = area (m^{-1})
e_w = wall energy ($J\,m^{-3}$)
$\boldsymbol{g}$ = gravity ($m\,s^{-2}$)
h = specific enthalpy ($J\,kg^{-1}$)
v = velocity ($m\,s^{-1}$)

Greek

α = volume fraction
Γ = mass transfer ($kg\,m^{-3}\,s^{-1}$)
K = conductivity ($W\,m^{-1}\,K^{-1}$)
ρ = density ($kg\,m^{-3}$)

Subscripts

f = liquid (fluid) phase
g = vapor (gas) phase
i = interface
j = discrete spatial location
s = saturation
w = wall

References

[1] Mousseau, V., 2004, "A Hybrid Solution Method for the Two-Phase Fluid Flow Equations," ICONE12-49536, *Proceedings of ICONE 12 2004 12th International Conference on Nuclear Engineering*, ASME, New York.
[2] Mousseau, V., 2004, "Implicitly Balanced Solution of the Two-phase Flow Equations Coupled to Nonlinear heat Conduction," J. Comput. Phys., **200**, pp. 104–132.
[3] The RELAP5 code development team, 2001, "RELAP5/MOD3.3 Code Manual Volume I: Code Structure, System Models, and Solution Methods," NUREG/CR-5535 ed., U.S. Nuclear Regulatory Commission, Washington, D.C., (http://www.edasolutions.com/RELAP5/manuals/index.htm)
[4] The RELAP5 code development team, 2002, "RELAP5-3D Code Manual Volume I: Code Structure, System Models, and Solution Methods," INEEL-EXT-98-00834 Rev. 2.0 ed., Idaho National Engineering and Environmental Laboratory, Idaho Falls, (http://www.inel.gov/relap5/r5manuals.htm)
[5] Frepoli, C., Mahaffy, J., and Ohkawa, K., 2003, "Notes on the Implementation of a Fully-Implicit Numerical Scheme for a Two-Phase Three-Field Flow Model," Nucl. Eng. Des., **225**, pp. 191–217.
[6] Thurgood, M., and George, T., 1983, "COBRA/TRAC—A Thermal-Hydraulic Code for Transient Analysis of Nuclear Reactor Vessels and Primary Coolant System," NUREG/CR-3046, Vols. 1–4, U.S. Nuclear Regulatory Commission, Washington D.C.
[7] Knoll, D., and Keyes, D., 2003, "Jacobian-free Newton-Krylov Methods: A Survey of Approaches and Applications," J. Comput. Phys., **193**, pp. 357–397.
[8] Knoll, D., Chacon, L., Margolin, L., and Mousseau, V., 2003, "On Balanced Approximations for Time Integration of Multiple Time Scale Systems," J. Comput. Phys., **185**, pp. 583–611.
[9] Knoll, D., Mousseau, V., Chacon, L., and Reisner, J., 2004, "Jacobian-free Newton-Krylov Methods for Accurate Time Integration of Stiff Wave Systems," J. Sci. Comput., in press.
[10] Chan, T., and Jackson, K., 1984, "Nonlinearly Preconditioned Krylov Subspace Methods for Discrete Newton Algorithms," SIAM J. Sci. Comput. (USA), **5**, pp. 533–542.
[11] Brown, P., and Saad, Y., 1990, "Hybrid Krylov Methods for Nonlinear Systems of Equations," SIAM J. Sci. Stat. Comput., **11**, pp. 450–481.
[12] Mousseau, V., 2004, "Transitioning from Interpretive to Predictive in Thermal Hydraulic Codes," 125514, *Proceedings of the International Meeting on Updates in Best Estimate Methods in Nuclear Installation Safety Analysis*, American Nuclear Society, La Grange Park, pp. 44–51.
[13] Dembo, R., Eisenstat, S., and Steihaug, T., 1982, "Inexact Newton Methods," SIAM J. Num. Anal., **19**, pp. 400–408.
[14] Saad, Y., and Schultz, M., 1986, "GMRES: A Generalized Minimal Residual Algorithm for Solving Non-Symmetric Linear Systems," SIAM J. Sci. Stat. Comput., **7**, pp. 856–869.
[15] Brown, P., and Hindmarsh, A., 1986, "Matrix-free Methods for Stiff Systems of ODE's," SIAM J. Num. Anal., **23**, pp. 610–638.
[16] Mortensen, G., 2004, personal communication, member of the NRC's RELAP5 code development team at ISL.
[17] Riemke, R., 2004, personal communication, member of the DOE's RELAP5-3D code development team at INEEL.

Journal of Heat Transfer

Technical Brief

Development of Taylor-Görtler Vortices Over the Pressure Surface of a Turbine Blade

H. P. Wang
Pratt & Whitney

S. J. Olson
TSI, Inc.

R. J. Goldstein
Department of Mechanical Engineering, University of Minnesota, Minneapolis, Minnesota

The naphthalene sublimation technique is used to investigate the development of Taylor-Görtler vortices over the pressure surface of a simulated high performance turbine blade. Large spanwise variation in mass transfer is observed downstream on the pressure surface in the two-dimensional flow region for cases with low freestream turbulence, indicating the existence of Taylor-Görtler vortices. Different average and local mass transfer rates for the same flow conditions suggest that roughness variation near the leading edge affects the initial formation of Taylor-Görtler vortices. Larger and more uniformly distributed roughness at the leading edge produces much stronger Taylor-Görtler vortices downstream and greatly enhances the mass transfer rate. The variation between the vortices does not change appreciably along the flow direction. The flow in the boundary layer is laminar over the entire pressure surface. In the presence of external disturbances such as high freestream turbulence or a boundary layer trip, no Taylor-Görtler vortices are observed. [DOI: 10.1115/1.1865219]

Introduction

A naphthalene test blade, as described in a study by Wang et al. [1], is used in a linear cascade of a blowing wind tunnel with low freestream turbulence (Tu=0.2%). The primary cascade geometry and blade profile along with static pressure distribution can be found in the above study. Naphthalene is cast around the test blade with a well-polished mold. Depending on casting temperatures of the mold and liquid naphthalene, a relative rough surface could occur at rapid cooling spots like the leading and trailing edges. Since some interesting mechanism has been observed with this rough surface, the casting temperatures were intentionally varied to obtain different roughness distributions along the blade leading edge for testing. The roughed surface mainly stays around the leading edge and hardly noticeable with naked eyes. The downstream surface is very smooth and considered as unaffected by casting temperature. A dimensionless Sherwood number is used to characterize mass transfer. The naphthalene property calculation, and heat/mass transfer analogy can be found in Goldstein and Cho [2].

It should be mentioned that it is hard to obtain a uniform roughness around the leading edge with the current casting procedure. The imperfect casting suggests that it needs more work on systematic study of the roughness effect on Taylor-Görtler vortices. This study, however, sheds a light that the development of vortices would be affected by the roughness distribution along the leading edge. The nature of roughness is essentially the boundary layer disturbance. In the absence of vortices, the leading edge roughness, uniform or nonuniform, smooth or rough, generates almost similar transport rate, pointing negligible lateral effect on mass transfer.

A hot wire is also used to verify laminar boundary. A single-sensor hot-wire probe (TSI-1210) is inserted through three opening holes from the top endwall. The probe is positioned parallel to the pressure surface using a special elbow which turns the probe 90°. The measurements are made at three selected pressure surface locations, $S_p/C=0.21$, 0.27, and 0.56. Note that since the probe slightly oscillates due to its long arm even with a solid arm support, it is possible the probe might touch the wall in the near wall region. So the near wall boundary layer profiles were not obtained. The velocity profiles away from the wall, however, are quite satisfactory to determine the boundary layer flow regime.

The uncertainty of Sherwood number measurement, using the method described by Coleman and Steele [3], is about 8%. The uncertainty of hot wire measurement is estimated around 3.8%.

Discussion

Photographic Images. Figure 1 shows two photographs of a section of the naphthalene coated pressure surface after Taylor-Görtler vortices have developed, one with a smooth leading edge and the other with a moderately rough leading edge. The pictures were taken after a one-hour wind tunnel exposure for the smooth leading edge test and a 40 min exposure for the rough leading edge test. The image for the rough leading edge is taken after a real scan measurement, same as that of Fig. 2(*c*). The surface was rubbed with carbon paper to show naphthalene peaks (local minima of mass transfer) on the surface more clearly. The dark traces are actually quite parallel in the streamwise direction.

The variations due to the Taylor-Görtler vortices are quite clear visually, and appear to be periodic. The wavelength for a pair of counter-rotating vortices is indicated by peak-to-peak distances on the naphthalene surface. The two images show that the wavelength of the Taylor-Görtler vortices is nearly constant in the streamwise direction.

Figure 1(*a*) shows that the gaps between the valleys for the smooth leading edge case are a little narrower and shallower, compared to the rough leading edge case, indicating lower mass transfer. There are some slight differences in the appearance around the hills/valley (minima/maxima in Sherwood numbers). The trace marks of the rough leading edge case have relatively

Manuscript received March 1, 2004; revision received October 31, 2004. Review conducted by: S. Acharya.

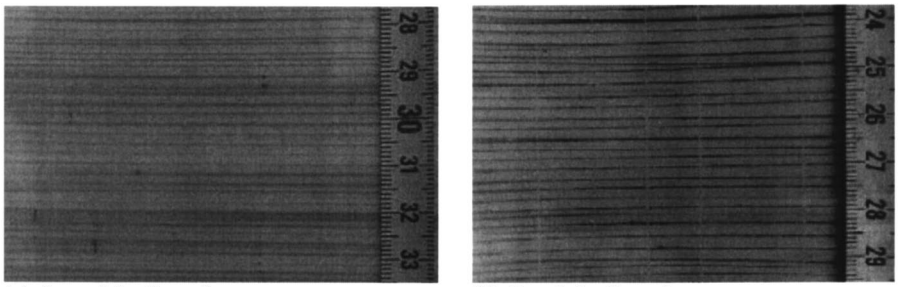

(a) Smooth leading edge (b) Rough leading edge

Fig. 1 Photographs of Taylor-Görtler vortices on a pressure surface at $Re_{ex}=5.2\times10^5$ (scale in centimeters). (*a*) Smooth leading edge and (*b*) Rough leading edge.

sharp hills while those of the other case are more blunt. The white spots in the surface with a rough leading edge are traces caused by the surface elevation measurement probe. It is possible that the probe rubs off some edges of the sharp peaks. If the probe happens to measure a spot right on a sharp edge (minimum in mass transfer), the measurement might overestimate Sherwood number on that spot, which in this case would make the Sherwood number fluctuation (peak-to-valley) smaller. So the real Sherwood number fluctuation could be even larger.

Boundary Layer and Görtler Number. Figure 2 shows the velocity profiles over a metal blade with a very smooth surface at three locations along the pressure surface. Also plotted in the figure are local similarity solutions (Sparrow et al. [4]) by assuming $Pr=Sc=2.28$. The measured boundary layer thicknesses at these three locations are listed in Table 1. Due to large curvature variation, the freestream velocity does not have a flat profile as for a flat plate and varies near-linearly outward especially at the locations of $S_p/C=0.21$ and 0.27. Consequently, the boundary layer thickness (δ) is defined, to a tangent point, along the asymptotic line approaching to the wall. It appears that the measurements match quite well with the local laminar similarity solution, indicating a laminar boundary layer flow regime along the surface at least up to $S_p/C=0.56$. Further observation from the mass transfer measurement seems to support that there is no boundary transition farther downstream. It is safe to conclude, therefore, at this Reynolds number ($Re_{ex}=5.2\times10^5$), that a laminar boundary layer exists over the entire pressure surface.

Based on the boundary layer measurement, the Görtler number can be determined, as shown in Fig. 3 and Table 1. Also shown in the figure are the calculated Görtler number and boundary layer thickness from local similarity solution. The Görtler number reaches a maximum ($G_{max}=6.2$ from calculation) at $S_p/C=0.15$, where Taylor-Görtler vortices commence (as found from the mass transfer measurement to be shown later) after an inflection point ($G=0$ at $S_p/C=0.065$) and decreases with the decreasing boundary layer thickness due to flow acceleration. Liepman [5] recommended that the Görtler number for laminar flow transition is around 6 to 9. The current Görtler number is at the lower bound of this recommended value. It appears that the disturbances in the boundary layer helped generate the Taylor-Görtler vortices, but the strong flow acceleration prevented further boundary layer growth and flow transition. The associated Görtler number is reduced along with boundary layer thickness.

Mass Transfer Results. Four mass transfer tests were conducted for $Re_{ex}\approx5.2\times10^5$ with low freestream turbulence ($Tu=0.2\%$) to study Taylor-Görtler vortices. An additional test at the same flow conditions used a boundary layer trip (a 0.5 mm wire), thinner than the boundary layer thickness, and glued on the sur-

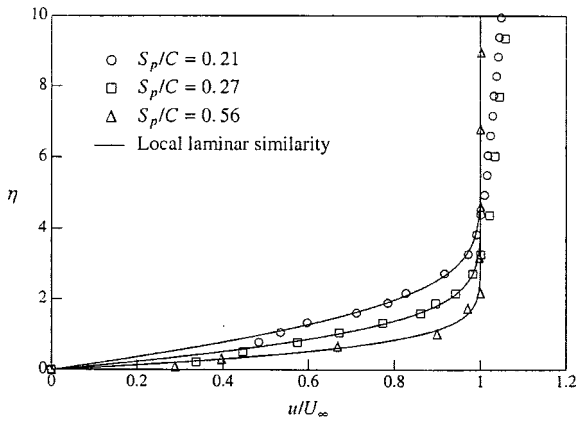

Fig. 2 Velocity profiles measured along pressure surface for $Re_{ex}=5.2\times10^5$

Table 1 Boundary layer values at $Re_{ex}=5.2\times10^5$

Sp/C	0.21	0.27	0.56
δ (mm)	1.29	1.11	0.68
θ (mm)	0.15	0.13	0.08
G	3.43	3.00	1.53

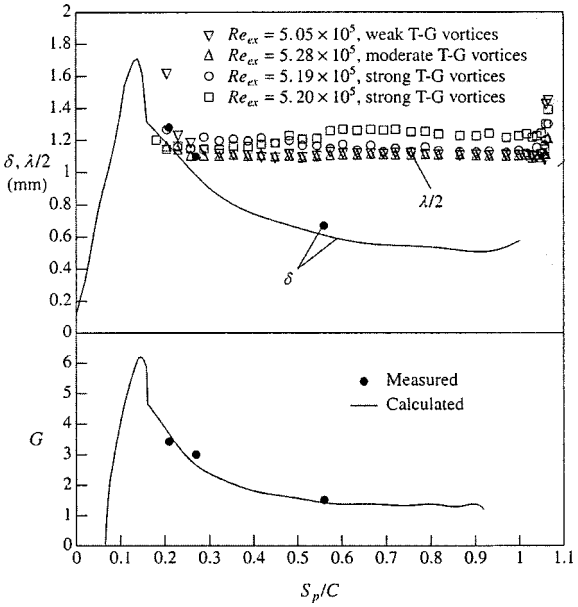

Fig. 3 Distribution of measured and calculated boundary layer thickness, wavelength, and Görtler number for $Re_{ex}=5.2\times10^5$

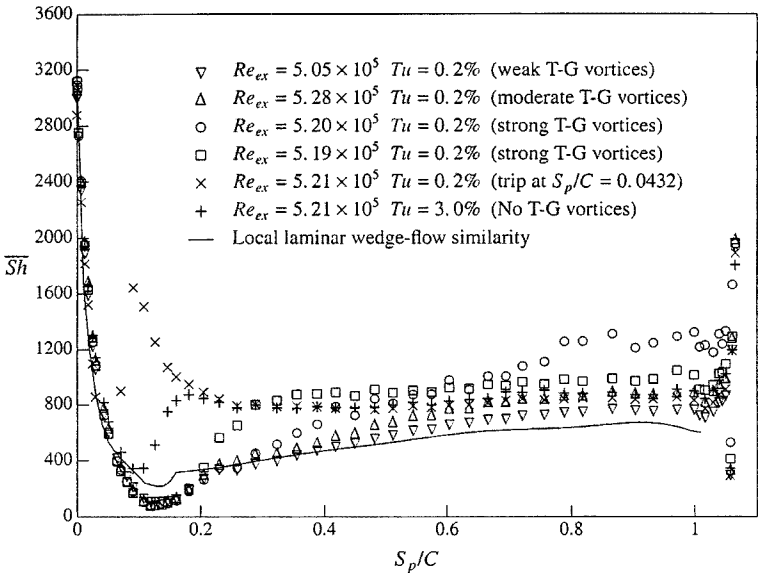

Fig. 4 Average Sherwood variation along blade surface at $Re_{ex}=5.2\times10^5$

face at $S_p/C=0.0432$. The spanwise-averaged Sherwood number distributions for these tests along the blade surface are shown in Fig. 4. Also shown in the figure are the results from a test with elevated incoming freestream turbulence (Tu=3%) generated by a turbulence grid inserted upstream as well as a local laminar wedge-flow similarity solution for the Sherwood number distribution. The local mass transfer distribution [three-dimensional 3D surface plots] for the four low turbulence cases are shown in Fig. 5.

Near the leading edge the mass transfer rates are nearly identical, but are quite different downstream for the four similar tests. It is observed that after exposure to a wind tunnel run, about $\frac{3}{4}$ of the entire pressure surface downstream has quite regularly distributed streaks (peaks and valleys) in the streamwise direction in this otherwise two-dimensional region as shown in Fig. 1. Those streaks appear to be caused by Taylor-Görtler vortices. Pairs of vortices produce upwash and downwash motion that in turn produces large spanwise variations in the Sherwood number. In the four tests with no freestream disturbance, the variation in the Sherwood number are quite different, suggesting stronger amplification of Taylor-Görtler vortices in two cases and relatively weaker amplification in the others. With a trip wire or high freestream turbulence, the spanwise variation in the Sherwood number is very small. There are no streaks found on the surface

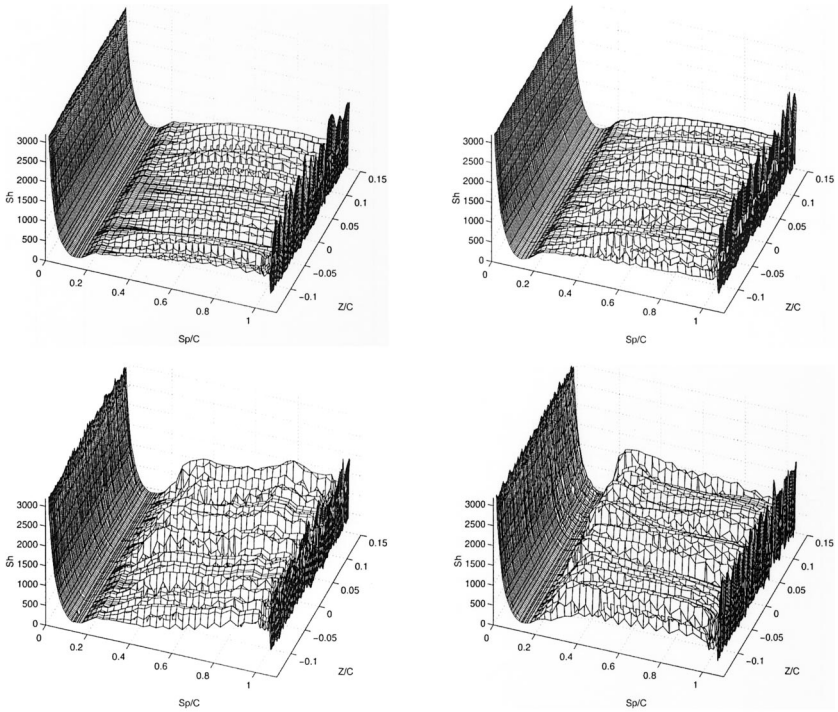

Fig. 5 Three-dimensional surface plots for $Re_{ex}=5.2\times10^5$. (*a*) $Re_{ex}=5.05\times10^5$, smooth LE, (*b*) $Re_{ex}=5.28\times10^5$, smooth LE, (*c*) $Re_{ex}=5.20\times10^5$, distributed rough LE, and (*d*) $Re_{ex}=5.19\times10^5$, distorted rough LE.

after the wind tunnel tests, indicating a typical two-dimensional flow and no development of Taylor-Görtler vortices.

Careful examination of the test blade and the mass transfer data reveals that the rough surface finish around the leading edge that can form during casting is a main factor in the variation of the Sherwood number. In the two cases studied, shown in Figs. 5(*c*)–5(*d*), the main effect of Taylor-Görtler vortices on mass transfer appears, relatively, in the downstream area for one and upstream for the other. Case (d) has slightly distorted spanwise roughness distribution around the leading edge, relatively rougher along one side (positive *Z*) and smoother along the other, causing different local boundary layer disturbances. As a result, relatively higher and lower fluctuation in mass transfer is observed in the corresponding downstream locations. The local variation in the Sherwood number reaches the maximum at $S_p/C \approx 0.3$, and its average value is much larger compared to the other cases at the same location. The Taylor-Görtler vortices appear to initiate earlier in this case than the others. Compared to the above case, Case (c) has a relatively uniformed leading edge roughness distribution. Interestingly, its fluctuation and average mass transfer rate is higher from midway through the trailing edge than all the other cases including those with a boundary layer trip or high incoming freestream disturbance. The other two cases [Figs. 5(*a*)–5(*b*)] have relatively smooth leading edges, compared to those discussed above. Taylor-Görtler vortices were still observed, but in a rather weak form. The average Sherwood number is not increased appreciably.

When the leading edge is rough the wavy surface pattern of peaks and valleys downstream can be observed visually almost immediately during the experiment once the wind tunnel reaches the desired speed. With a relatively smooth leading edge, however, it takes several minutes or more before the wavy surface pattern can be visualized. Also, the waviness is not as distinguishable as that for the rougher leading edge.

When Taylor-Görtler vortices form, two clear features are observed; the spanwise wavelength of the vortices remains relatively unchanged and the vortices persist downstream near the trailing edge, even though the surface shape downstream near the trailing edge is quite flat. A Fourier-series transform analysis was conducted along blade surface to find a wavelength distribution for these tests. The height of the vortex pair that is compatible to boundary layer thickness can be approximated by one half of its wavelength ($\lambda/2$). Its distribution is shown in Fig. 3. The cases with rougher leading edges have a slightly larger wavelength than those with smoother leading edges. Note $\lambda/2$ remains almost constant at 1.15 to 1.2 mm for the four runs conditions.

Conclusions

A series of naphthalene mass transfer experiments at $\mathrm{Re}_{ex} = 5.2\times10^5$ are conducted to investigate the effect of leading edge roughness on the development of Taylor-Görtler vortices on a simulated high performance turbine blade with incoming freestream turbulence level of $\sim 0.2\%$. Conclusions drawn from the tests are:

1. Taylor-Görtler vortices are observed for $\mathrm{Re}_{ex} = 5.2\times10^5$ without external disturbance over the pressure surface with a laminar boundary layer in a highly accelerated turbine cascade. The maximum Görtler number (calculated) is about 6.2 at $S_p/C = 0.15$, where Taylor-Görtler vortices initiate. The boundary layer does not undergo transition to turbulence due to a strong flow acceleration.

2. Surface roughness distribution near the leading edge is a main factor in triggering Taylor-Görtler vortices along the pressure surface and affects their growth even at a very low Görtler number. The disturbance in a laminar boundary layer caused by the leading edge roughness increases the chance for earlier formation of Taylor-Görtler vortices. Larger disturbances lead to stronger vortex pairs downstream and enhance mass transfer.

3. Larger variation along the span of the leading edge roughness that trigger the Taylor-Görtler vortices leads to higher mass transfer at corresponding downstream locations.

4. Taylor-Görtler vortices can increase significantly the mass transfer along the pressure surface, up to 100% increase has been found for $\mathrm{Re}_{ex} = 5.2\times10^5$ at some locations. The mass transfer rate can be higher in the presence of Taylor-Görtler vortices than in a flow disturbed by external means (boundary layer tripping or high freestream turbulence).

5. The wavelength of the Taylor-Görtler vortices remains almost constant along the pressure surface even though the boundary layer thickness decreases along the pressure surface. It is enlarged slightly with increasing leading edge roughness. The boundary layer thickness does not appear to affect the size of the vortices.

Nomenclature

- C = chord length of blade, = 184 mm in present study
- G = Görtler number, $= U_\infty \theta/\nu\sqrt{\theta/R}$
- Pr = Prandtl number
- R = radius of curvature along pressure service
- Re_{ex} = exit Reynolds number based on chord
- Sc = Schmidt number of naphthalene vapor, = 2.28 in this study
- S_p = curvilinear surface distance on pressure side
- Sh = Local Sherwood number based on blade chord
- Tu = turbulence intensity
- U_∞ = local freestream velocity along blade surface
- y = general boundary layer coordinate normal to blade surface
- Z = spanwise coordinates, = 0 is the midspan

Greek Symbols

- δ = boundary layer thickness, see Table 1
- θ = momentum thickness, see Table 1
- η = local similarity variable, $= y/S_p\sqrt{U_\infty S_p/\nu}$
- λ = wavelength of Taylor-Görtler vortex pair
- ν = kinetic viscosity of air

References

[1] Wang, H. P., Goldstein, R. J., and Olson, S. J., 1999, "Effect of High Free-Stream Turbulence with Large Length Scale on Blade Heat/Mass Transfer," ASME J. Turbomach., **121**, pp. 1–8.

[2] Goldstein, R. J., and Cho, H. H., 1995, "A Review of Mass Transfer Measurements using Naphthalene Sublimation," Exp. Therm. Fluid Sci., **10**, pp. 416–434.

[3] Coleman, H. W., and Steel, W. G., Jr., 1999, *Experimentation and Uncertainty Analysis for Engineers*, 2nd ed., Wiley, New York.

[4] Sparrow, E. M., Quack, H., and Boerner, C. J., 1970, "Local Nonsilmilarity Boundary-Layer Solutions," AIAA J., **8**, pp. 1936–1942.

[5] Liepmann, H. W., 1945, "Investigation of Boundary Layer Transition on Concave Walls," NACA Wartime Report.

Journal of Heat Transfer

Technology Review

Impingement Heat Transfer: Correlations and Numerical Modeling

Neil Zuckerman
e-mail: zuckermn@seas.upenn.edu

Noam Lior
e-mail: lior@seas.upenn.edu

The University of Pennsylvania,
Department of Mechanical Engineering and Applied Mechanics,
297 Towne Building,
Philadelphia, PA 19104-6315

Uses of impinging jet devices for heat transfer are described, with a focus on cooling applications within turbine systems. Numerical simulation techniques and results are described, and the relative strengths and drawbacks of the k-ε, k-ω, Reynolds stress model, algebraic stress models, shear stress transport, and v^2f turbulence models for impinging jet flow and heat transfer are compared. Select model equations are provided as well as quantitative assessments of model errors and judgments of model suitability.
[DOI: 10.1115/1.1861921]

1 Introduction

This is a brief review of numerical methods applied to problems in impingement heat transfer with the goal to identify preferred methods of predicting and optimizing the impinging flow performance. An emphasis is on heat transfer in turbine systems. Due to page limitations the equations and governing physics will not be presented in this article, but sufficient citations are included so that interested readers could find them at the appropriate sources.

Impinging jets provide an effective and flexible way to transfer energy or mass between a surface and the fluid in various applications. Heat transfer applications include cooling of stock material during material forming processes, heat treatment [1], cooling of electronic components, heating of optical surfaces for defogging, cooling of critical machinery structures, cooling of turbine components (the focus of this paper), and many other industrial processes. Typical mass transfer applications include drying and removal of small surface particulates. General physics, uses of, and performance of impinging jets have been discussed in a number of reviews [2–5] and will only be briefly described here. Figure 1 shows the arrangement of a set of impinging jets including the various regions of flow. The flow progresses from a free jet to a stagnating jet and then turns into a wall jet. Adjacent wall jets may combine to form a fountain region.

Compared to other heat or mass transfer arrangements that do not employ phase change, the jet impingement device offers efficient use of the fluid, and high transfer rates. For example, compared with conventional convection cooling by confined flow parallel to (under) the cooled surface, impingement produces heat transfer coefficients that are up to threefold higher at a given maximum flow speed, because the impingement boundary layers are much thinner, and often the spent flow after the impingement serves to further turbulate the surrounding fluid. Given a required heat transfer coefficient, the flow required from an impinging jet device may be two orders of magnitude smaller than that required for a cooling approach using a free wall-parallel flow. For more uniform coverage over larger surfaces, multiple jets may be used. The impingement cooling approach offers a compact hardware arrangement with no additional moving parts.

In turbine applications, impinging jet flows may be used to cool several different sections of the engine such as the combustor case, combustor can walls, turbine case/liner, and the critical high-temperature turbine blades. The gas turbine compressor offers a steady flow of pressurized air at temperatures lower than those of the turbine and of the hot gases flowing around it. Typical high-pressure bleed flows used to cool the blades are available at 600°C and must cool a turbine immersed in gas of around 1400°C total temperature [6]. This requires heat transfer coefficients in the range of 1000–3000 W/m^2 K, which equates to a heat flux on the order of 1 MW/m^2. The ability to cool these components in high temperature regions and increase the cooling rates allows higher cycle temperature ratios and higher power efficiency, improving fuel economy and raising turbine power output per unit weight. Modern turbines have gas temperatures in the main turbine flow in excess of the continuous operation temperature limits of the materials used for the blades, meaning the structural strength and component life are dependent upon effective cooling.

Compressor bleed flow is commonly used to cool the turbine blades by routing it through internal passages to keep the blades at an acceptably low temperature. As shown schematically in Fig. 2, the same air can be routed to a perforated internal wall to form impinging jets directed at the blade exterior wall. Upon exiting the blade, the air may combine with the turbine core airflow. Variations on this design may combine the impinging jet device with internal fins, smooth or roughened cooling passages, and effusion holes for film cooling. Figure 3 shows a general layout of an impinging jet cooling arrangement incorporated into a double-walled combustor liner. The operation of this device depends on flow acceleration through the liner holes, driven by the compressor, and carries an associated pressure drop penalty typically in the range of 1–3% of compressor fluid pressure, depending on the degree of cooling needed. In both arrangements the designer may alter the spacing or locations of jet and effusion holes to concentrate the flow in the regions requiring the greatest cooling. Though the use of bleed air carries a performance penalty (cf. Taniguchi et al. [7]), the small amount of flow extracted has a small influ-

Contributed by the Heat Transfer Division of ASME for publication in the JOURNAL OF HEAT TRANSFER. Manuscript received February 29, 2004; revised manuscript received October 21, 2004. Review conducted by: S. Acharya.

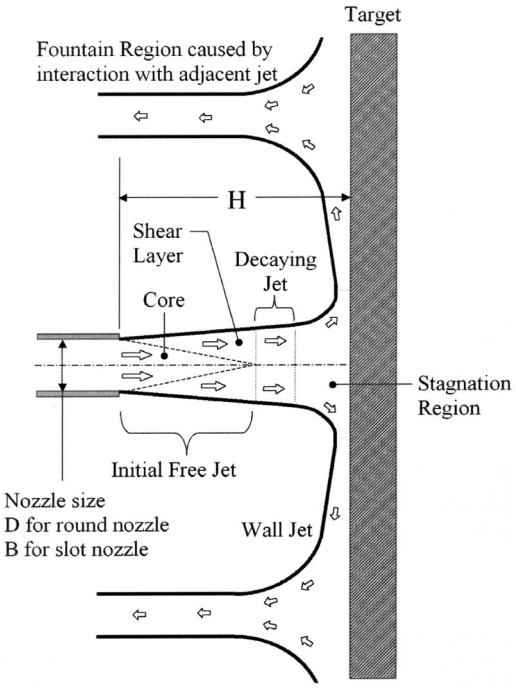

Fig. 1 The flow regions of impinging jets

ence on bleed air supply pressure and temperature. In addition to high pressure compressor air, turbofan engines provide cooler fan air at lower pressure ratios, which can be routed directly to passages within the turbine liner. A successful design uses the bleed air in an efficient fashion to minimize the bleed flow required to maintain a necessary cooling rate.

1.1 Nondimensional Heat Transfer Coefficients and Parameters. A set of common definitions and parameters are used to compare submerged impinging jet designs with a wide variety of operating temperatures, geometric scales, and fluids. The Nusselt number for jet impingement is typically defined as

$$\mathrm{Nu} = hD/k_c, \tag{1}$$

where h is the convective heat transfer coefficient defined as

$$h = \frac{-k_c \dfrac{\partial T}{\partial \vec{n}}}{T_{\mathrm{wall}} - T_{0\mathrm{jet}}} \tag{2}$$

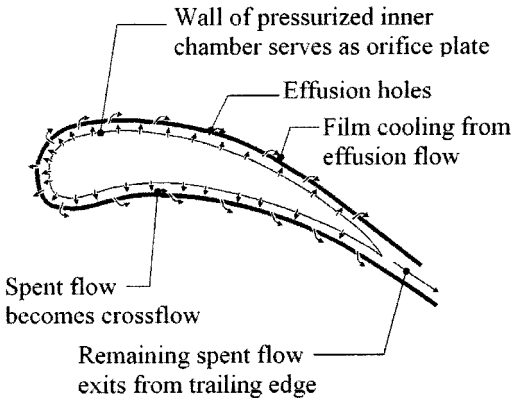

Fig. 2 Turbine blade impingement cooling flow path

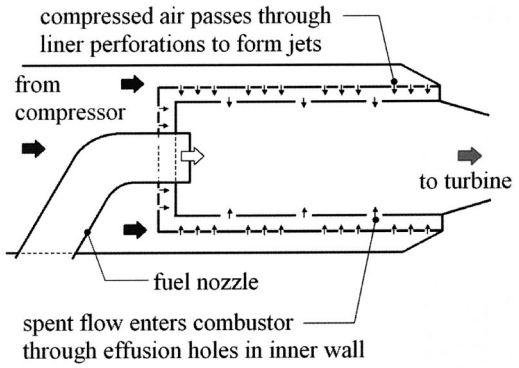

Fig. 3 Combustor section impinging-jet-cooled liner

The term $\partial T/\partial n$ gives the temperature gradient component normal to the wall.

The nondimensional parameters selected to describe the impinging jet heat transfer problem include the fluid properties such as Prandtl number Pr (the ratio of fluid thermal diffusivity to viscosity, fairly constant), plus the following:

- H/D—nozzle height to nozzle diameter ratio
- r/D—radial position from the center of the jet
- z/D—vertical position measured from the wall
- Tu—turbulence intensity, evaluated at the nozzle, $= \sqrt{\overline{u_j' u_j'}/\overline{u_i u_i}}$
- Re—jet Reynolds number $U_0 D/\nu$
- M—Mach number, based on nozzle exit average velocity (of smaller importance at low speeds, i.e., $M<0.3$)
- p_{jet}/D—jet center-to-center spacing (pitch) to diameter ratio, for multiple jets
- A_f—free area (=[total nozzle exit area/total target area]-1)
- f—relative nozzle area (=total nozzle exit area/total target area)

Jet behavior is typically categorized and correlated by its Reynolds number $\mathrm{Re}=U_0 D/\nu$, defined using initial average flow speed (U_0), the fluid viscosity (ν), and the characteristic length that is the nozzle exit diameter D or twice the slot width, $2B$ (the slot jet hydraulic diameter). At Re<1000 the flow field exhibits laminar flow properties, at Re>3000 the flow has turbulent features, and a transition regions occurs between these regimes. Turbulence has a large beneficial effect on the heat transfer rates. For example, an isolated round jet at Re=2000 (transition to turbulence), Pr =0.7, $H/D=6$ will deliver an average Nu of 19 over a circular target spanning six jet diameters, while at Re=100,000 the average Nu on the same target will reach 212 [2]. In contrast, laminar jets at close target spacing will give Nu values in the range of 2 to 20. In general, the exponent b in the relationship $\mathrm{Nu}\propto \mathrm{Re}^b$, ranges from $b=0.5$ for low-speed flows with a low-turbulence wall jet, up to $b=0.85$ for high Re flows with a turbulence-dominated wall jet.

1.2 Nozzle Design. The geometry and flow conditions for the impinging jet depend upon the nature of the target and the fluid source (compressor). In cases where the pressure drop associated with delivering and exhausting the flow is negligible, the design goal is to extract as much cooling as possible from a given air mass flow. Turbine blade passage cooling is an example of such an application; engine compressor air is available at a pressure sufficient to choke the flow at the nozzle (or perhaps some other point in the flow path). As the bleed flow is a small fraction of the overall compressor flow, the impinging jet nozzle pressure ratio will vary very little with changes in the amount of airflow

extracted. The cooling characteristics (based on flow and temperature) will instead vary greatly with changes in corrected compressor speed.

The details of the impingement device design affect the nozzle pressure drop, which then equates to a power requirement for the device. In the simplest of devices, this power is simply the volumetric flow rate multiplied by the nozzle exit dynamic pressure. In real installations, after passing over the target surface, the ''spent flow'' must exit the device. The overall power requirement then depends upon the details of the compressor intake pathway, compressor efficiency, flow path leading to the nozzle, and backpressure of the fluid exiting the target region. For this reason, one or more long, narrow supply pipes (common in experimental studies but not common to turbine designs) may not make an efficient device. Compact orifice plate nozzles have up to 2.5 times the pressure drop of a short, smooth pipe nozzle at a given mass flow and nozzle area, but provide a larger velocity gradient in the shear layer and thereby promote turbulence in the free-jet region [8]. Such orifice plates take up small volume for the hardware, are easy and inexpensive to make, and integrate well into the contoured airfoil surfaces of turbine blades. A thicker orifice plate (thickness from $0.3D$ to $1.5D$) allows the use of orifice holes with rounded entry pathways, approaching an ideal bellmouth shape, as with the contoured nozzle. This successful compromise comes at the expense of greater hardware volume and complexity, but reduces the static pressure losses to those required to accelerate the flow to the exit speed plus that of mild contraction into the rounded passageway. The orifice plate nozzle array remains the most practical and flexible geometry for turbine cooling due to its compact size and its ability to focus additional flow on regions requiring higher heat flux (e.g., blade leading edges) by variation in the nozzle hole spacing.

A series of additional holes in the fluid supply plate of an orifice array, designed for the spent flow, can provide benefits in cases with restrictive exit pathways. These effusion holes vent to exit ducting or the surroundings to provide a lower-restriction exit pathway for spent air. In a turbine blade (Fig. 2) the preferred effusion pathways are either through holes in the target wall itself (the blade exterior) to form a film cooling layer on the opposing surface, or through the confined flow region leading to aerodynamically favorable exit holes on or near the trailing edge of the blade. In highly confined flows, the use of sharp-edged nozzles and well-positioned effusion holes rather than simple pipe jets can increase Nu by a factor of 2 at a given Re, which is important in turbine cooling where jet mass flow directly affects turbine performance.

1.3 Typical Impinging Jet Device Characteristics. Typical gas jet installations for heat transfer span a Reynolds number range from 4000 to 80,000. H/D typically ranges from 2 to 12. Ideally, Nu increases as H decreases, so a designer would prefer to select the smallest tolerable H value, noting the effects of exiting flow, manufacturing and assembly capabilities, and physical constraints, and then select nozzle size D accordingly. For small-scale turbomachinery applications jet arrays commonly have D values of 0.2–2 mm, while for larger scale industrial applications, jet diameters are commonly in the range of 5–30 mm.

2 Prediction and Modeling of Impinging Jet Performance

The designer of an impinging jet device needs to predict the transfer coefficient profile (Nu), necessary fluid flow per unit of target area (G), and pressure drops in advance of manufacturing the hardware. Accurate models or calculation methods are desirable as they minimize the amount of testing required. A reliable set of models provides the designer with a rapid, inexpensive, and flexible alternative to conducting a series of hardware tests. Modeling of the turbulent flow, incompressible except for the cases where the Mach number is high, is based on using the well-established mass, momentum, and energy conservation equations.

2.1 Empirical Correlations. First, simple correlations such as those supplied by Martin [2] (with a summary in Ref. [1]) predict Nu as a function of the governing parameters (as listed in Sec. 1.1) in cases where the fluid has a continuously laminar flow over the entire fluid and target region of interest ($\mathrm{Re}_{\mathrm{jet}} < 1000, \mathrm{Re}_{\mathrm{wall}} < 10{,}000$). A list of available impingement heat transfer correlations for laminar and turbulent flows is presented in the Appendix.

2.2 Laminar Impingement. For laminar flows in many geometries, the governing equations may be reduced to analytical solutions, such as that for a stagnating flow field placed above a wall boundary layer [9]. Numerical modeling of steady laminar flows is fairly straightforward, using the mass, momentum, and energy conservation equations in time-invariant forms. This simulation approach may even yield useful results for flows which are laminar over most but not all of the domain. Kang and Greif [10] successfully predicted flow field properties, separation locations, and heat transfer coefficients for impinging jets on cylinders for $100 \leqslant \mathrm{Re} \leqslant 1000$, including exploration of buoyancy effects.

2.3 Turbulent Impingement Models. Most impinging jet industrial applications involve turbulent flow in the whole domain downstream of the nozzle, and modeling turbulent flow presents the greatest challenge in the effort to rapidly and accurately predict the behavior of turbulent jets. Numerical modeling of impinging jet flows and heat transfer is employed widely for prediction, sensitivity analysis, and device design. Finite element, finite difference, and finite volume computational fluid dynamics (CFD) models of impinging jets have succeeded in making rough predictions of heat transfer coefficients and velocity fields. The difficulties in accurately predicting velocities and transfer coefficients stem primarily from modeling of turbulence and the interaction of the turbulent flow field with the wall.

The computation grid must resolve both the upstream and downstream flow around the nozzles or orifices and must extend sufficiently far to the side of a single jet or array (typically 8–10 diameters) to provide realistic exit conditions. Zero-gradient and constant-static-pressure conditions have been used at the far-field model boundaries. Successful, stable modeling using both of these conditions can depend on properly shaping the boundary at the edge of the model domain. Turbulent impinging jet CFD employs practically all available numerical methods, which will be critically and briefly reviewed below. For brevity the governing equations are not listed here. Full equation sets for each model are available in the referenced publications.

2.3.1 DNS and LES. The direct numerical simulation (DNS) method solves the full Navier–Stokes, continuity, and energy/mass diffusion equations using discrete units of time and space, but requires an extremely small grid to fully resolve all the turbulent flow properties, because the microscopic turbulent length scales involved in jet impingement are far smaller than the macroscopic lengths involved (e.g., D_0 or H). The consequently long computation time practically limits the use of DNS to Reynolds numbers much lower than those in the gas turbine impingement heat transfer application. In an attempt to remedy this situation, some CFD models use large eddy simulation (LES). The time-variant LES approach tracks flow properties with the full equations down to some user-defined length scale (typically the grid spacing), and then uses additional subgrid-scale equations to describe turbulent flow behavior at smaller scales. The LES method has shown encouraging results and clarified the understanding of formation, propagation, and effects of flow eddies upon the velocity fields and jet transfer characteristics [11–14], but it requires high resolution in space for accuracy, may require high resolution in time for stability and accuracy, and therefore still needs a great amount of computing power or time to produce satisfactory solu-

tions for the transitional and turbulent flows of interest here (Re >1000). LES modeling by Cziesla et al. [15] demonstrated the ability of LES to predict local Nu under a slot jet within 10% of experimental measurements. The use of LES does not necessarily have an upper or lower limit on Re (though particular codes may be limited to $M \leqslant 1$), but for laminar flows ($\mathrm{Re} < 1000$) the influence of turbulence is small enough that the DNS approach offers little improvement in accuracy over the time-averaged techniques detailed below. For those cases where computational cost is not a primary concern, the LES method offers the greatest information about the impinging jet flow field.

2.3.2 The RANS Approach. Steady-state time-averaged solution techniques, typically Reynolds-averaged Navier–Stokes (RANS) models, use some version of the Navier–Stokes equations adjusted for the presence of turbulent flow. The majority of RANS models used for jet flows fit into one of two categories, the eddy-viscosity models and the computationally more costly full second moment closure (SMC) models. Eddy viscosity models treat the turbulent viscosity as a scalar quantity, assuming or forcing an isotropy in the normal stresses [16]. The various full SMC models track all Reynolds stresses or track the various components of a nonuniform turbulent viscosity. These models approximate the Reynolds stresses and heat fluxes using semi-empirical equations based on expected physical trends rather than direct derivations. The semi-empirical equations provide approximations of undetermined terms within the second-moment equations, typically two-parameter correlations. With further manipulation a series of higher-order-moment equations can be generated, but these more complex models have even more correlation terms and unknowns, which require approximate modeling.

2.3.3 Near-Wall Treatment. In addition to the portions of the CFD model describing the fluid flow inside the computational domain, the steady and transient models require a description of how the flow behaves next to the wall (the target surface). This part of the model typically plays the major role in properly predicting both the flow and the heat transfer [17]. The fundamental difficulty comes from the need to describe how the turbulent regions of a decelerating flow field interact with the wall, including in the wall's boundary layer. A variety of often very different wall damping and reflection terms have been implemented. Numerical solutions have shown that heat transfer rates within the viscous sublayer are of a larger magnitude than outside the layer. The spatial region in which the turbulence models have the greatest difficulty approximating the flow is the same region in which the largest heat and mass gradients occur, and so this region cannot be neglected.

Numerical models of turbulence near the wall commonly feature one of two approaches. In the first obvious approach, the grid near the wall is constructed at sufficiently high resolution to properly resolve flow in the entire viscous sublayer and turbulent boundary layer with turbulence equations intended for use at low cell Reynolds numbers. This requires a model capable of resolving turbulent behaviors very close to the wall, and a large computation effort.

The alternate method uses algebraic equations to relate steady and fluctuating velocity and scalar profiles to wall distance and surrounding fluid properties. These wall functions predict the flow properties in and above the viscous sublayer. This method requires only a single cell in the sublayer, and thus requires less computational time. Relations for high Re parallel flows such as the "law of the wall" are based upon flows in different geometry than that of the impinging jet and may not produce a correct velocity profile near the wall, especially in cases where the flow separates or reverses on the target surface. The standard law of the wall is based upon the absence of pressure gradients near or along the wall, clearly a different flow field than that seen in the stagnation region of an impinging jet. The nonequilibrium law of the wall is based upon differing turbulent energy generation and destruction rates and accounts for pressure gradients. Bouainouche et al. [18] performed modeling with various wall equations and concluded that the standard logarithmic law of the wall poorly predicted shear stresses (errors of up to -30% in the stagnation region) and that a generalized nonequilibrium law of the wall performed well in the stagnation region but under predicted wall shear stress in the wall-jet region (errors of up to -12%). Their "hybrid law of the wall" model produced improved results by using the nonequilibrium law in the stagnation region and switching to the logarithmic law in the wall-jet region.

Specific difficulties arise with the numerical modeling of impinging jets. A number of models reviewed below, such as k-ε, have been optimized for free-shear flows such as submerged jets. Some models, such as k-ω, perform best in boundary-layer flows such as the wall-jet region. Unfortunately, the impinging jet problem contains both of these as well as significant pressure gradients in the stagnation region. The normal strain and the rise in fluid pressure in the stagnation region affect the turbulent flow through distinct terms in the second-moment RANS equations. The pressure plays a part in the turbulent diffusion term. The effects of changing pressure play an even greater role in the pressure-strain rate correlation term. Unlike the turbulent diffusion term, which most models focus on approximating, the pressure-strain correlation was usually of secondary interest. As a result, most models have simpler and less accurate predictions for turbulent effects in the stagnation region. A wide variety of equation sets have been implemented to model these pressure-strain rate correlation terms related to $\nabla u'$ and ∇u, with varying success. The two equation eddy-viscosity models, such as k-ε, contract the rank-2 tensors in the equations to eliminate terms, and thus drop these terms. That is, the two-equation models are based around assumptions about the low importance of pressure gradients and the minimal anisotropy of the Reynolds stresses, and experiments have shown that these modeling assumptions do not apply in the stagnation region.

2.3.4 The Boussinesq Approximation. The simplified RANS models need some approximation to determine the Reynolds stresses. An equation known as the Boussinesq approximation (or hypothesis) describes a simple relationship between turbulent stresses and mean strain rate. Given a strain rate tensor S_{ij}, where $S_{ij} = 1/2[(\partial \overline{u_i}/\partial x_j) + (\partial \overline{u_j}/\partial x_i)]$ the approximation gives a formula for the Reynolds stress tensor

$$-\rho \overline{u_i' u_j'} = 2\mu'(S_{ij} - \tfrac{1}{3} S_{kk}\delta_{ij}) - \tfrac{2}{3}\rho k \delta_{ij} \tag{3}$$

By itself, the Boussinesq approximation does not constitute a complete turbulence model, as the value of μ' is unknown and depends on turbulence scales unique to each problem.

2.3.5 The k-ε Model. The commonly tested "k-ε" eddy-viscosity model is widely acknowledged as producing poor results in the impinging jet problem, but remains a benchmark against which to compare better models [17]. The k-ε model remains in use due to its common implementation and comparatively low computational cost. The model uses the Boussinesq hypothesis to calculate the Reynolds stresses as a direct function of the velocity gradients and is based on flow behavior at higher Reynolds numbers (fully turbulent fluid flow). It independently tracks turbulent energy k and turbulence destruction or dissipation rate ε, with a dissipation equation based upon expected trends. As with most RANS models it requires experimentally determined constants to fully close the equations. The k-ε model can produce acceptable results for free-shear flows but provides poor simulation of wall-jet flows. The model requires the user to specify ε at each boundary, but at the walls ε has a finite, nonzero value that is not known in advance. For the impinging jet problem it gives useful results in the free-jet region but poor results in the stagnation region and wall jet region, as detailed below. It gives poor predictions of the location of separation points on solid boundaries and for the impinging jet problem it may fail to predict the occurrence of secondary peaks in Nu. The standard k-ε model is formulated for

flows at high Reynolds number and does not apply in regions where viscous effects on the flow field are comparable in magnitude to turbulent effects (such as in the sublayer next to a wall). In many cases the model uses wall functions to determine the velocity profiles. Alternately, k-ε models have been built with additional terms and damping functions to allow the model to simulate portions of the flow at low Reynolds numbers.

The Launder and Sharma low Reynolds number model used by Craft et al. [17] in a comparative CFD study of various turbulence models used for the impinging jet problem incorporates conservation equations for k and ε as well as a simple equation to set the velocity-temperature correlation (heat flux) proportional to the temperature gradient. This version of the model includes the Yap correction term to adjust the dissipation rate $\tilde{\varepsilon}$ as a function of k, $\tilde{\varepsilon}$, and distance from the wall y. At low Re a damping function is used to add an adjustment to the turbulent viscosity used in the conservation equations. It increases the dissipation to reduce the turbulent length scale. Without the correction the model will over predict turbulent length scale and overpredict turbulent viscosity. The model constants depend on empirical data, and the correction terms and associated constants are therefore somewhat arbitrary, so engineers continually invent alternate adjustment terms with different closure coefficients.

Heyerichs and Pollard [19] conducted a numerical comparison of three different wall function and five different wall damping functions with an impinging jet test case and concluded that the selected k-ε models with wall functions gave consistently poor results, with Nu errors in the range of -21.5–-27.8% in the stagnation region, and $+32$–$+38.4\%$ at the secondary peak. Somewhat better matches were produced using models with damping functions, but those models still produced errors in Nu of up to 50% and misplaced the secondary peak. They concluded that basing the damping functions on wall position y^+ caused the poor results, as the damping functions using y^+ were based upon simple wall-parallel flows with simple boundary layers, rather than the flow found in the stagnation region of the impinging jet.

Craft et al. [17] presented a comparison of a two-dimensional implementation of the k-ε model versus test data. For the test case at Re=23,000 the model predicted centerline wall-normal-root-mean-square (rms) velocity levels up to four times larger than those measured in the experimental work of Cooper et al. [20]. A specific problem noted in the k-ε model was that the model equation relating turbulent kinetic energy to turbulent viscosity caused increasing and erroneous turbulent kinetic energy levels in the stagnation region (increasing turbulent viscosity caused increasing turbulence intensity). The model similarly over predicted wall normal r.m.s. velocity at $r/D=0.5$, corresponding to the edge of the jet. Wall-parallel velocity errors were in the range of 15–20%, with errors of up to 50% in the $y/D<0.05$ region very close to the wall. The model over predicted Nu in the center of the impingement region by up to 40% and failed to predict the secondary Nu peak at $r/D=2$. Craft et al. [21] continued work with this type of model, developing an alternate k-ε model which produced greatly improved impingement centerline wall-normal fluctuating velocity values and better Nu predictions in the $r/D<2$ region. The largest errors in Nu were typically 15%, occurring in the range of $1<r/D<3$. Turgeon and Pelletier [22] built adaptive k-ε models which succeeded in generating a solution with minimal grid dependence, showing that the difficulties with applying the k-ε model are independent of grid resolution and persist for small mesh sizes. Merci et al. [23] devised and tested an altered nonlinear variation of the k-ε model, yielding improved results over the standard model but an under prediction of $\mathrm{Nu}/\mathrm{Nu}_0$ of up to 25% (alternately interpreted as an over prediction of Nu_0). Souris et al. [24] showed that the upstream errors in low Reynolds number k-ε model predictions resulted in large downstream errors, giving wall-jet thicknesses up to double that of experiment, and wall-jet peak velocity as much as 44% below experimental results. From the various studies conducted, we conclude that the even the best k-ε models and associated wall treatments will yield Nu profiles with local errors in the range of 15–30%, and the standard k-ε model is not recommended for use in the impinging jet problem. These shortcomings are attributed to the assumption of isotropic turbulence and the use of wall functions that poorly approximate near-wall velocity fluctuation and associated transport properties.

2.3.6 The k-ε RNG Model. Other variations of the model have been applied, such as the renormalization group theory k-ε model (RNG). The RNG model incorporates an additional term in the turbulent energy dissipation equation based on strain rates, and includes adjustments for viscous effects at lower Re and a calculation of turbulent Pr. Heck et al. [25] showed the RNG model provided a close match of Nu in the wall-jet region but an error of up to 10% in the stagnation region. This is in part due to the RNG model's tendency to predict jet spreading rates that are as high as twice that found in experiment [26]. This flaw on the upstream end of the model leads one to question how the downstream results did not stray as far from measured values. It offers some improved performance over the standard k-ε at a slightly higher computational cost and is recommended when only moderate accuracy is required.

2.3.7 The k-ω Model. The k-ω model solves for turbulent kinetic energy (k) and energy dissipation rate per unit of turbulent kinetic energy (ω), where ω is determined through a conservation equation including experimentally determined functions, rather than direct calculation from the velocity field [26]. The equations for ω treat it as a vorticity level or vortex fluctuation frequency. The model then produces turbulent viscosity as a function of k and ω.

As with the k-ε model, the latest versions of the k-ω model include correction terms to improve predictions in the low Reynolds number flow regions. The k-ω model typically produces Nu profiles with a local error of up to 30% of the experimental Nu value. It can produce better predictions of the turbulent length scale than the k-ε model. The k-ω model can generate good predictions of flow properties in the wall jet, both in the sublayer and logarithmic region, without the need for damping functions. For a flow near a wall the boundary conditions are known—turbulent viscosity and the turbulent time scale are set to zero. The value of ω at or near the wall-adjacent cell may be set proportional to ν/y^2, meaning the user can fully specify the turbulence conditions at the wall, unlike in the k-ε model. Unfortunately the k-ω model is sensitive to far-field boundary conditions, much more so than the k-ε model. Park et al. [27] demonstrated some improved results using the k-ω equations but noted that at higher Re (25,100) the secondary Nu peaks appeared too far inward, as low as 50% of the experimentally measured value of x/B. The local levels of Nu were overpredicted by as much as 100% as the result of misplacing this peak. A comparative study by Heyerichs and Pollard [19] found that the k-ω model over predicted Nu by up to 18% and generated a secondary peak closer to the jet center than found in experiment, but concluded that for the impinging jet problem it clearly outperformed the nine different implementations of the k-ε model used in the study. The low-Re k-ω model gave good results by matching the shape of the experimental curves, but alternate formulations of the impinging jet CFD model using k-ω with wall functions gave poor results—they replaced the k-ω model with a cruder approximation in the very region where it gives the best results, overpredicting wall jet Nu by as much as 40%. Chen and Modi [28] successfully applied the k-ω model for mass transfer at high Sc, and claimed agreement within 10% of experimental results, given very high grid densities. The addition of cross-diffusion terms in various k-ω models have succeeded in reducing its sensitivity to far-field ω boundary conditions, a problem known to arise during use of the k-ω model for unconfined or partially confined flows. With the inaccurate free-jet modeling, dense wall grid requirement, and undesirable sensitivity

to unknown far-field conditions, we conclude the k-ω model is only moderately better than the k-ε; it offers better predictions of Nu, with a higher computational cost.

2.3.8 Realizability Constraints. In cases of high strain rate the simple Boussinesq approximation may predict negative normal Reynolds stresses or excessively high Reynolds shear stresses. The k-ε, k-ω, and v^2f models described herein have been commonly modified to use realizability limits to prevent these problems. A common fix is to allow variation in the constant of proportionality C_μ found in the turbulent viscosity equation $\nu' = C_\mu(k^2/\varepsilon)$ [29]. Physical measurements have demonstrated variation in this ''constant'' in differing fluid flows. Other approaches put simple limits on time scales, length scales, strain rates, and/or terms including strain rates.

Abdon and Sunden [30] used nonlinear k-ε and k-ω models with realizability constraints to model impinging jets. These model adjustments produced results closer to experimental data, with the realizable k-ε model predicting Nu_0 within 10% (within the experimental data scatter) and the realizable k-ω model over predicting Nu_0 by 20%. Further studies with nonlinear versions of the k-ε and k-ω models produced Nu profiles with errors equal to or greater than the standard linear models. The nonlinear models captured a secondary peak in Nu in the proper location at $r/D = 2$, but overpredicted the Nu value by up to 50%. Park and Sung [31] constructed a k-ε-f_μ model for low Re flows, where the turbulent viscosity damping function f_μ incorporated terms to describe damping near the wall and terms to describe the equilibrium flow farther from the wall. With the inclusion of realizability limits on eddy viscosity they were able to improve the Nu profile predictions for $r/D < 1.5$ to within 10–20% of experimental results, primarily by limiting overprediction of turbulent kinetic energy in the jet center. For the region of $r/D < 1$ the model was tuned to predict the Nu profile within 15%, giving a flat profile matching the experimental results. Given the slightly higher computational cost but potentially better results, realizability constraints are recommended for use in impinging jet flow CFD.

2.3.9 Algebraic Stress Models. Algebraic stress models (ASM) can provide a computationally inexpensive approach valid for some simple flows. The ASM models may be built with lower grid resolution in the wall region which contributes to the computational efficiency. Rather than solve complete discretized differential transport equations this category of models solves algebraic equations which require fewer calculations. In cases where the turbulent velocity fluctuations change slowly compared to changes in the mean velocity, the Reynolds stresses can be approximated as algebraic functions of the dominant mean velocity derivatives in time and space. In a simple case the ASM may use equations for calculating a length scale which are particular to the problem geometry. This length scale is used to calculate turbulent viscosity, which is used with the Boussinesq approximation to determine the Reynolds stresses. Use of this approach requires enough advance knowledge of turbulent length and time scales for the problem of interest that the quantities may be calculated using algebraic equations, a potential source of large error. For simple geometries such as pipe flow or free jets a set of equations for mixing length are available. Some ASMs simply drop the time and space derivatives of the Reynolds stresses from the equations, leaving only gradients of the mean flow velocity [32]. This approach assumes the turbulent convection and turbulent diffusion effects either are insignificant or balance each other. Unfortunately, for the impinging jet problem the boundary layer along the wall is not in equilibrium and this type of ASM is a crude approximation.

Comparative modeling by Funazaki and Hachiya showed that for an impingement problem their ASM overpredicted Nu by approximately 30%, outperforming k-ε and RNG k-ε models which typically showed 50–55% error [33]. Numerical work by Souris et al. [24] found that the ASM had better free-jet modeling than the k-ε model, which generated better results in the wall region downstream. Both models over predicted the centerline velocity decay but the ASM over prediction was not as high. The error in jet width prediction of the ASM was as high as 35% close to the wall, better than the 59% error produced by the low Reynolds number version of the k-ε model. This ASM model used the standard logarithmic law of the wall and generated poor predictions of velocity profile in the region closest to the wall (within the first quarter of the wall-jet thickness), with high jet thicknesses (up to 65% error at $r/D = 2.5$) and wall jet velocity magnitudes as much as 45% below experiment. These results do not mean the ASM correctly described the impinging flow, but rather the k-ε model resulted in gross errors, larger than the errors present when using the ASM. The ASM may be better than a number of poor k-ε models, but is not recommended as it does not yield high accuracy.

2.3.10 Complete RSM Modeling. The SMC Reynolds stress model (RSM), also known as the Reynolds stress transport model (RSTM), independently tracks all six components of the rank-2 Reynolds stress tensor, accounting for production, diffusive transport, dissipation, and turbulent transport. Common implementations require a number of constants to resolve terms such as a pressure-strain term and terms in the turbulence dissipation equation. Because the RSM model does not assume isotropic stresses it can give much better predictions of fluid behavior in turning or rotating flows that those of the two-equations models.

RSM modeling of impinging jets by Demuren [34] showed velocity predictions ranging from -40% to $+40\%$ of the experimentally measured velocities, and Reynolds Stress errors of over 100%, which was attributed to a need for an extremely dense grid (denser than that utilized in the modeling). Craft et al. [17] presented computed centerline wall-normal rms turbulent velocity levels, which matched within 25% of experiment at $H/D = 2$, but had errors as large as 80–100% for $H/D = 6$. The RSM can predict the occurrence of a secondary peak in Nu but not necessarily at the correct location [35]. This shows that although the various RSM implementations preserve all the Reynolds stress terms, they still use approximation equations based on a number of assumptions. That is, they eliminate the isotropy assumptions which yield the two-equation models but still rely upon other empirically generated equations to predict the stresses and do not give a ''perfect'' solution. Given the high computational cost compared to the eddy-viscosity models, these results are disappointing and the RSM is not recommended as an alternative.

2.3.11 The v^2f Model. Durbin's v^2-f model, also known as the ''normal velocity relaxation model,'' has shown some of the best predictions to date, with calculated Nu values falling within the spread of experimental data [36,37]. The v^2-f model uses an eddy viscosity to increase stability (rather than using a full RSM) with two additional differential equations beyond those of the k-ε model, forming a four-equation model. It uses the turbulent stress normal to the streamlines (referred to as $\overline{v^2}$) to determine the turbulent eddy viscosity, rather than the scalar turbulence intensity used in the k-ε model. It incorporates upper and lower limits on the turbulent time and length scales. In some implementations the limits on these terms have been further modified to impose realizability constraints [38].

As with the k-ω model, the v^2f model requires a dense wall grid. In some cases the v^2-f model has been shown to predict realistic levels of turbulence in the decelerating jet core but excessive turbulence levels in the shearing flow outside the core and in the wall jet [39]. Despite this difficulty and its moderately high computational cost, it is acknowledged as one of the best predictors of Nu distribution. It has an advantage over the standard k-ε series of models because it can predict the occurrence, position, and magnitude of the secondary Nu peak for low H/D. This

Table 1 Comparison of common CFD turbulence models used for impinging jet problems. The relative performance of the various models is rated qualitatively on a scale from "*" indicating undesirable model characteristics, to "**" indicating excellent model characteristics.**

Turbulence Model	Computational cost (computation time required)	Impinging jet transfer coefficient prediction	Ability to predict secondary peaks in Nu
k-ε	**** Low cost	* Poor: Expect Nu errors of 15–60%	* Poor
k-ω	**** Low-moderate	** Poor-fair: Anticipate Nu errors of at least 10–30%	** Fair: May have incorrect location or magnitude
Realizable k-ε and other k-ε variations	**** Low	** Poor-fair: Expect Nu errors of at 15–30%	** Poor-fair: May have incorrect location or magnitude
Algebraic stress model	**** Low	** Poor-fair: Anticipate Nu errors of at least 10–30%	* Poor
Reynolds stress model (full SMC)	** Moderate-high	* Poor: Anticipate Nu errors of 25–100%	** Fair: May have incorrect location or magnitude
SST	*** Low-moderate	*** Good: Typical Nu_0 errors of 20–40%	** Fair
v^2f	*** Moderate	**** Excellent: Anticipate Nu errors of 2–30%	**** Excellent
DNS/LES time-variant models	* Extremely high	**** Good-excellent	**** Good-excellent

model is highly recommended for the impinging jet problem, and its moderate computational cost is offset by its ability to closely match experimental results.

2.3.12 Hybrid Modeling. The impinging jet problem has at least three distinct flow regions with distinct flow physics. The computationally efficient two-equation models discussed previously are adjusted to perform best in one physical situation, with closure equations and coefficients based on a set of simple turbulent flows. Application to alternate geometries demonstrates the weakness of each model. No simple model has produced the ultimate answer, but by combining two or more models the CFD code can produce a compromise. For example, the model may calculate in which region the flow lies (free jet, stagnation, or wall jet) and use a model successfully tested for that particular region. The solution from the multiple models in multiple regions must then be combined at the boundaries in a smooth fashion to produce a hybrid turbulence model. In doing so the CFD program may utilize the strengths and minimize the weaknesses of each model.

Menter's shear stress transport (SST) model is one of the more successful hybrid models [40]. The SST model combines the k-ω model near the wall and the k-ε model farther from the wall to utilize the strengths of each. Smooth transition between the two is accomplished by use of a blending or weighting function based upon distance from the wall. Menter's SST model uses a variant equation for determining turbulent viscosity incorporating a number of limits, with the goal of improving predictions of turbulence in adverse pressure gradients. The SST model still requires a finely spaced mesh near the wall to produce accurate results. Validation comparisons by Esch et al. [41] showed Nu predictions within 20% of experimental results, and a Nu profile no farther than 5% above or below the profile predicted by the v^2-f model. The SST model also predicted mean velocities well, clearly better than the k-ε model and within the uncertainty of the experimental measurements. This indicates the SST model may provide predictions as good as those of the v^2-f model but at a lower computational cost, and it is recommended for this reason.

2.4 Numerical Modeling Validation by Experiments. Ultimately, all CFD results should be validated by comparison to reliable experimental results and to determine overall model error in predicting the real situation. Obviously, the model should match the experimental conditions, including all of the geometry, fluid entry, exit conditions, and target surface properties. This matching must include not only the domain boundary average velocities, pressures, and temperatures, but also their turbulent components.

3 Conclusions and Recommendations

A large number of informative studies have been conducted using the k-ε model to attempt to predict the heat/mass transfer of impinging jets, with only limited success. Examination of RANS numerical modeling techniques showed that even with high-resolution grids, the various implementations of the k-ε, k-ω, RSM, and ASM models give large errors compared to experimental data sets. The v^2f and SST models can produce better predictions of fluid properties in impinging jet flows and are recommended as the best compromise between solution speed and accuracy. Modeling work conducted by the authors indicates the v^2f model will provide more accurate predictions than the SST model. Table 1 summarizes the relative performance of the various models.

The review of recent impinging jet research publications identified a particular need of the engineering design community. Specifically, it needs a turbulence model, and associated wall treatment (if necessary), that reliably and efficiently provides time-averaged transfer coefficients for impinging jet flowfields. Given

the varied and inaccurate results of the alternatives, the SST and v^2-f models offer the best results for the least amount of computation time. Even so, they are imperfect. The improved turbulence model must correctly predict the jet spreading, turbulent flow effects in the stagnation region, and turbulent flow properties along the wall. Though inelegant, the solution by means of a hybrid model would serve this purpose if it included a turbulence model carefully adjusted to properly simulate the turning anisotropic flow field in the stagnation region.

Nomenclature

A_f = target free area
b = correlation exponent, used in $\mathrm{Nu} \propto \mathrm{Re}^b$
B = slot jet nozzle width
c_p = specific heat of fluid
D = nozzle diameter
D_h = hydraulic diameter of nozzle
f = relative nozzle area or v^2f model function
G = jet mass flow per unit of target area
h = heat transfer coefficient
H = nozzle-to-target spacing (nozzle height)
k_c = fluid thermal conductivity
k = turbulent kinetic energy
M = Mach number
n = length in wall-normal direction
Nu = Nusselt number
$\mathrm{Nu}_{\mathrm{avg}}$ = area-averaged Nusselt number
Nu_0 = Nusselt number at stagnation point
p = fluid pressure
p_{jet} = jet pitch (center-to-center distance)
Pr = Prandtl number = fluid thermal diffusivity/fluid viscosity
q'' = heat flux
Re = Reynolds Number ($=U_0D/\nu$ for a jet)
r = radial position measured from center of jet axis
Sc = Schmidt number = fluid kinematic viscosity ν/species (mass transfer) diffusivity
S_{ij} = strain rate tensor
t = time
T = temperature
$T_{0\mathrm{jet}}$ = jet adiabatic wall temperature, exiting nozzle
T_{wall} = wall surface temperature
Tu = turbulence intensity (equal to square root of [turbulent kinetic energy divided by mean kinetic energy])
U or u = fluid velocity (overbar indicates average, prime indicates fluctuating portion)
U_0 = jet initial speed, average
x = coordinate direction
y = distance from wall referenced in CFD models (normalized to "y^+" using friction velocity)
z = axial position or height, measured off of target surface
δ_{ij} = identity tensor
ε, $\tilde{\varepsilon}$ = turbulent kinetic energy dissipation rate
μ = fluid viscosity
ν = fluid kinematic viscosity
ρ = fluid density
σ_{ij} = steady stress tensor
τ_{ij} = turbulent stress tensor (Reynolds stress tensor)

Appendix: Correlation Reference in Table 2

Table 2 Correlation sets

Source	Nozzle type	Provides	Reynolds number, nozzle height range
Goldstein and Behbahani [42]	Single round nozzle	$\mathrm{Nu}_{\mathrm{avg}}$	$35{,}200 \leq \mathrm{Re} \leq 120{,}500$ $H/D = 6$ *or* 12
Goldstein et al. [43]	Single round nozzle	$\mathrm{Nu}_{\mathrm{avg}}$	$61{,}000 \leq \mathrm{Re} \leq 124{,}000$ $2 \leq H/D \leq 12$
Lytle and Webb [44]	Single round nozzle	Nu_0 and $\mathrm{Nu}_{\mathrm{avg}}$	$3600 \leq \mathrm{Re} \leq 27{,}600$ $0.1 \leq H/D \leq 1$
Martin [2]	Single round nozzle	$\mathrm{Nu}_{\mathrm{avg}}$	$2000 \leq \mathrm{Re} \leq 400{,}000$ $2 \leq H/D \leq 12$
Meola et al. [45]	Single round nozzle	$\mathrm{Nu}_{\mathrm{avg}}$	$10{,}000 \leq \mathrm{Re} \leq 100{,}000$ $10 \leq H/D$
Mohanty and Tawfek [46]	Single round nozzle	Nu_0	$4860 \leq \mathrm{Re} \leq 34{,}500$ $6 \leq H/D \leq 58$
Tawfek [47]	Single round nozzle	$\mathrm{Nu}_{\mathrm{avg}}$	$3400 \leq \mathrm{Re} \leq 41{,}000$ $6 \leq H/D \leq 58$
Wen and Jang [48]	Single round nozzle	$\mathrm{Nu}_{\mathrm{avg}}$	$750 \leq \mathrm{Re} \leq 27{,}000$ $3 \leq H/D \leq 16$
Martin [2]	Single slot nozzle	$\mathrm{Nu}_{\mathrm{avg}}$	$3000 \leq \mathrm{Re} \leq 90{,}000$ $2 \leq H/(2B) \leq 10$
Chan et al. [49]	Single slot nozzle (convex target)	Nu_0	$5600 \leq \mathrm{Re} \leq 13{,}200$ $2 \leq H/B \leq 10$
Florschuetz et al. [50]	Array of round nozzles (inline orifice nozzles)	$\mathrm{Nu}_{\mathrm{avg}}$	$2500 \leq \mathrm{Re} \leq 70{,}000$ $1 \leq H/D \leq 3$
Gori and Bossi [51]	Single slot nozzle (on cylinder)	$\mathrm{Nu}_{\mathrm{avg}}$	$4000 \leq \mathrm{Re} \leq 20{,}000$ $2 \leq H/B \leq 12$
Huber and Viskanta [52]	Array of round nozzles	$\mathrm{Nu}_{\mathrm{avg}}$	$3400 \leq \mathrm{Re} \leq 20{,}500$ $0.25 \leq H/D \leq 6$
Martin [2]	Array of round nozzles	$\mathrm{Nu}_{\mathrm{avg}}$	$2000 \leq \mathrm{Re} \leq 100{,}000$ $2 \leq H/D \leq 12$
San and Lai [53]	Array of round nozzles (staggered orifice nozzles)	Nu_0	$10{,}000 \leq \mathrm{Re} \leq 30{,}000$ $2 \leq H/D \leq 6$
Goldstein and Seol [54]	Row of round nozzles (square orifice)	$\mathrm{Nu}_{\mathrm{avg}}$	$10{,}000 \leq \mathrm{Re} \leq 40{,}000$ $0 \leq H/D \leq 6$
Martin [2]	Array of slot nozzles	$\mathrm{Nu}_{\mathrm{avg}}$	$1500 \leq \mathrm{Re} \leq 40{,}000$ $1 \leq H/(2B) \leq 40$

References

[1] Ferrari, J., Lior, N., and Slycke, J., 2003, ''An Evaluation of Gas Quenching of Steel Rings by Multiple-jet Impingement,'' J. Mater. Process. Technol., **136**(1-3), pp. 190–201.

[2] Martin, H., 1977, ''Heat and Mass Transfer between Impinging Gas Jets and Solid Surfaces,'' Adv. Heat Transfer, **13**, pp. 1–60.

[3] Jambunathan, K., Lai, E., Moss, M. A., and Button, B. L., 1992, ''A Review of Heat Transfer Data for Single Circular Jet Impingement,'' Int. J. Heat Fluid Flow, **13**(2), pp. 106–115.

[4] Donaldson, C. D., and Snedeker, R. S., 1971, ''A Study of Free Jet Impingement. Part 1. Mean Properties of Free and Impinging Jets,'' J. Fluid Mech., **45**(2), pp. 281–319.

[5] Viskanta, R., 1993, ''Heat Transfer to Impinging Isothermal Gas and Flame Jets,'' Exp. Therm. Fluid Sci., **6**, pp. 111–134.

[6] Han, J.-C., Dutta, S., and Ekkad, S., 2000, *Gas Turbine Heat Transfer and Cooling Technology*, Taylor and Francis, New York.

[7] Taniguchi, H., Miyamae, S., Arai, N., and Lior, N., 2000, ''Power Generation Analysis for High Temperature Gas Turbine in Thermodynamic Process,'' AIAA J., **16**, pp. 557–561.

[8] Lee, J., and Lee, S, 2000, ''The Effect of Nozzle Configuration on Stagnation Region Heat Transfer Enhancement of Axisymmetric Jet Impingement,'' Int. J. Heat Mass Transfer, **43**, pp. 3497–3509.

[9] Burmeister, L. C., 1993, *Convective Heat Transfer*, Wiley, New York.

[10] Kang, S. H., and Greif, R., 1992, ''Flow and Heat Transfer to a Circular Cylinder with a Hot Impinging Jet,'' Int. J. Heat Mass Transfer, **35**, pp. 2173–2183.

[11] Beaubert, F., and Viazzo, S., 2002, ''Large Eddy Simulation of a Plane Impinging Jet,'' C. R. Mecanique, **330**, pp. 803–810.

[12] Gao, S., and Voke, P. R., 1995, ''Large-eddy Simulation of Turbulent Heat Transport in Enclosed Impinging Jets,'' Int. J. Heat Fluid Flow, **16**, pp. 349–356.

[13] Hällqvist, T., 2003, ''Numerical Study of Impinging Jets with Heat Transfer,'' Licentiate Thesis, Royal Institute of Technology, Stockholm, Sweden.

[14] Olsson, M., and Fuchs, L., 1998, ''Large Eddy Simulations of a Forced Semi-confined Circular Impinging Jet,'' Phys. Fluids, **10**(2), pp. 476–486.

[15] Cziesla, T., Biswas, G., Chattopadhyay, H., and Mitra, N. K., 2001, ''Large-Eddy Simulation of Flow and Heat Transfer in an Impinging Slot Jet,'' Int. J. Heat Fluid Flow, **22**, pp. 500–508.

[16] Chen, C.-J., and Jaw, S.-Y., 1998, *Fundamentals of Turbulence Modeling*, Taylor and Francis, Washington, D. C.

[17] Craft, T. J., Graham, L. J. W., and Launder, B. E., 1993, ''Impinging Jet Studies for Turbulence Model Assessment—II. An Examination of the Performance of Four Turbulence Models,'' Int. J. Heat Mass Transfer, **36**, pp. 2685–2697.

[18] Bouainouche, M., Bourabaa, N., Desmet, B., 1997, ''Numerical Study of the Wall Shear Stress Produced by the Impingement of a Plane Turbulent Jet on a Plate,'' Int. J. Numer. Methods Heat Fluid Flow, **7**, pp. 548–564.

[19] Heyerichs, K., and Pollard, A., 1996, ''Heat Transfer in Separated and Impinging Turbulent Flows,'' Int. J. Heat Mass Transfer, **39**, pp. 2385–2400.

[20] Cooper, D., Jackson, C., Launder, B. E., and Liao, G. X., 1993, ''Impinging Jet Studies for Turbulence Model Assessment—I. Flow-field Experiments,'' Int. J. Heat Mass Transfer, **36**, pp. 2675–2684.

[21] Craft, T. J., Launder, B. E., and Suga, K., 1996, ''Development and Application of a Cubic Eddy-Viscosity Model of Turbulence,'' Int. J. Heat Fluid Flow, **17**, pp. 108–115.

[22] Turgeon, E., and Pelletier, D., 2001, ''Verification and Validation of Adaptive Finite Element Method for Impingement Heat Transfer,'' J. Thermophys. Heat Transfer, **15**, pp. 284–292.

[23] Merci, B., Vierendeels, I., DeLange, C., and Dick, E., 2003, ''Numerical Simulation of Heat Transfer of Turbulent Impinging Jets with Two-Equation Turbulence Models,'' Int. J. Numer. Methods Heat Fluid Flow, **13**, pp. 110–132.

[24] Souris, N., Liakos, H., Founti, M., Palyvos, J., and Markatos, N., 2002, ''Study of Impinging Turbulent Jet Flows Using the Isotropic Low-Reynolds Number and the Algebraic Stress Methods,'' Comput. Mech., **28**, pp. 381–389.

[25] Heck, U., Fritsching, K., and Bauckhage, K., 2001, ''Fluid Flow and Heat Transfer in Gas Jet Quenching of a Cylinder,'' Int. J. Numer. Methods Heat Fluid Flow, **11**, pp. 36–49.

[26] Wilcox, D. C., 2002, *Turbulence Modeling For CFD*, DCW Industries, La Cañada, CA.

[27] Park, T. H., Choi, H. G., Yoo, J. Y., and Kim, S. J., 2003, ''Streamline Upwind Numerical Simulation of Two-Dimensional Confined Impinging Slot Jets,'' Int. J. Heat Mass Transfer, **46**, pp. 251–262.

[28] Chen, Q., and Modi, V., 1999, ''Mass Transfer in Turbulent Impinging Slot Jets,'' Int. J. Heat Mass Transfer, **42**, pp. 873–887.

[29] Shih, T.-H., Liou, W. W., Shabbir, A., Yang, Z., and Zhu, J., 1995, ''A New k-ε Eddy-Viscosity Model for High Reynolds Number Turbulent Flows—Model Development and Validation,'' Comput. Fluids, **24(3)**, pp. 227–238.

[30] Abdon, A., and Sunden, B., 2001, ''Numerical Investigation of Impingement Heat Transfer using Linear and Nonlinear Two-Equation Turbulence Models,'' Numer. Heat Transfer, Part A, **40**, pp. 563–578.

[31] Park, T. S., and Sung, H. J., 2001, ''Development of a Near-wall Turbulence Model and Application to Jet Impingement Heat Transfer,'' Int. J. Heat Fluid Flow, **22**, pp. 10–18.

[32] Chen, C.-J., and Jaw, S.-Y., 1998, *Fundamentals of Turbulence Modeling*, Taylor and Francis, Washington, D. C.

[33] Funazaki, K., and Hachiya, K., 2003 ''Systematic Numerical Studies on Heat Transfer and Aerodynamic Characteristics of Impingement Cooling Devices Combined with Pins,'' Proceedings of ASME Turbo Expo 2003, 16–19 June 2003, Atlanta, GA.

[34] Demuren, A. O., 1994, ''Calculations of 3D Impinging Jets in Crossflow with Reynolds Stress Models,'' *Heat Transfer in Turbomachinery*, R. J. Goldstein, D. E. Metzger, A. I. Leontiev, eds., Begell House, New York, pp. 527–540.

[35] Shi, Y., Ray, M. B., and Mujumdar, A. S., 2002, ''Computational Study of Impingement Heat Transfer under a Turbulent Slot Jet,'' Ind. Eng. Chem. Res., **41**, pp. 4643–4651.

[36] Behnia, M., Parneix, S., Durbin, P. A., 1998, ''Prediction of Heat Transfer in an Axisymmetric Turbulent Jet Impinging on a Flat Plate,'' Int. J. Heat Mass Transfer, **41**, pp. 1845–1855.

[37] Behnia, M., Parneix, S., Shabany, Y., and Durbin, P. A., 1999, ''Numerical Study of Turbulent Heat Transfer in Confined and Unconfined Impinging Jets,'' Int. J. Heat Fluid Flow, **20**, pp. 1–9.

[38] Sveningsson, A., and Davidson, L., 2003, ''Assessment of Realizability Constraints and Boundary Conditions in v^2-f Turbulence Models,'' Turbulence, Heat, and Mass Transfer, **4**, pp. 585–592.

[39] Thielen, L., Jonker, H. J. J., and Hanjalić, K., 2003, ''Symmetry Breaking of Flow and Heat Transfer in Multiple Impinging Jets,'' Int. J. Heat Fluid Flow, **24**, pp. 444–453.

[40] Menter, F. R., ''Zonal Two Equation k-ω Turbulence Models for Aerodynamic Flows,'' AIAA-93-2906.

[41] Esch, T., Menter, F., and Vieser, W., 2003, ''Heat Transfer Predictions Based on Two-Equation Turbulence Models,'' TED-AJ03-542, The 6th ASME-JSME Thermal Engineering Joint Conference, 16–20, March 2003.

[42] Goldstein, R. J., and Behbahani, A. I., 1982, ''Impingement of a Circular Jet With and Without Crossflow,'' Int. J. Heat Mass Transfer, **25**, pp. 1377–1382.

[43] Goldstein, R. J., Behbahani, A. I., and Heppelmann, K. K., 1986, ''Streamwise Distribution of the Recovery Factor and the Local Heat Transfer Coefficient to an Impinging Circular Air Jet,'' Int. J. Heat Mass Transfer, **29**, pp. 1227–1235.

[44] Lytle, D., and Webb, B. W., 1994, ''Air Jet Impingement Heat Transfer at low Nozzle-plate Spacings,'' Int. J. Heat Mass Transfer, **37**, pp. 1687–1697.

[45] Meola, C., de Luca, L., and Carlomagno, G. M., 1996, ''Influence of Shear Layer Dynamics on Impingement Heat Transfer,'' Exp. Therm. Fluid Sci., **13**, pp. 29–37.

[46] Mohanty, A. K., and Tawfek, A. A., 1993, ''Heat Transfer Due to a Round Jet Impinging Normal to a Flat Surface,'' Int. J. Heat Mass Transfer, **36**, pp. 1639–1647.

[47] Tawfek, A. A., 1996, ''Heat Transfer and Pressure Distributions of an Impinging Jet on a Flat Surface,'' Heat Mass Transfer, **32**, pp. 49–54.

[48] Wen, M.-Y., and Jang, K.-J., 2003, ''An Impingement Cooling on a Flat Surface by Using Circular Jet with Longitudinal Swirling Strips,'' Int. J. Heat Mass Transfer, **46**(24), pp. 4657–4667.

[49] Chan, T. L., Leung, C. W., Jambunathan, K. J, Ashforth-Frost, S., Zhou, Y., and Liu, M. H., 2002, ''Heat Transfer Characteristics of a Slot Jet Impinging on a Semi-circular Convex Surface,'' Int. J. Heat Mass Transfer, **45**, pp. 993–1006.

[50] Florschuetz, L. W., Truman, C. R., and Metzger, D. E., 1981, ''Streamwise Flow and Heat Transfer Distributions for Jet Array Impingement with Crossflow,'' ASME J. Heat Transfer, **103**, pp. 337–342.

[51] Gori, F., and Bossi, L., 2003, ''Optimal Slot Height in the Jet Cooling of a Circular Cylinder,'' Appl. Therm. Eng., **23**, pp. 859–870.

[52] Huber, A. M., and Viskanta, R., 1994, ''Effect of Jet-Jet Spacing on Convective Heat Transfer to Confined, Impinging Arrays of Axisymmetric Jets,'' Int. J. Heat Mass Transfer, **37**, pp. 2859–2869.

[53] San, J. Y., and Lai, M., 2001, ''Optimum Jet-to-Jet Spacing of Heat Transfer for Staggered Arrays of Impinging Air Jets,'' Int. J. Heat Mass Transfer, **44**, pp. 3997–4007.

[54] Goldstein, R., and Seol, W. S., 1991, ''Heat Transfer to a Row of Impinging Circular Air Jets Including the Effect of Entrainment,'' Int. J. Heat Mass Transfer, **34**, pp. 2133–2147.